
Site U1359¹

Expedition 318 Scientists²

Chapter contents

Site summary	1
Operations	3
Lithostratigraphy	5
Biostratigraphy	8
Paleomagnetism	13
Geochemistry and microbiology	17
Physical properties	19
Stratigraphic correlation and composite section	21
Downhole measurements	21
References	23
Figures	26
Tables	108

Site summary

Integrated Ocean Drilling Program Site U1359 (proposed Site WL-RIS-04A) is located on the continental rise at 3009 meters below sea level (mbsl) (Fig. F1). The main objective at Site U1359 was to obtain an expanded record for the late Neogene to Quaternary to provide a history of climate and paleoceanographic variability and to investigate the stability of the East Antarctic Ice Sheet (EAIS) during the middle Miocene to Pleistocene extreme warm periods (e.g., Miocene climate optimum, early Pliocene, and Pleistocene marine isotope Stages 31 and 11). This record was to also provide the timing and nature of deposition of the upper seismic units (i.e., above unconformity WL-U6) defined on the Wilkes Land margin (De Santis et al., 2003; Donda et al., 2003). These units include a shift in sedimentary depocenters from the continental rise to the outer shelf, possibly corresponding to the transition from a dynamic wet-based EAIS to a more persistent cold-based EAIS (Escutia et al., 2002; De Santis et al., 2003) and inferred to occur during the late Miocene–Pliocene (Escutia et al., 2005; Rebesco et al., 2006). At Site U1359, unconformities WL-U6, WL-U7, and WL-U8 lie at approximately 4.61, 4.44, and 4.23 s two-way traveltime, respectively (approximately 520, 323, and 126 meters below seafloor [mbsf], respectively) (Fig. F2).

Site U1359 is located on the eastern levee of the Jussieu submarine channel (Figs. F1, F2). The Jussieu channel is one of the intricate networks of slope canyons that develop downslope into channels and coalescing deep-sea fans (Escutia et al., 2000). Site U1359 is positioned in an upper fan environment where the levee relief (measured from the channel thalweg to the top of the levee) is ~400 m. Multichannel seismic profiles across the site show that widespread channels with high-relief levees occur on the Wilkes Land margin above unconformity WL-U5 (Escutia et al., 1997, 2000; Donda et al., 2003). The fine-grained components of the turbidity flows traveling through the channel and hemipelagic drape are inferred to be the dominant sedimentary processes building these large sedimentary levees (Escutia et al., 1997, 2000; Donda et al., 2003). Bottom currents can further influence sedimentation in this setting (Escutia et al., 2002; Donda et al., 2003). Similar depositional systems were drilled during Ocean Drilling Program (ODP) Leg 178 along the Antarctic Peninsula (Barker, Camerlenghi, Acton, et al., 1999) and ODP Leg 188 in Prydz Bay (O'Brien, Cooper, Richter, et al., 2001).

¹Expedition 318 Scientists, 2011. Site U1359. In Escutia, C., Brinkhuis, H., Klaus, A., and the Expedition 318 Scientists, *Proc. IODP, 318*: Tokyo (Integrated Ocean Drilling Program Management International, Inc.).

doi:10.2204/iodp.proc.318.107.2011

²Expedition 318 Scientists' addresses.



At Site U1359, Holes U1359A–U1359D were drilled to total depths of 193.50, 252.00, 168.70, and 602.2 mbsf, respectively. In Holes U1359A and U1359B, the advanced piston corer (APC) system was used to refusal, followed by extended core barrel (XCB) drilling. Only the APC system was used in Hole U1359C. Hole U1359D was drilled using the rotary core barrel (RCB) system and core was only recovered below 152.2 mbsf. Silty clay with dispersed clasts is the dominant lithology observed throughout all holes at Site U1359. There are noticeable variations in the amount of biogenic components, bioturbation, and sedimentary structures, in particular the presence or absence of packages of silt–fine sand laminations and large variations in diatom abundance. Five distinct lithofacies are identified based on variations in the style of lamination, bioturbation, or the relative abundance of the biogenic component. Three lithostratigraphic units are defined on the basis of observed changes in facies associations (Figs. F3, F4). Lithostratigraphic Unit I (0–42.07 meters composite depth [mcd]) consists of decimeter-scale alternations of yellow-brown and olive-gray diatom-rich silty clays with dispersed clasts with occasional foraminifer-bearing clayey silt and sandy silt. Unit II (42.07–264.24 mcd) consists of bioturbated diatom-bearing silty clays interbedded with olive-gray diatom-bearing silty clays, which are mostly massive but contain decimeter-scale packages of olive-brown silty clay with silt laminations. Unit III extends from 264.24 mcd to the bottom of the cored section at 613.46 mcd and consists of bioturbated diatom-bearing silty clays interbedded with laminated silty clays. The laminated silty clays contain more subtle, but persistent, sub-millimeter- to millimeter-scale laminations compared to Unit II. Clasts >2 mm in size occur throughout all lithostratigraphic units and are mostly dispersed in nature (i.e., trace to 1% in abundance).

The sedimentology of Units I and II is consistent with levee deposition by low-density turbidity currents, whereas the facies associations in Unit III probably represent deposition in an environment influenced by periodic variations in contour current strength or saline density flows related to bottom water production, with turbidity currents having less influence than in the overlying units. The regular nature of the interbedding (i.e., beds 2–5 m thick) of the laminated and bioturbated facies within all three lithostratigraphic units suggests that the sedimentary record recovered from Site U1359 is cyclic in nature (Figs. F5, F6). The diatom-bearing and diatom-rich silty clays (Facies 1 and 2) were probably deposited by hemipelagic sedimentation in a higher productivity environment relative to the other facies. The clays and silty clays (Facies 3–5) indicate high terrigenous sedimentation rates and/or lower biogenic

productivity, perhaps related to the duration of seasonal sea ice cover regulating light availability in surface water or wind-regulated control of the mixed layer depth, which in turn controls productivity. The opposite scenario may apply for the diatom-bearing to diatom-rich silty clay facies (Facies 1 and 2). An increase in terrigenous input may result from ice advance across the shelf or increase in sedimentation from bottom currents. The passage of cold saline density flows related to bottom water production at the Wilkes Land margin (e.g., high-salinity shelf water flowing from the shelf into the deep ocean to form Antarctic Bottom Water [AABW]) should also be considered as a potentially important sediment transport mechanism. The depositional model for recovered sediments at Site U1359 may represent a continuum of all three processes, in addition to pelagic and ice-rafted components, as indicated by the presence of diatom remains and dispersed clasts throughout.

Combined micropaleontology assigns the recovered successions at Site U1359 to the late middle Miocene to late Pleistocene (Fig. F7). Integrated diatom, radiolarian, foraminifer, and magnetostratigraphic data highlight a late Pliocene to early Pleistocene condensed interval (between ~2.5 and 1.5 Ma) and another one during the early late to mid-late Miocene (between ~9.8 and 7 Ma).

Miocene diatom assemblages mainly include open-water taxa. In addition, a notable increase in the abundance of stephanopyxid specimens may be interpreted as either an indication of shallowing water depths or an increase in reworking of shallower water sediments. The lack of planktonic and benthic foraminifers suggests that bottom waters were corrosive during the late middle Miocene to calcareous foraminifers except for brief periods (e.g., around ~10 Ma, when calcareous benthic foraminifers were preserved). Also during the Pliocene, open-water taxa and variable abundances of benthic, neritic, and sea ice-associated taxa dominated diatom assemblages. The dinocyst assemblages predominantly comprise heterotrophic taxa, indicating that the biosiliceous-rich sediments were deposited in a high-productivity and sea ice-influenced setting. High abundances of sporomorphs reworked from Paleogene, Mesozoic, and Paleozoic strata suggest continuous strong erosion in the hinterland. The general lack of planktonic and calcareous benthic foraminifers suggests that Pliocene bottom waters were corrosive to the thin-shelled tests of planktonic foraminifers. Diatom and radiolarian Pleistocene assemblages at Site U1359 are dominated by typical Neogene Southern Ocean open-water taxa with variable abundances of benthic, neritic, and sea ice-associated diatom taxa. This indicates a pelagic, well-ventilated, nutrient-rich, sea ice-influenced setting, corroborated by the presence

of heterotrophic-dominated dinocyst assemblages. The preservation of planktonic foraminifers in the Pleistocene indicates that bottom waters were favorable to the preservation of calcium carbonate. Further, pervasive reworked sporomorphs of Paleogene, Mesozoic, and Paleozoic age again point to continuing strong erosion in the hinterland.

Paleomagnetic investigations at Site U1359 involved analysis of discrete samples from Holes U1359A, U1359B, and U1359D and measurement of archive halves from all four holes. A composite polarity log was correlated to the geomagnetic polarity timescale (GPTS) of Gradstein et al. (2004), documenting a complete Pliocene section from the top of Chron C2An to the bottom of Chron C3An (Fig. F8). A gap including Chron Cn2 and a period of extremely slow (and probably discontinuous) sediment accumulation from Chron C3Ar to the top of Chron C5n aligns with the biostratigraphic assessments.

Routine headspace gas analyses were carried out on samples from Holes U1359A–U1359D, and 71 samples were taken for analyses of weight percent carbonate, carbon, nitrogen, and sulfur content, as well as major and trace element analyses. Furthermore, 51 interstitial water samples were taken close to the microbiology samples from the top ~20 m (0.1–20.1 mbsf) of the holes.

CaCO₃ contents for most samples vary between <1 and 3.2 wt%. A distinct carbonate-rich layer with a CaCO₃ content of 39.7 wt% was found at 372.45 mbsf and corresponds to a minor lithology of diatom-bearing nannofossil ooze. On the basis of the distribution patterns of the major and trace elements, four broad intervals can be distinguished between 0 and ~200, ~210 and ~310, ~310 and 536, and 547.39 and 594.79 mbsf.

The interstitial water measurements reveal chemical gradients that are consistent with active diagenesis of buried organic matter within the sulfate reduction zone (SRZ). Significant levels of sulfate at the bottom of the observed profile (~23 mM at 20.1 mbsf) imply that the sampled interval did not reach the carbon dioxide (methanic) reduction zone (see the “[Site U1357](#)” chapter for contrasting behavior).

Microbiological sampling was conducted in Hole U1359B and was supported with pore water sampling (Fig. F9). A total of 52 ten-centimeter whole rounds were taken from the top 20 m and frozen at –80°C for onshore phospholipid analyses and molecular 16S rRNA sequencing. Between 20 and 200 mbsf, seventeen 5 cm³ samples were taken and preserved for onshore molecular 16S rRNA sequencing.

The physical property program for Site U1359 includes routine runs on the Whole-Round Multi-sensor Logger (WRMSL), which includes the gamma

ray attenuation (GRA) bulk density, magnetic susceptibility, and *P*-wave velocity logger (PWL) sensors, as well as natural gamma ray (NGR) measurements. *P*-wave velocity was also analyzed, and samples were taken for moisture, density, and porosity measurements from Holes U1359A, U1359B, and U1359D. Thermal conductivity measurements were taken in cores from all holes. Cyclicities at several scales are observed in the intervals where the magnetic susceptibility ranges between 40 and ~100 instrument units. Furthermore, the NGR data together with the magnetic susceptibility and GRA density data were used to correlate the four holes drilled at Site U1359 and to define a composite record (see “[Stratigraphic correlation and composite section](#)”). In addition, pronounced lower density values between 50 and 65 mbsf (50 and 65 m core composite depth below seafloor, method A [CCSF-A]), below the lithostratigraphic Unit I–II transition, suddenly drop at ~99.5 mbsf (~101 m CCSF-A), which coincides with the lithologic change from diatom-bearing to diatom-rich silty clays (lithostratigraphic Subunit IIa–IIb transition), as well as a shift to slightly lower values at ~248 mbsf (~264 m CCSF-A; lithostratigraphic Unit II/III boundary).

Downhole logging measurements in Hole U1359D were made after completion of RCB coring to a total depth of 602.2 mbsf (drilling depth below seafloor [DSF]). Three tool strings were deployed in Hole U1359D, the triple combination (triple combo), Formation MicroScanner (FMS)-sonic, and Versatile Sonic Imager (VSI). Hole U1359D was divided into two logging units (100–260 and 260–606 mbsf) on the basis of the logs (Fig. F10). The upper logging unit is characterized by high-amplitude swings in bulk density, NGR, and resistivity values. The transition to the unit below is gradual. Logging Unit 2 is characterized by generally lower amplitude bulk density and resistivity variations than the unit above, but the 2–5 m scale alternations are still clearly defined. NGR continues to show high variability, and several large drops in NGR values are observed between 350 and 450 mbsf. Near the base of the hole at 574–580 mbsf, a 6 m interval of higher bulk density and resistivity indicates a cemented bed or series of cemented beds. Heat flow at Site U1359 was estimated at 62.4 mW/m², a typical value for the ocean floor.

Operations

Transit to Site U1359

We began transit to Site U1359 at 1530 h on 7 February 2010. While departing the shelf, we had to negotiate around and through an assortment of pack ice and grounded ice bergs; these became less concen-

trated and finally disappeared as we moved off the shelf. As we arrived in the vicinity of Site U1359 at midnight, we experienced near-gale force winds, rough seas, and visibility down to 4 nmi in freezing rain. We lowered the thrusters and stabilized near the site using the Global Positioning System but waited on the weather to improve until the next morning (Table T1). The 73 nmi transit to Site U1359 was accomplished in 8.5 h at 8.6 kt. All times in this section are given in local ship time, which was Universal Time Coordinated + 11 h.

Site U1359

Hole U1359A

After 7 h, the weather conditions improved enough so that we could assemble the drill string to the seafloor. We started APC coring in Hole U1359A at 1800 h on 8 February 2010 with the bit at 3012 meters below rig floor (mbrf). Based on recovery of the first core, the water depth was 3020.9 mbrf, 9.1 m deeper than the corrected depth from the precision depth recorder. Cores 318-U1359A-1H through 17H penetrated to 145.4 mbsf and recovered 124.27 m (86%). Temperature measurements were made while taking Cores 318-U1359A-4H, 7H, 10H, and 13H (29.1, 57.6, 86.1, and 114.6 mbsf, respectively). Non-magnetic core barrels were used for all piston cores after Core 318-U1359A-1H but were not oriented. After APC refusal, we deepened the hole with XCB Cores 318-U1359A-18X through 22X from 145.4 to 193.5 mbsf and recovered 29.81 m (62%). Total recovery for Hole U1359A was 80%. Rather than continuing to deepen the hole with the XCB, we decided to stop so that we could core two more APC holes to provide a more complete section.

The bit cleared the seafloor at 1700 h on 9 February, and we offset the vessel 25 m west-southwest.

Hole U1359B

Coring in Hole U1359B began at 1815 h with the bit at 3017 mbrf. Seafloor was established at 3018.8 mbrf. APC Cores 318-U1359B-1H through 23H penetrated to 209.0 mbsf and recovered 183.59 m (88%) (Table T1). Nonmagnetic core barrels were used for all APC cores. We deepened the hole with XCB for Cores 318-U1359B-24X through 28X from 209.0 to 252.0 mbsf and recovered 15.33 m (36%). The total recovery for Hole U1359B was 79%. The bit was pulled clear of the seafloor at 2240 h on 10 February, and the vessel was offset 25 m west-southwest of Hole U1359B.

Hole U1359C

Coring in Hole U1359C began at 2340 h on 11 February with the bit at 3020 mbrf. Seafloor depth was

established at 3022.3 mbrf. APC Cores 318-U1359C-1H through 18H penetrated to 168.7 m and recovered 150.73 m (89%). We planned to stop coring at this time to be able to depart for high-priority shelf sites so that we could take advantage of a forecasted period of good weather. We planned on returning to this site, so we did not retrieve the seafloor beacon at this time. The bit cleared the seafloor at 1620 h and was back onboard at 2340 h on 11 February. We departed for Site U1360 at 2345 h on 11 February. The total time on Site U1359 was 89.25 h.

Return to Site U1359

After operations at Site U1360 and multiple attempts to return to that site and other shelf sites, we returned to Site U1359 at 2200 h on 19 February 2010.

Hole U1359D

A RCB bottom-hole assembly was assembled and lowered to the seafloor. Seafloor was tagged with the bit at 3023.0 mbrf, and drilling started at 0530 h on 20 February. We drilled without coring to 152.2 mbsf and then started RCB coring at that depth to overlap with previous APC/XCB coring that had penetrated to 252 mbsf. RCB Cores 318-U1359D-2R through 48R penetrated from 152.2 to 602.2 mbsf and recovered 269.7 m (60%). The last core was recovered on deck at 1145 h on 23 February.

In preparation for downhole logging, we flushed the hole with a 50 bbl mud sweep and made a wiper trip up to 82.6 mbsf and then back down to 602.2 mbsf. After another 50 bbl sepiolite mud sweep, we released the bit at the bottom of the hole, displaced the hole with 191 bbl of 10.5 ppg mud, and raised the end of the pipe to 96.9 mbsf for logging.

We were able to conduct two very successful logging runs in excellent hole conditions. The triple combo and FMS-sonic tool strings were able to log the entire hole from 602 mbsf up to the end of the pipe. The FMS-sonic tool string was back on deck at 2000 h on 23 February. In accordance with our Marine Mammal Protocol, we waited until daylight the next day before conducting the check shot log utilizing the Schlumberger VSI.

We rigged up the VSI and started lowering it downhole at 0745 h on 24 February. The VSI was able to reach within 5 m of bottom of the hole, but we had to postpone starting the check shots because a few whales had entered within the mammal exclusion zone. Once we were able to start, we discovered that the VSI caliper arm could not be extended to clamp the tool against the borehole wall. However, we were able to set the tool on the bottom of the hole and get good enough coupling with the formation to collect

data at that depth. We could have retrieved the VSI tool for repair/replacement, but we decided conclude logging so we could attempt to reach one of our high-priority shelf sites. After we recovered the VSI at 1330 h on 24 February, we retrieved the drill string, with the end of the pipe clearing the seafloor at 1440 h and arriving back on the rig floor at 2050 h. We departed for the last attempt at occupation of one of the high-priority shelf sites at 2245 h on 24 February.

Lithostratigraphy

Four holes were drilled at Site U1359. Holes U1359A–U1359D were drilled to total depths of 193.50, 252.00, 168.70, and 602.2 mbsf, respectively. In Holes U1359A and U1359B, the APC system was used to refusal, followed by XCB drilling. Only the APC was used in Hole U1359C. Hole U1359D was drilled using the RCB system, and core was only recovered below 152.2 mbsf. Silty clay with dispersed clasts is the dominant lithology observed throughout all holes at Site U1359 (Figs. F3, F4). Noticeable variations in the amounts of biogenic components and bioturbation and sedimentary structures are apparent, in particular the presence or absence of packages of silt/fine sand laminations and large variations in diatom abundance.

Although texturally almost all of the sediments cored at Site U1359 are silty clays with dispersed clasts, five distinct lithofacies are identified based on variations in the style of laminations, bioturbation, or the relative abundance of the biogenic component. Three lithostratigraphic units are defined on the basis of observed changes in facies associations (Figs. F3, F4). Because four overlapping holes were cored at this site, unit boundary depths in meters below seafloor are not consistent between holes. The unit boundaries are defined in the hole where their depths (in meters below seafloor) are the greatest. Table T2 shows the unit boundary depths in all holes and conversion to meters composite depth as defined in “[Stratigraphic correlation and composite section.](#)” Lithostratigraphic Unit I (0–42.07 mcd) consists of decimeter-scale alternations of yellow-brown and olive-gray diatom-rich silty clays with dispersed clasts and occasional foraminifer-bearing clayey silt and sandy silt. Unit II (42.07–264.24 mcd) consists of bioturbated diatom-bearing silty clays interbedded with olive-gray diatom-bearing silty clays that are mostly massive but contain decimeter-scale packages of olive-brown silty clay with silt laminations. Unit III extends from 264.24 mcd to the bottom of the cored section at 613.46 mcd and consists of bioturbated diatom-bearing silty clays interbedded with laminated silty clays. The laminated silty clays con-

tain more subtle, but persistent, submillimeter- to millimeter-scale laminations compared to Unit II.

Clasts >2 mm in size occur throughout all lithostratigraphic units and are mostly dispersed in nature (i.e., trace to 1% in abundance). However, there are some variations in clast abundance (Fig. F3). Silty clays with common clasts (i.e., 1%–5%) are present between 200.1 and 247.1 mbsf (Cores 318-U1359D-7R through 12R), whereas below 372.4 mbsf (interval 318-U1359D-25R-1, 0 cm) clasts occur in trace amounts only (Fig. F4).

Sediments from lithostratigraphic Units I and II are consistent with levee deposition by low-density turbidity currents, whereas the facies associations in Unit III probably represent deposition in an environment influenced by periodic variations in contour current strength or saline density flows related to bottom water production, with turbidity currents having less influence than the overlying units. The regular nature of the interbedding (i.e., beds 2–5 m thick) of the laminated and bioturbated facies within all three lithostratigraphic units suggests that the sedimentary record recovered at Site U1359 is cyclic in nature.

Facies descriptions

Five lithofacies were identified at Site U1359:

- Facies 1: interbeds of yellowish brown to olive-gray diatom-bearing to diatom-rich silty clays with foraminifer-bearing horizons (Fig. F11). The yellow-brown silty clay units have a mottled appearance attributed to bioturbation on the basis of centimeter-scale oblate burrows. The olive-gray silty clays vary locally to include clayey silt and sandy silt intervals, particularly in the foraminifer-bearing horizons.
- Facies 2: bioturbated diatom-bearing to diatom-rich silty clays and diatom oozes that are light greenish gray (Fig. F12). In unlithified sediments of this lithofacies, a mottled appearance that is attributed to bioturbation on the basis of centimeter-scale oblate burrows is common. In lithified sediments, common to abundant bioturbation with well-defined horizontal burrows with backfill and centimeter-scale oblate burrows is displayed. Some intervals exhibit faint decimeter-scale bedding defined by slight color variations. Based on smear slide estimates, these appear to reflect changes in diatom abundance.
- Facies 3: massive silty clays and clays that are olive-gray in color and contain <10% diatoms (Fig. F13). These silty clays are mostly massive, but subtle centimeter- to meter-scale colored interbeds are apparent with a light gray color grading down

into a darker gray color. Typically the colored interbeds have a sharp basal contact.

- Facies 4: laminated silty clays and clays, olive-gray to olive-brown, with packages as thick as 25 cm of rhythmic millimeter- to centimeter-scale silt and clay parallel laminations (Figs. F14, F15). The composition of individual laminations can be highly variable with some laminations rich in silt-sized quartz and others rich in diatoms (Fig. F16).
- Facies 5: finely laminated dark greenish gray silty clays and clays with persistent parallel submillimeter- to millimeter-scale laminations as defined by color or grain-size variations up to silt grade (Fig. F17). Discrete packages of rhythmic laminations, as noted in Facies 4, are absent to rare. Individual beds of this facies are as thick as several meters.

Smear slide analysis indicates (Figs. F18, F19, F20, F21, F22; see also Site U1359 smear slides in “Core descriptions”) that carbonate-cemented clay occasionally occurs as a minor component throughout the core. Pyrite occurs as a minor component (2%–10%) in most of the major lithofacies. Pyrite is found in higher abundance within some dark-layered laminations (15%–40%), particularly within the diatom-rich silty clay lithofacies (see below).

Interpretation

The diatom-bearing and diatom-rich silty clays (Facies 1 and 2) were probably deposited by hemipelagic sedimentation in a higher productivity environment relative to the other facies. The clays and silty clays (Facies 3–5) indicate high terrigenous sedimentation rates and/or lower biogenic productivity, perhaps related to the duration of seasonal sea ice cover regulating light availability in surface water or wind-regulated control of the mixed-layer depth, which in turn controls productivity. The opposite scenario may apply for the diatom-bearing to diatom-rich silty clay facies (Facies 1 and 2). An increase in terrigenous input may result from ice advance across the shelf or increase in sedimentation from bottom currents.

The laminated silty clays (Facies 4 and 5) may originate from three potential depositional mechanisms: low-density turbidity currents, contour currents, and saline density flows. The rhythmic couplets of silt and clay laminations with sharp bases (Facies 4) are commonly overlain by massive silty clays (Facies 3) passing upward into bioturbated diatom-bearing silty clays (Facies 2). These facies associations have similarities to the distal muddy turbidite model of Stow and Piper (1984) (Bouma divisions T_{D-E}). The absence of coarser grained deposits and ripple laminations in the Site U1359 section hints at levee

deposition by low-density turbidity currents, which is consistent with the channel-levee complex interpretation of seismic profiles that cross the drill site (Escutia et al., 2008). Sediment redistribution may have occurred because of contour current influence, with variations in lamination thickness and particle size in Facies 4 or 5 indicating fluctuations in bottom current strength. The passage of cold saline density flows related to bottom water production at the Wilkes Land margin (e.g., High-Salinity Shelf Water flowing from the shelf into the deep ocean to form AABW) should also be considered as a potentially important sediment transport mechanism. The depositional model for recovered sediments at Site U1359 may represent a continuum of all three processes, in addition to pelagic and ice-rafted components as indicated by the presence of diatom remains and dispersed clasts throughout.

Unit descriptions

Based on visual core descriptions and smear slide analyses, Site U1359 is divided into three lithostratigraphic units (Fig. F3).

Unit I

Intervals: 318-U1359A-1H-1, 0 cm, through 6H-4, 44 cm (0–43.54 mbsf); 318-U1359B-1H-1, 0 cm, through 5H-CC, 21 cm (7.58 to >41.60 mbsf [base of unit not recovered]); and 318-U1359C-1H-1, 0 cm, through 5H-2, 144 cm (0–38.64 mbsf)

Depth: 0–42.07 mcd

Age: Pleistocene

Unit I consists of yellowish brown diatom-bearing to diatom-rich silty clays (Facies 1) interbedded at decimeter scale with olive-gray silty clay (Facies 3), both with dispersed clasts. Foraminifers are present throughout Unit I but are most abundant (>10%) in Cores 318-U1359A-4H, 318-U1359B-4H, and 318-U1359C-3H and 4H, where they are concentrated in decimeter-scale beds of clayey silt/silty sand (Fig. F11). The base of Unit I is defined as the lowermost foraminifer-bearing horizon identified by smear slide and macroscopic analysis. Millimeter-scale pockets of silt and fine sand occur throughout the unit. Dispersed clasts also occur throughout Unit I and are granule to pebble in size. Clast lithologies include basalt and quartzite. Millimeter- to centimeter-scale silt laminations are present in this interval below 5.6 mbsf (Section 318-U1359A-2H-4) and occur in ~25 cm thick packages (Facies 4) (Fig. F14).

Interpretation

Deposition of these facies is interpreted to result from hemipelagic sedimentation, with possible

transport and resorting by currents related to low-density turbidity currents, saline density flows, or contour currents. Coarse-grained gravel clasts interpreted as ice-rafted detritus occur throughout this unit. The mottled appearance of the yellow-brown intervals (Facies 1) is attributed to moderate levels of bioturbation.

Unit II

Subunit IIa

Intervals: 318-U1359A-6H-4, 44 cm, through 12H-3, 127 cm (43.54–99.87 mbsf); 318-U1359B-5H-CC, 21 cm, through 11H-6, 15 cm (>41.6–100.85 mbsf); and 318-U1359C-5H-2, 144 cm, through 11H-2, 97 cm (38.64–95.17 mbsf)

Depth: 42.07–102.1 mcd

Age: early to late Pliocene

Subunit IIb

Intervals: 318-U1359A-12H-3, 127 cm, through 22X-CC, 38 cm (99.87 to >190.26 mbsf [base of subunit is below last recovered core]); 318-U1359B-11H-6, 15 cm, through 23H-1, 0 cm (100.85–208.18 mbsf); 318-U1359C-11H-2, 97 cm, through 18H-CC, 20 cm (95.17 to >169.08 mbsf [base of subunit is below last recovered core]); and 318-U1359D-2R-1, 0 cm, through 7R-1 (<152.20–200.10 mbsf)

Depth: 102.1–217.24 mcd

Age: late Miocene to early Pliocene

Subunit IIc

Interval: 318-U1359D-7R-1, 0 cm, through 11R-6, 122 cm (200.10–247.11 mbsf)

Depth: 217.24–264.24 mcd

Age: late Miocene

Unit II consists of massive to laminated (olive-gray to liver-brown) silty clays interbedded with mottled greenish gray diatom-bearing/diatom-rich silty clays. Unit II is distinguished from Unit I on the basis of a lack of foraminifers (e.g., Facies 1) and a distinct change in color. The olive-gray silty clays (Facies 3) commonly pass sharply into and out of dark olive-brown silty clays that contain discrete intervals of silt laminations (Facies 4), many of which are defined as rhythmic couplets of silt and clay, as discussed in the facies section above. However, wispy and indistinct silt laminations, stringers, and silt/fine sand pockets (<4 mm in size) are also present. The olive-gray intervals commonly grade upward into greenish gray massive diatom-bearing (to diatom-rich) silty clays with a mottled appearance (Facies 2). The mottling is attributed to moderate levels of bioturbation, as there are common centimeter-scale oblate burrows,

particularly near contacts with olive-gray and olive-brown silty clays. Dispersed clasts occur throughout Unit II. This unit is further divided into three subunits (IIa, IIb, and IIc). Subunit IIb is distinguished from Subunit IIa on the basis of a notable increase in diatom abundance with diatom-bearing and diatom-rich sediments (Facies 2, 3, and 4) becoming more common (Figs. F3, F4). Subunit IIc is defined on the basis of a significant increase in clast abundance with silty clays with common clasts (i.e., 1%–5%) occurring throughout.

Interpretation

These facies associations are interpreted to result from hemipelagic sedimentation and deposition by contour currents, possibly interrupted by episodic low-density turbidity currents. The presence of well-defined packages of silt laminations (Facies 4) suggests levee deposition of low-density muddy turbidity currents, as discussed in the facies section. However, transport and resorting by currents related to saline density flows or contour currents is also a possibility. There is clear evidence of cyclical variability (meter scale) in the lithologic and physical properties expressed as alternating intervals of bioturbated silty clays (Facies 2) and massive (Facies 3) and laminated (Facies 4) silty clay facies (Fig. F5), as well as at decimeter scale between the massive and laminated silty clay lithofacies (Fig. F6). The down-hole increase in diatom content associated with Subunit IIb and below is suggestive of increased surface water productivity or reduction in terrigenous input. Ice rafting of coarse-grained gravel clasts is interpreted to have occurred throughout the deposition of Unit II but was a more significant sediment contributor during the deposition of Subunit IIc.

Unit III

Interval: 318-U1359D-11R-6, 120 cm, through 48R-CC, 25 cm (247.11–596.31 mbsf)

Depth: 264.24–613.46 mcd

Age: middle to late Miocene

Unit III is characterized by dark greenish gray planar-laminated clays and silty clays (Facies 5) that are interbedded at meter scale with light greenish gray diatom-bearing to diatom-rich silty clay with abundant bioturbation (Facies 2). Unit III is differentiated from Unit II on the basis of dark greenish gray clay and silty clay interbeds that are sparsely bioturbated and display planar submillimeter-scale (pinstripe) to millimeter-scale laminations throughout (Facies 5). The diatom-rich silty clays with abundant bioturbation (Facies 2) are similar to those documented in Unit II. The increased lithification of Unit III allows for improved identification of bioturbation style and

intensity, and well-defined centimeter-scale horizontal and oblate burrows are common (Fig. F23). Above 452.6 mbsf (interval 318-U1359D-33R-3, 44 cm), laminations are faintly defined by color or very subtle grain-size variations and are submillimeter (pinstripe) to millimeter scale in thickness. Below this depth, laminations are characterized by more distinct grain-size variations and consist of pinstripe to millimeter-scale (generally <5 mm thick) layers of well-sorted quartz-rich silt. Dispersed granule- to pebble-sized clasts occur throughout, but below 372.4 mbsf (Section 318-U1359D-25R-1) they are rare relative to the overlying units (Fig. F3). Unit III contains a conspicuous diatom-bearing nannofossil-bearing ooze (Fig. F24) interval between Sections 318-U1359D-24R-6 and 25R-1 (see “**Biostratigraphy**”). This ooze also contains a minor foraminifer component.

Interpretation

The laminated intervals most likely represent an environment that is influenced by saline density flows and contour currents and, relative to overlying Units I and II, probably less turbidity current influence was present. This may represent a depositional environment that is more distal on the levee than Units I and II. However, meter-scale cyclicity similar to that noted in Unit II continues into Unit III, with alternating beds of bioturbated silty clays (Facies 2) and laminated silty clays (Facies 5) occurring throughout. The intervals of bioturbated silty clays (Facies 2) may represent variations in terrigenous input or bottom water oxygenation that in turn may ultimately be tied to changes in ice sheet or sea ice extent. Evidence of ice rafting of gravel-sized clasts is present throughout this unit but is noticeably less below 372.4 mbsf (Section 318-U1359D-25R-1).

Clay mineralogy

Forty-eight samples from Site U1359 were prepared for X-ray diffraction (XRD) analysis of the clay fraction. These samples were taken from all four holes drilled at this site (Holes U1359A–U1359D), but the majority are derived from Holes U1359A and U1359D. The combined sample set provides a low-resolution clay mineral stratigraphy for the entire section (0–596 mbsf), with an average sample spacing of one sample every 15 m (Fig. F25).

The clay mineral assemblages at Site U1359 are dominated by the illite, smectite, and chlorite groups (Fig. F25). The relative proportion of illite remains relatively invariant through the sequence, whereas larger fluctuations are noted in the chlorite and smectite records. Specifically, a higher fraction of smectite (corresponding to a lower fraction of chlo-

rite) is present between ~14 and 64 mbsf and between ~120 and 240 mbsf. Increased concentration of smectite in these intervals may represent periods of increased supply of clay material transported by currents from the Ross Sea because smectite is not presently produced in abundance locally on the Wilkes Land margin but instead is thought to be derived from weathering of volcanic rock in the Ross Sea (see Damiani et al., 2006).

Kaolinite is generally present in trace amounts in the samples analyzed from Site U1359. The only interval in which kaolinite is present in greater abundance, but still representative of a minor clay component, is between ~14 and 25 mbsf within the Pleistocene section (Cores 318-U1359A-3H and 4H) (Fig. F25). Kaolinite has been previously observed in Quaternary cores from the Wilkes Land margin (Busetti et al., 2003; Damiani et al., 2006) and represents reworked material from Paleogene or older sediments.

Overall, the clay mineral assemblages present in the upper Miocene–Pleistocene succession recovered at Site U1359 are similar to those previously reported from Neogene records in the Antarctic margin (e.g., Ehrmann et al., 1991; Hillenbrand and Ehrmann, 2005). Abundant illite and chlorite indicate active physical weathering of granitoid and metamorphic parent rocks in a glacial regime.

Given the low-resolution sampling for clay XRD analyses, the degree of variability on short-length scales through the section is uncertain. Five samples, however, were taken from different lithofacies in Core 318-U1359D-4R (171.30–180.00 mbsf). Within this core, substantial variation in the relative abundance of smectite (Fig. F25) suggests that higher resolution analysis may reveal significant changes in the clay composition of the cyclically deposited diatom-rich and diatom-poor beds present in Units II and III.

Biostratigraphy

Core catcher samples from all holes and selected core samples from Holes U1359A and U1359D, as well as selected samples from Holes U1359B and U1359C, were analyzed for diatoms, silicoflagellates, ebridians, actiniscidians, chrysophyte cysts, and sponge spicules (Tables T3, T4, T5, T6). All core catcher samples from Holes U1359A, U1359B, and U1359D were examined for radiolarians (Table T7). Fourteen samples were examined for calcareous nannofossils from Hole U1359B (Table T8). Thirteen samples from Hole U1359A and seventeen samples from Hole U1359D were processed for palynology (Table T9). Selected core catcher samples from Holes U1359A, U1359B, and U1359D were examined for foraminifers (Table T10).

The abundance data for each of these microfossil groups are summarized in Figure F26. Siliceous microfossils are present throughout the recovered intervals in variable preservation. Diatoms are present in all samples examined except for Sample 318-U1359A-3H-3, 82 cm (13.92 mbsf), whereas radiolarians occur in all samples studied. Rare and poorly preserved calcareous nannofossils occur in Holes U1359A, U1359B, and U1359C but are common and well preserved in Hole U1359D (Fig. F26). Palynomorphs are present in most core catcher samples processed for palynology. Planktonic and benthic foraminifers occur sporadically in core catcher samples from all holes; planktonic foraminifers are common to abundant in Samples 318-U1359A-4H-CC (28.56 mbsf) and 5H-CC (29.34 mbsf) and 318-U1359D-24R-CC (371.86 mbsf).

An upper middle Miocene through upper Pleistocene sedimentary succession was recovered at Site U1359. Integrated diatom, radiolarian, foraminifer, and magnetostratigraphic data indicate a late Pliocene to early Pleistocene hiatus (~2.5–1.5 Ma) and a lower to mid upper Miocene condensed interval (~9.8–7 Ma). All index events (biostratigraphy and magnetostratigraphy) are compiled in Table T11. The age-depth models for individual holes are presented in Figure F27 and combined for all four holes in Figure F7 (in meters below seafloor) and in Figure F28 (in meters composite depth).

Siliceous microfossils

Recovered sediments at Site U1359 contain well-preserved biogenic silica dominated by diatoms and radiolarians, with variable abundances of silicoflagellates, ebridians, chrysophyte cysts, and sponge spicules. Diatoms and radiolarians provide the primary age control in holes drilled at Site U1359. Assemblages are dominated by typical Neogene Southern Ocean open-water taxa with variable abundances of benthic, neritic, and sea ice-associated diatom taxa, indicating a high-nutrient, high-productivity sea ice-influenced setting throughout the depositional history of Site U1359.

Diatoms

Combined holes at Site U1359 revealed a clear succession of index species (e.g., Cody et al., 2008) (Figs. F7, F27, F28; Table T11). Samples 318-U1359A-1H-1, 2 cm, through 5H-CC (0.02–29.34 mbsf) and 318-U1359C-1H-1, 40.0 cm, through 5H-1, 35.0 cm (0.40–36.05 mbsf), are assigned to the Pleistocene; Samples 318-U1359A-6H-2, 132.5 cm, through 22X-CC (41.42–190.26 mbsf), 318-U1359B-5H-2, 131.0 cm, through 17H-1, 35 cm (39.01–150.55 mbsf), and 318-U1359C-5H-2, 140.0 cm, through 16H-3, 35 cm

(38.60–143.55 mbsf), are assigned to the Pliocene; and Samples 318-U1359B-20H-4, 25 cm, through 28X-CC (183.45–243.11 mbsf), and 318-U1359D-4R-5, 105 cm, through 48R-CC (178.35–596.31 mbsf) are assigned to the middle Miocene.

Pleistocene

Four diatom datums were recognized in Samples 318-U1359A-1H-1, 2 cm, through 5H-CC (0.02–29.34 mbsf) and 318-U1359C-1H-1, 40.0 cm, through 5H-1, 35.0 cm (0.40–36.05 mbsf) (Tables T3, T5, T11):

- Last occurrences (LOs) of
 - *Actinocyclus ingens* (0.54 Ma),
 - *Thalassiosira elliptipora* (0.68 Ma),
 - *Fragilariopsis barronii* (1.24 Ma), and
 - *Rouxia antarctica* (1.50 Ma).

The succession of diatom species (and radiolarians) indicates the Pliocene/Pleistocene boundary interval (1.81 Ma) is missing in a ~1 m.y. hiatus between ~2.5 and 1.5 Ma (Figs. F7, F28).

Pliocene

Fifteen diatom datums were recognized in Samples 318-U1359A-6H-2, 132.5 cm, through 22X-CC (41.42–190.26 mbsf), 318-U1359B-5H-2, 131.0 cm, through 17H-1, 35 cm (39.01–150.55 mbsf), and 318-U1359C-5H-2, 140.0 cm, through 16H-3, 35 cm (38.60–143.55 mbsf) (Tables T3, T4, T5, T11):

- LOs of
 - *Thalassiosira vulnifica* (2.17 Ma),
 - *Actinocyclus fasciculatus* (2.16 Ma),
 - *Fragilariopsis interfrigidaria* (2.43 Ma),
 - *Thalassiosira insigna* (2.48 Ma),
 - *Thalassiosira inura* (2.54 Ma),
 - *Rouxia diploneides* (2.62 Ma), and
 - *Fragilariopsis clementia* (4.56 Ma) and
- First occurrences (FOs) of
 - *Fragilariopsis kerguelensis* (2.20 Ma),
 - *T. vulnifica* (3.15 Ma),
 - *T. insigna* (3.25 Ma),
 - *F. interfrigidaria* (4.06 Ma),
 - *F. barronii* (4.40 Ma),
 - *Thalassiosira complicata* (4.68 Ma),
 - *T. inura* (4.74 Ma), and
 - *Shionodiscus oestrupii* (4.88 Ma).

The major discrepancy between magnetostratigraphic (see “Paleomagnetism”) and diatom data between ~5.5 and 4.5 Ma (Figs. F7, F28) highlights an interval where using the mid-point absolute age value for diatom events from the average range model of Cody et al. (2008) is not appropriate and, therefore, where the biochronology or biostratigraphic methodologies of Expedition 318 may be

improved. Since the magnetostratigraphy at Site U1359 is supported by radiolarian datums in this interval, we suggest that recalibration of the pertinent diatom datums to the local magnetostratigraphy is necessary in this case.

Miocene

Fourteen diatom datums were recognized in Samples 318-U1359B-20H-4, 25 cm, through 28X-CC (183.45–243.11 mbsf), and 318-U1359D-4R-5, 105 cm, through 48R-CC (178.35–596.31 mbsf) (Tables T4, T6, T11):

- Last abundant occurrence (LAO) of *Denticulopsis simonsenii* (8.63 Ma);
- LOs of
 - *Denticulopsis ovata* (9.64 Ma),
 - *Denticulopsis dimorpha* var. *areolata* (10.25 Ma),
 - *D. dimorpha* (10.28 Ma),
 - *Nitzschia denticuloides* (11.72 Ma),
 - *Actinocyclus ingens* var. *nodus* (12.56 Ma), and
 - *Crucidenticula nicobarica* (12.62 Ma); and
- FOs of
 - *Thalassiosira oliverana* var. *sparsa* (8.53 Ma),
 - *D. dimorpha* var. *areolata* (10.31 Ma),
 - *D. ovata* (11.09 Ma),
 - *D. dimorpha* sensu lato (12.50 Ma),
 - *Fragilariopsis claviceps* (12.68 Ma),
 - *Denticulopsis praedimorpha* sensu lato (12.97 Ma), and
 - *N. denticuloides* (13.49 Ma).

Diatom biostratigraphy is not sufficiently well resolved to define the Miocene/Pliocene boundary. Instead, the boundary is defined by magnetostratigraphy (see “Paleomagnetism”) at ~155 mbsf in Hole U1359B (Figs. F7, F27).

Silicoflagellates, ebridians, chrysophyte cysts, and sponge spicules

Silicoflagellates and sponge spicules occur sporadically in trace to rare abundance throughout the recovered intervals, whereas ebridians were observed in Samples 318-U1359B-12H-CC (112.55 mbsf), 13H-CC (120.30 mbsf), 16H-CC (146.35 mbsf), and 20H-CC (188.12 mbsf) and 318-U1359C-5H-1, 35 cm (36.05 mbsf), and 5H-2, 140 cm (38.60 mbsf). Chrysophyte cysts were only rarely noted (Tables T3, T4, T5, T6).

Radiolarians

Radiolarians occur in all samples examined from Holes U1359A, U1359B, and U1359D with good to moderate preservation. No material from Hole U1359C was examined. Radiolarian-based age constraints on the individual samples examined are summarized in Table T7.

Calcareous nannofossils

Rare and poorly preserved calcareous nannofossils occur in Holes U1359A, U1359B, and U1359C; however, they are common and moderately to well preserved in Hole U1359D (Fig. F26; Table T8). A diatom-bearing nannofossil ooze occurs within the lowermost part of Core 318-U1359D-24R and the uppermost part of Core 25R, and nannofossil-bearing sediments were observed within Sample 14R-CC and Cores 23R through 29R (see “Lithostratigraphy”). A more detailed analysis of selected samples (Table T8) permitted identification of a low diversity calcareous nannofossil assemblage, mainly consisting of *Reticulofenestra pseudoumbilicus*, *Reticulofenestra minuta*, and *Reticulofenestra minutula* (whereby closed central area morphotypes are dominant; e.g., *Reticulofenestra gelida*, *Dictyococcites antarcticus*, and *Dictyococcites productus*) characteristic of the late Miocene–early Pliocene from high latitudes. No standard biozonal markers were found.

Palynology

Thirty samples were analyzed for palynology from core catcher material from Holes U1359A and U1359D. With the exception of Sample 318-U1359D-6R-CC (200.32 mbsf), all samples proved palynologically productive. The palynological associations are strongly dominated by reworked sporomorphs, with the exception of the material studied between Samples 318-U1359D-12R-CC and 40R-CC (253.66–520.60 mbsf), which is dominated by dinocysts. All palynological data from Site U1359 are presented in Table T9.

Dinocysts

Dinocysts occur in trace to common abundances in Samples 318-U1359A-6H-CC (47.73 mbsf), 8H-CC (66.60 mbsf), 9H-CC (75.80 mbsf), 15H-CC (133.70 mbsf), and 18X-CC (153.96 mbsf) and in all samples from Hole U1359D except Sample 318-U1359D-6R-CC (200.32 mbsf) (Fig. F26; Table T9). The overall preservation of dinocysts is poor to moderate but generally improves downhole. Dinocyst assemblages are overwhelmingly dominated by protoperidinioid (heterotrophic) dinocysts. Within these assemblages, specimens of *Brigantedinium* spp. and *Selenopemphix nephroides* are most abundant; specimens attributable to *Lejeunecysta* spp. are only present in trace amounts. Specimens of *Selenopemphix* spp. found in samples from Holes U1359A and U1359D are remarkably small. This phenomenon is consistent with the coeval record obtained at Site U1356A (Cores 318-U1356A-1R through 14R; 4.60–130.70 mbsf). In contrast, the *Selenopemphix* spp. specimens from Oligocene strata at Sites U1356 and

U1360 are approximately twice the size of middle and late Miocene specimens. Although more data are needed to substantiate this observation, the size differences of *Selenopemphix* spp. specimens may eventually provide a convenient stratigraphic marker for the middle to late Miocene.

Besides protoperidinioid dinocysts, Samples 318-U1359A-6H-CC (47.73 mbsf), 8H-CC (66.60 mbsf), and 18X-CC (153.96 mbsf) and 318-U1359D-35R-CC (474.91 mbsf) through 45R-CC (567.44 mbsf) yield *Impagidinium* spp., which are characteristic of oceanic, oligotrophic settings. In addition, several samples, particularly from Hole U1359D (Table T9), contain numerous specimens of a previously unknown dinocyst taxon, here informally termed “*Impagidinium* brown.” Morphologically, this taxon appears to be attributable to the genus *Impagidinium*. However, its conspicuous brown color is unknown from any *Impagidinium* species and strongly reminiscent of protoperidinioid cysts. An in-depth characterization and formal description of this taxon will be carried out during postexpedition research. Several samples also contain specimens of *Vozzhennikovia* spp. and *Enneadocysta* spp.; these are considered to be reworked from the Eocene (Table T9). Sample 318-U1359A-16R-CC (295.95 mbsf) contains specimens of *Habibacysta tectata*, which suggests a maximum age of 14.0 Ma for that sample (see Tables T3 and T4 in the “Methods” chapter for references).

Sporomorphs

Sporomorphs are present in all samples except Samples 318-U1359D-29R-CC (412.83 mbsf) and 318-U1359D-32R-CC (446.36 mbsf) (Fig. F26; Table T9) and they are remarkably well preserved in general. All sporomorphs encountered are considered to be reworked from older (Paleogene, Mesozoic, and Paleozoic) strata. This is suggested by the dominance of thick-walled spores and the generally dark color (i.e., strong thermal maturity) of sporomorphs. Sporomorph genera identified include *Classopollis/Corollina* spp., *Baculatisporites/Osmundacidites* spp., *Cicatricosisporites* spp., *Deltoidospora/Triletes* spp., and *Ischyosporites* spp.

Foraminifers

Thirty-nine samples were examined for foraminifers from Holes U1359A, U1359B, and U1359D (Table T10). Calcareous benthic and planktonic foraminifers are common to abundant in Samples 318-U1359A-4H-CC (28.56 mbsf) and 5H-CC (29.34 mbsf) and 318-U1359D-14R-CC (276.07 mbsf), 24R-CC (371.86 mbsf), and 30R-CC (424.08 mbsf) (Table T10). Relatively diverse assemblages of foraminifers occur in Samples 318-U1359D-14R-CC and 24R-CC. Most other samples examined are barren of foraminifers or limited to a few agglutinated specimens.

The low-diversity planktonic foraminifer assemblages and species identified at Site U1359 are characteristic of sub-Antarctic waters (Berggren, 1992).

Planktonic foraminifers

Samples 318-U1359A-4H-CC (28.56 mbsf) and 5H-CC (29.34 mbsf) are characterized by relatively high abundances of *Neogloboquadrina pachyderma* and *Globigerina bulloides*. *Neogloboquadrina pachyderma* comprises >80% of the total planktonic foraminifer assemblages. Based on these taxa, and using the Subantarctic zonal scheme of Berggren (1992), the upper 29.34 mbsf of Hole U1359A can be assigned to Subantarctic Zone AN7, which ranges from 9.2 Ma to the present (Gradstein et al., 2004).

Neogloboquadrina nympha (LO at 10.1 Ma) and *Neogloboquadrina acostaensis* (FO at 10.9 Ma) were identified in Samples 318-U1359D-24R-CC (371.86 mbsf) and 27R-CC (391.62 mbsf), constraining the 371.86–391.62 mbsf interval in Hole U1359D to between 10.1 and 10.9 Ma. Long-ranging *G. bulloides* and *Globigerina woodi* comprise the other planktonic species in the assemblage.

Globorotalia miozea (FO at 16.6 Ma; Gradstein et al., 2004) was recorded in Sample 318-U1359D-34R-CC (464.36 mbsf). We therefore assign a maximum age of 16.6 Ma to this sample.

Benthic foraminifers

Calcareous benthic foraminifers were observed in Sample 318-U1359A-4H-CC (28.56 mbsf) and sporadically between Samples 318-U1359D-14R-CC (276.07 mbsf) and 34R-CC (464.36 mbsf). In all other samples, foraminifers are either absent or limited to few specimens (<3 per sample) of agglutinated taxa, such as *Hyperammia laevigata*, *Rhabdammina linearis*, and *Martinotiella nodulosa*. Sample 318-U1359A-4H-CC (28.56 mbsf) yielded a single specimen of *Melonis sphaeroides*, a bathymetric indicator for abyssal depths (van Morkhoven et al., 1986), and several agglutinated specimens of *Hyperammia* spp., *Martinotiella communis*, and *R. linearis*.

Samples 318-U1359D-14R-CC (278.07 mbsf) and 24R-CC (371.86 mbsf) contain relatively diverse benthic foraminifer assemblages. For example, *M. sphaeroides* and *Pullenia bulloides* collectively dominate the assemblage in Sample 318-U1359D-14R-CC (276.07 mbsf), contributing 47% and 18% of the total foraminiferal assemblage, respectively, whereas *Cibicidoides mundulus* and *Bolivina* spp. occur in lower abundances (<15%).

Samples 318-U1359D-15R-CC (283.43 mbsf), 17R-CC (300.99 mbsf), and 19R-CC (320.83 mbsf) each contain single specimens of the calcareous foraminifer

Epistominella exigua. In Sample 318-U1359D-24R-CC (371.86 mbsf), *E. exigua*, *P. bulloides*, and *M. sphaeroides* comprise 20%, 19%, and 16% of the total benthic assemblage, respectively; *C. mundulus* and agglutinated species each contribute <10%. This assemblage is similar to that recovered from core top material from deepwater sites between Antarctica and Australia that are associated with cold (−0.2° to +0.4°C) AABW (Corliss, 1979). The preservation of foraminifers within calcareous nannofossil ooze (see “[Lithostratigraphy](#)”) (e.g., Sample 318-U1359D-24R-CC; 371.86 mbsf) is excellent, with many specimens exhibiting a glassy appearance.

Age model and sedimentation rates

In this section, we summarize and integrate the biostratigraphic interpretations inferred from the individual microfossil groups. The resulting integrated age-depth model presented in Table [T11](#) and Figures [F7](#) and [F27](#) also incorporates paleomagnetostratigraphic age constraints presented in “[Paleomagnetism](#).”

An upper middle Miocene through upper Pleistocene sedimentary succession was recovered at Site U1359. A late Pliocene–early Pleistocene ~1 m.y. hiatus (~2.5 to 1.5 Ma) is recognized between Samples 318-U1359A-5H-CC and 6H-2, 132.5 cm (29.34–41.42 mbsf) and between Samples 318-U1359C-5H-1, 35 cm, and 5H-2, 140 cm (36.05–38.60 mbsf). In addition, a condensed interval (low sedimentation rate) is recognized within the lower to mid upper Miocene succession between Samples 318-U1359B-21H-CC and 25X-4, 58 cm (198.15–218.78 mbsf), and between Sample 318-U1359D-7R-CC and 8R-CC (209.40–216.64 mbsf). This period of low sedimentation rate lasted from ~9.8 to 7 Ma. High sedimentation rates are inferred for the strata below this condensed interval to the bottom of Hole U1359D at 596.31 mbsf (see below).

Pleistocene (0.54–1.5 Ma)

Diatoms and radiolarians resolve the sedimentary sequence for the Pleistocene within Holes U1359A (0.02–29.34 mbsf) and U1359C (0.40–36.05 mbsf). The top of Hole U1359A is dated as latest Pleistocene (0.54 Ma), below which we infer continuous sedimentation of ~1 m.y. duration accumulating ~33 m of sediment (to 29.34 mbsf in Hole U1359A and 36.05 mbsf in Hole U1359C) (i.e., average rate = ~33 m/m.y.). Below this, a ~1 m.y. hiatus is inferred for the interval ~2.5–1.5 Ma based on diatom and radiolarian biostratigraphy in corroboration with magnetostratigraphy. This indicates the Pliocene/Pleistocene boundary interval (1.81 Ma; Gradstein et al., 2004) is not preserved at Site U1359.

Pliocene (2.5–5.33 Ma)

Diatoms, radiolarians, and magnetostratigraphy provide primary age control for the Pliocene sedimentary succession recovered in Holes U1359A (41.42–190.26 mbsf), U1359B (39.01 to ~155 mbsf), and U1359C (38.60 to ~155 mbsf). Magnetostratigraphy and radiolarian bioevents are well correlated within this section and suggest a sedimentation rate of ~44 m/m.y. (~126 m of sediment in 2.83 m.y.) (Fig. [F7](#)); diatom bioevents in disagreement with this chronostratigraphy should be recalibrated. Pliocene sedimentation therefore continued to be deposited at the same rate as that for the latest Miocene (see below).

The recognition of the Miocene/Pliocene boundary (5.33 Ma) is constrained by magnetostratigraphy (see “[Paleomagnetism](#)”), occurring between the termination of Chron C3An.1n and the onset of Chron C3n.4n (i.e., ~155 mbsf in Hole U1359B). Biostratigraphic information cannot provide more detail.

Latest middle Miocene and late Miocene (5.33–12.42 Ma)

Uppermost Miocene sediments (above ~198.15 mbsf in Hole U1359B) were deposited at a sedimentation rate of 44 m/m.y. (Fig. [F7](#)), defined by magnetostratigraphy and radiolarians. The underlying ~15 m of sediment (197.35–212.8 mbsf in Hole U1359D) of early to mid late Miocene age was deposited within 3.3 m.y. (10–6.7 Ma) according to diatom, radiolarian, and magnetostratigraphic age control. This suggests a reduced average sedimentation rate of just 4.5 m/m.y. and therefore a condensed interval for this part of the record (Fig. [F7](#)).

Below the condensed interval, diatoms, radiolarians, and magnetostratigraphy resolve an upper middle to lower upper Miocene stratigraphy between 212.80 and 596.31 mbsf (bottom of Hole U1359D). This ~384 m of sediment was deposited in ~2.5 m.y., giving an average sedimentation rate of 153 m/m.y., the highest for the entire sedimentary succession at Site U1359 (Fig. [F7](#)).

Paleoenvironmental interpretation

Pleistocene

Diatom and radiolarian Pleistocene assemblages at Site U1359 are dominated by typical Neogene Southern Ocean open-water taxa with variable abundances of benthic, neritic, and sea ice-associated diatom taxa. This indicates a pelagic, well-ventilated, nutrient-rich, sea ice-influenced setting, corroborated by the presence of heterotrophic-dominated dinocyst assemblages. The preservation of planktonic foraminifers in the Pleistocene indicates that bottom waters were favorable to the preservation of calcium carbonate.

Further, pervasive reworked sporomorphs of Paleogene, Mesozoic, and Paleozoic age point to strong erosion in the hinterland.

Pliocene

Pliocene diatom assemblages are also dominated by open-water taxa and variable abundances of benthic, neritic, and sea ice-associated taxa. The dinocyst assemblages predominantly comprise heterotrophic taxa, indicating that, as for the Pleistocene, Pliocene biosiliceous-rich sediments were deposited in a pelagic, well-ventilated setting characterized by high productivity and sea ice influence.

The presence of dinocysts attributed to *Impagidinium* spp., which are indicative of oceanic settings and relatively warm surface waters, within some intervals (e.g., Samples 318-U1359A-6H-CC [47.73 mbsf], 8H-CC [66.60 mbsf], and 15H-CC [133.70 mbsf]) suggests that transient pulses of warmer surface waters bathed Site U1359. High abundances of sporomorphs reworked from Paleogene, Mesozoic, and Paleozoic strata suggest strong erosion in the hinterland.

The general lack of planktonic and calcareous benthic foraminifers suggests that bottom waters were corrosive to the thin-shelled tests of planktonic foraminifers.

Latest middle Miocene and late Miocene

As in the Pliocene and Pleistocene, Miocene diatom assemblages at Site U1359 mainly include open-water taxa. In addition, a notable increase in the abundance of stephanopyxid specimens occurs within Samples 318-U1359D-47R-CC (589.96 mbsf) and 48R-CC (596.31 mbsf) (Table T6). The stephanopyxid group comprises many robust neritic forms that may be easily swept up into the plankton and survive reworking. This increase may therefore be interpreted as either an indication of shallowing water depths or an increase in reworking of shallower water sediments. The presence of *Impagidinium* spp. in Samples 318-U1359D-29R-CC (412.83 mbsf) and 48R-CC (596.31 mbsf) indicates an open-water, well-ventilated setting in agreement with the diatom data, but also higher sea surface temperatures. The lack of planktonic and benthic foraminifers below Sample 318-U1359D-34R-CC (464.36 mbsf) to the bottom of Hole U1359D (596.31 mbsf) suggests that late middle Miocene bottom waters were corrosive to calcareous foraminifers except for brief periods (e.g., ~10 m.y., represented by Sample 318-U1359D-14R-CC; 276.07 mbsf) when calcareous benthic foraminifers were preserved.

Paleomagnetism

Paleomagnetic investigations at Site U1359 involved analysis of discrete samples from Holes U1359A, U1359B, and U1359D and measurement of archive halves from all four holes. In general, we took 2–7 samples per core. A subset of these (45 samples) were subjected to step-wise alternating-field (AF) demagnetization. After measuring the natural remanence of the archive halves, the halves were demagnetized at either 15 or 20 mT, based on the analysis of the discrete samples. The anisotropy of magnetic susceptibility (AMS) was measured on all discrete samples and the rock magnetic properties of a selected subset were also studied. We constructed a composite polarity log from the overlapping sedimentary sections relying on the composite depth determinations in “[Stratigraphic correlation and composite section](#),” which we correlate to the GPTS of Gradstein et al. (2004), documenting a complete Pliocene section from the top of Chron C2An to the bottom of Chron C3An. There is a gap including Chron C2n as well as a period of extremely slow (and possibly discontinuous) sediment accumulation from Chron C3Ar to the top of C5n.

Analysis of discrete samples

Selected discrete samples were measured and demagnetized in fields of 5, 10, 15, 20, 30, and 40 mT and, when strong enough, 50 and 60 mT using the three-step protocol described in “[Paleomagnetism](#)” in the “Methods” chapter. Examples of the range of behavior during demagnetization are shown in Figure F29. We encountered two kinds of experimental challenges with these samples. The first challenge stemmed from the fact that the sediments are very weakly magnetized and instrumental noise cannot be neglected. The second challenge results from a bias in directions caused by acquisition of anhysteretic remanence (ARM) during AF demagnetization. After removing the effects of these two types of problems as described in the following sections, the data can in most cases be interpreted in terms of magnetic polarity.

Instrumental noise

The shipboard cryogenic magnetometer suffered from a very sensitive γ -axis that undergoes “flux jumps,” which are noise in the form of quantized offsets in a particular detector. All cryogenic magnetometers suffer from this problem, but the shipboard instrument seems to suffer more than shore-based instruments. At the end of the expedition, we discovered that flux jumps could be virtually eliminated by treating the sample track with antistatic

spray. However, our results from Site U1359 preceded this discovery. The shipboard sample measurement protocol exacerbated the problem because we measured the discrete samples in batches using the discrete sample tray on the cryogenic magnetometer and not one at a time. By measuring the background before and after measurement the offsets can be detected and the samples can be reinsured. However, if a jump occurs during measurement of a whole sequence of samples, appearing after the first baseline but disappearing again prior to the second baseline measurement, it cannot be easily detected. Incorporation of instantaneous visualization of the data would greatly facilitate the detection of contaminated data, but we have not yet had the time to do this. As a result, flux jumps only became evident during data processing. Because the samples at Site U1359 are so weak, flux jumps profoundly affect the results.

In Figure F29A, F29C, and F29D, we show an example of a demagnetization experiment done on Sample 318-U1359A-12H-5, 70 cm. These data exhibit 4 jumps out of the 26 different measurements. The jumps are readily identifiable as they manifest themselves as spikes in directions along a particular axis (most frequently the γ -axis, as in the red symbols in Figure F29A and F29B, but also infrequently on the x - and z -axes) and in the intensity decay curve (jumps in Fig. F29C). Moreover, we measured batches of 14–16 samples at a time and the jump is observed in several sequential samples at the same step. We show the data after removal of the steps suffering from flux jumps and after averaging the data from a given demagnetization step (as described in “Paleomagnetism” in the “Methods” chapter) in Figure F29D. We calculate best-fit lines through these averaged data using principal component analysis (see “Paleomagnetism” in the “Methods” chapter); the best-fit line is shown in green and represents the direction of the characteristic remanence in this sample.

Acquisition of anhysteretic remanent magnetization during alternating-field demagnetization

The data shown in Figure F29E–F29H suffer from the second challenge encountered in analysis of Site U1359 samples: ARM acquisition during AF demagnetization. The AF demagnetizer inline with the cryogenic magnetometer has three coils aligned along the instrument’s x -, γ -, and z -axes. In turn, each coil ramps up to the specified peak field, the samples (or core) travel through the coil and then the field ramps down again. The procedure is done first on the x -coil, then the γ -coil, and finally the z -coil. ARM is acquired parallel to the axis of demagne-

tization and so is evident in sample coordinates along the last axis exposed to AF demagnetization, the instrument’s z -axis.

During Expedition 318, we developed a protocol whereby each sample gets demagnetized along all three instrumental axes in first the “top-toward” orientation, in which the sample’s z -axis is demagnetized by the AF coil’s z -axis last and could acquire an ARM parallel to the z -axis before measurement. The sample is then demagnetized again at the same peak field, but in the “top-to-right” orientation. In this orientation, the sample’s γ -axis is demagnetized by the AF coil’s z -axis last and would acquire an ARM parallel to that axis. Finally, the sample is rotated to the “away-up” orientation, and the sample’s x -axis is exposed to the final demagnetization. This procedure is repeated for each demagnetization step. If a particular sample is susceptible to ARM, it will acquire a magnetization along the z -, γ -, and x -axes sequentially, making the distinctive triangular pattern in Figure F29E and the three groups of directions in Figure F29F (labeled x , γ , and z). Our demagnetization protocol was designed to compensate for this tendency and, although the example in Figure F29E is a very extreme case, the data averaged for each demagnetization step (Fig. F29H) trend to the origin and can be interpreted in terms of polarity.

Most samples exhibited the behavior shown in Figure F29I–F29L and Figure F29M–F29P. These show only moderate scatter (from ARM) with occasional flux jumps (see a typical reverse sample in Fig. F29L and a typical normal sample in Fig. F29M and F29P). The downward-directed drill string remanence is removed by demagnetization to 10 or 15 mT.

Analysis of archive halves

We measured the natural remanent magnetization (NRM) of archive halves from all holes. Based on the step-wise demagnetization experiments described in the last section, archive halves from Holes U1359A–U1359C were demagnetized to 20 mT and archive halves from Hole U1359D were demagnetized to 15 mT. All NRM data are shown as gray circles in Figure F30 for Holes U1359A–U1359C and the top and bottom of Hole U1359D. The directions of the best-fit lines from step-wise AF demagnetization of discrete samples (e.g., as in Fig. F29) are shown as red triangles and the data from the archive halves after demagnetization and deletion of disturbed sedimentary sections are shown as blue circles. In general, there is excellent agreement between the discrete sample measurements and those from the archive halves, which lends support to an interpretation of the data as to polarity: negative inclinations are normal and positive inclinations are reversed.

Anisotropy of magnetic susceptibility

In addition to remanence analyses, we measured the AMS (including the bulk susceptibility, χ_b) on all discrete samples (Fig. F31). Samples were taken to avoid to the extent possible disturbed intervals and all but a few (those with V_3 inclinations less than $\sim 60^\circ$ and distinct maximum and intermediate eigenvalues) had characteristic sedimentary fabrics.

There are two pronounced zones of very low bulk magnetic susceptibility (Fig. F31C), one between ~ 90 and 125 mbsf coincident with a zone of very low remanent intensity (Fig. F30) and a second between ~ 210 and 275 mbsf. These will be referred to as the Pliocene and Miocene low-susceptibility zones, respectively.

All discrete samples that were subjected to step-wise AF demagnetization were also given an ARM in an alternating field of 100 mT with a direct-current bias field of 50 μ T and subjected to progressive IRM acquisition experiments (see “Paleomagnetism” in the “Methods” chapter). We show plots of the progressive acquisition of isothermal remanent magnetization (IRM) for the two low-susceptibility zones and the surrounding sediment (Pliocene and Miocene high-susceptibility zones) in Figure F32. The Pliocene samples from high-susceptibility zones (Fig. F32A) and the low-susceptibility zone (Fig. F32B) are quite different from one another. High-susceptibility sediments display an approach to saturation near 200 mT (characteristic of magnetite), whereas Pliocene low-susceptibility sediments are, for the most part, not saturated by even 1 T, indicating a very high coercivity. Note also the difference in magnitude in the strengths of the IRMs, the low-susceptibility samples being more than an order of magnitude weaker than the high-susceptibility ones. Such high coercivities are characteristic of hematite, a surprising mineral to find in such pyrite-rich, olive-green sediments.

The high-susceptibility Miocene samples are quite similar to those of the Pliocene. The low-susceptibility Miocene samples, however, are on the whole different from the low-susceptibility Pliocene samples. The strongest sample is virtually identical to high-susceptibility samples, displaying the characteristics of a magnetic mineralogy dominated by magnetite. The two weakest samples appear to acquire no stable IRM. The middle sample, though it does not saturate by 200 mT, does appear to reach saturation by ~ 400 mT, behavior that is more characteristic of magnetite than hematite. These samples do not appear to have a hematite mineralogy but may have either magnetite, an oxidized version of magnetite (e.g., maghemite), or be virtually nonmagnetic.

Discussion

Drop in intensity

The Pliocene low-susceptibility zone is associated with a profound drop in intensity at ~ 95 mbsf and return to higher values at ~ 125 mbsf (Fig. F30A, F30B, F30C). A sudden loss of remanence with depth has been reported before (see e.g., Ruddiman, Sarnthein, Baldauf, et al., 1988; Kroenke, Berger, Janecek, et al., 1991; Mayer, Pisias, Janecek, et al., 1992; Barker, Camerlenghi, Acton, et al., 1999; O’Brien, Cooper, Richter, et al., 2001) and has been attributed to dissolution of magnetite during diagenesis (e.g., Tarduno, 1995; Florindo et al., 2003). The situation in the Pliocene low-susceptibility zone is different, however, because the remanence, at least in Hole U1359B, is measurable and stable; it is just extremely weak. The behavior of the IRM acquisition curves (Fig. F32A, F32B) suggests that the magnetization is dominated by hematite within the Pliocene low-susceptibility zone. The magnetite-dominated samples above and below this zone could well have hematite in them, but magnetite is two orders of magnitude stronger and could mask the presence of hematite.

Considering that (1) the lithology shows that the Pliocene low-susceptibility zone has much higher diatom abundance than the overlying sediments (see “Lithostratigraphy”) and (2) trace element data show higher Ba/Al ratios and lower MnO and Na concentrations (see “Geochemistry and microbiology”), it seems likely that the low-susceptibility zone was a period of high biotic productivity. Dissolution of magnetite has been associated with higher productivity (e.g., Hartl et al., 1995) and it is likely that the magnetite originally in the sediments has disappeared through diagenesis. The recovered sediments at Site U1359 are unusual because of the persistence of a magnetic remanence in the form of hematite and the reappearance of high intensities at depth. Secondary hematite is generally found in red pigmented rocks, which these sediments emphatically are not and it would be quite surprising to have hematite forming diagenetically along with such reduced forms as pyrite. We surmise that the hematite is detrital. Our preliminary interpretation is that both magnetite and hematite are present throughout the sequence, but the magnetite is largely gone from the Pliocene low-susceptibility zone, leaving primarily hematite. Alternatively, there is an influx of detrital hematite during the Pliocene low-susceptibility zone, indicating a difference in provenance for the detrital fraction. Further investigations are necessary to resolve the issue of the origin of the magnetic minerals.

Interestingly, the Miocene low-susceptibility zone does not appear to have a hematite-dominated magnetic

mineralogy, supporting the change in provenance hypothesis for the Pliocene low-susceptibility zone. The Miocene low-susceptibility zone also appears to have an extremely weak but measurable magnetic remanence.

Correlation of magnetostratigraphy to the geomagnetic polarity timescale

Comparison of the paleomagnetic records from the three holes was greatly facilitated by the composite depth scheme based on physical properties (see “[Stratigraphic correlation and composite section](#)”). The inclinations for Holes U1359A–U1359C are shown placed on the composite depth scale in Figure [F8A](#). Data from Hole U1359D are shown in Figure [F8B](#) and [F8C](#).

We constructed a composite polarity log for Holes U1359A–U1359C by using the most complete and best resolved intervals from the three holes. The hole from which the composite was constructed is indicated by the colored solid, dashed, or dotted lines to the left of the composite. The major normally magnetized intervals are labeled N1–N12 for convenience.

The composite log can be correlated to the GPTS of Gradstein et al. (2004), shown to the right. Our correlation tie points are listed in Table [T12](#). Starting from the top, the three polarity intervals N1–N3 correspond to Chrons C1n, C1r.1r, and C1r.2r, respectively. The next normal package downhole (intervals N4–N6), starting at ~45 mcd, is not easily matched to Chron C2n without a major change in sediment accumulation rate and/or a hiatus; the inferred part of Chron C1r is too short. A micropaleontological sample taken from Section 318-U1359B-5H-2 at 131 cm is in the *T. vulnifica* Zone, with an age of 2.17–2.49 Ma (see “[Biostratigraphy](#)”). This rules out a tie of the top of interval N4 to the top of Chron C2n and suggests instead a tie to Chron C2An at 2.58 Ma, as shown in Figure [F8](#). It appears that both Chrons C2An.1r and C2An.2r are found in Holes U1359C and U1359A, respectively. There is a strong constraint on hole to hole correlation based on the physical properties in this interval, demanding that these two reverse intervals be different polarity zones as shown in the composite. The reverse interval below interval N6 is a straightforward match to Chron C2Ar and normal intervals N7–N10 correspond to Subchrons C3n.1n–C3n.4n, respectively. Intervals N11 and N12 are the two normal parts of Chron C3An. This correlation is in general agreement with the available radiolarian identifications but conflict with the diatom age estimates within Chron C3n.

The stratigraphic interval from 160 to 220 mbsf in Hole U1359D is shown in Figure [F8B](#). The polarity intervals N11 and N12 are the same as those in

Figure [F8A](#) and correspond to Chron C3An. The radiolarian stratigraphy (see “[Biostratigraphy](#)”) suggests that the interval comprising polarity intervals N13–N15 is highly condensed, ranging in age from ~7 to 9 Ma. Based on these constraints, we correlate Interval N15 to Chron C4An and intervals N13 and N14 to Chron C4n.

The entire record of Hole U1359D is shown in Figure [F8C](#). The biostratigraphy (see “[Biostratigraphy](#)”) suggests that the bottom of Hole U1359D is ~12.5 Ma in age, supporting a correlation of polarity interval N17 to Chron C5An, although Chron C5An.1r is missing. Polarity interval N15 can be comfortably correlated to Chron C5n, although there are numerous reverse polarity intervals within it that are not in the standard GPTS. Polarity interval N16 could be Subchron C5r.2n, although it appears a bit higher than expected.

Missing and mislocated polarity intervals can be explained by the highly variable sedimentation expected on a levy. The additional polarity intervals observed in Chron C5n could be either the elusive “tiny wiggles” of Blakely (1974) and Cande and LaBrecque (1974) or the unremoved influence of ice-rafted debris (IRD). To address the latter possibility, we have deleted all intervals associated with visible IRD and those associated with large intensity spikes. Small IRD could influence the record, contributing short perturbations that could be mistaken for geomagnetic field behavior. However, some of the reverse polarity intervals within interval N15 are quite long, spanning a meter or more, and cannot be attributed to hidden IRD. Moreover, a discrete sample from one of the reverse polarity intervals (marked with an arrow in Fig. [F8C](#)) also shows a stable reverse polarity (Fig. [F30D](#)) and is not contaminated by IRD. Bowles et al. (2003) investigated the issue of “tiny wiggles” within Chron C5n and concluded that if reverse polarity zones exist at all, they must be very short in duration and probably not global in nature. Therefore, although we suspect that at least some of the reverse polarity intervals within interval N15 are in fact geomagnetic in origin, they are probably only locally expressed (excursions as opposed to reversals of the entire dipole field). We surmise that we have recovered these excursions in intervals of extremely high sediment accumulation (100 m/m.y. on average and perhaps much higher for brief periods of time) for which we have very high sampling density (every 5 cm).

Trends in anisotropy of magnetic susceptibility data

The AMS data shown in Figure [F31](#) reflect changes in sedimentary fabric with depth. In simple sedimentary

systems, dewatering and compaction of sediment results in a monotonic increase in the degree of anisotropy of an essentially oblate fabric with a vertical axis of minimum susceptibility (V_3 in the terminology used here; see “Paleomagnetism” in the “Methods” chapter). The degree of anisotropy is reflected by the difference between the minimum and maximum eigenvalues (plotted in Fig. F31A and referred to as τ_3 and τ_1 , respectively). Instead of a monotonic increase in the difference between these two values, rapid swings between high and low degrees of anisotropy (0 to 20 mcd), intervals of monotonic increase in anisotropy with depth (e.g., 20–25, 90–95, and 115–130 mcd), and intervals of monotonic decrease in anisotropy with depth (e.g., 25–30, 40–50, and 95–100 mcd) occur. Moreover, there are several intervals with very low anisotropy (indicated by stars). Two of these intervals correspond to the two low-susceptibility zones in the Pliocene and Miocene already discussed. The other intervals also correspond to brief intervals of low susceptibility. In fact, with one exception at ~475 mcd, whenever we encountered low susceptibility, we also found a low degree of anisotropy. At least in the Pliocene, these intervals of low susceptibility are also associated with high diatom abundances and may well represent zones of high productivity.

There are several possible explanations for the variations in anisotropy degree with depth at Site U1359. First, there are changes in magnetic mineralogy as discussed earlier, especially with respect to the high- and low-susceptibility regions. If the hematite, for example, is diagenetic in origin, it would not have a sedimentary fabric (e.g., Tauxe et al., 1990), so the changes in anisotropy could result from changes in origin of the magnetic phases. Second, pronounced changes in bioturbated versus laminated beds could also explain alternations between highly oblate and virtually isotropic sedimentary fabrics. Finally, there may be differences in excess pore water caused by the more clay rich versus more diatom rich layers, creating compaction disequilibria of the sort observed by Schwehr et al. (2006) (Fig. F33). The solution to this interesting problem must await further shore-based analyses.

Geochemistry and microbiology

Organic geochemistry

Gas analysis was performed once per core from Holes U1359A–U1359D using the methods described in “Geochemistry and microbiology” in the “Methods” chapter.

Methane concentrations varied by four orders of magnitude downhole (from undetected to ~43,000 ppmv

(Fig. F34). Concentrations increase from undetected at 90 mbsf to ~15,000 ppmv at 200 mbsf. From 200 to 586 mbsf, concentrations average ~15,000 ppmv, with large variations from 6,000 to 43,000 ppmv superimposed on the mean. Ethane was detected below 100 mbsf, but C_1/C_2 levels were high throughout the hole (Fig. F34).

Inorganic geochemistry

Bulk sediments

Seventy-one samples from Holes U1359A–U1359D were taken for analyses of weight percent carbonate, carbon, nitrogen, and sulfur content, as well as major and trace element analyses (silicon, titanium, aluminum, iron, manganese, calcium, magnesium, sodium, potassium, phosphorus, strontium, barium, vanadium, scandium, and cobalt) (Table T13). Samples were collected in close collaboration with the sedimentology group to sample the main lithologies represented.

$CaCO_3$ (in weight percent) was determined on all sediment samples by coulometric methods (see “Geochemistry and microbiology” in the “Methods” chapter). $CaCO_3$ contents for most samples vary between <1 and 3.2 wt% (Fig. F35). A distinct carbonate-rich layer, with $CaCO_3$ contents of 39.7 wt%, was found at 372.45 mbsf and corresponds to a minor lithology of diatom-bearing nannofossil ooze (see “Lithostratigraphy”).

Carbon, nitrogen, and sulfur contents were measured on 17 selected samples covering the full range of $CaCO_3$ contents. Except for two samples at 81.44 and 372.45 mbsf (Samples 318-U1359B-9H-5, 122–124 cm, and 318-U1359D-13R-4, 71–73 cm), which represent minor lithologies (i.e., sand layer and diatom-bearing nannofossil ooze), all samples show very low carbon (<0.9 wt%), nitrogen (<0.05 wt%), and sulfur concentrations (<0.2 wt%). Calculated total organic carbon contents are <0.6 wt% and C/N ratios vary between 6 and 21 (outliers: sand layer = C/N ratio of 82; nannofossil ooze layer = C/N ratio of 390) (Fig. F36).

The concentrations of silicon, titanium, aluminum, iron, manganese, calcium, magnesium, sodium, potassium, phosphorus, strontium, barium, vanadium, scandium, and cobalt were obtained for all 71 bulk sediment samples by inductively coupled plasma-atomic emission spectrophotometry (ICP-AES). Representative results are shown in Figure F37 and data are reported in Table T13.

Four geochemical intervals can be distinguished:

1. An upper interval (0 to ~200 mbsf),
2. A transitional interval between ~210 and ~310 mbsf,
3. An interval from ~310 to 536 mbsf, and

4. A lower interval containing the deepest six samples analyzed (547.39–594.79 mbsf).

The uppermost geochemical interval (0 to ~210 mbsf) is characterized by large concentration ranges for most elements. Silicon dioxide values vary from 63.4 to 77.4 wt% and are positively correlated with CaO (1.0–2.5 wt%) and Ba concentrations (494–1158 ppm), indicating association with biogenic phases. Aluminum, titanium, potassium, and iron oxides reveal large fluctuations (9.5–16.6, 0.6–0.9, 2.1–4.1, and 3.4–8.7 wt%, respectively), which have an inverse correlation with SiO₂ that points to an association with detrital mineral phases. All ranges are reported neglecting the sand layer (minor lithology), sampled at 81.44 mbsf, which shows anomalously low Al₂O₃, TiO₂, K₂O, and Ba values (Fig. F37). One striking feature in the uppermost interval is a gradual increase in Ba concentrations from 747 ppm at 91.1 mbsf to 1041 ppm at 113.65 mbsf, which coincides with an interval of low magnetic susceptibility and high diatom productivity (see “Paleomagnetism” and “Biostratigraphy”).

The second interval, from ~210 to ~310 mbsf, can be described as transitional. Some elements display clearly defined changes (i.e., TiO₂), whereas others continue to show fluctuating concentrations (e.g., SiO₂, K₂O, and Al₂O₃), though sometimes with decreased amplitudes (i.e., Fe₂O₃ and SiO₂). This transitional interval broadly correlates with the lithostratigraphic interpretation of a transition from levee-type deposits by low-turbidity currents (lithostratigraphic Units I and II; bottom depth = 247.1 mbsf) and deposits from an environment dominated by contour currents and/or saline density flows (below 247.1 mbsf; see “Lithostratigraphy”).

The third interval (~310–535.68 mbsf) is characterized by significantly reduced variability in most elemental concentrations (omitting the diatom-bearing nannofossil ooze layer at 372.45 mbsf) and a change in elemental correlations. Silicon dioxide concentrations vary between 66.2 and 75.5 wt% and are now inversely correlated with Al₂O₃ (11.1–14.9 wt%), TiO₂ (0.6–0.7 wt%), K₂O (2.8–3.8 wt%), Ba (470–602 ppm), CaO (1.4–3.1 wt%), and Fe₂O₃ (4.0–6.9 wt%) concentrations (Fig. F37).

The lowermost interval (547.39–594.79 mbsf) displays a notable shift in the different elemental patterns while maintaining the general elemental correlations described for the third interval. Silicon dioxide values show a pattern of increasing values, by ~7 wt%, before decreasing again by ~6 wt%. This trend is mirrored by Al₂O₃, TiO₂, K₂O, Fe₂O₃, and Ba.

The chemical index of alteration (CIA = [Al₂O₃ / (Al₂O₃ + CaO* + K₂O + Na₂O)] × 100, where CaO*

represents the CaO fixed in silicate minerals; Nesbitt and Young, 1982) (Fig. F37) shows highly variable values (47–63) between 0 and ~310 mbsf (first and second geochemical intervals). These values are comparable to values observed for the upper parts of Hole U1356A and imply environmental conditions dominated by physical weathering of terrigenous material (e.g., Passchier and Krissek, 2008; see also “Geochemistry and microbiology” in the “Site U1356” chapter). In the third interval (~310–535.68 mbsf), CIA values are constant between 55 and 58, indicating less variability in continental weathering. Lower values occur again in the lowermost samples.

Pore water chemistry

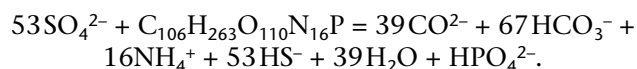
Fifty-one interstitial water samples were taken in close collaboration with the microbiology samples from the top ~20 m (0.1–20.1 mbsf) of cores from Hole U1359B (Fig. F9; Table T14). Samples were stored in the onboard cold room (<8°C) and squeezed as quickly as possible (~48 h until the last sample was squeezed). However, because of the large number of interstitial water samples collected in a short amount of time, the uppermost sample from each 1.5 m section and the fifth sample from the uppermost five cores were prioritized for squeezing to obtain a minimally compromised, coarse initial interstitial water profile. These first 18 samples were all squeezed within 12 h of sampling. Shipboard chemical analyses on all interstitial water samples included pH, salinity, chlorinity, alkalinity, dissolved inorganic carbon (DIC), sulfate, phosphate, ammonium, nitrite and nitrate, sodium, potassium, magnesium, calcium, boron, manganese, iron, strontium, barium, and silica measurements. The data are provided in Table T14 and shown in Figures F38, F39, and F40. Throughout the following text, cited values for average seawater composition are taken from Millero and Sohn (1992) and Broecker and Peng (1982).

Sulfate, alkalinity, dissolved organic carbon, pH, and magnesium

Dissolved sulfate concentrations within the top 2.4 m of the core are indistinguishable from seawater values (~28 mM). From 2.4 to 20.1 mbsf, sulfate contents decrease linearly, reaching a minimum value of 22.9 mM at 19 mbsf (Fig. F38). Magnesium contents follow a parallel trend of decreasing values. Absolute concentrations, however, only change by ~10%, from 50.1 to 44.6 mM. The overall decreasing pattern of Mg in interstitial waters is punctuated by two positive excursions at 5.4 and 15.5 mbsf (72.3 and 71.8 mM, respectively). Sulfate depletion is further negatively correlated with pH, alkalinity, and DIC (Fig. F38). In detail, pH increases downhole from 7.0

to 7.67, with an excursion to more acidic values of 6.76 at 1.8 mbsf coinciding with the onset of manganese and phosphate enrichment (see section below). Alkalinity increases throughout the profile from 0.1 to 5.4 (0.1–20.1 mbsf). Between 15.5 and 18.0 mbsf, alkalinity fluctuates between 5.2 and 4.2. This behavior is paralleled by the profile of DIC.

All previously described observations are consistent with active diagenesis of buried organic matter within the SRZ:



Significant levels of sulfate at the bottom of the observed profile (~23 mM at 20.1 mbsf) imply that the sampled interval did not reach the carbon dioxide (methanic) reduction zone (see “[Pore water chemistry](#)” in the “[Site U1357](#)” chapter for contrasting behavior).

Manganese, phosphate, ammonium, and silica

Dissolved manganese concentrations are below the detection limit of the ICP-AES for the top 1.8 mbsf. Below this depth, manganese levels increase steadily until a relative maximum is reached at 8 mbsf (108 μM). Between 8 and 20.1 mbsf, manganese concentrations oscillate between 62 and 112 μM (Fig. [F39](#)). The increase of manganese is most likely caused by the reduction of manganese during organic matter decay in the suboxic zone of the sediment column (i.e., where reduction of nitrate, Mn, and Fe happens; Froelich et al., 1979). Phosphate concentrations show a less smooth pattern than manganese concentrations but also increase from low values at shallow depths (0–2.2 mbsf; 0.8–3.5 μM) to higher values, reaching a relative maximum of 12.8 μM at 7.4 mbsf. Below 7.4 mbsf, phosphate values vary between 4.9 and 13.6 μM (Fig. [F39](#)). The correlation between phosphate and manganese in the upper part of the interstitial water profile suggests a common origin related to the microbial degradation of organic matter. Contrasting trends below 7.4 mbsf may be the result of different affinities of Mn and phosphate for absorption onto particle surfaces and/or coprecipitation with minerals formed in situ. The scatter in the phosphate data can be partially explained by the timing of pore water squeezing. As explained above, the top sample from each of the 13 sections plus 5 samples from lower in the uppermost five sections were squeezed first. The data corresponding to these 18 samples are shown as open circles in Figure [F39](#), suggesting that phosphate concentrations decline when samples are stored too long prior to squeezing.

Dissolved silica displays a more complex pattern, with high values (539–570 μM) for the uppermost 0.9 mbsf and lower values (480–533 μM) between 1.1 and 7.2 mbsf. After a sharp increase in Si concentrations, values are scattered around 540 μM from 8 to 14.5 mbsf. The lowest part of the profile shows a large scatter in Si concentrations (Fig. [F39](#)). In general, variations in silica could be related to early diagenetic clay mineral reactions, but such an interpretation will need to be confirmed by future studies. Ammonium concentrations show no general trend and fluctuate between 70.8 and 181.5 μM along the profile. A slight increase in ammonium concentrations at 2.2 mbsf appears to coincide with increased phosphate and manganese concentrations.

Nitrate, nitrite, boron, strontium, and chlorine

The sum of nitrite and nitrate concentrations (NO_x) in interstitial waters decrease overall from values of 4.6 μM at 0.1 mbsf to 3.7 μM at 7 mbsf (Fig. [F40](#)). The same interval, however, also contains major oscillations to absolute values of 5.0 μM at 2 mbsf and 1.2 μM at 2.2 mbsf. From 7 to 20.1 mbsf, NO_x concentrations are invariable around 4 μM . In general, reduction of nitrate to nitrite should follow reduction of manganese and sulfate during the mineralization of organic matter. The observed decrease in total concentrations of nitrite and nitrate in the topmost meter of the core is in line with this statement, although concentrations are very low throughout the profile. Dissolved strontium, boron, and chloride concentrations show fluctuations throughout the investigated uppermost 20 m of the sediment column centered around absolute values of 33, 339, and 560 μM , respectively (Fig. [F40](#)).

Microbiology

Microbiological sampling was conducted in Hole U1359B and supported with pore water sampling (Fig. [F9](#)). Fifty-two 10 cm whole rounds were taken from the top 20 m and frozen at -80°C for onshore phospholipid analyses and molecular 16S rRNA sequencing. Between 20 and 200 mbsf, seventeen 5 cm^3 samples were taken and preserved for onshore molecular 16S rRNA sequencing.

Physical properties

The physical properties program for Site U1359 included routine runs on the WRMSL, which includes the GRA bulk density, magnetic susceptibility, and PWL sensors, as well as NGR measurements. *P*-wave velocity was also analyzed and samples taken for moisture, density, and porosity measurements of cores from Hole U1359A, Hole U1359B, and Hole

U1359D. Thermal conductivity measurements were taken in cores from all holes.

Whole-Round Multisensor Logger and Special Task Multisensor Logger measurements

All Site U1359 cores were measured on the WRMSL (Figs. F41, F42, F43, F44, F45, F46, F47, F48) except for Core 318-U1359B-2H (intensive whole-round samples) and 318-U1359C-2H (no recovery).

Starting with Core 318-U1359B-3H, all cores from Holes U1359B and U1359C (except Core 318-U1359C-2H) were first run through the Special Task Multisensor Logger (STMSL) with the overall strategy to use these data for quick correlation to the Hole U1359A data to evaluate the offset during drilling of Holes U1359B and U1359C. Afterward, the core sections were allowed to equilibrate to room temperature and then run through the WRMSL. Hole U1359D cores were only run through the WRMSL.

Magnetic susceptibility

Whole-core magnetic susceptibility was measured at 2.5 cm intervals (2 s measurement time). The raw data values are as high as 1168 instrument units, with the peaks representing gravel clasts throughout the section (Figs. F41, F43, F45). The most prominent features in the magnetic susceptibility data are the two intervals of relatively low values (<20 instrument units) between 94 and 123 mbsf (95 and 124 m CCSF-A), as well as between 220 and 278 mbsf (230 and 295 m CCSF-A). In the intervals where the magnetic susceptibility is between 40 and ~100 instrument units, we observe a cyclicity at several scales throughout the section.

Natural gamma radiation

The total counts per second ranged from 3 to 101 cps, with the peaks representing dispersed gravel clasts (Figs. F41, F42, F43, F44, F45). However, the majority of measurements fall between 15 and 65 cps, and the values show an especially pronounced cyclicity. The NGR, magnetic susceptibility, and the GRA density data were used to correlate the four holes drilled at Site U1359 and to define a composite record (see “Stratigraphic correlation and composite section”).

Gamma ray attenuation bulk density

GRA bulk density was measured at 5 cm intervals on the STMSL (5 s integration time) and at 2.5 cm intervals at the WRMSL (10 s integration time). Measured values are as high as 2.57 g/cm³. The variations in GRA density reflect the regular fluctuations in lithology and porosity at Site U1359 (Figs. F46, F47, F48).

We observe especially pronounced lower density values between 50 and 65 mbsf (50 and 65 mcd; below the lithostratigraphic Unit I–II transition) and a sudden drop at ~99.5 mbsf (~101 mcd) that coincides with the lithologic change from diatom-bearing to diatom-rich silty clays (lithostratigraphic Subunit IIa–IIb transition) as well as a shift to slightly lower values at ~248 mbsf (~264 mcd) (lithostratigraphic Unit II/III boundary).

P-wave velocity

P-wave velocity measurements were made at 5 cm intervals on the WRMSL for all cores. The raw values are as high as 2770 m/s, including data from dispersed gravel clasts (Figs. F49, F50).

Additionally, discrete measurements of P-wave velocity were made on the working halves in Holes U1359A and U1359D. One measurement per section was targeted, however, because of the composition and expansion of the sediment, the Section Half Velocity Gantry could hardly obtain any valid measurements below 135 mbsf in Hole U1359A. However, discrete P-wave velocity measurements were successful in most cases in Hole U1359D cores, especially on sediment cubes taken below 450 m CCSF-A. These multiaxis measurements exhibit an anisotropy between the x-axis (perpendicular to the split-core surface) and the y-axis (parallel to the split-core surface) with generally higher velocities (Fig. F50). Because of the poor quality of the sediment cubes, in many cases we were not able to get readings along the z-axis (perpendicular to both x- and y-axes).

Because of the high water content and poor consolidation, the upper four cores in Hole U1359A (lithostratigraphic Unit I), a poor correlation between the PWL velocities and the discrete velocities measured on the split core (Fig. F49) is present. Overall, velocities slightly increase with depth from ~1650 m/s at 142 mbsf (150 mcd) to ~1730 m/s at 463 mbsf (480 mcd). Below 463 mbsf (480 mcd), about the level of Core 318-U1359-36R, the rise in velocity is much steeper (Fig. F50).

Moisture and density measurements

Moisture and density (MAD) measurements were undertaken on 105 samples taken of cores from Hole U1359A (Cores 318-U1359A-1H through 22X), 40 samples from Hole U1359B (318-U1359B-16H through 26X), and 157 samples from Hole U1359D (Cores 318-U1359D-7R through 48R). Depending on core recovery and quality, one sample was taken per section. These samples were carefully selected to cover the representative lithology of each core section and were taken in undisturbed sediments whenever

possible. These samples were measured for wet mass, dry mass, and dry volume and, using these measurements, porosity, percent water mass, dry density, bulk density, and grain density were calculated.

The wet bulk densities (MAD) from discrete samples range from 1.36 to 1.99 g/cm³ in Holes U1359A and U1359B (Figs. F46, F47) and from 1.46 to 1.93 g/cm³ in Hole U1359D (Figs. F46, F48). In the upper 248 mbsf (264 mcd) of the hole, both the GRA densities and the wet bulk densities on samples (MAD) are in good agreement. However, starting below 248 mbsf (264 mcd), and even more pronounced below 463 mbsf (480 mcd), the GRA density results are consistently lower than those measured from discrete samples. We interpret this to be a result of the reduced diameter of the RCB cores recovered in the lower, more lithified portions of Hole U1359D. This reduced diameter likely systematically underestimated the bulk density as measured by the GRA densiometer and is especially noticeable in the bioturbated diatom-bearing silty clays and silty clays with millimeter-scale laminations of lithostratigraphic Unit III (248–593 mbsf; 264–610 mcd).

All MAD parameters reflect the overall cyclic variations in the record (Figs. F46, F47, F48, F51, F52, F53) and also especially exhibit the lower density interval between 50 and 65 mbsf, as well as a relatively sudden change at ~100 mbsf. Grain density values are in the expected range of clayey to silty sediments (~2.6–2.7 g/cm³), and the values slightly decrease with depth to 463 mbsf (~480 mcd) but are stronger below (Figs. F46, F48). Porosity ranges from 75% to 55%, and these values only slightly decrease with depth (Figs. F51, F52, F53). Bulk density fluctuates between 1.4 and 1.8 g/cm³, and dry density varies between 0.8 and 1.2 g/cm³ (Figs. F54, F55, F56). Moisture content and void ratio show similar trends to porosity, as expected (Figs. F57, F58, F59).

Thermal conductivity

Thirty-two measurements were made on full cores in Holes U1359A, U1359B, and U1359C and 30 measurements on cores in Hole U1359D (Fig. F60). The thermal conductivity data slightly decrease with depth and are discussed in more detail in relation to downhole temperature measurements for calculating heat flow (see “Downhole measurements”).

Stratigraphic correlation and composite section

Magnetic susceptibility, GRA density, and NGR data collected from cores of Holes U1359A–U1359D were used to construct the composite section for Site

U1359. The NGR and magnetic susceptibility measurements were primarily used for core to core correlation and to construct the composite section (Figs. F61, F62, F63). The depth offsets that define the composite section for Site U1359 are given in Table T15.

There are two gaps in the upper 30 m of the composite record. This is a direct result of intensive sampling for microbiologic and geochemical analysis in the first two cores from Hole U1359B and the lack of recovery in the second core in Hole U1359C. The gaps in the composite record occur at ~10.9 mcd (between Cores 318-U1359A-2H and 3H) and ~29.8 mcd (between Cores 318-U1359B-4H and 318-U1359C-4H).

Following construction of the composite depth section for Site U1359, a single spliced record was assembled from the aligned core intervals from all four holes (Table T16). The composite data show that the cores from Site U1359 provide two continuous sequences from 36.84 mcd (top of Section 318-U1359A-6H-1) to 162.08 mcd (bottom of Core 318-U1359B-17H) and from 162.29 mcd (top of Core 318-U1359B-18H) to 214.49 mcd (bottom of Core 318-U13459B-22H). Below this depth, Cores 318-U1359B-23H through 24X and 318-U1359D-7R through 48R were appended to the record (Figs. F61, F62, F63; Table T16).

Cores that had been significantly stretched, squeezed, or disturbed by the coring process were not used for the splice. Without a stretching or squeezing correction, all points within each core are offset equally. As a result, some of the patterns are not perfectly aligned between holes (e.g., at ~45 and ~72 mcd in Fig. F61). Thus, the meters composite depth values of the different holes will approximate but not precisely correspond to the same stratigraphic horizon in alternate holes.

The Site U1359 splice (Table T16) can be used as a guide to sample the sedimentary sequence and was used to plot other data sets from this site. The meters composite depth to meters below seafloor growth factors for Holes U1359A–U1359C were ~5%, ~6%, and ~4%, respectively (Fig. F64A, F64B, F64C).

Downhole measurements

Logging operations

Downhole logging measurements in Hole U1359D were made after completion of RCB coring to a total depth of 602.2 mbsf (DSF). In preparation for logging, the hole was flushed with a 50 bbl sweep of sepiolite mud, and the bit was released at the bottom of the hole. The hole was then displaced with 191 bbl of barite-weighted mud (10.5 ppg), and the

pipe was pulled up to 96.9 mbsf (DSF). No tight spots were encountered during the reaming. Three tool strings were deployed in Hole U1359D: the triple combo, FMS-sonic, and VSI (Fig. F65; see “**Down-hole logging**” in the “Methods” chapter).

At 0045 h on 23 February 2010, the triple combo tool string (resistivity, density, porosity, and natural gamma ray tools) started down the pipe and logged down to the bottom of the hole at 606.5 mbsf (wireline depth below seafloor [WSF]). The hole was then logged up to seafloor. The tools provided continuous and good-quality log data. The hole was drilled with a 9 $\frac{7}{8}$ inch diameter RCB bit and the borehole diameter ranged between 10 and 13 inches (25.4–33.0 cm) below 380 mbsf (WSF), increasing to 12–16 inches (30.5–40.6 cm) shallower than 380 mbsf, with a few thin washouts between 110 and 160 mbsf (WSF).

The seafloor depth of 3019.5 mbrf (wireline depth below rig floor) was determined from the step increase in gamma ray values at the sediment/water interface on both the downward and upward passes of the tool string. A driller’s seafloor depth of 3023 mbrf was established from the seafloor tag in Hole U1359D, and the top 150 m of the hole was washed down. But based on differences between the wireline and driller’s depths to the base of pipe and the base of hole and also on the offset in correlations between core and log data from Hole U1359D (e.g., Fig. F66), the actual seafloor depth is ~5 m shallower, at ~3018 mbrf (drilling depth below rig floor) at the location of Hole U1359D.

At 0800 h, the FMS-sonic tool string (FMS microresistivity imager, sonic, and natural gamma ray tools) was run into the pipe and recorded one downward pass and three upward passes in Hole U1359D. All passes reached the base of the hole at 606.5 mbsf. The opportunity was taken to run a third pass with the FMS-sonic tool string because a mis-wrap of the cable on the winch meant the cable had to be run back down and re-wrapped. The tools were back at the surface at 1855 h on 23 February.

The VSI check shot survey was delayed until the next day because of high winds, misty conditions, and the approach of nightfall. Marine mammal watch started at 0600 h on 24 February, and the VSI tool started down the pipe at 0730 h. The air gun was positioned on the port side of the R/V *JOIDES Resolution* at a water depth of ~7 mbsl and offset laterally ~30 m from the borehole. The soft-start of the Sercel G. Gun Parallel Cluster (composed of two 250 in³ air guns separated by 1 m) started at 0930 h. Whales entered the safety radius (940 m) once, so air gun firing was stopped until the whales left; we began the air gun soft-start again. It was planned to make check shot stations at 25 m intervals, but after the tool

reached the bottom of the hole the caliper arm would not open to clamp the VSI’s geophone against the borehole wall. Waveforms were extremely noisy without clamping, and it was not possible to determine a check shot traveltime. However, with the tool resting on the infill at the bottom of the hole at 601.5 mbsf (WSF), noise was sufficiently reduced and it was possible to get four reliable waveforms. These waveforms were stacked to yield a one-way traveltime of 2.3867 s. The VSI tool string was brought back to the surface and disassembled, concluding logging operations at Site U1359 at 1400 h.

Logging units

Hole U1359D was divided into two units on the basis of the logs (Fig. F10).

Logging Unit 1: base of drill pipe to 260 mbsf

The upper logging unit is characterized by high-amplitude fluctuations in bulk density, NGR, and resistivity values on the scale of 1–5 m. It is also characterized by a lack of a compaction trend with depth; the mean bulk density value remains quite constant, whereas the resistivity values decrease with depth. The transition to the unit below is gradual.

Logging Unit 2: 260–606 mbsf

Logging Unit 2 is characterized by generally lower amplitude bulk density and resistivity variations than the unit above, but the several meter-scale alternations are still clearly defined. A normal compaction trend resumes in bulk density and sonic velocity. NGR continues to show quite high variability, and several large drops in NGR values are observed between 350 and 450 mbsf. Near the base of the hole at 574–580 mbsf, a 6 m interval of higher bulk density and resistivity occurs, indicating a cemented bed or series of cemented beds.

Identification of microfossil-rich intervals from natural gamma radiation logs

Spectral NGR logs were obtained using the Hostile Environment Natural Gamma Ray Sonde tool on all six passes of the triple combo and FMS-sonic tool strings. The triple combo main (upward) pass has the best statistics because it was run at the slowest speed (300 m/h rather than 600 m/h as used on the other passes). The NGR signal is strong (average = ~70 gAPI) and is dominated by the radioactivity of potassium and thorium, with uranium contributing a relatively minor component. Potassium and thorium concentrations co-vary closely (Fig. F66), suggesting they are present in the same fraction of the sediment. Both of these elements are found in clay

minerals, and the sediments at Site U1359 are clay rich, so at first order the NGR signal is probably tracking clay content. Less abundant minerals like potassium feldspar also contribute to the NGR signal.

The NGR downhole logs contain an abundance of distinctive peaks and troughs that can be easily correlated to the NGR data measured on cores (Figs. F66, F67). In terms of lithology, intervals of low NGR values correspond to diatom-rich layers in the core, because diatoms are not radioactive and they dilute the NGR signal from K, Th, and U in the clays and terrigenous minerals that make up the balance of the sediment. The NGR logs promise to be a useful method for identifying diatom-rich and diatom-bearing zones in the core (where they are not always apparent to the eye) and complete the stratigraphy in unrecovered intervals.

The density log also helps to identify diatom-rich zones. Relatively low density values result from the intragranular porosity contained in the diatom shells and the low grain density of the opal that forms the diatom shells (2.1–2.2 g/cm³ compared to 2.6–2.75 g/cm³ for the other major sediment minerals). Shallower than 350 mbsf, the resistivity and sonic velocity logs also follow the pattern of the NGR and density logs because the higher porosity in the diatom-rich intervals leads to low resistivity and low velocity. However, deeper than 350 mbsf, the opposite relation holds: low NGR values often correspond to higher resistivity and sonic velocity (Fig. F10). One possible explanation is that the diatom- and nannofossil-rich intervals are more easily cemented than the clay-rich sediments that enclose them.

Formation MicroScanner resistivity images

FMS resistivity images reveal stratigraphic information including layered bedding, inclined bedding at the base of the hole, and dropstones and IRD larger than ~1 cm. The dropstones appear as resistive (light colored) spots in the image (Fig. F68A, F68B), and it will be possible to map their occurrence from 105 to 600 mbsf. The dipping beds between 575 to 579 mbsf appear as light-colored sinusoids in the image and are the most resistive sediment in the stratigraphy. The steepness of dip is highly variable (up to ~45°), and the beds dip to the east and west (Fig. F68C), indicating slumps.

Sonic velocity

The Dipole Sonic Imager tool recorded four passes of *P*- and *S*-wave velocity logs in Hole U1359D (Fig. F65). Below 250 mbsf, both *P*- and *S*-wave velocity logs repeat very well in shape and amplitude, giving confidence in the measured values (Fig. F69). How-

ever, shallower than 250 mbsf, *P*-wave velocities could not be determined from the initial slowness time coherence picks from the monopole source data by the Schlumberger data acquisition software. A substitute *P*-wave velocity log for 100–250 m was provided by the dipole source, usually used solely for *S*-wave velocities, which gave a noisy but generally reliable *P*-wave arrival (Fig. F69). The *P*-wave velocity logs will be critical to constructing a synthetic seismogram for this site.

Sonic check shots were successful at only one station, at the bottom of the hole at 601.5 mbsf, where a one-way traveltime of 2386.7 ms was found from the first arrival of four stacked waveforms. This puts the base of the hole at the bottom of the package of low-amplitude reflectors in the WEGA-26 seismic section. Given a seafloor two-way traveltime of 4060 ms (Escutia et al., 2008), an average *P*-wave velocity of ~1686 m/s can be calculated for Hole U1359D. When this average is converted to a linearly increasing velocity with depth, it matches the values from the core and log velocity measurements quite well (Fig. F69).

Heat flow

Heat flow at Site U1359 was determined according to the procedure of Pribnow et al. (2000). Four advanced piston corer temperature tool (APCT-3) measurements in Hole U1359A ranged from 2.05°C at 29.1 mbsf (DSF) to 7.17°C at 119.6 mbsf (DSF) (Table T17), giving a geothermal gradient of 62.1°C/km (Fig. F67). The seafloor temperature was -0.29°C based on the average of the four minimum temperature values in the APCT-3 temperature profiles (Fig. F70A). The thermal conductivity under in situ conditions was estimated from laboratory-determined thermal conductivity using the method of Hyndmann et al. (1974) (see “Physical properties” in the “Methods” chapter). The calculated in situ values are ~2% lower than the measured laboratory values. Thermal resistance was then calculated by cumulatively adding the inverse of the in situ thermal conductivity values over depth intervals downhole (Fig. F70B). Heat flow was obtained from the linear fit between temperature and thermal resistance (Fig. F70C). The heat flow estimate for Site U1359 is 62.4 mW/m², which is a typical value for the ocean floor.

References

- Barker, P.F., Camerlenghi, A., Acton, G.D., et al., 1999. *Proc. ODP, Init. Repts.*, 178: College Station, TX (Ocean Drilling Program). doi:10.2973/odp.proc.ir.178.1999
- Berggren, W.A., 1992. Neogene planktonic foraminifer magnetobiostratigraphy of the southern Kerguelen Pla-

- teau (Sites 747, 748, and 751). In Wise, S.W., Jr., Schlich, R., et al., *Proc. ODP, Sci. Results*, 120: College Station, TX (Ocean Drilling Program), 631–647. doi:10.2973/odp.proc.sr.120.153.1992
- Blakely, R.J., 1974. Geomagnetic reversals and crustal spreading rates during the Miocene. *J. Geophys. Res., [Solid Earth]*, 79(20):2979–2985. doi:10.1029/JB079i020p02979
- Bowles, J., Tauxe, L., Gee, J., McMillan, D., and Cande, S., 2003. Source of tiny wiggles in Chron C5: a comparison of sedimentary relative intensity and marine magnetic anomalies. *Geochem., Geophys., Geosyst.*, 4(6):1049–1068. doi:10.1029/2002GC000489
- Broecker, W.S., and Peng, T.-H., 1982. *Tracers in the Sea*: Palisades, NY (Eldigio Press).
- Buseti, M., Caburlotto, A., Armand, L., Damiani, D., Giorgetti, G., Lucchi, R.G., Quilty, P.G., and Villa, G., 2003. Plio-Quaternary sedimentation on the Wilkes Land continental rise: preliminary results. *Deep-Sea Res., Part II*, 50(8–9):1529–1562. doi:10.1016/S0967-0645(03)00078-X
- Cande, S.C., and LaBrecque, J.L., 1974. Behaviour of the Earth's paleomagnetic field from small scale marine magnetic anomalies. *Nature (London, U. K.)*, 247(5435):26–28. doi:10.1038/247026a0
- Cody, R.D., Levy, R.H., Harwood, D.M., and Sadler, P.M., 2008. Thinking outside the zone: high-resolution quantitative diatom biochronology for the Antarctic Neogene. *Palaeogeogr., Palaeoclimatol., Palaeoecol.*, 260(1–2):92–121. doi:10.1016/j.palaeo.2007.08.020
- Corliss, B.H., 1979. Recent deep-sea benthonic foraminiferal distributions in the southeast Indian Ocean: inferred bottom-water routes and ecological implications. *Mar. Geol.*, 31(1–2):115–138. doi:10.1016/0025-3227(79)90059-8
- Damiani, D., Giorgetti, G., and Memmi Turbanti, I., 2006. Clay mineral fluctuations and surface textural analysis of quartz grains in Pliocene–Quaternary marine sediments from Wilkes Land continental rise (East Antarctica): paleoenvironmental significance. *Mar. Geol.*, 226(3–4):281–295. doi:10.1016/j.margeo.2005.11.002
- De Santis, L., Brancolini, G., and Donda, F., 2003. Seismostratigraphic analysis of the Wilkes Land Continental Margin (East Antarctica): influence of glacially driven processes on the Cenozoic deposition. *Deep-Sea Res., Part II*, 50(8–9):1563–1594. doi:10.1016/S0967-0645(03)00079-1
- Donda, F., Brancolini, G., De Santis, L., and Trincardi, F., 2003. Seismic facies and sedimentary processes on the continental rise off Wilkes Land (East Antarctica): evidence of bottom current activity. *Deep-Sea Res., Part II*, 50(8–9):1509–1527. doi:10.1016/S0967-0645(03)00075-4
- Ehrmann, W.U., Grobe, H., and Fütterer, D.K., 1991. Late Miocene to Holocene glacial history of East Antarctica as revealed by sediments from Sites 745 and 746. In Barron, J., Larsen, B., et al., *Proc. ODP, Sci. Results*, 119: College Station, TX (Ocean Drilling Program), 239–260. doi:10.2973/odp.proc.sr.119.208.1991
- Escutia, C., Brinkhuis, H., and Klaus, A., 2008. Cenozoic East Antarctic ice sheet evolution from Wilkes Land margin sediments. *IODP Sci. Prosp.*, 318. doi:10.2204/iodp.sp.318.2008
- Escutia C., De Santis, L., Donda, F., Dunbar, R.B., Cooper, A.K., Brancolini, G., and Eittreim, S.L., 2005. Cenozoic ice sheet history from East Antarctic Wilkes Land Continental Margin sediments. *Global Planet. Change*, 45(1–3):51–81. doi:10.1016/j.gloplacha.2004.09.010
- Escutia, C., Eittreim, S.L., and Cooper, A.K., 1997. Cenozoic sedimentation on the Wilkes Land continental rise, Antarctica. In Ricci, C.A. (Ed.), *The Antarctic Region: Geological Evolution and Processes*. Proc. Int. Symp. Antarct. Earth Sci., 7:791–795.
- Escutia, C., Eittreim, S.L., Cooper, A.K., and Nelson, C.H., 2000. Morphology and acoustic character of the Antarctic Wilkes Land turbidite systems: ice-sheet-sourced versus river-sourced fans. *J. Sediment. Res.*, 70(1):84–93. doi:10.1306/2DC40900-0E47-11D7-8643000102C1865D
- Escutia, C., Nelson, C.H., Acton, G.D., Eittreim, S.L., Cooper, A.K., Warnke, D.A., and Jaramillo, J.M., 2002. Current controlled deposition on the Wilkes Land continental rise, Antarctica. In Stow, D.A.V., Pudsey, C.J., Howe, J.A., Faugeres, J.-C., and Viana, A.R. (Eds.), *Deep-Water Contourite Systems: Modern Drifts and Ancient Series, Seismic and Sedimentary Characteristics*. Mem.—Geol. Soc. London, 22(1):373–384. doi:10.1144/GSL.MEM.2002.022.01.26
- Florindo, F., Roberts, A.P., and Martin, P., 2003. Magnetite dissolution in siliceous sediments. *Geochem., Geophys., Geosyst.*, 4(7):1053–1066. doi:10.1029/2003GC000516
- Froelich, P.N., Klinkhammer, G.P., Bender, M.L., Luedtke, N.A., Heath, G.R., Cullen, D., Dauphin, P., Hammond, D., Hartman, B., and Maynard, V., 1979. Early oxidation of organic matter in pelagic diagenesis of the eastern equatorial Atlantic: suboxic diagenesis. *Geochim. Cosmochim. Acta*, 43(7):1075–1090. doi:10.1016/0016-7037(79)90095-4
- Gradstein, F.M., Ogg, J.G., and Smith, A. (Eds.), 2004. *A Geologic Time Scale 2004*: Cambridge (Cambridge Univ. Press). <http://cambridge.org/uk/catalogue/catalogue.asp?isbn=9780521781428>
- Hartl, P., Tauxe, L., and Herbert, T., 1995. Earliest Oligocene increase in South Atlantic productivity as interpreted from “rock magnetism” at Deep Sea Drilling Project Site 522. *Paleoceanography*, 10(2):311–325. doi:10.1029/94PA03150
- Hillenbrand, C.-D., and Ehrmann, W., 2005. Late Neogene to Quaternary environmental changes in the Antarctic Peninsula region: evidence from drift sediments. *Global Planet. Change*, 45(1–3):165–191. doi:10.1016/j.gloplacha.2004.09.006
- Hyndman, R.D., Erickson, A.J., and Von Herzen, R.P., 1974. Geothermal measurements on DSDP Leg 26. In Davies, T.A., Luyendyk, B.P., et al., *Init. Repts. DSDP*, 26: Washington, DC (U.S. Govt. Printing Office), 451–463. doi:10.2973/dsdp.proc.26.113.1974

- Kroenke, L.W., Berger, W.H., Janecek, T.R., et al., 1991. *Proc. ODP, Init. Repts.*, 130: College Station, TX (Ocean Drilling Program). [doi:10.2973/odp.proc.ir.130.1991](https://doi.org/10.2973/odp.proc.ir.130.1991)
- Mayer, L., Pias, N., Janecek, T., et al., 1992. *Proc. ODP, Init. Repts.*, 138: College Station, TX (Ocean Drilling Program). [doi:10.2973/odp.proc.ir.138.1995](https://doi.org/10.2973/odp.proc.ir.138.1995)
- Millero, F.J., and Sohn, M.L., 1992. *Chemical Oceanography*: Boca Raton (CRC Press).
- Nesbitt, H.W., and Young, G.M., 1982. Early Proterozoic climates and plate motions inferred from major element chemistry of lutites. *Nature (London, U. K.)*, 299(5885):715–717. [doi:10.1038/299715a0](https://doi.org/10.1038/299715a0)
- O'Brien, P.E., Cooper, A.K., Richter, C., et al., 2001. *Proc. ODP, Init. Repts.*, 188: College Station, TX (Ocean Drilling Program). [doi:10.2973/odp.proc.ir.188.2001](https://doi.org/10.2973/odp.proc.ir.188.2001)
- Passchier, S., and Kriesek, L., 2008. Oligocene–Miocene Antarctic continental weathering record and paleoclimatic implications, Cape Roberts drilling project, Ross Sea, Antarctica. *Palaeogeogr., Palaeoclimatol., Palaeoecol.*, 260(1):30–40. [doi:10.1016/j.palaeo.2007.08.012](https://doi.org/10.1016/j.palaeo.2007.08.012)
- Pribnow, D.F.C., Kinoshita, M., and Stein, C.A., 2000. *Thermal Data Collection and Heat Flow Recalculations for ODP Legs 101–180*: Hanover, Germany (Inst. Joint Geosci. Res., Inst. Geowiss. Gemeinschaftsauf. [GGA]). <http://www-odp.tamu.edu/publications/heatflow/ODPreprt.pdf>
- Rebesco, M., Camerlenghi, A., Geletti, R., and Canals, M., 2006. Margin architecture reveals the transition to the modern Antarctic ice sheet (AIS) ca. 3 Ma. *Geology*, 34(4):301–304. [doi:10.1130/G22000.1](https://doi.org/10.1130/G22000.1)
- Ruddiman, W., Sarnthein, M., Baldauf, J., et al., 1988. *Proc. ODP, Init. Repts.*, 108: College Station, TX (Ocean Drilling Program). [doi:10.2973/odp.proc.ir.108.1988](https://doi.org/10.2973/odp.proc.ir.108.1988)
- Schwehr, K., Tauxe, L., Driscoll, N., and Lee, H., 2006. Detecting compaction disequilibrium with anisotropy of magnetic susceptibility. *Geochem., Geophys., Geosyst.*, 7(11):Q11002. [doi:10.1029/2006GC001378](https://doi.org/10.1029/2006GC001378)
- Stow, D.A.V., and Piper, D.J.W., 1984. Deep-water fine-grained sediments: facies models. In Stow, D.A.V., and Piper, D.J.W. (Eds.), *Fine-Grained Sediments: Deep-Water Processes and Facies*. Geol. Soc. Spec. Publ., 15(1):611–646. [doi:10.1144/GSL.SP.1984.015.01.38](https://doi.org/10.1144/GSL.SP.1984.015.01.38)
- Tarduno, J.A., 1995. Superparamagnetism and reduction diagenesis in pelagic sediments: enhancement or depletion? *Geophys. Res. Lett.*, 22(11):1337–1340. [doi:10.1029/95GL00888](https://doi.org/10.1029/95GL00888)
- Tauxe, L., Constable, C., Stokking, L., and Badgley, C., 1990. Use of anisotropy to determine the origin of characteristic remanence in the Siwalik red beds of northern Pakistan. *J. Geophys. Res., [Solid Earth]*, 95(B4):4391–4404. [doi:10.1029/JB095iB04p04391](https://doi.org/10.1029/JB095iB04p04391)
- van Morkhoven, F.P.C.M., Berggren, W.A., and Edwards, A.S., 1986. *Cenozoic Cosmopolitan Deep-Water Benthic Foraminifera*. Bull. Cent. Rech. Explor.—Prod. Elf-Aquitaine, 11.

Publication: 2 July 2011
MS 318-107



Figure F2. Multichannel seismic reflection profile across Site U1359 showing regional unconformities WL-U3, WL-U4, and WL-U5 targeted by drilling. Red rectangle = approximate penetration achieved at Site U1359. Location of seismic profiles is shown in Figure F1.

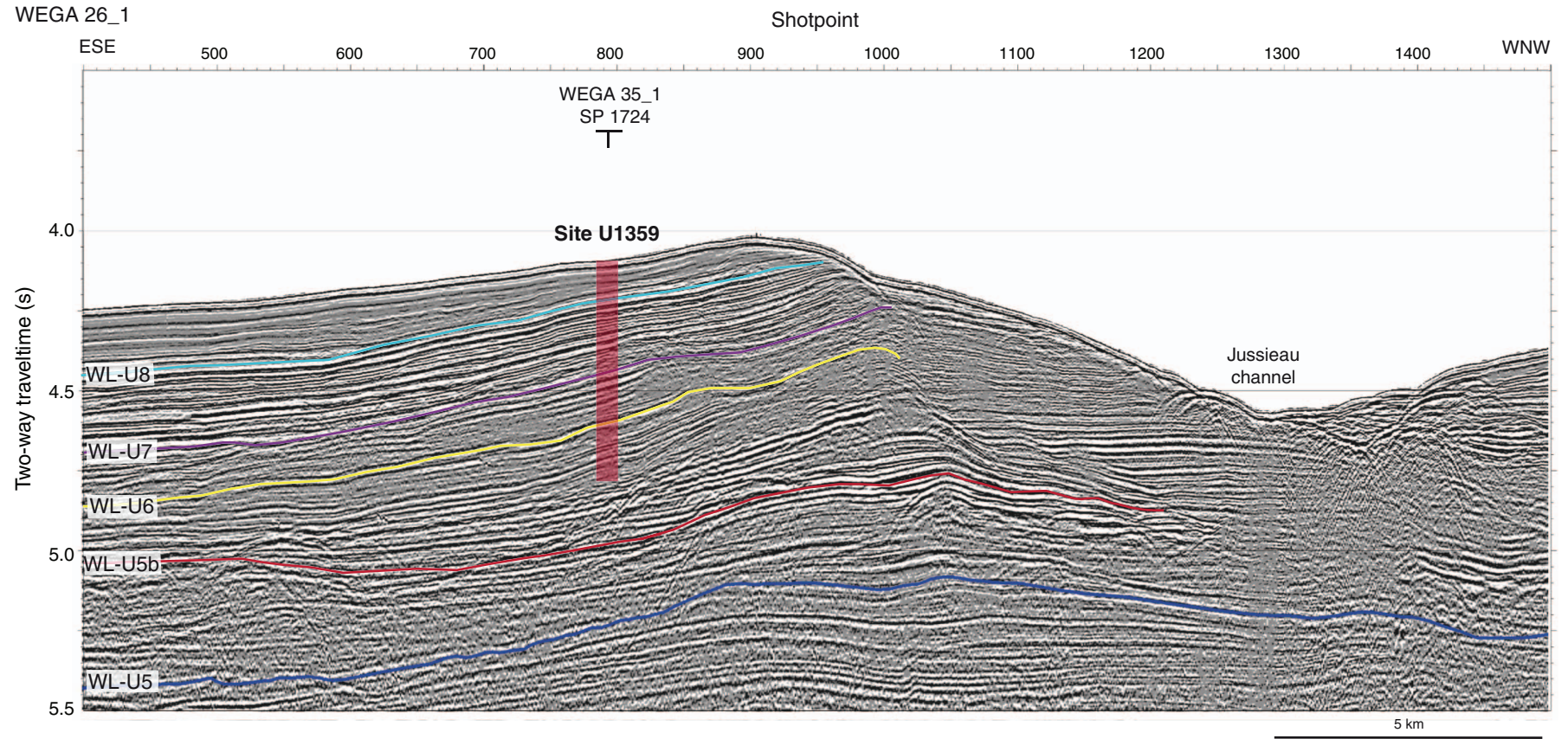


Figure F3. Composite summary lithologic log, Site U1359.

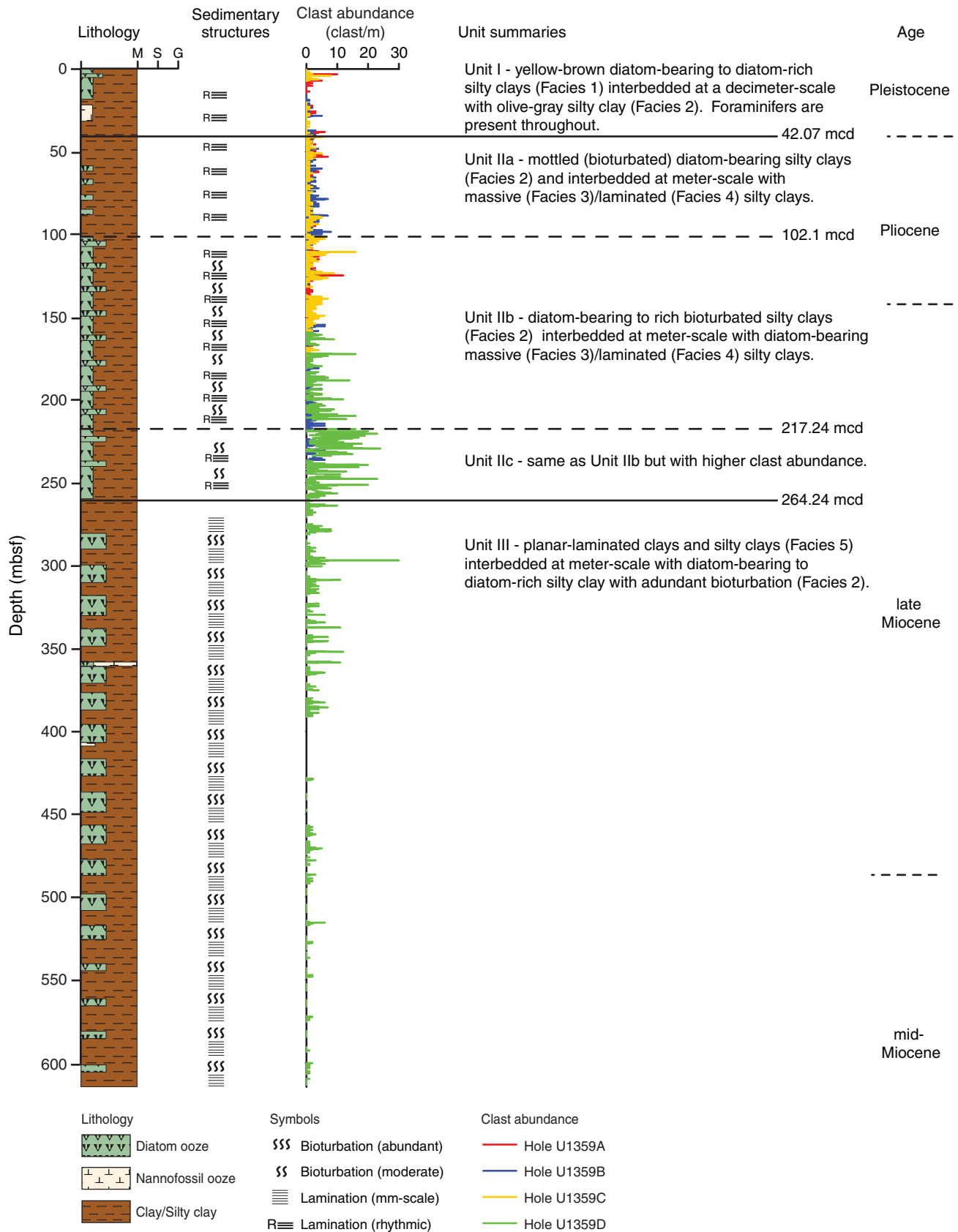


Figure F4. Summary logs, Holes U1359A–U1359D.

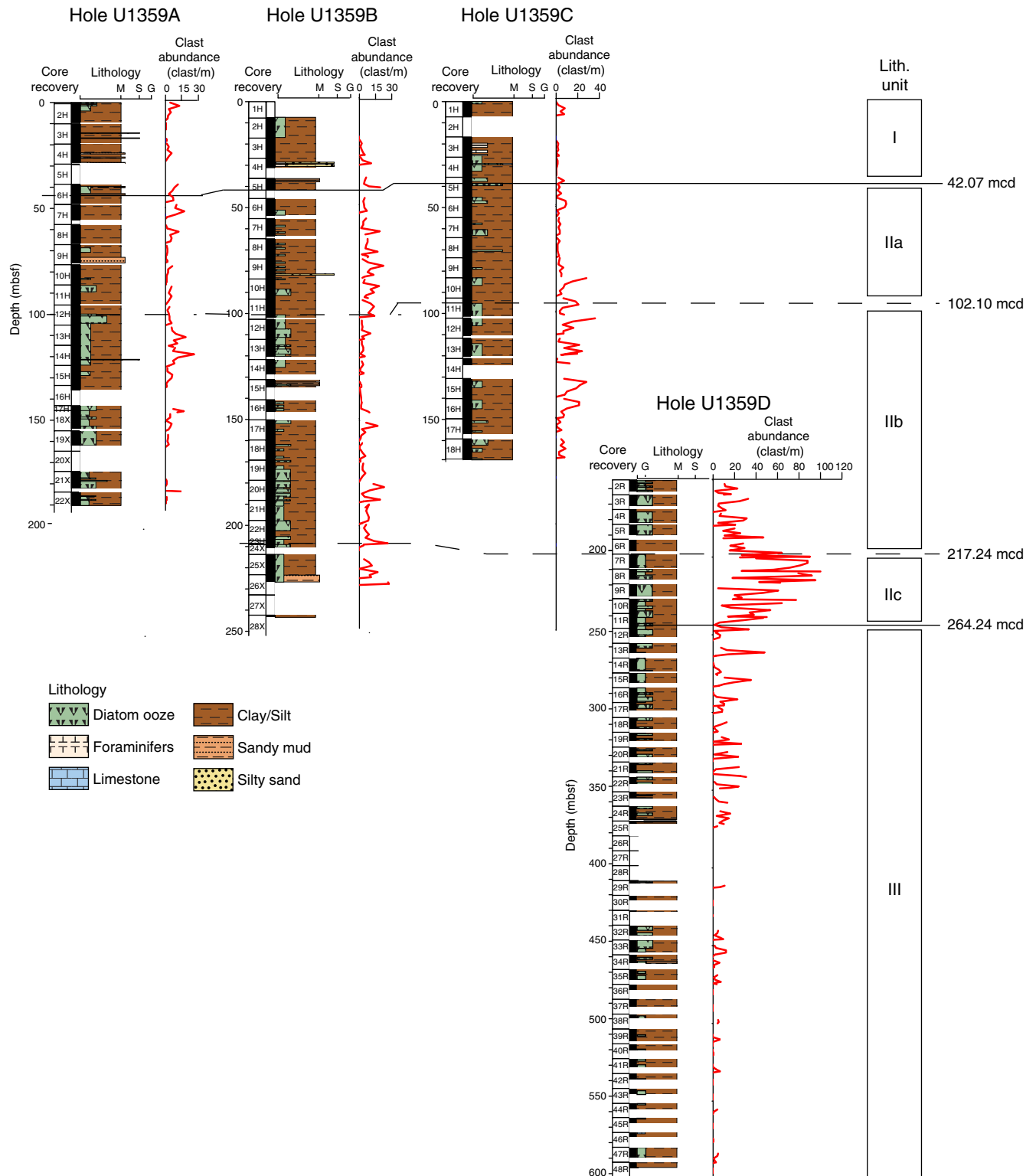


Figure F5. Core image of alternating beds of silty clay with dispersed clasts and diatom-rich silty clay with dispersed clasts in lithostratigraphic Subunit IIb plotted with physical property data (Core 318-U1359A-15H). GRA = gamma ray attenuation. Red line = five-point running mean, gray plus symbols = raw data.

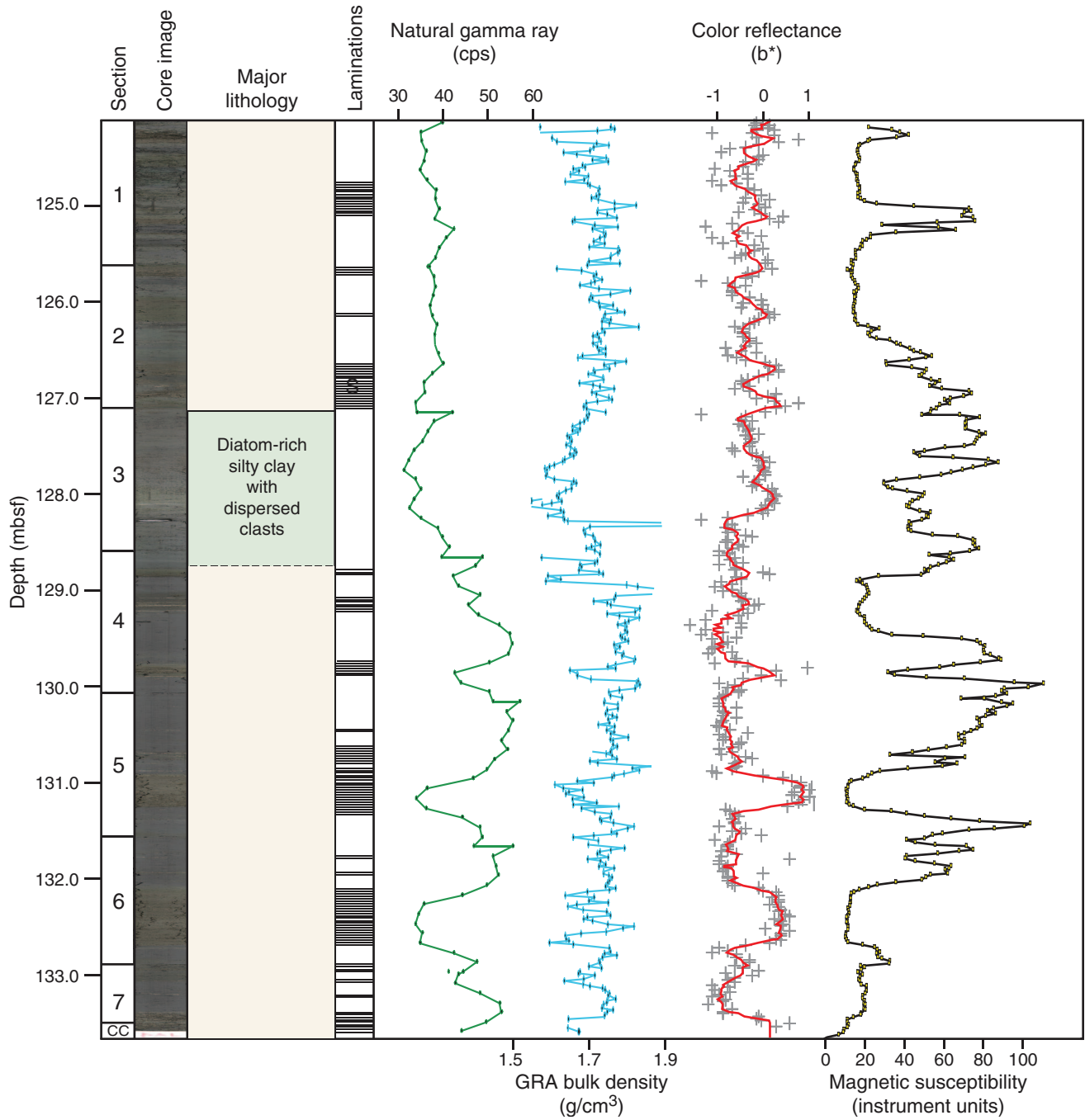


Figure F6. Core image of alternating beds of silty clay with dispersed clasts and diatom-rich silty clay with dispersed clasts in lithostratigraphic Subunit IIb plotted with physical property data (interval 318-U1359B-17H-1, 80 cm, through 17H-4, 130 cm). * = position of the silt laminations highlighted in Figure F16. GRA = gamma ray attenuation. Red line = five-point running mean, gray plus symbols = raw data.

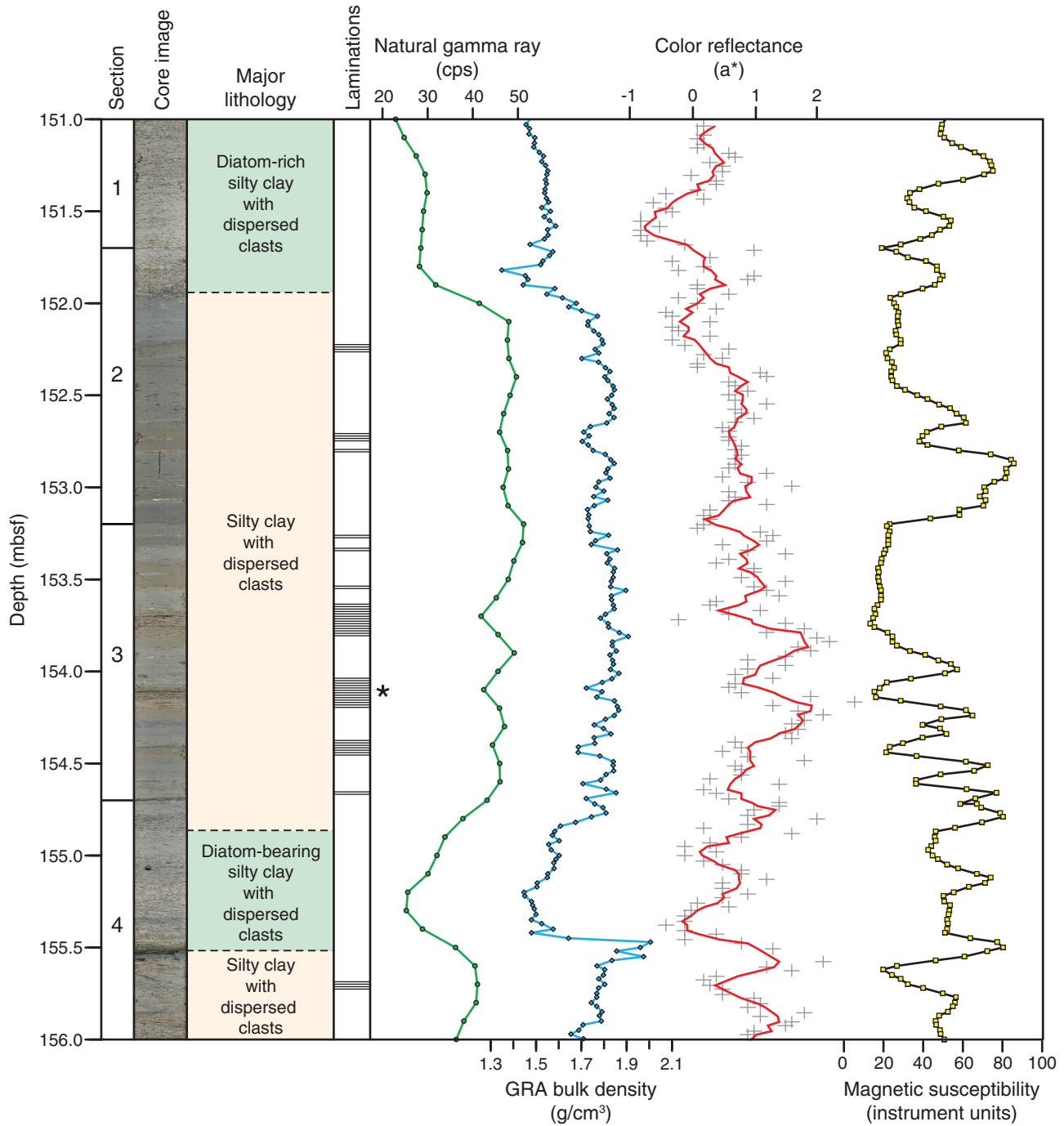


Figure F7. Biomagnetostratigraphic age-depth plot, Holes U1359A–U1359D. Yellow shading = chronostratigraphic preservation, light yellow shading = low sedimentation rates. Microfossil datums are plotted by using the median depth between upper and lower samples (Table T11). Mid-point absolute age in the average range model of Cody et al. (2008) is used for the diatom datums. t = top, b = bottom, o = oldest, y = youngest. Blue line = best-fit sedimentation rate. Offsets within the stratigraphic overlap between holes may be a function of plotting these data in mbsf space. (Figure shown on next page.)



Figure F7 (continued). (Caption shown on previous page.)

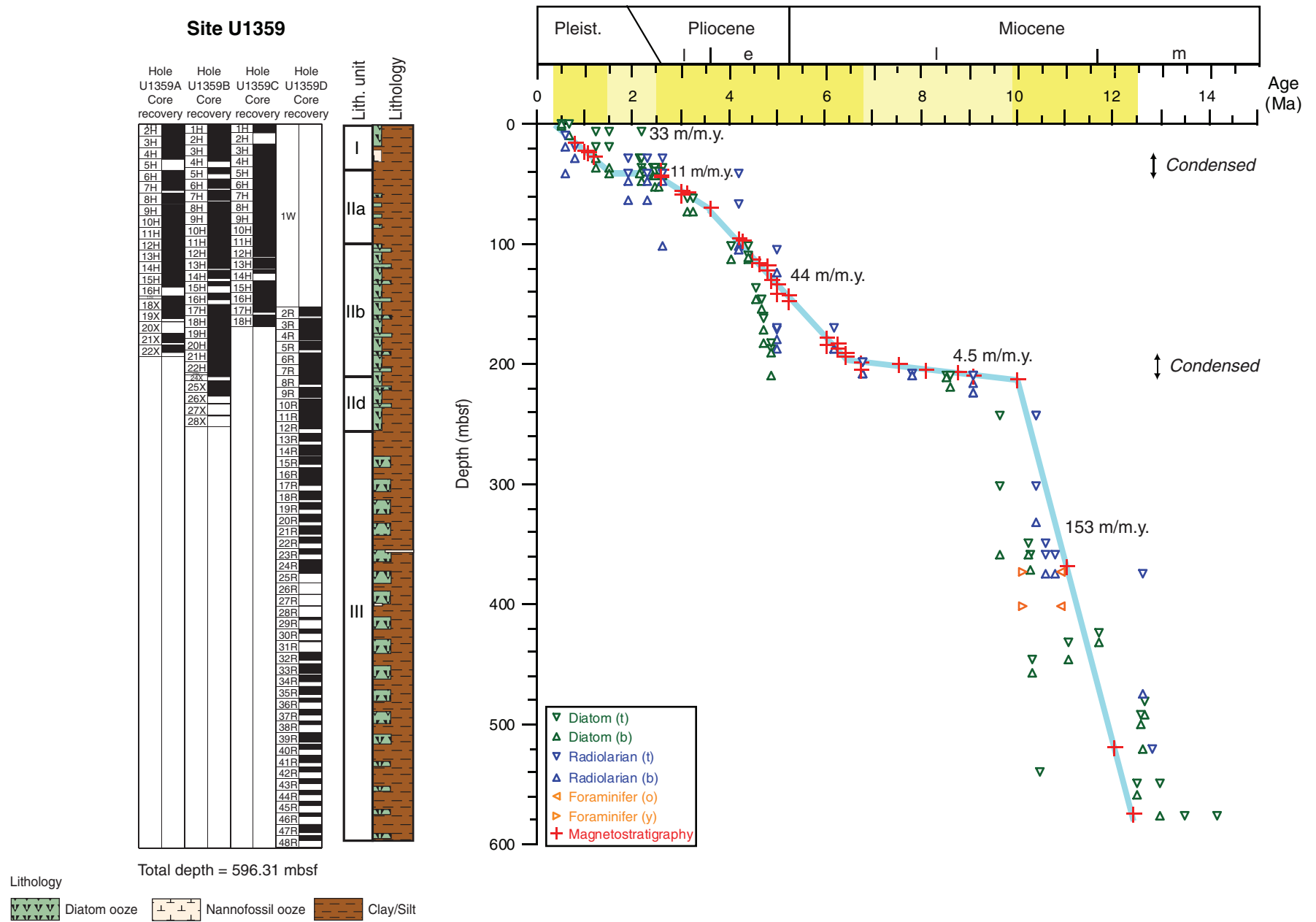




Figure F8. Plots of correlation of magnetostratigraphy to the geomagnetic polarity time scale (GPTS) of Gradstein et al. (2004). Tie-point lines between polarity logs and GPTS are listed in Table T12. Purple shaded areas = gaps in recovery. **A.** Holes U1359A–U1359C placed on the composite depth scale (see “Stratigraphic correlation and composite section”). The composite polarity log is constructed from the best records from each of the three holes. (Continued on next two pages.)

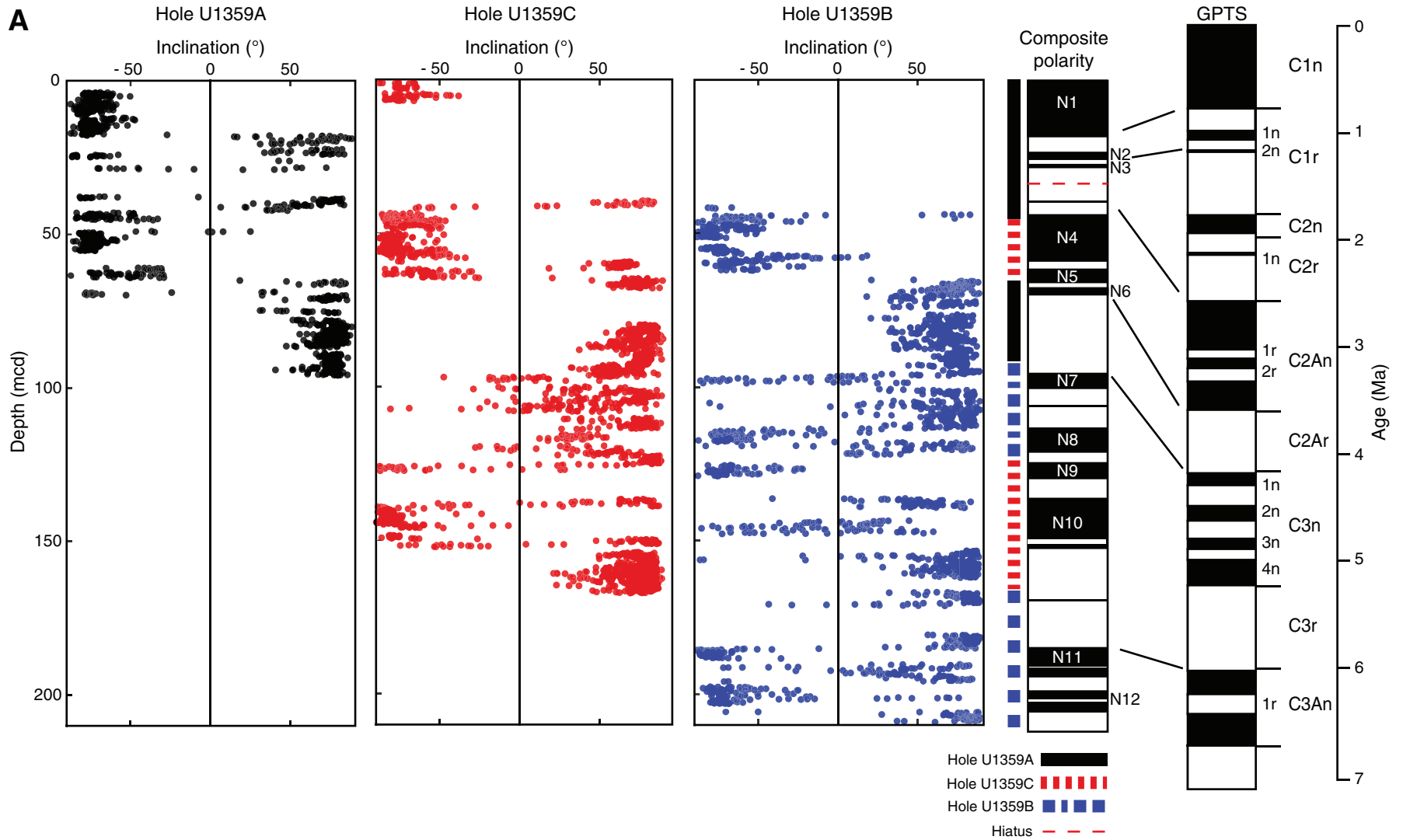




Figure F8 (continued). B. Upper part of Hole U1359D. (Continued on next page.)

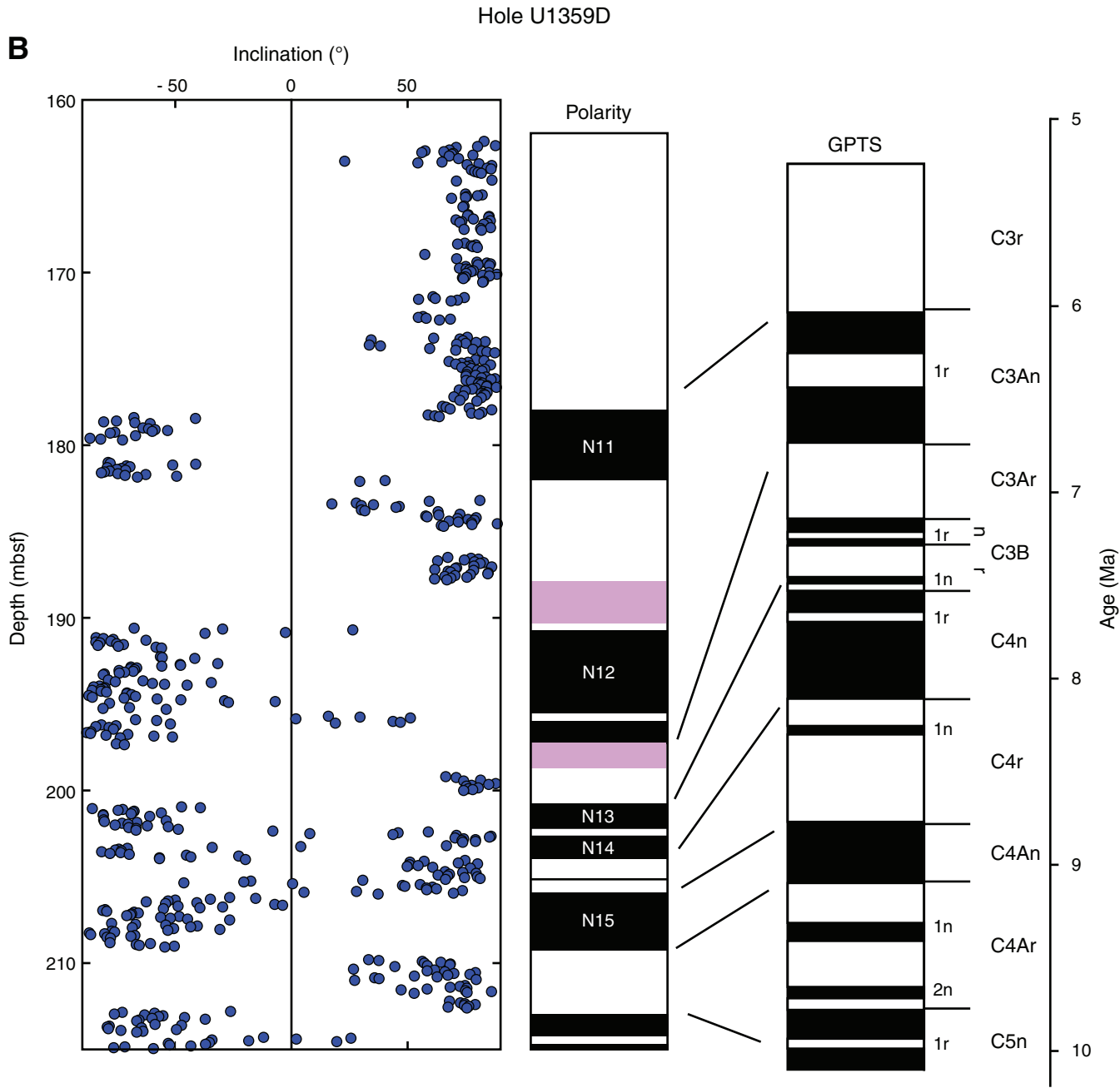




Figure F8 (continued). C. Hole U1359D. Red box = plotted in expanded form in Figure F8B. Arrow = location of discrete sample (see text).

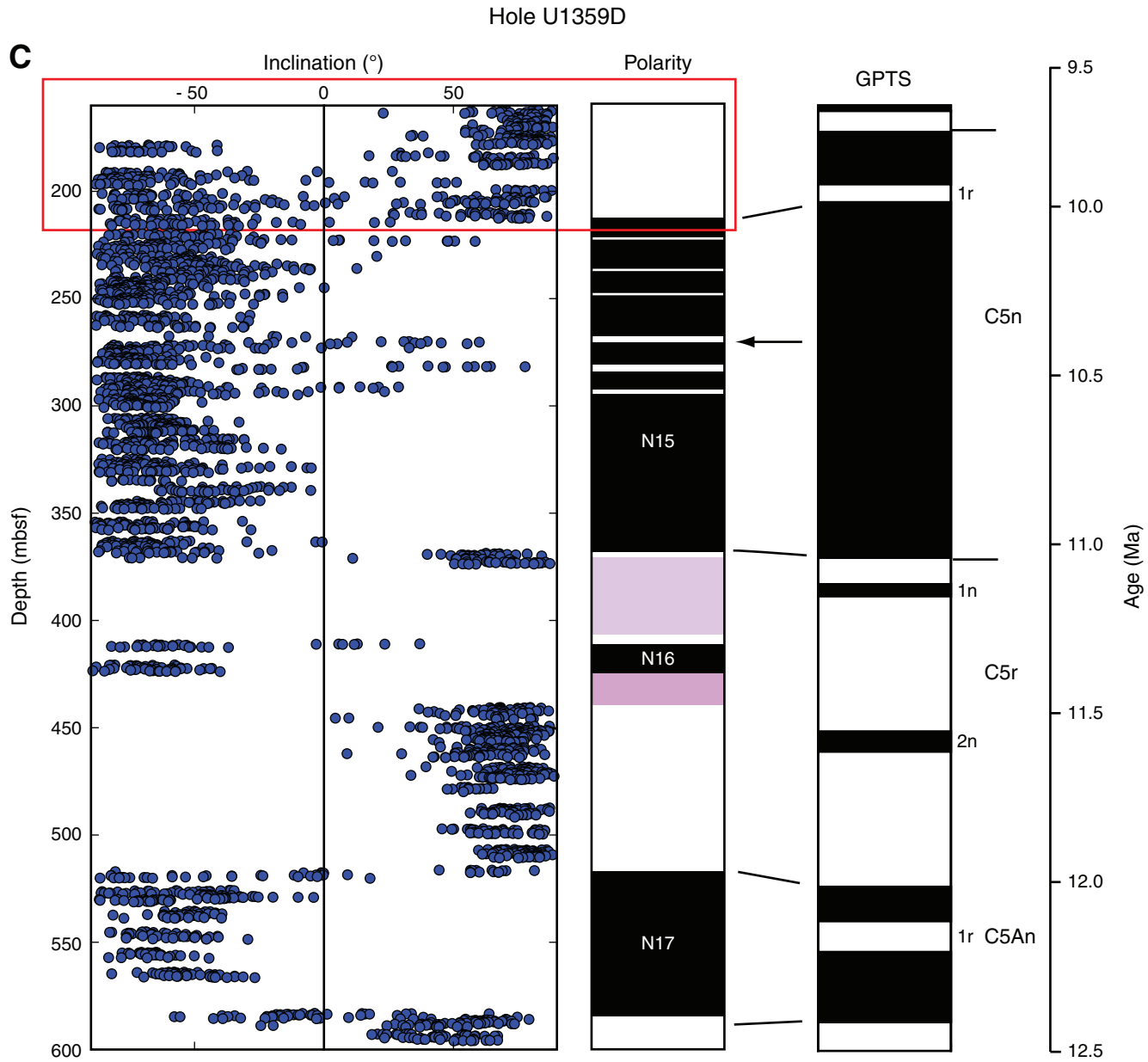


Figure F9. Microbiology and pore water sampling strategy (high resolution sampling within the top 20 m), Hole U1359B.

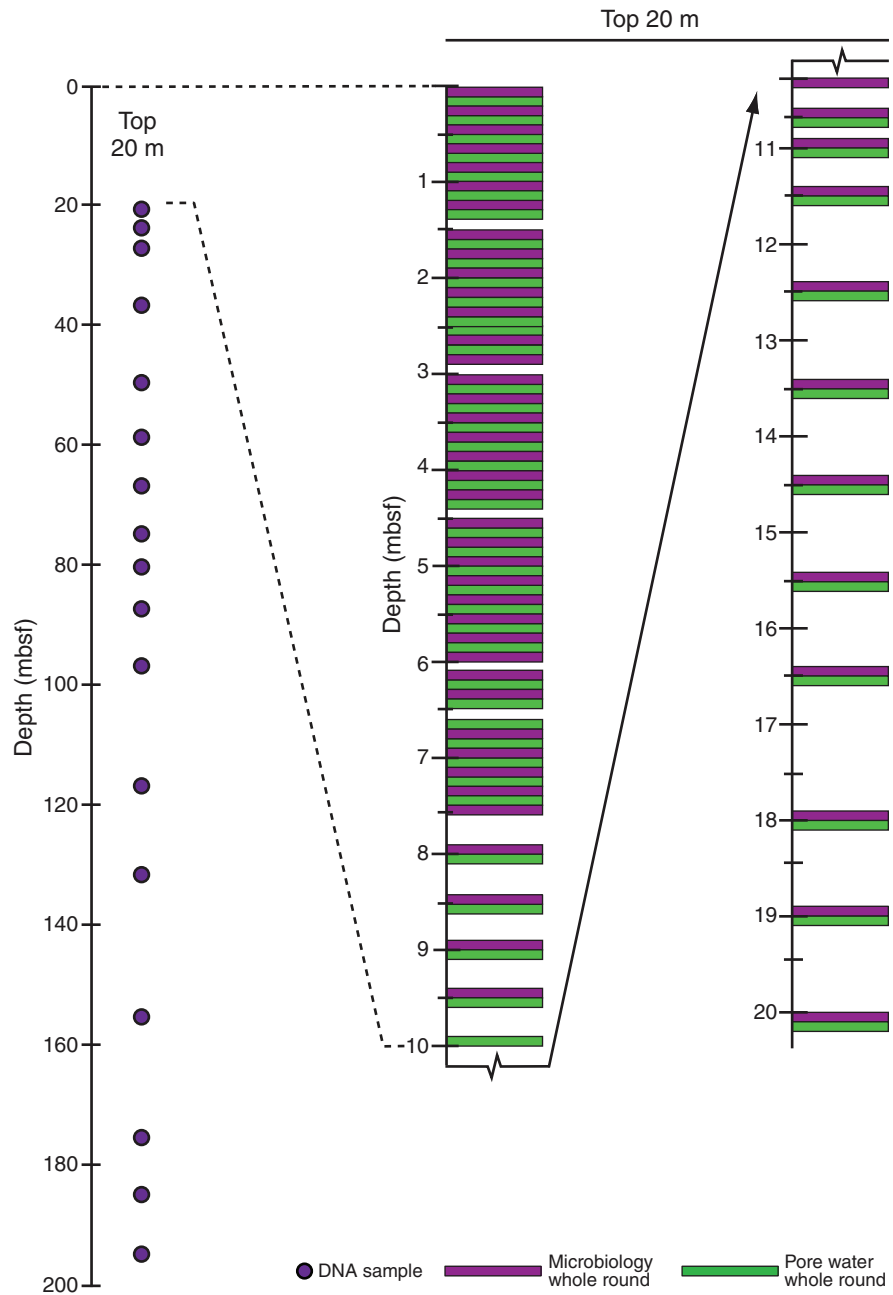


Figure F10. Downhole geophysical logs, Hole U1359D. Logging units are described in text. Core data have been shifted down by ~5 m to give a better depth match to the log data. HSGR = total spectral gamma ray, MAD = moisture and density, IDPH = deep induction phasor-processed resistivity, IMPH = medium induction phasor-processed resistivity.

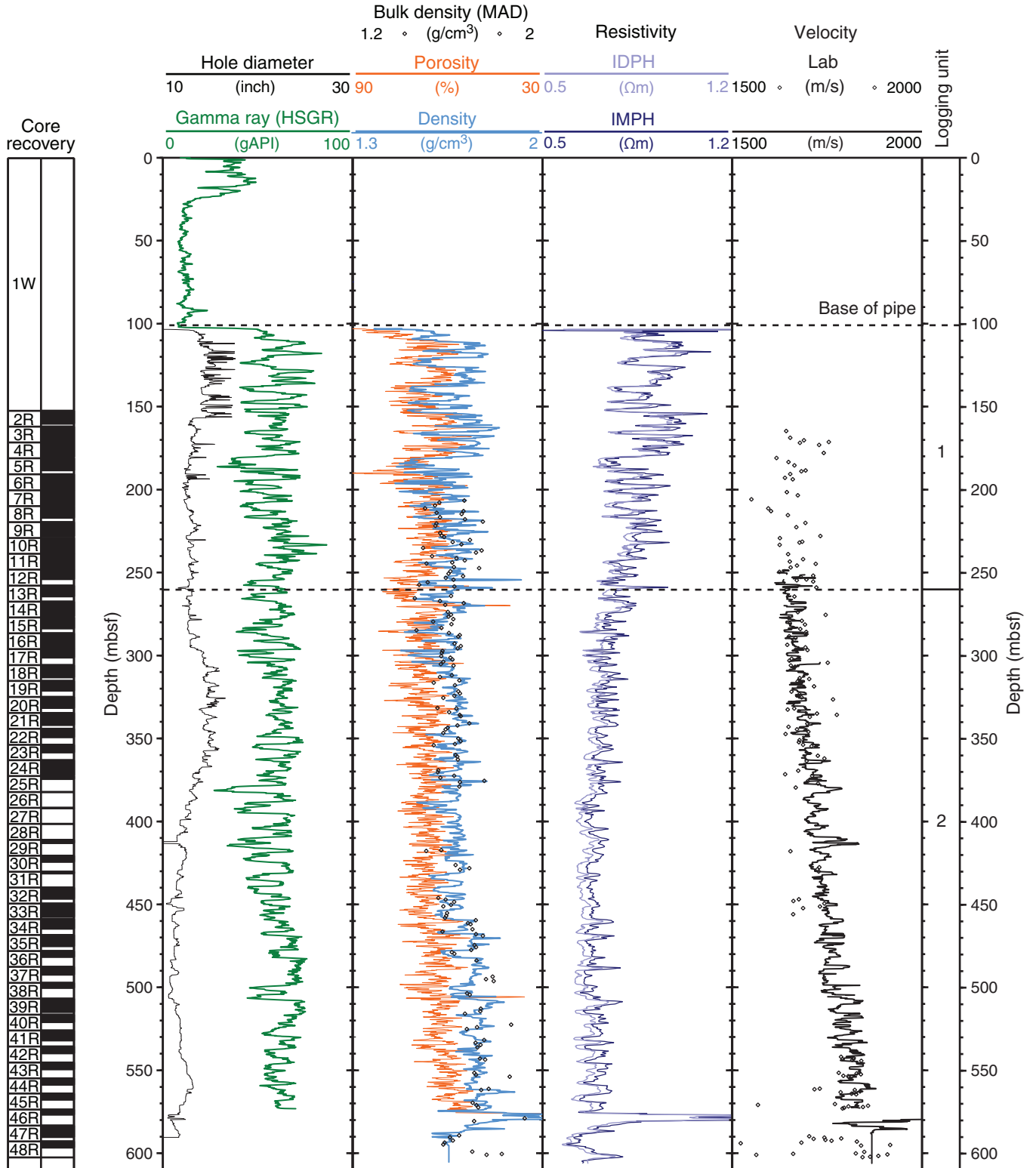


Figure F11. Core image of foraminifer-bearing clayey silt overlying yellow brown silty clay in lithostratigraphic Unit I, Hole U1359A (interval 318-U1359A-4H-5, 24–81 cm).

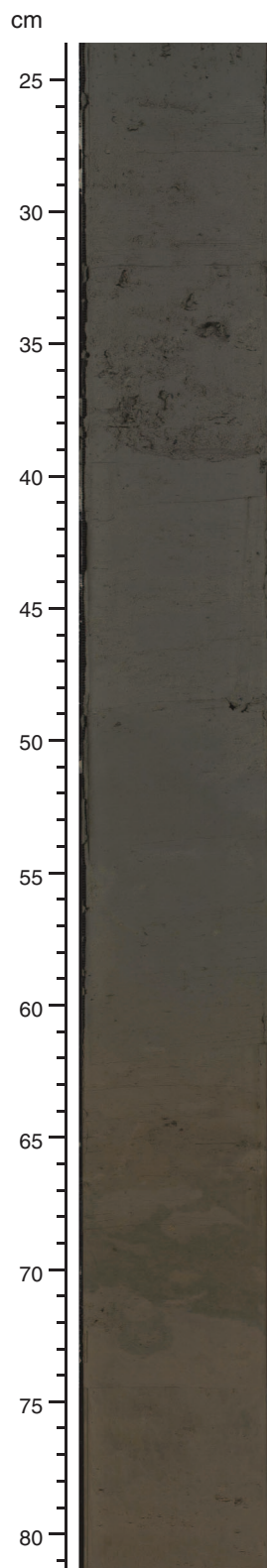


Figure F12. Core image of clay-bearing diatom ooze with slight color change, probably related to diatom content, in lithostratigraphic Subunit IIb, Hole U1359A (interval 318-U1359A-12H-6, 112–150 cm).

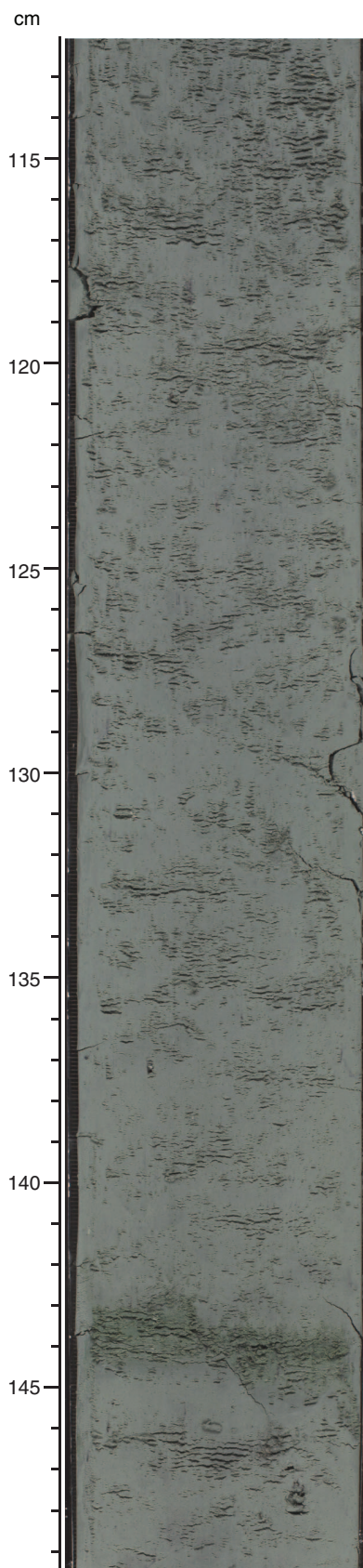


Figure F13. Core image of olive-gray silty clay with subtle centimeter-scale changes in color and silty blebs in lithostratigraphic Subunit IIa, Hole U1359A (interval 318-U1359A-9H-3, 117–149 cm).

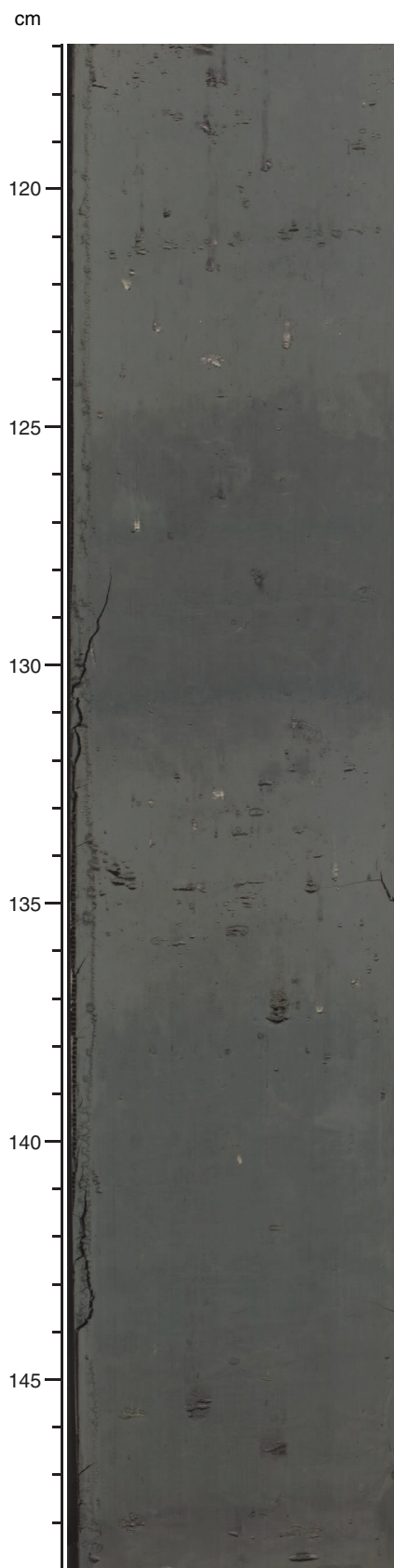


Figure F14. Core image of parallel silt laminations in lithostratigraphic Unit I, Hole U1359A (interval 318-U1359A-2H-4, 90–113 cm).

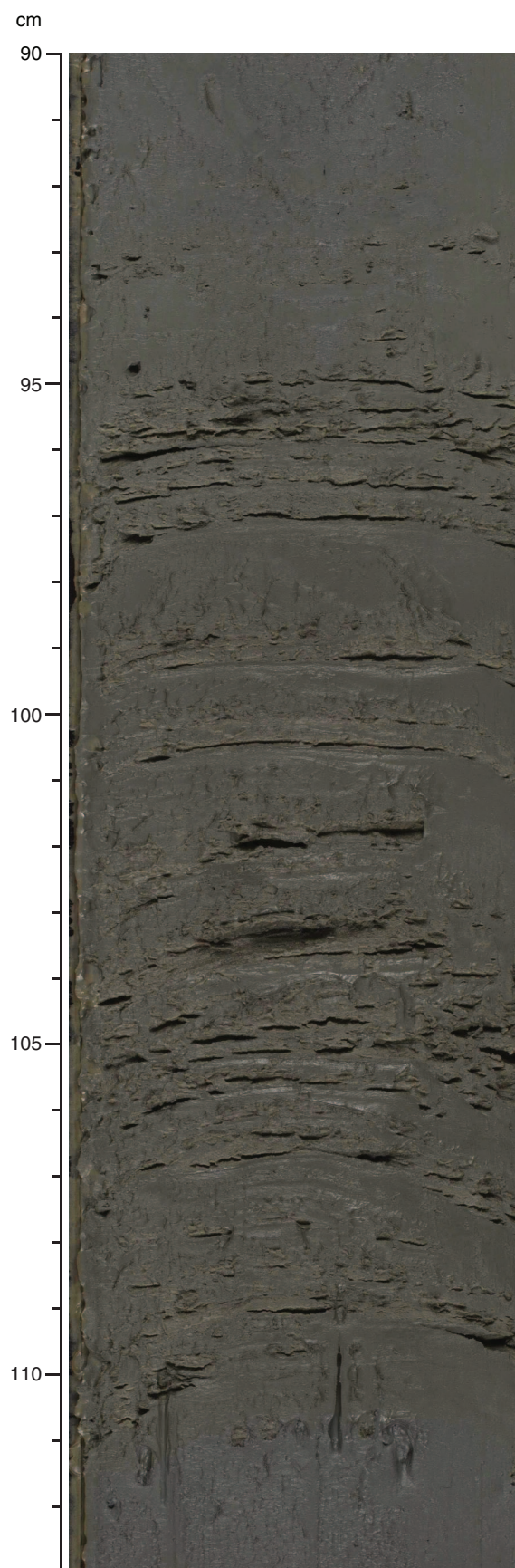


Figure F15. Core image of silty clay with two packages of silt laminations in lithostratigraphic Unit I, Hole U1359A (interval 318-U1359A-2H-4, 67–112 cm).

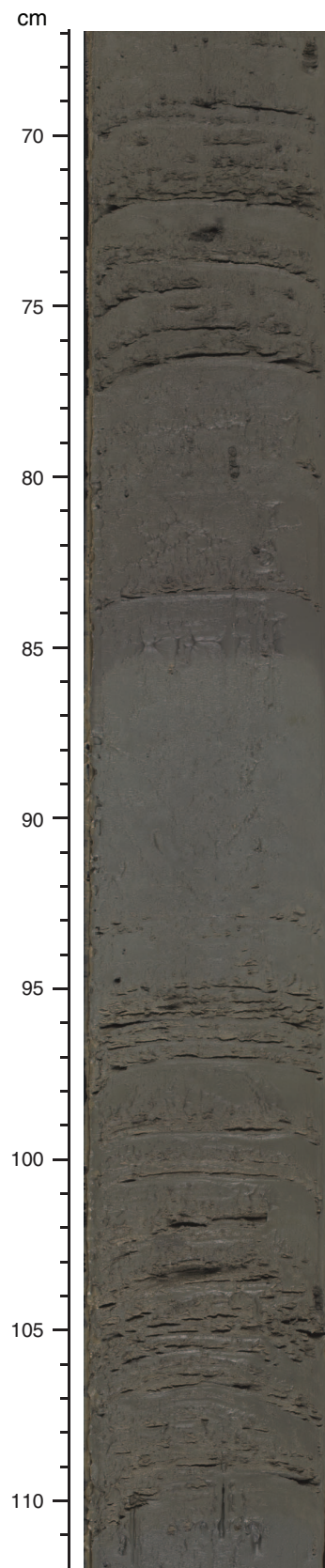


Figure F16. Core image of parallel silt laminations plotted with a reflectance curve generated from the core photo and light photomicrographs of toothpick samples from lithostratigraphic Subunit IIb, Hole U1359B (interval 318-U1359B-17H-3, 80–105 cm).

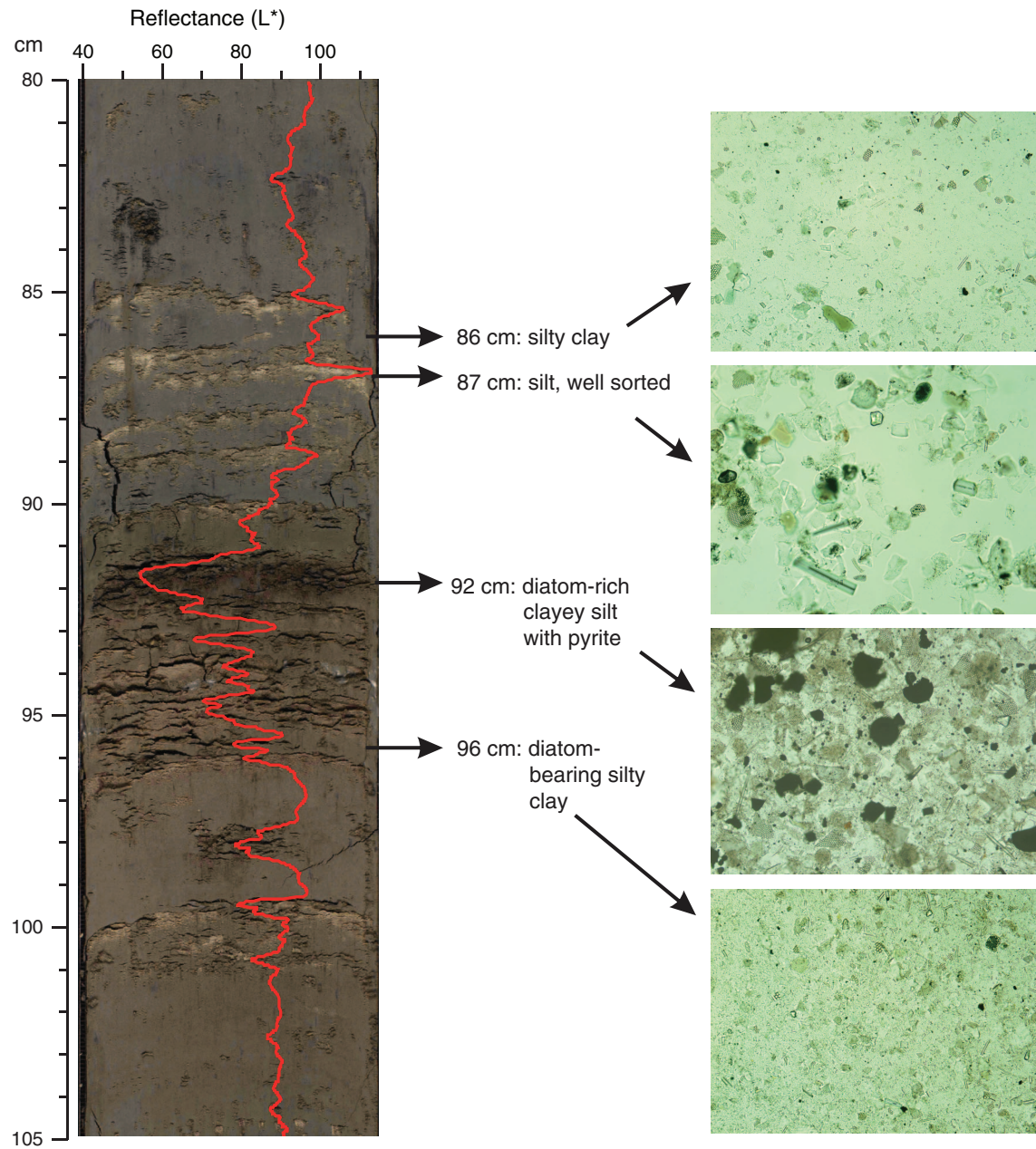


Figure F17. Core image of dark greenish gray silty clays and clays with persistent parallel laminations, as defined by submillimeter- to millimeter-scale laminations as defined by color or grain size variations, in lithostratigraphic Unit III, Hole U1359A (interval 318-U1359A-34R-3, 107–150 cm).

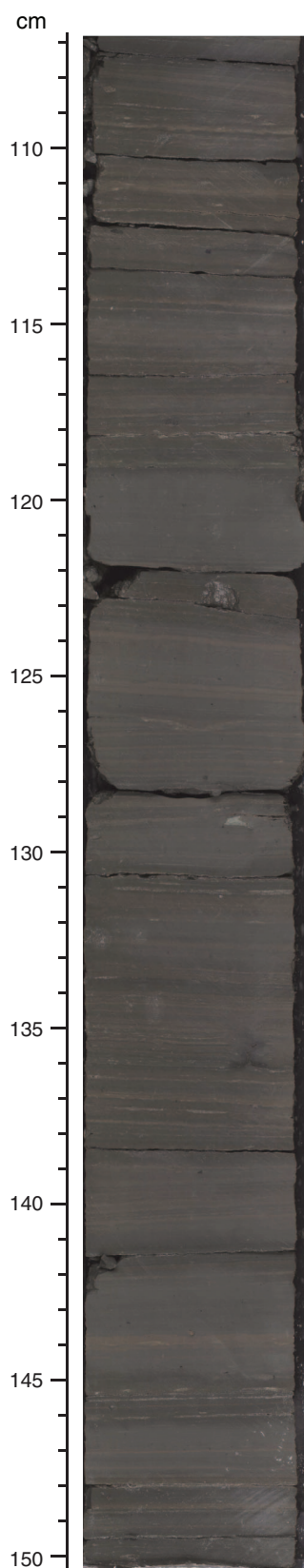


Figure F18. Downhole compositional changes from smear slide data, Hole U1359A.

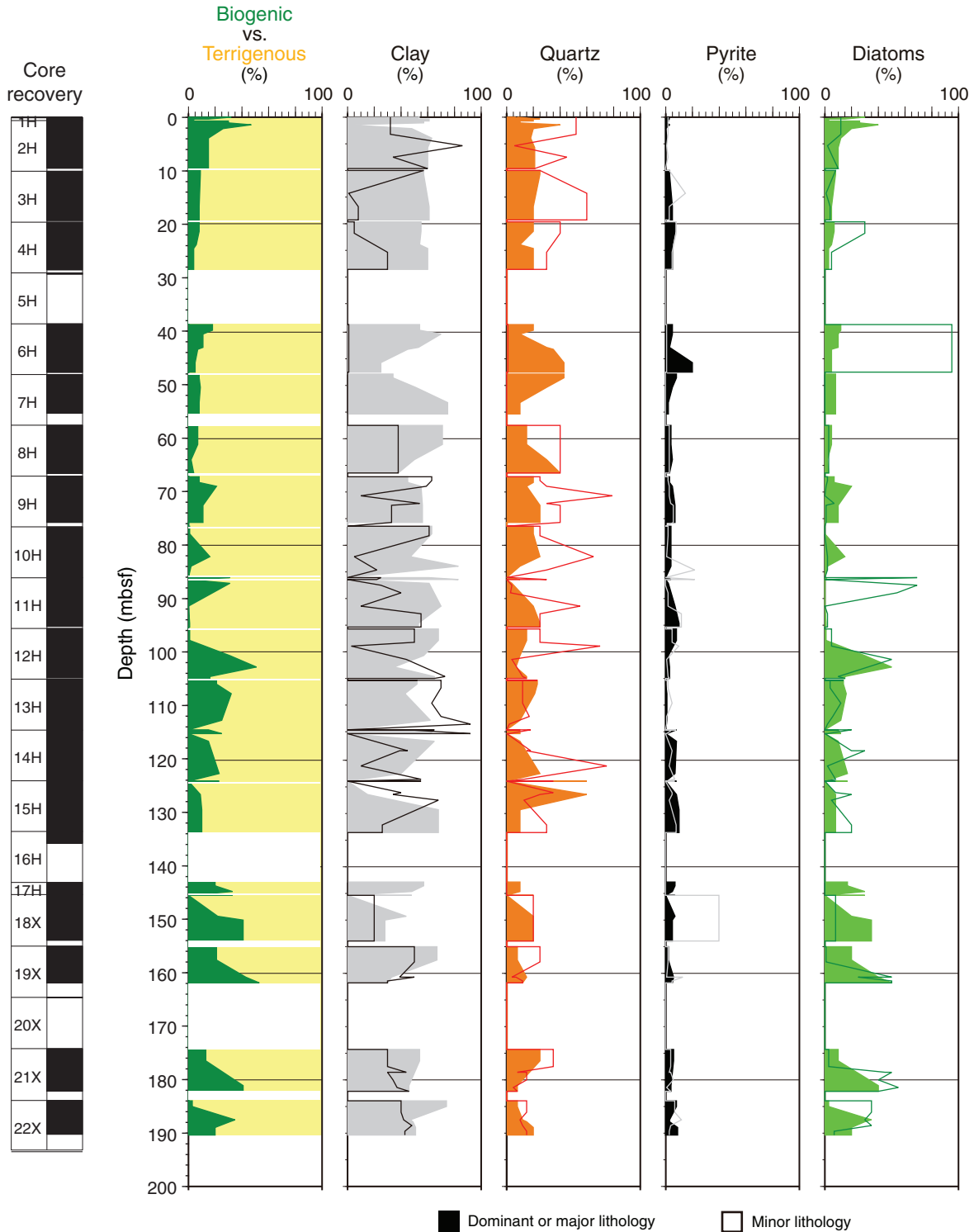


Figure F19. Downhole compositional changes from smear slide data, Hole U1359B.

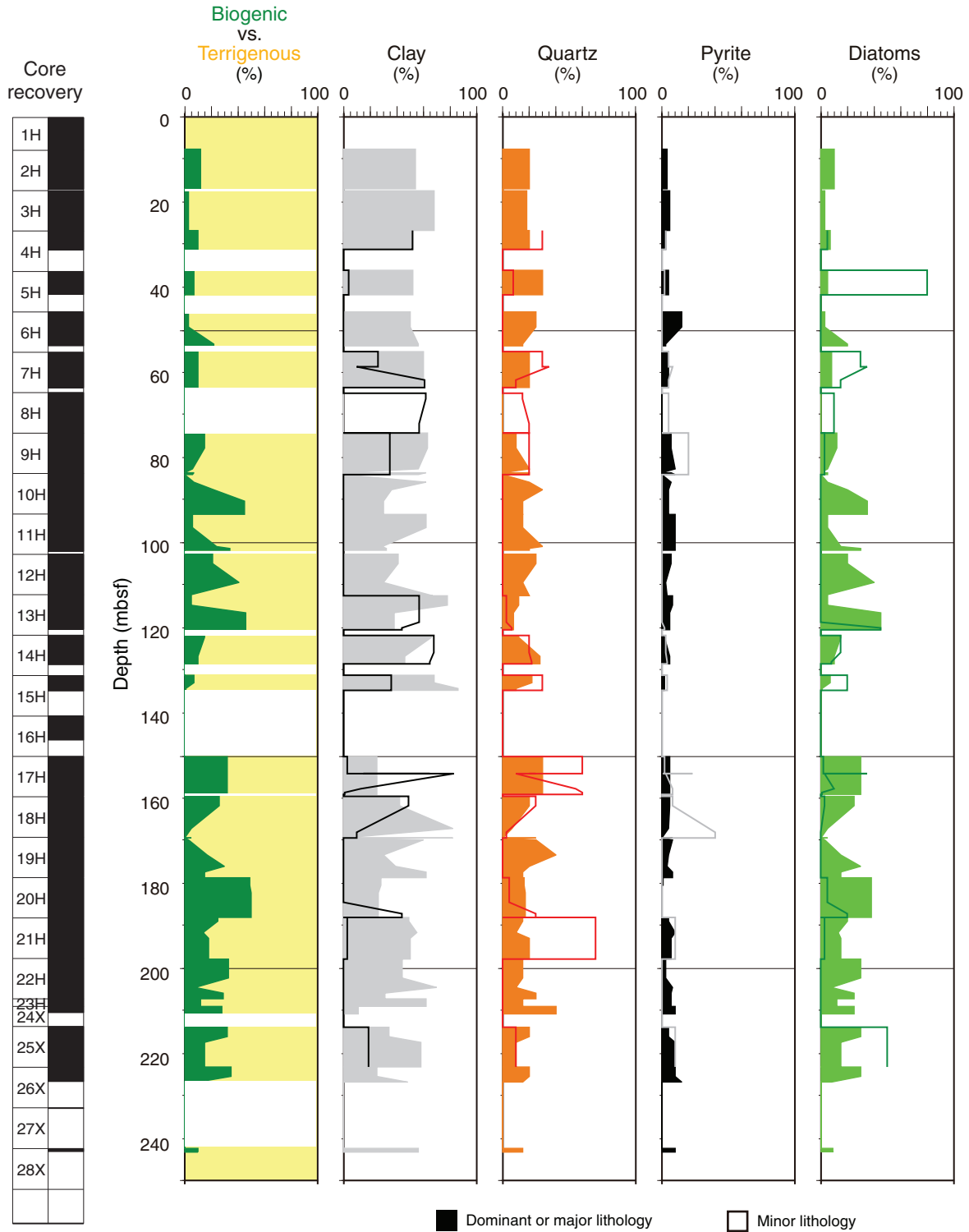


Figure F20. Downhole compositional changes from smear slide data, Hole U1359C.

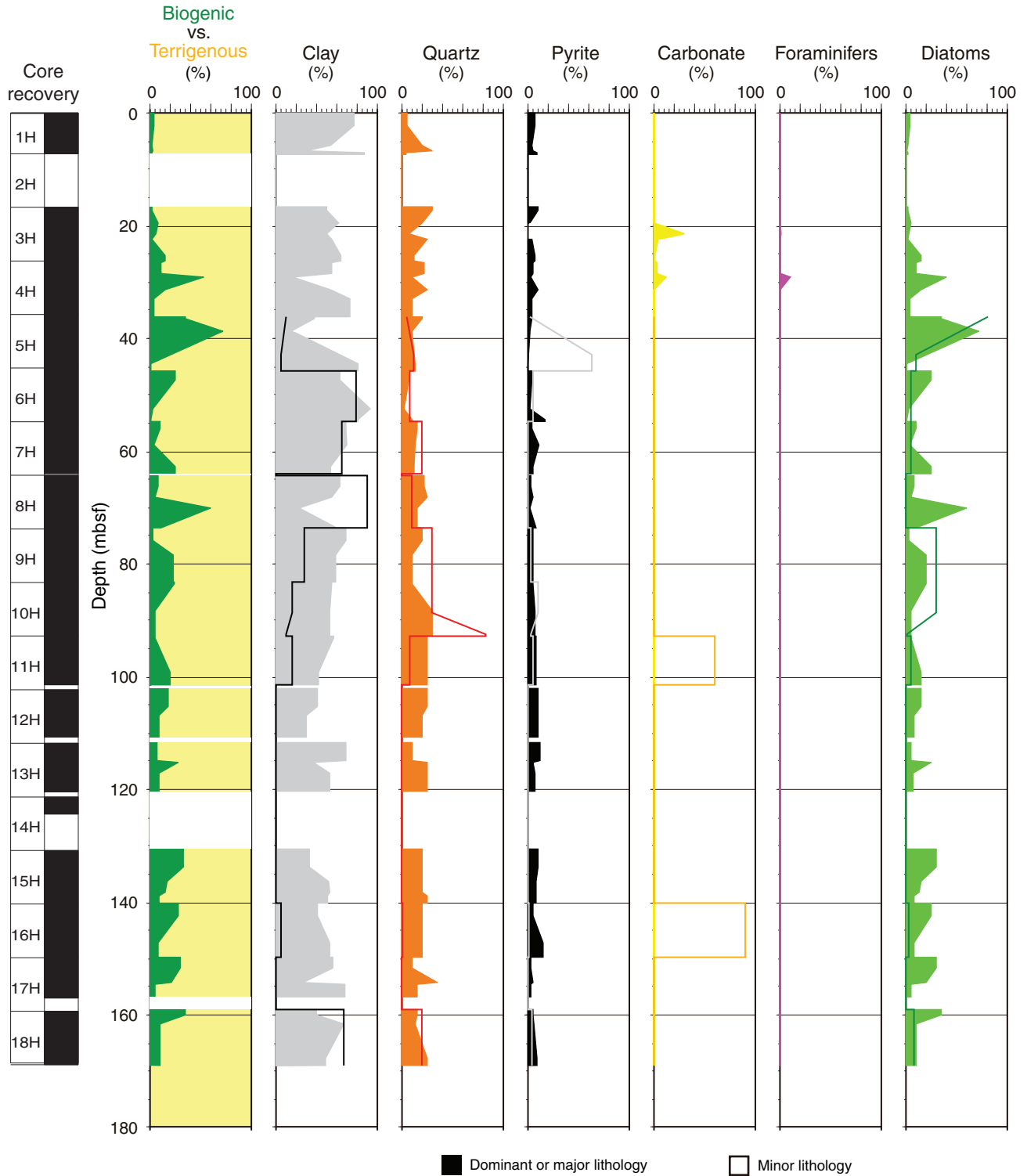


Figure F21. Downhole compositional changes from smear slide data, Hole U1359D.

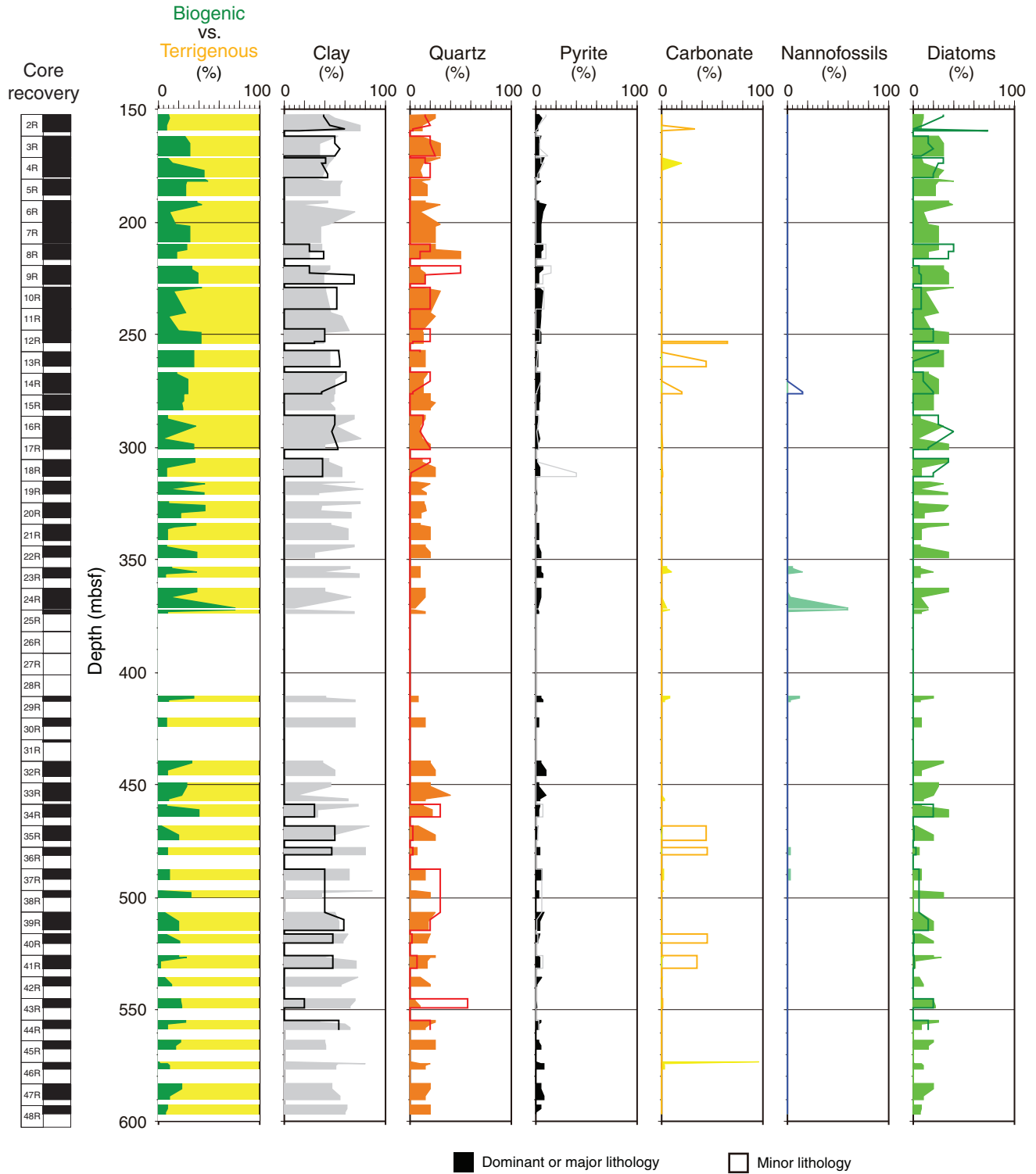


Figure F22. Photomicrographs of smear slides of sediments from Unit II, Holes U1359A–U1359C. **A.** Silty clay (Sample 318-U1359A-12H-2, 86 cm). **B.** Diatom-rich silty clay (Sample 318-U1359A-12H-4, 70 cm). **C.** Silty clay (Sample 318-U1359B-11H-3, 20 cm). **D.** Diatom-rich silty clay (Sample 318-U1359B-11H-6, 60 cm). **E.** Silty clay (Sample 318-U1359C-11H-1, 50 cm). **F.** Diatom-bearing silty clay (Sample 318-U1359C-11H-5, 50 cm).

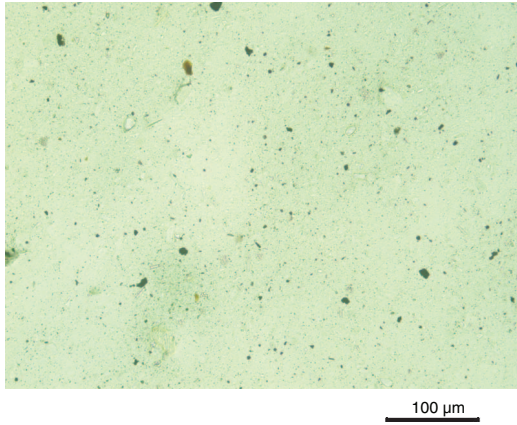
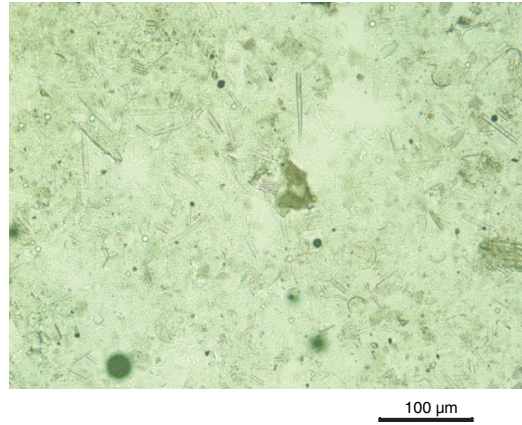
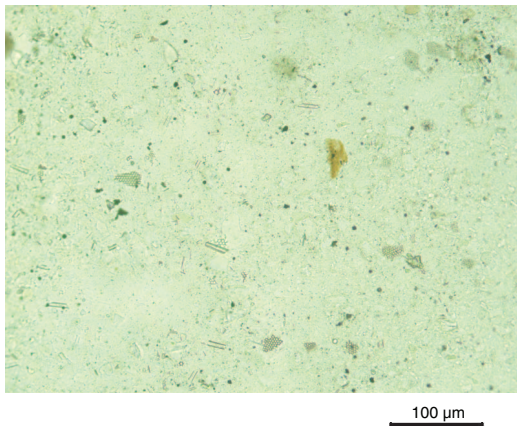
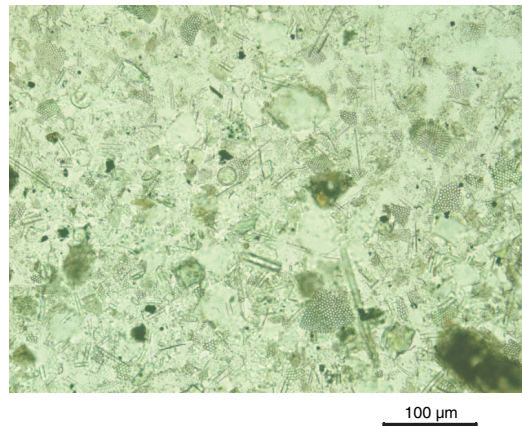
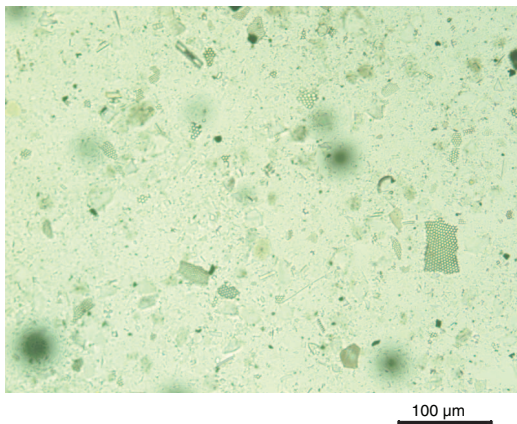
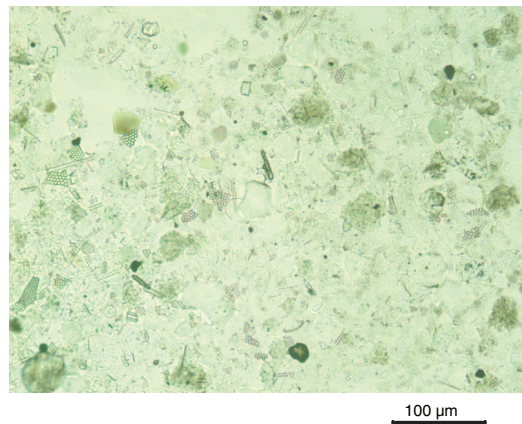
A**B****C****D****E****F**

Figure F23. Core image of diatom-bearing silty clay with abundant bioturbation in lithostratigraphic Unit III, Hole U1359D (interval 318-U1359D-47R-3, 101–150 cm).

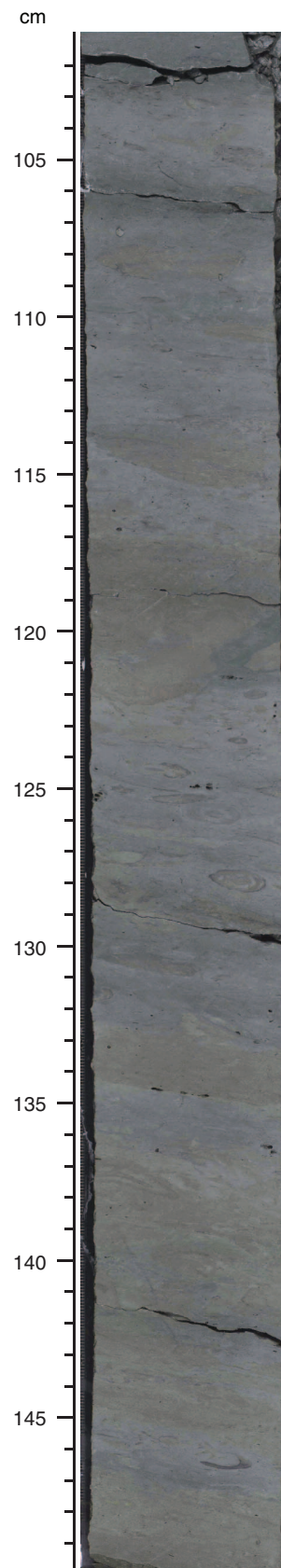


Figure F24. Core image of diatom-bearing nannofossil ooze (0–20 cm) overlying clay (20–50 cm) in lithostratigraphic Unit III, Hole U1359D (interval 318-U1359D-25R-1, 0–50 cm).





Figure F25. A, B. Clay mineral assemblage records, Site U1359. Peak heights were summed and normalized to an arbitrary unit of 10, and the peak height for each mineral group was recalculated as a fractional component of this sum.

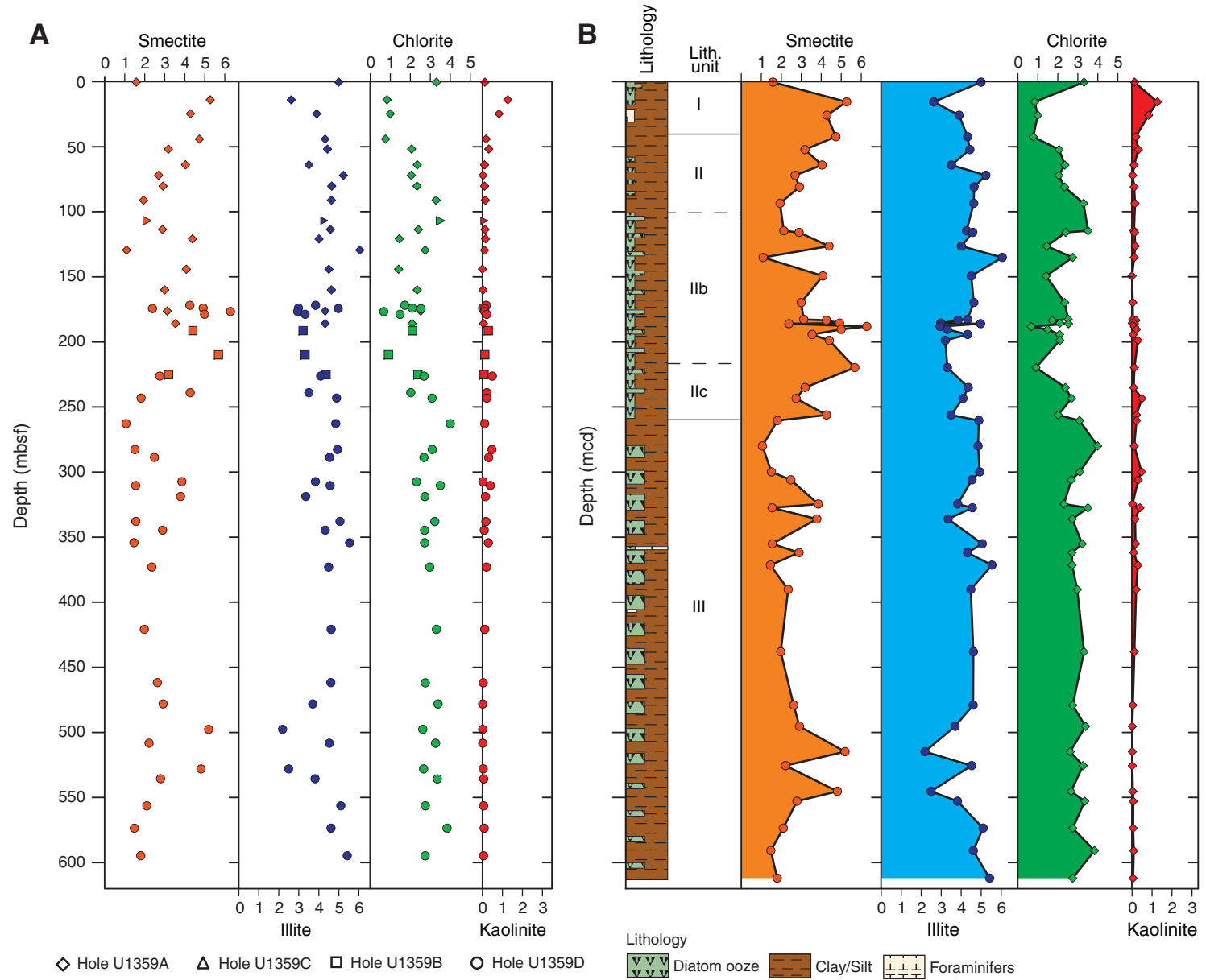




Figure F26. Plots of microfossil abundance vs. depth, Site U1359. Green = Hole U1359A, blue = Hole U1359B, red = Hole U1359D. B = barren, T = trace, R = rare, F = few, C = common, A = abundant. Foraminifer abundance: orange = planktonic plus benthic, blue = planktonic only.

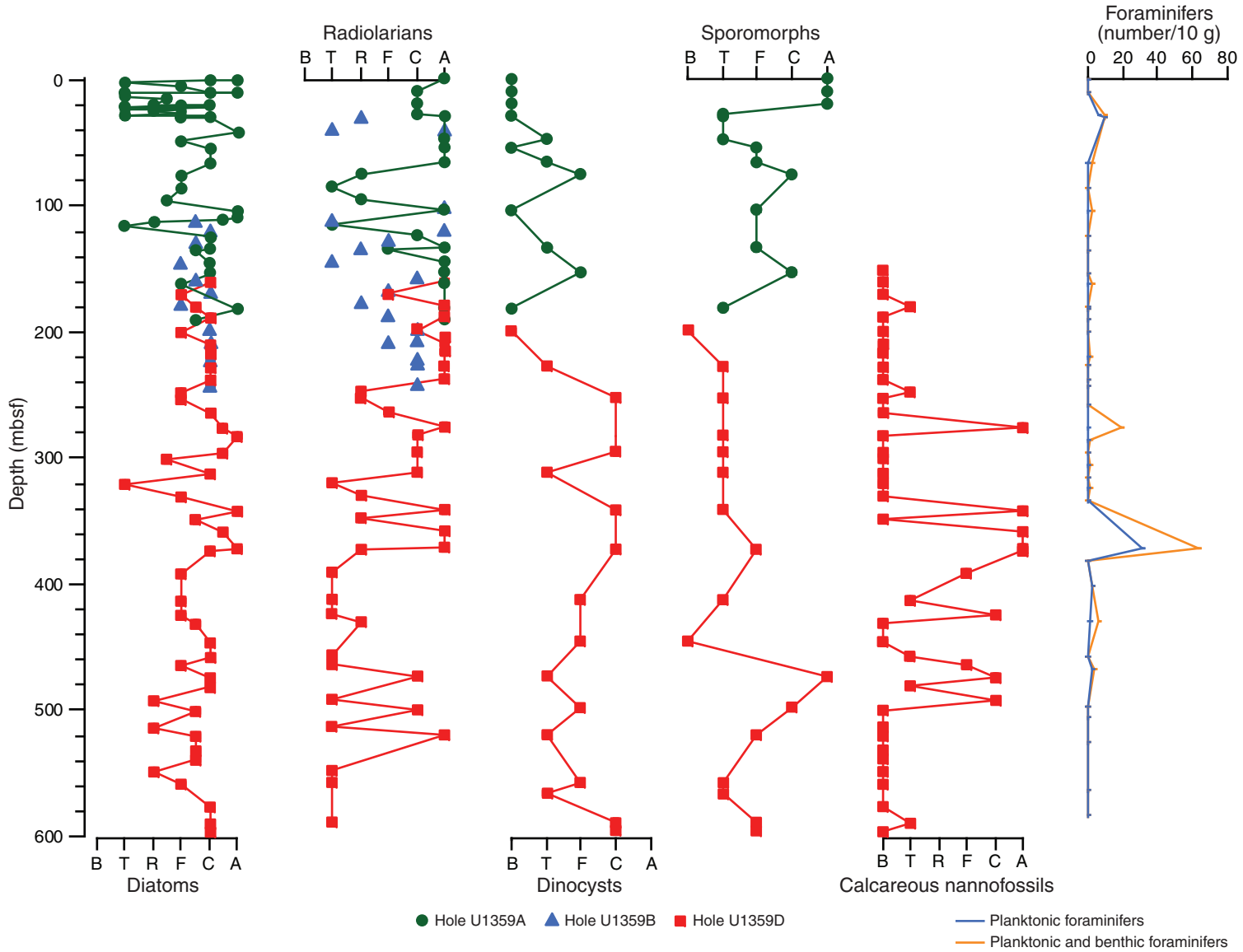


Figure F27. Biomagnetostratigraphic age-depth plots, Site U1359. t = top, b = bottom, o = oldest, y = youngest.

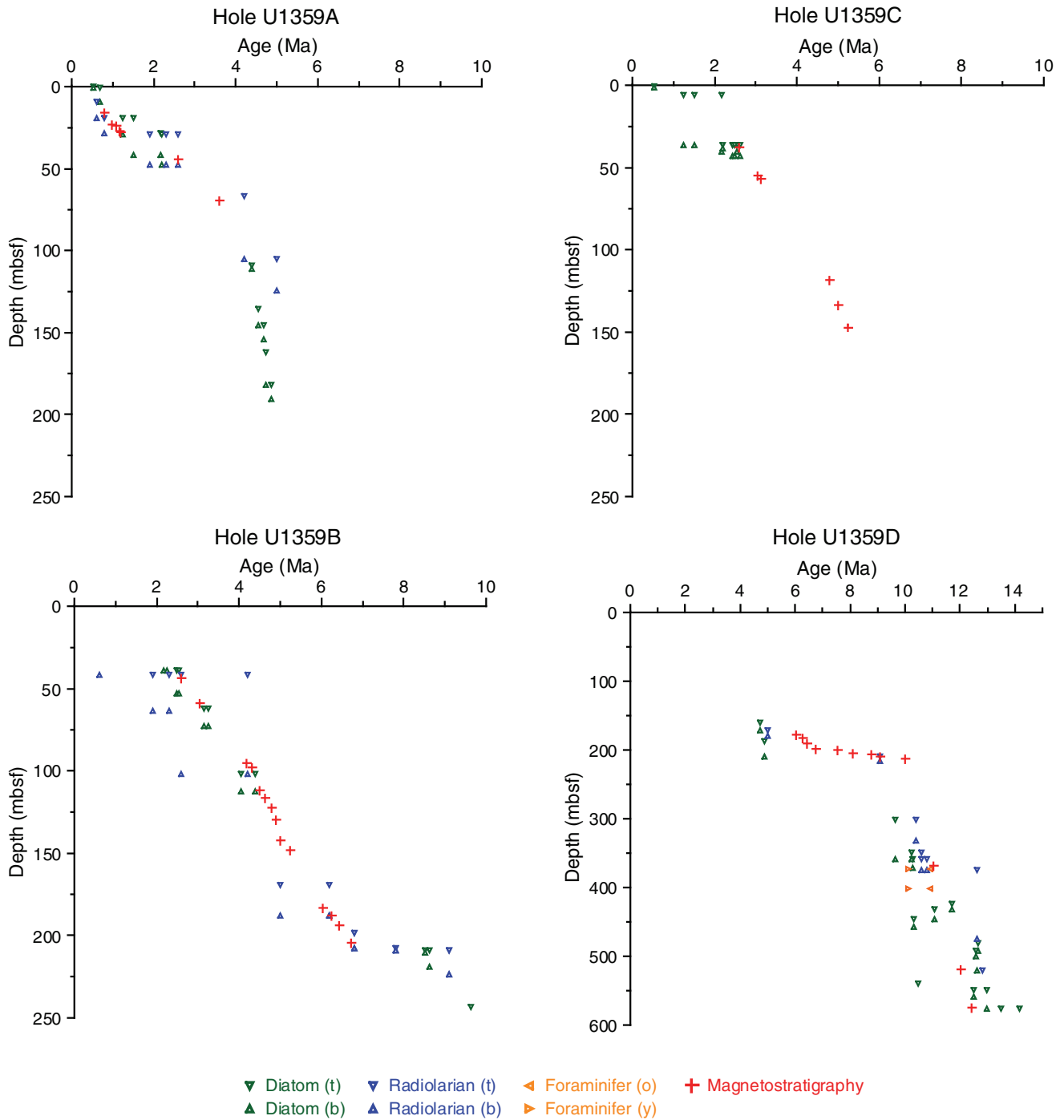


Figure F28. Biomagnetostratigraphic age-depth plot, Site U1359. Yellow shading = chronostratigraphic preservation, light yellow shading = low sedimentation rates. Microfossil datums are plotted by using the median depth between upper and lower samples (Table T11). Mid-point absolute age in the average range model of Cody et al. (2008) is used for the diatom datums. t = top, b = bottom, o = oldest, y = youngest. Blue line = best-fit sedimentation rate.

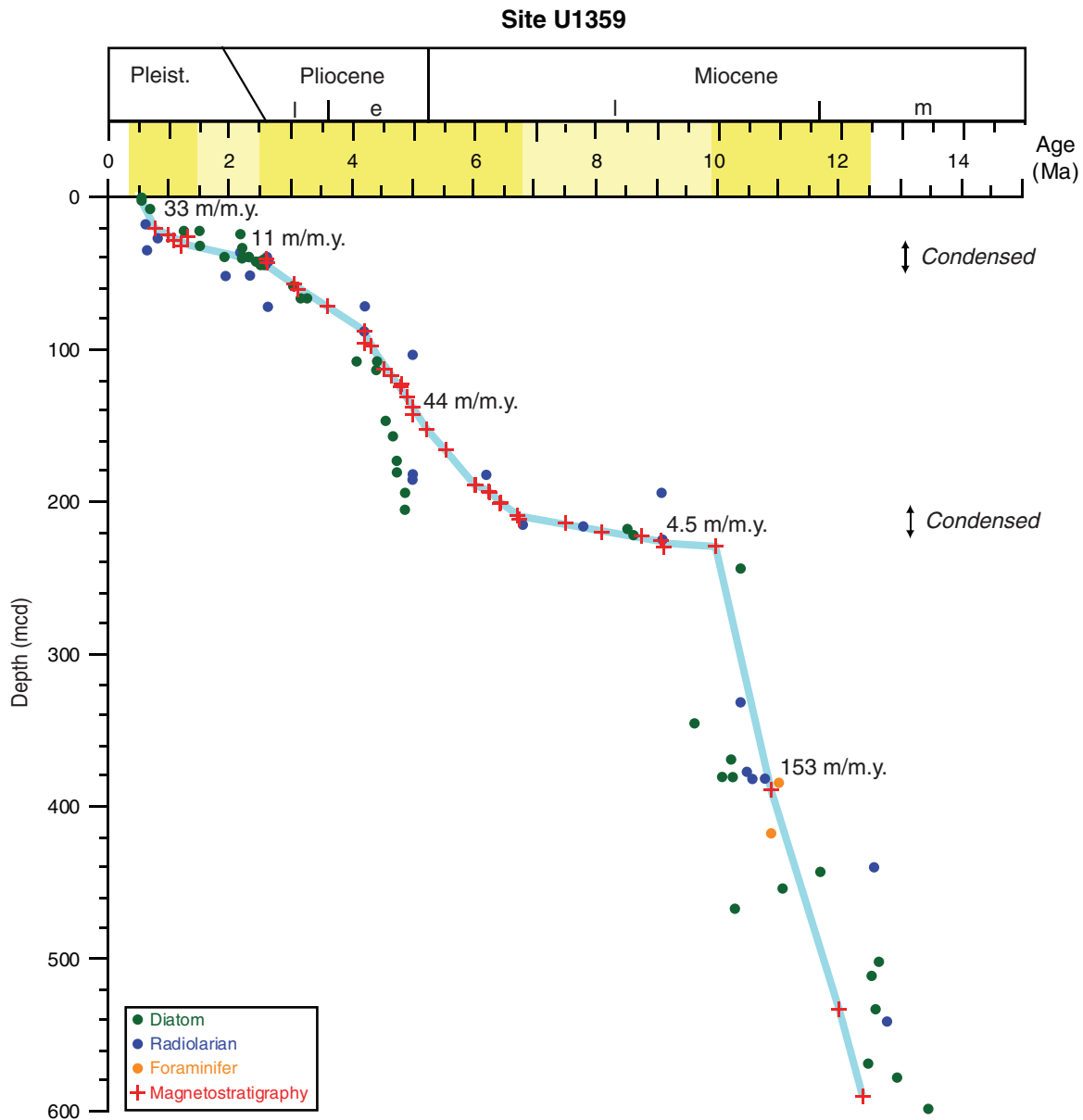




Figure F29. Diagrams of behavior of discrete samples during step-wise alternating-field demagnetization. For each sample, the (A, E, I, M) left diagrams are vector endpoint diagrams before deletion of flux jumps or averaging the three measurements at each step. The (B, F, J, N) equal area projections are the directional data at each demagnetization step. Note the points along the x -, y - and z -axes; these are flux jumps (see text). The (C, G, K, O) intensity decay curves plot the remanent strength after demagnetization at each step. Note the large spikes in C and G, indicating flux jumps. The right diagrams are (D, H, L, P) vector endpoint diagrams after deletion of flux jumps and averaging multiple measurements at each step. Green lines = best-fit lines. NRM = natural remanent magnetization. A–D. Sample 318-U1359A-12H-5, 70 cm. (Continued on next three pages.)

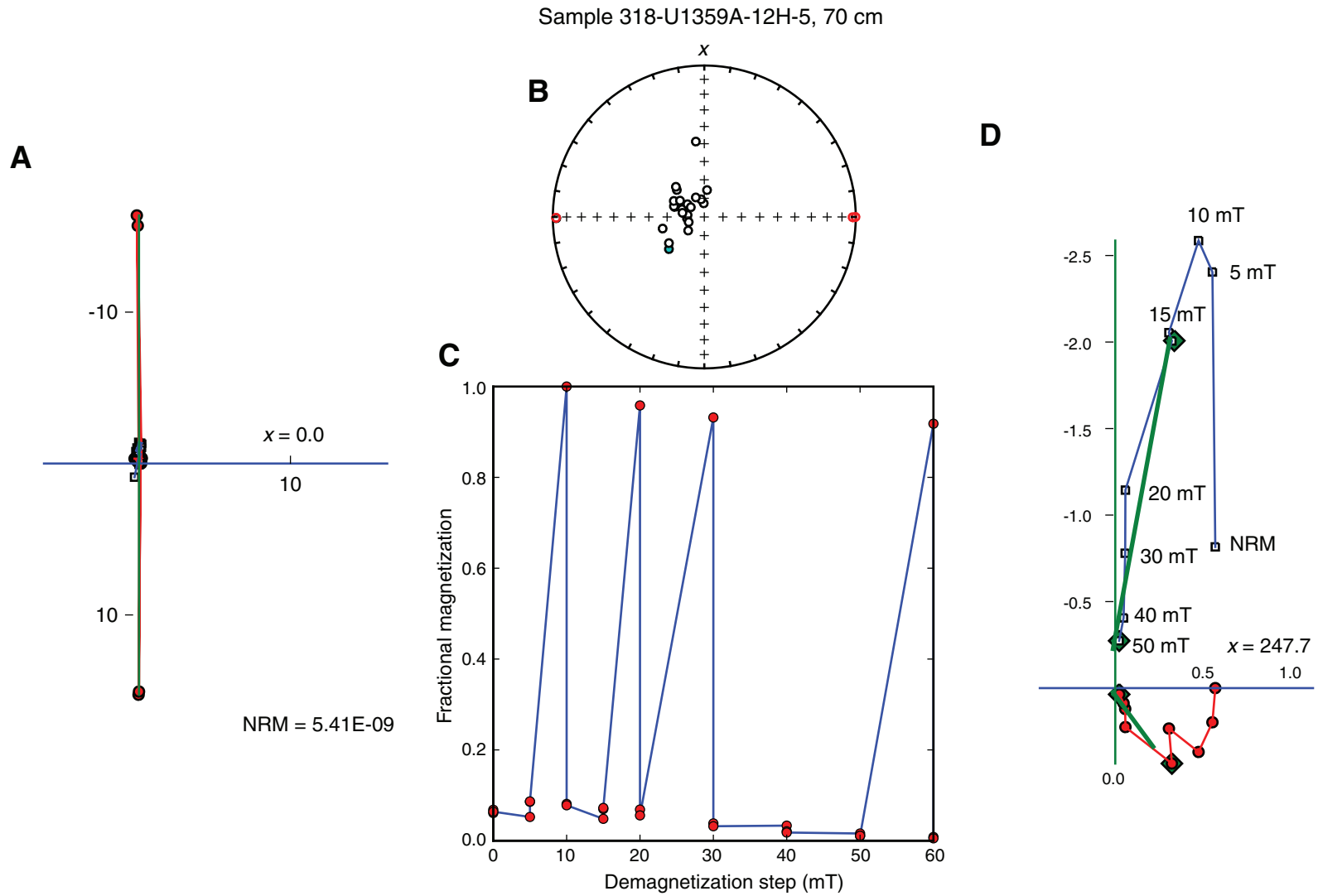




Figure F29 (continued). E-H. Sample 318-U1359A-11H-3, 70 cm. (Continued on next page.)

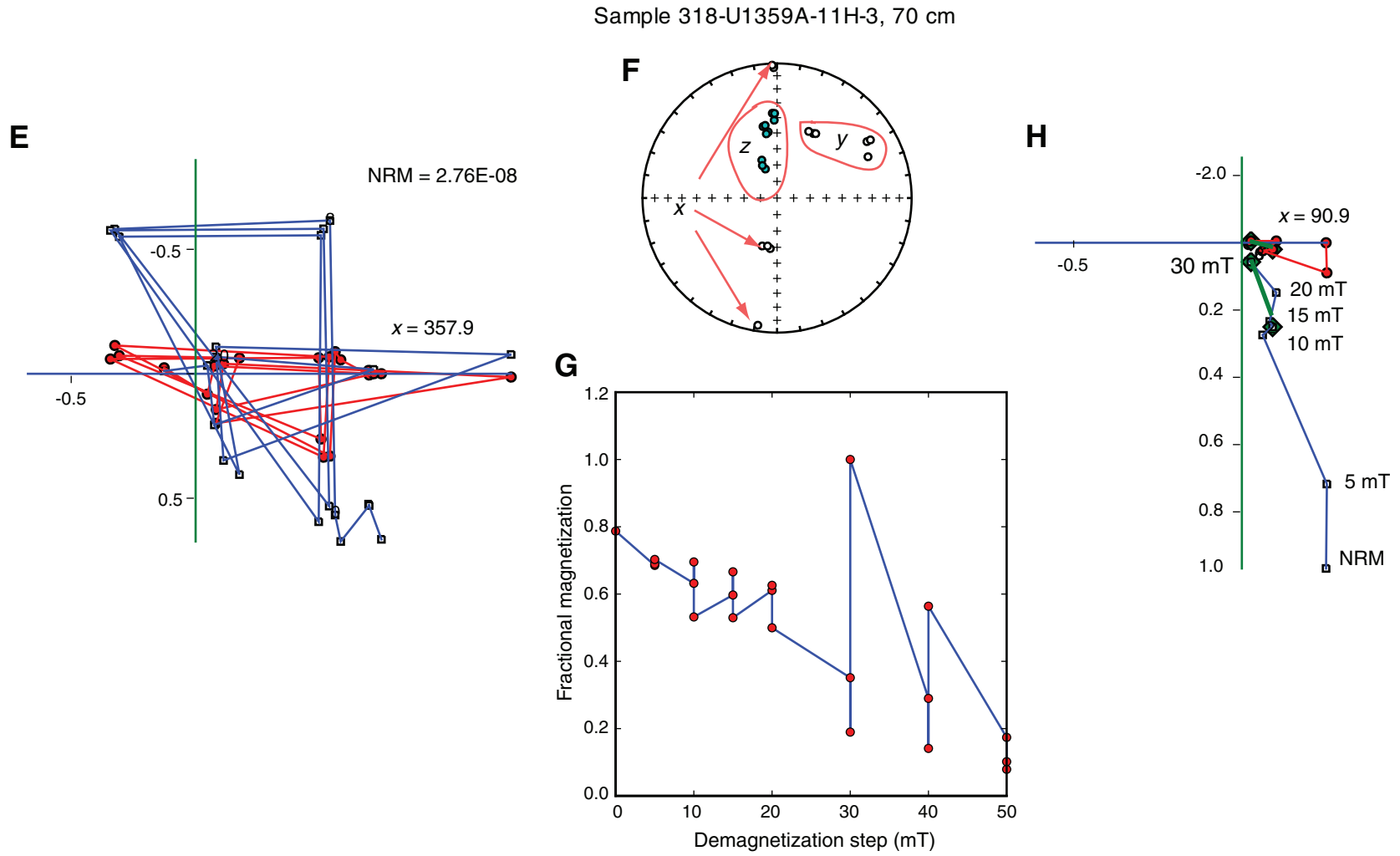




Figure F29 (continued). I-L. Sample 318-U1359A-10H-5, 101 cm. (Continued on next page.)

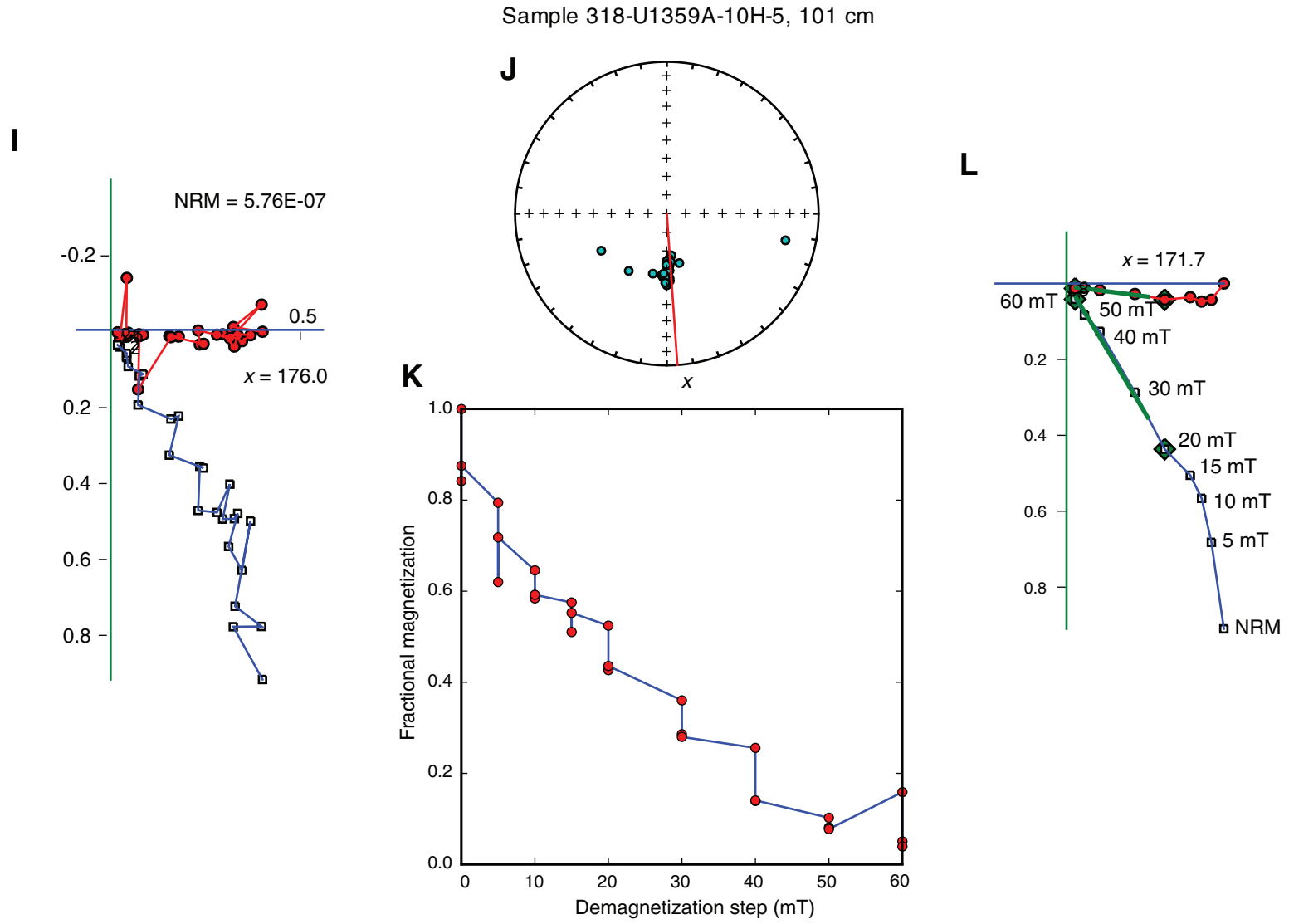
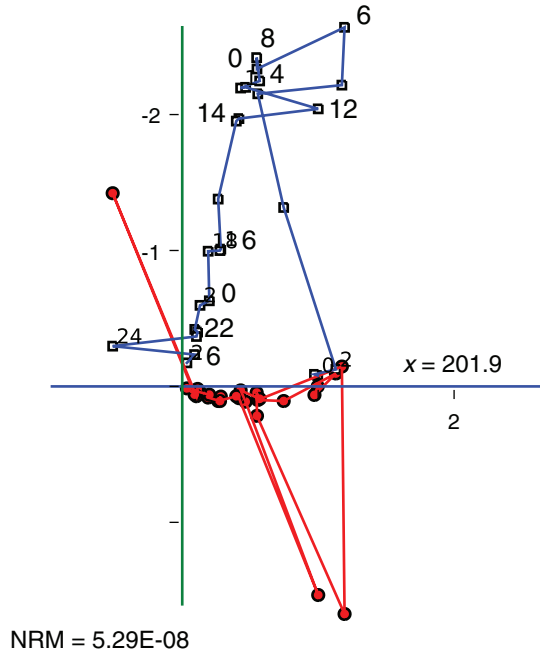




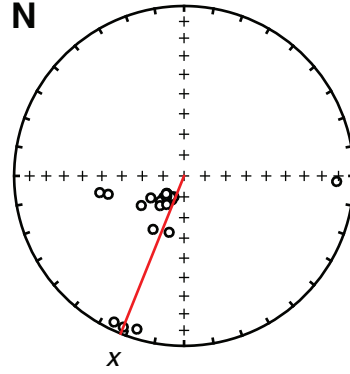
Figure F29 (continued). M-P. Sample 318-U1359A-14H-6, 13 cm.

Sample 318-U1359A-14H-6, 13 cm

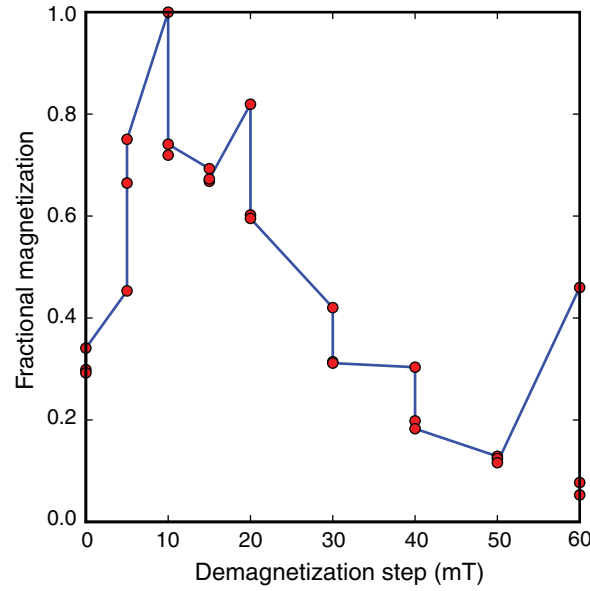
M



N



O



P

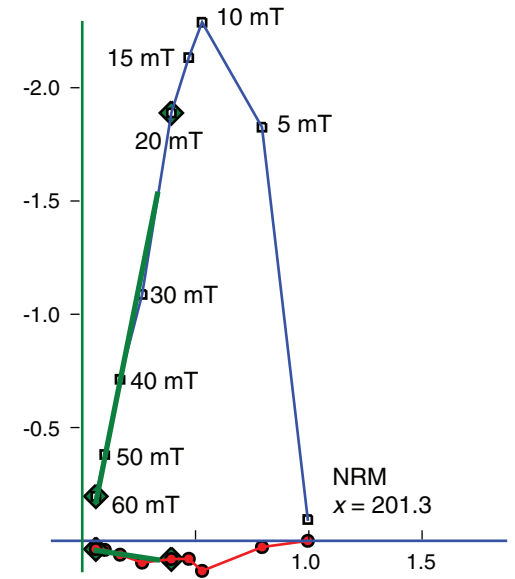


Figure F30. Plots of archive-half measurements and directions of best-fit lines (BFLs), Site U1357. Data from intervals of disturbed or missing intervals (void spaces) have been removed. Dashed blue lines = core top depths. NRM = natural remanent magnetization. A. Hole U1359A. (Continued on next four pages.)

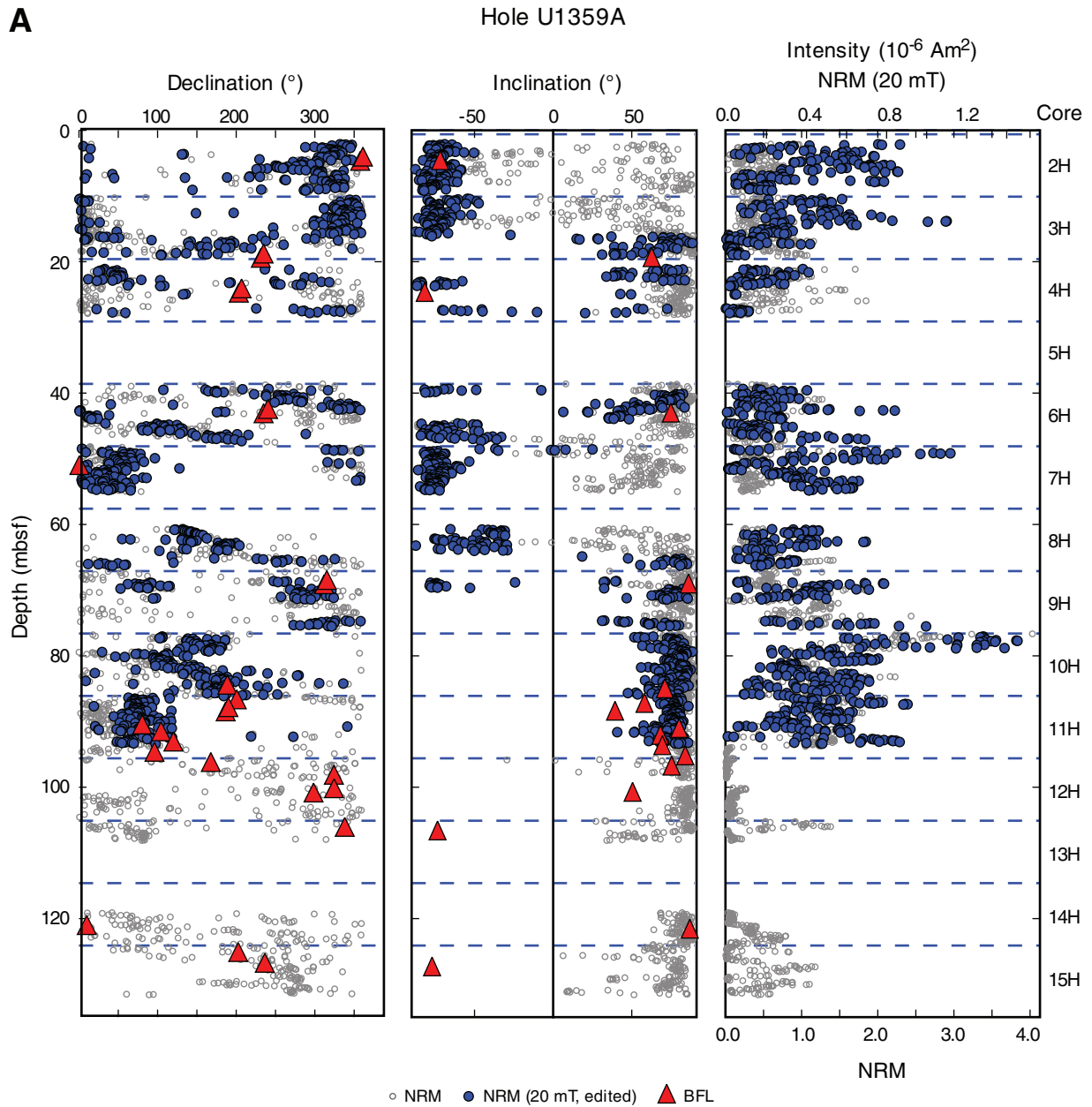


Figure F30 (continued). B. Hole U1359B. (Continued on next page.)

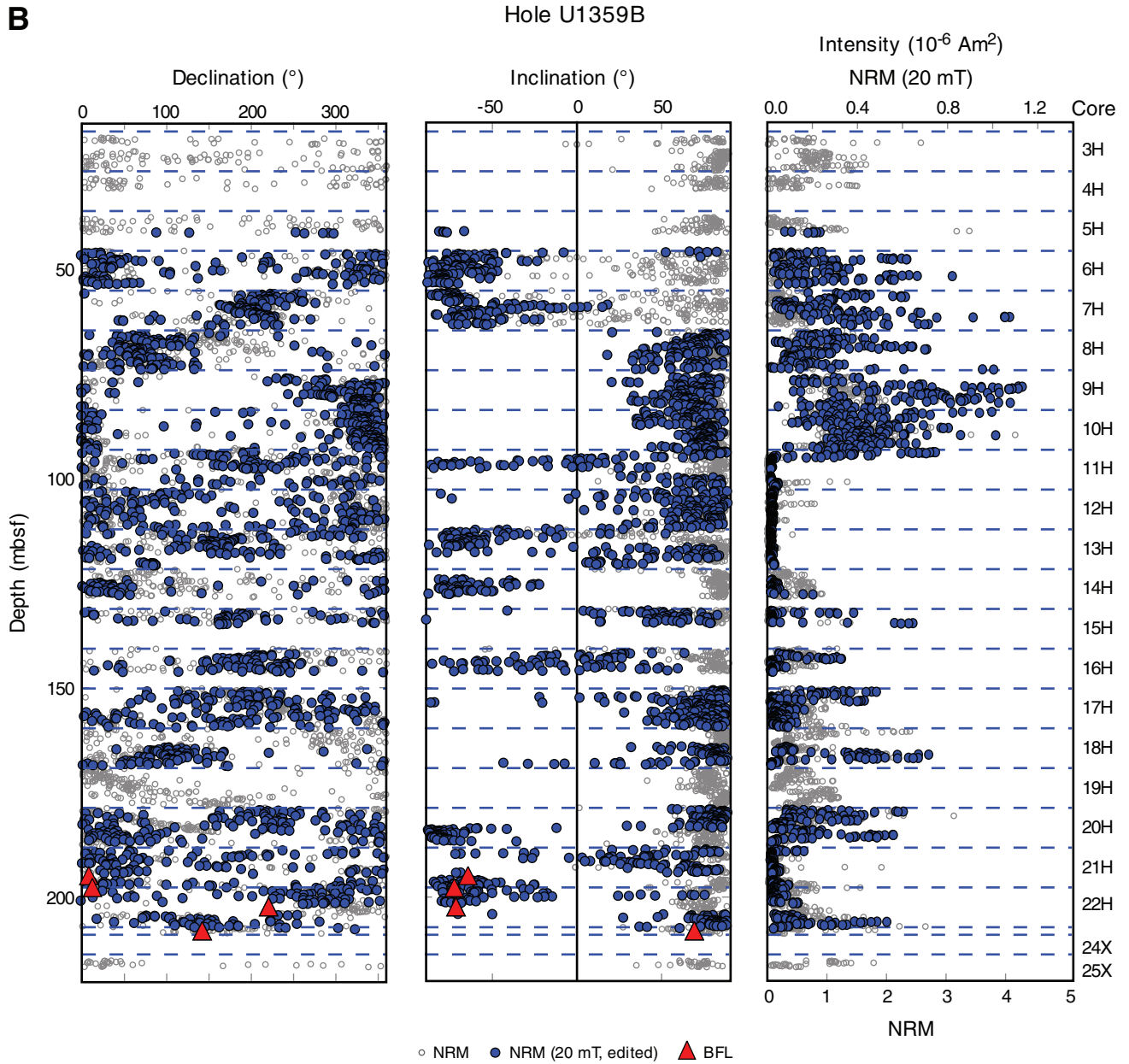


Figure F30 (continued). C. Hole U1359C. (Continued on next page.)

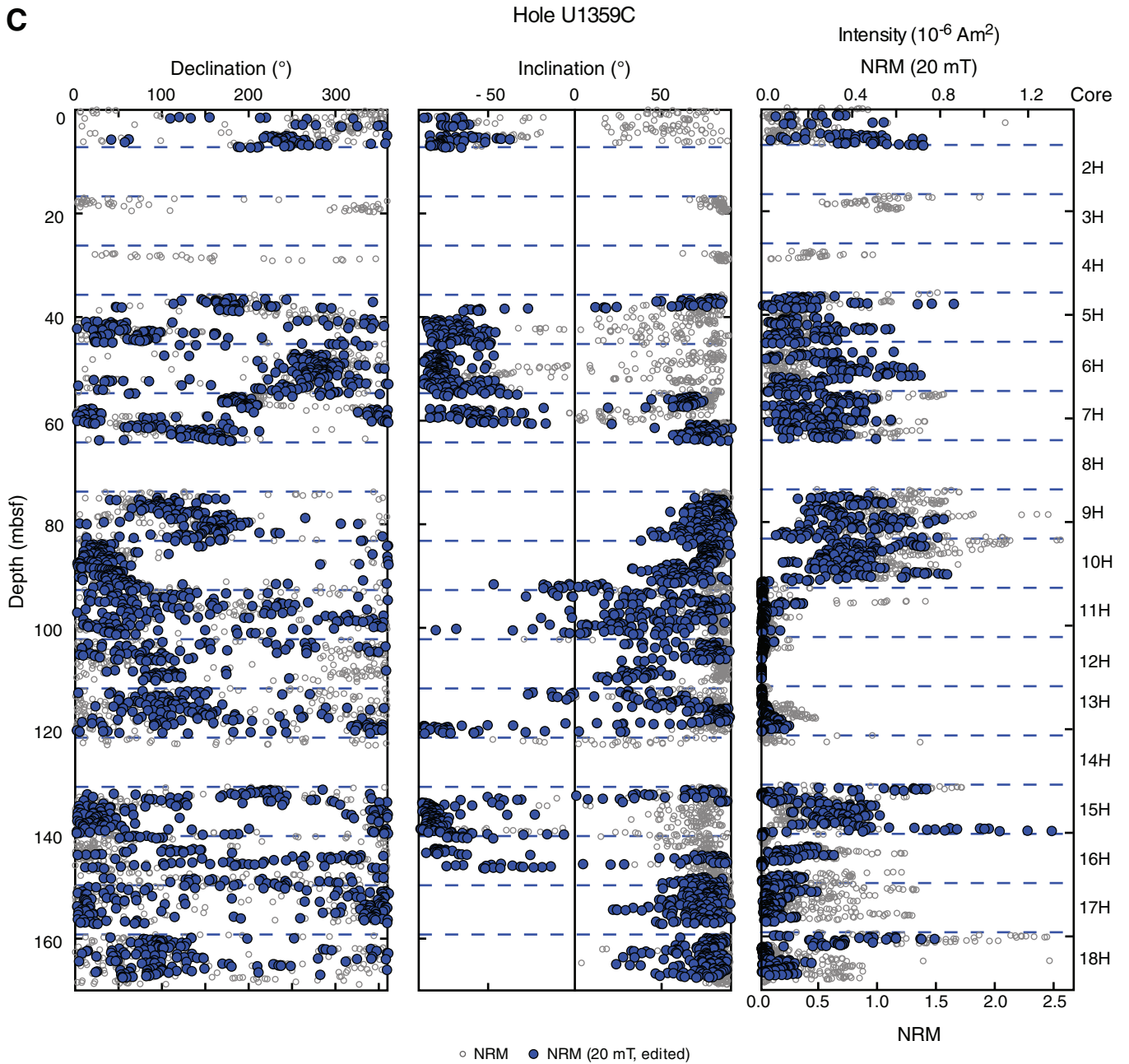


Figure F30 (continued). D. Upper part of Hole U1359D. (Continued on next page.)

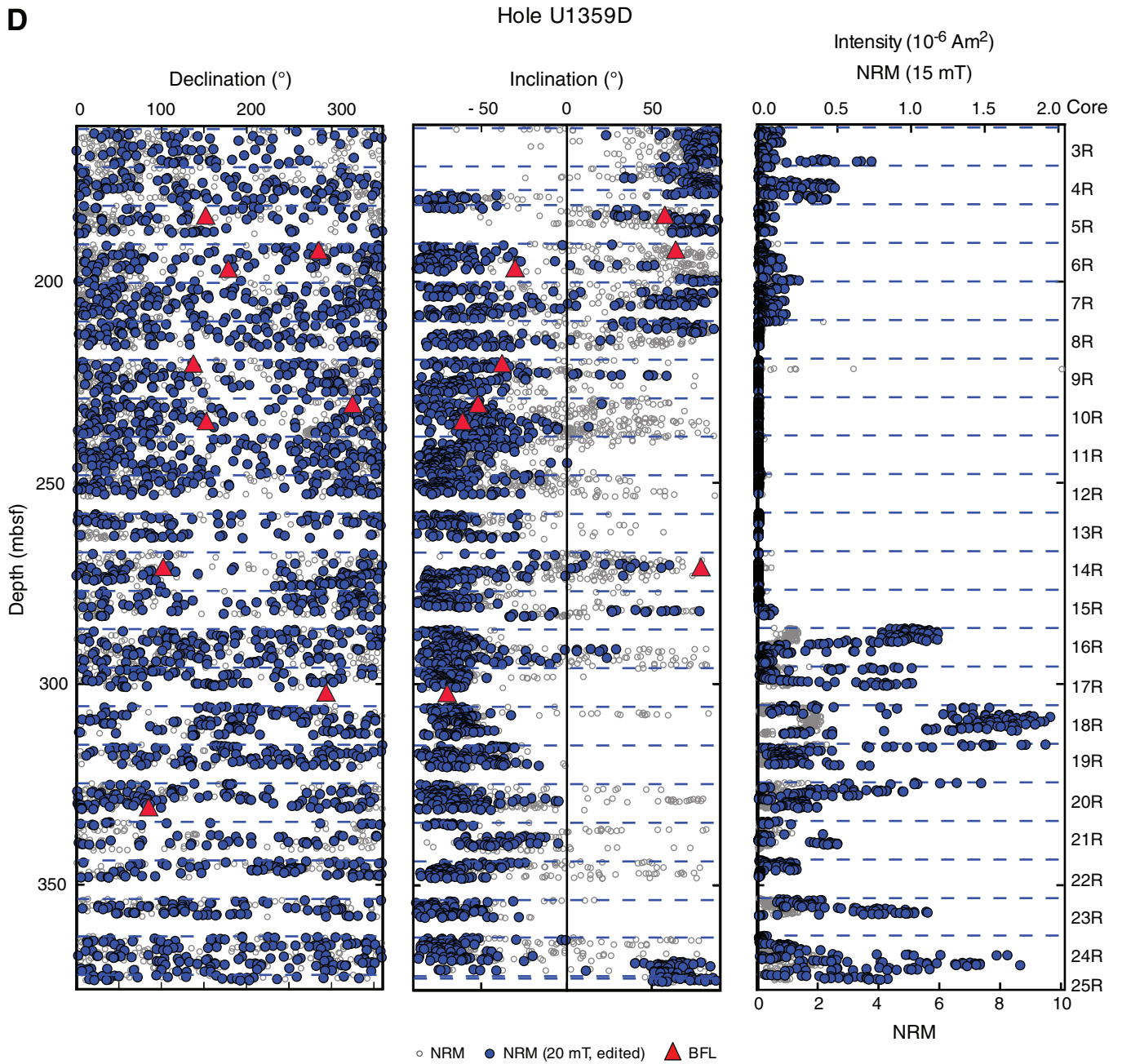


Figure F30 (continued). E. Lower part of Hole U1359D.

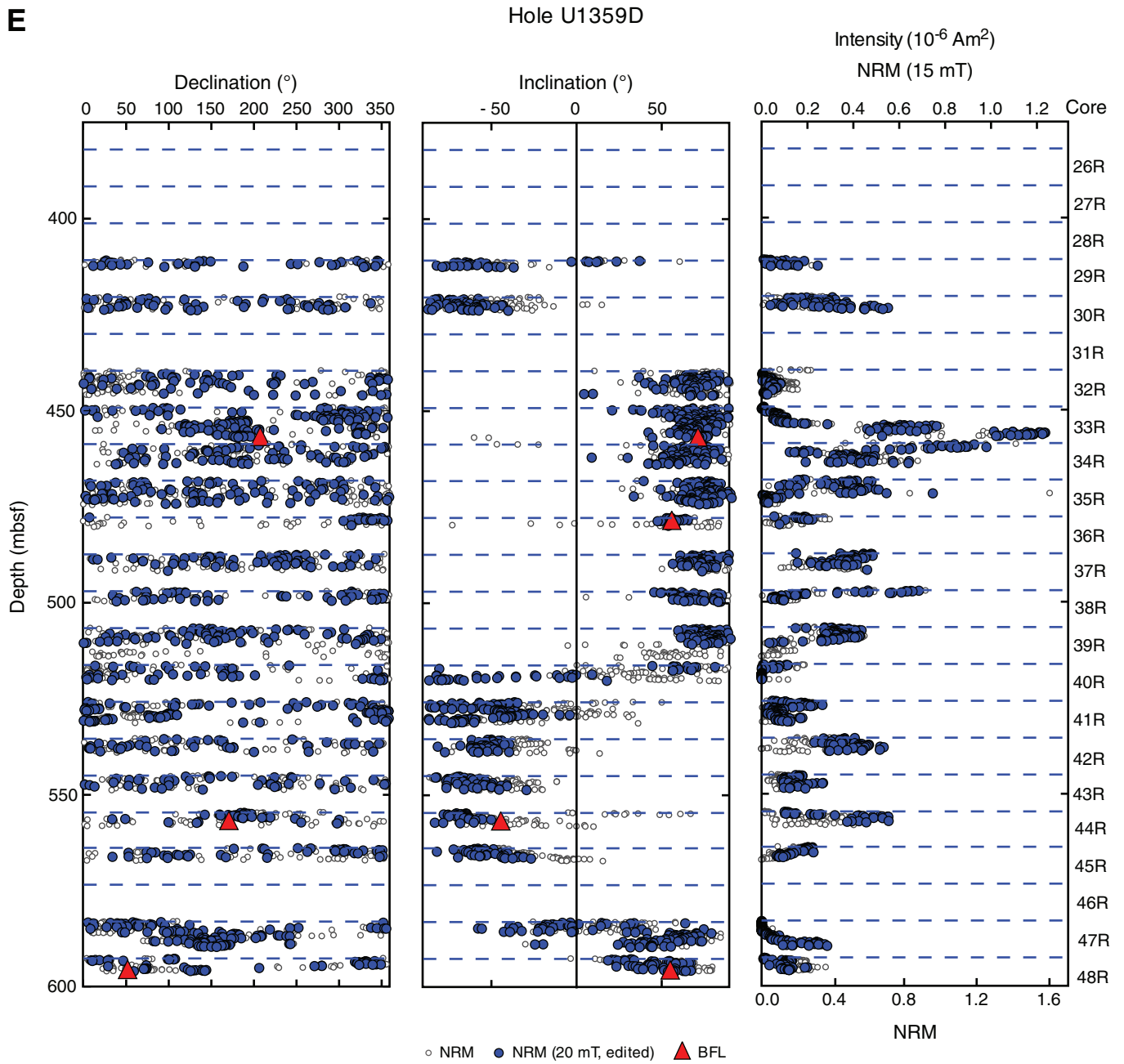


Figure F31. Anisotropy of magnetic susceptibility vs. depth. **A.** Eigenvalues. Stars = very low anisotropy zones, circles = minimum eigenvalue, triangles = intermediate eigenvalue, squares = maximum eigenvalue. Separation of minimum and maximum eigenvalues is related to degree of anisotropy, and the position of the intermediate relative to the other two is an indication of magnetic fabric (see the “**Methods**” chapter) (e.g., if the triangle is quite close to the square, the fabric is oblate). **B.** Inclination of V_3 eigenvector. **C.** Bulk susceptibility (χ).

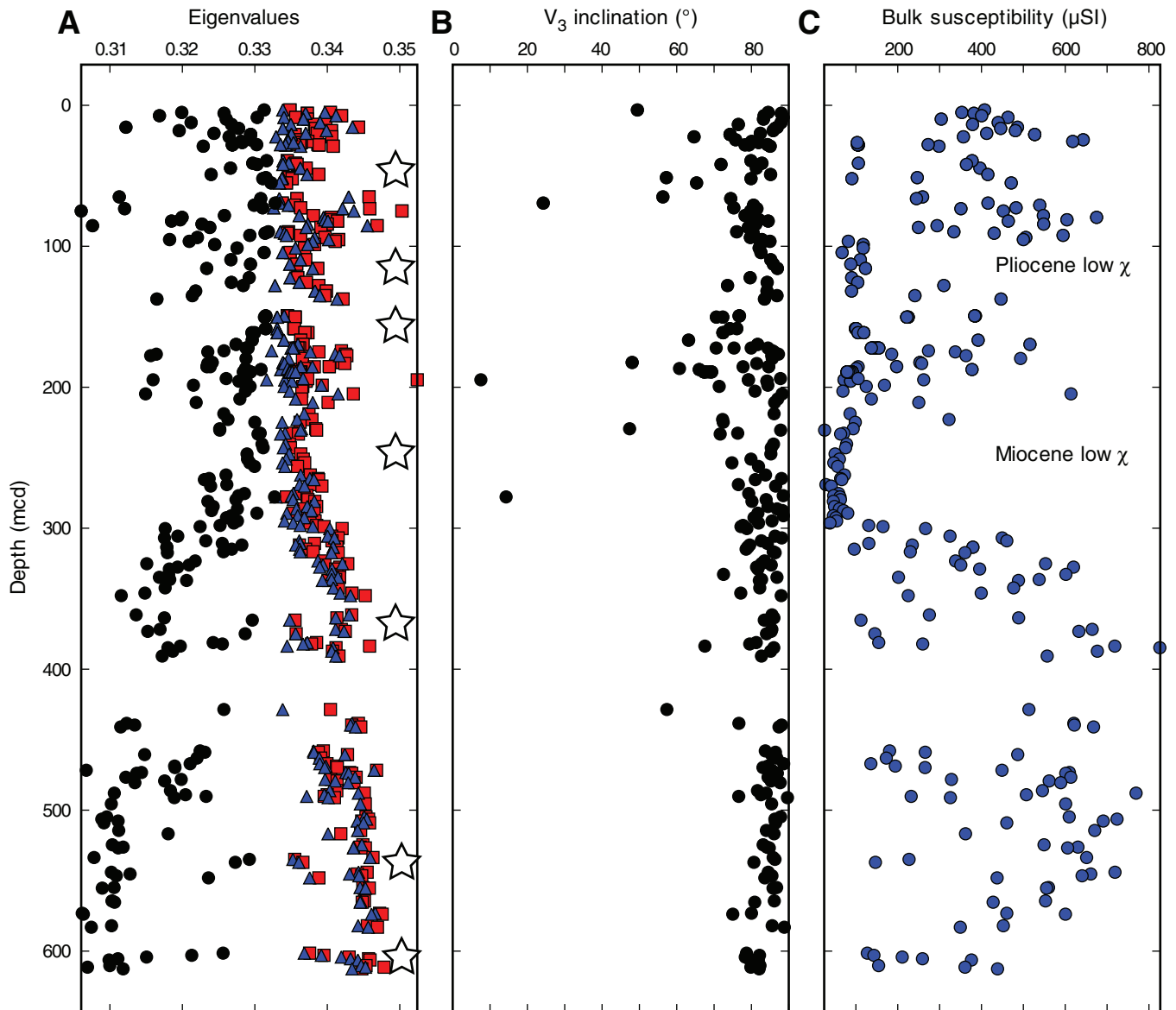


Figure F32. Progressive acquisition of isothermal remanence for samples from the low- and high-susceptibility (χ) zones. **A.** Pliocene high-susceptibility zones. **B.** Pliocene low-susceptibility zone (95–125 mbsf). **C.** Miocene high-susceptibility zones. **D.** Miocene low-susceptibility zone (225–295 mbsf).

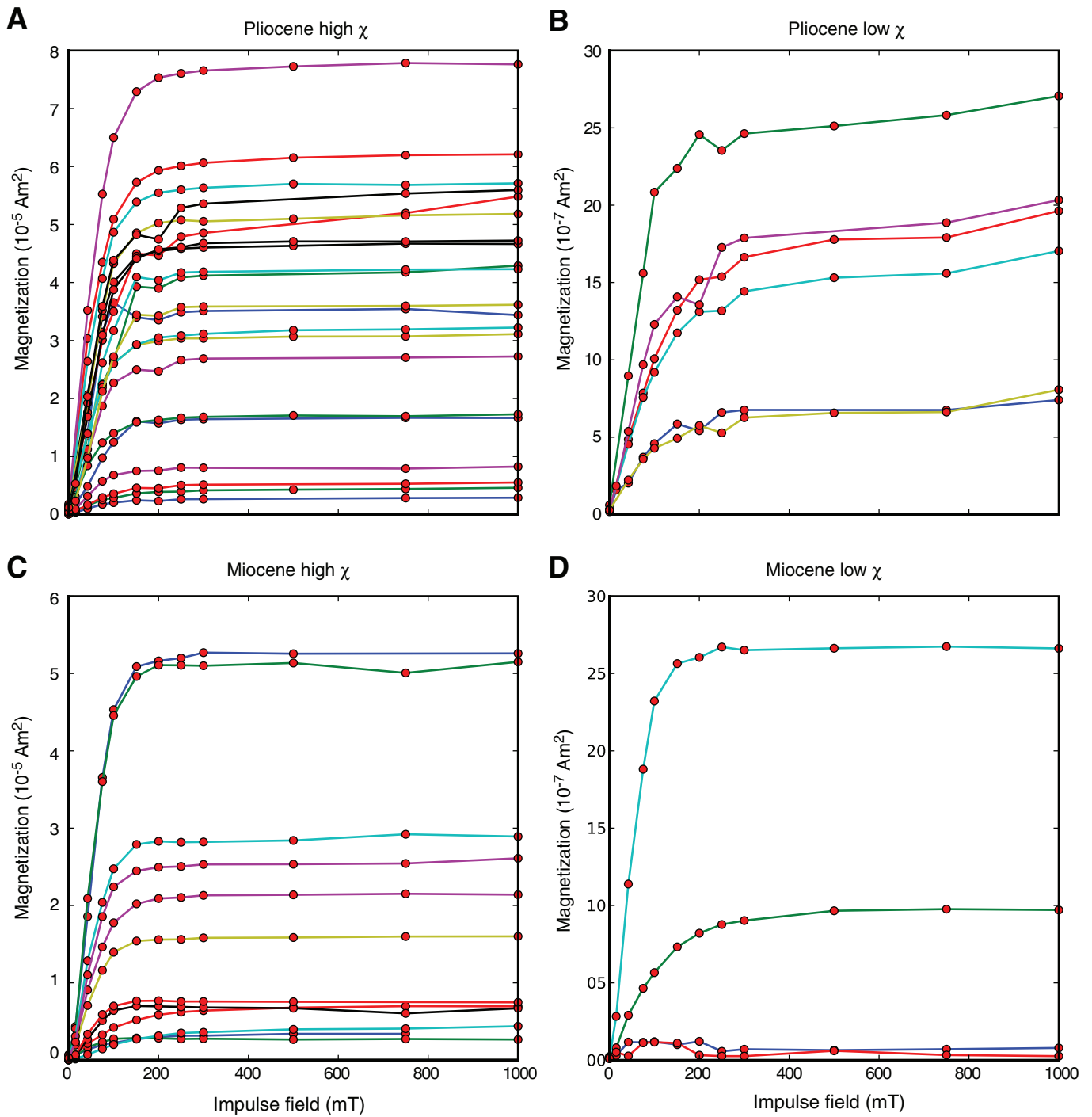


Figure F33. Schematic of compaction disequilibrium. Clay particles in sediment undergoing compaction. In the model of Schwehr et al. (2006), excess water content can retard compaction. The excess could be generated by a variety of factors, including high diatom abundance. Below the zone of excess water, compaction increases downsection. Figure from Schwehr et al. (2006).

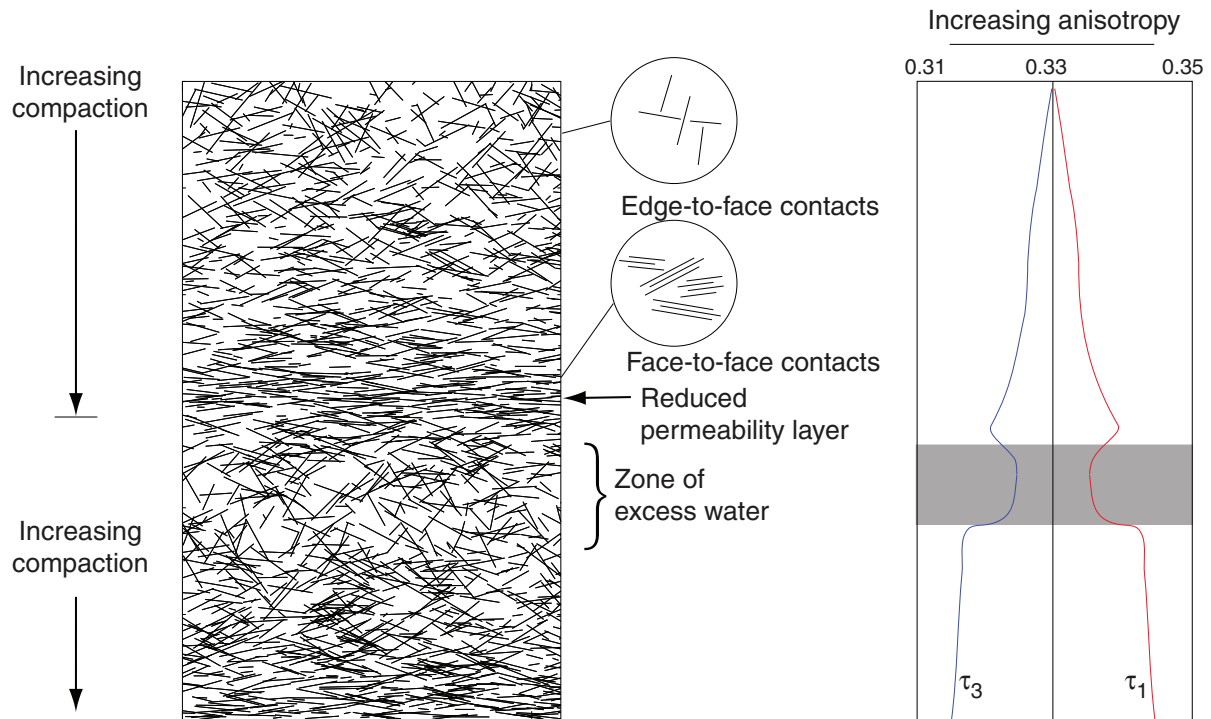


Figure F34. Plots of (A) methane concentrations and (B) methane/ethane ratios, Site U1359.

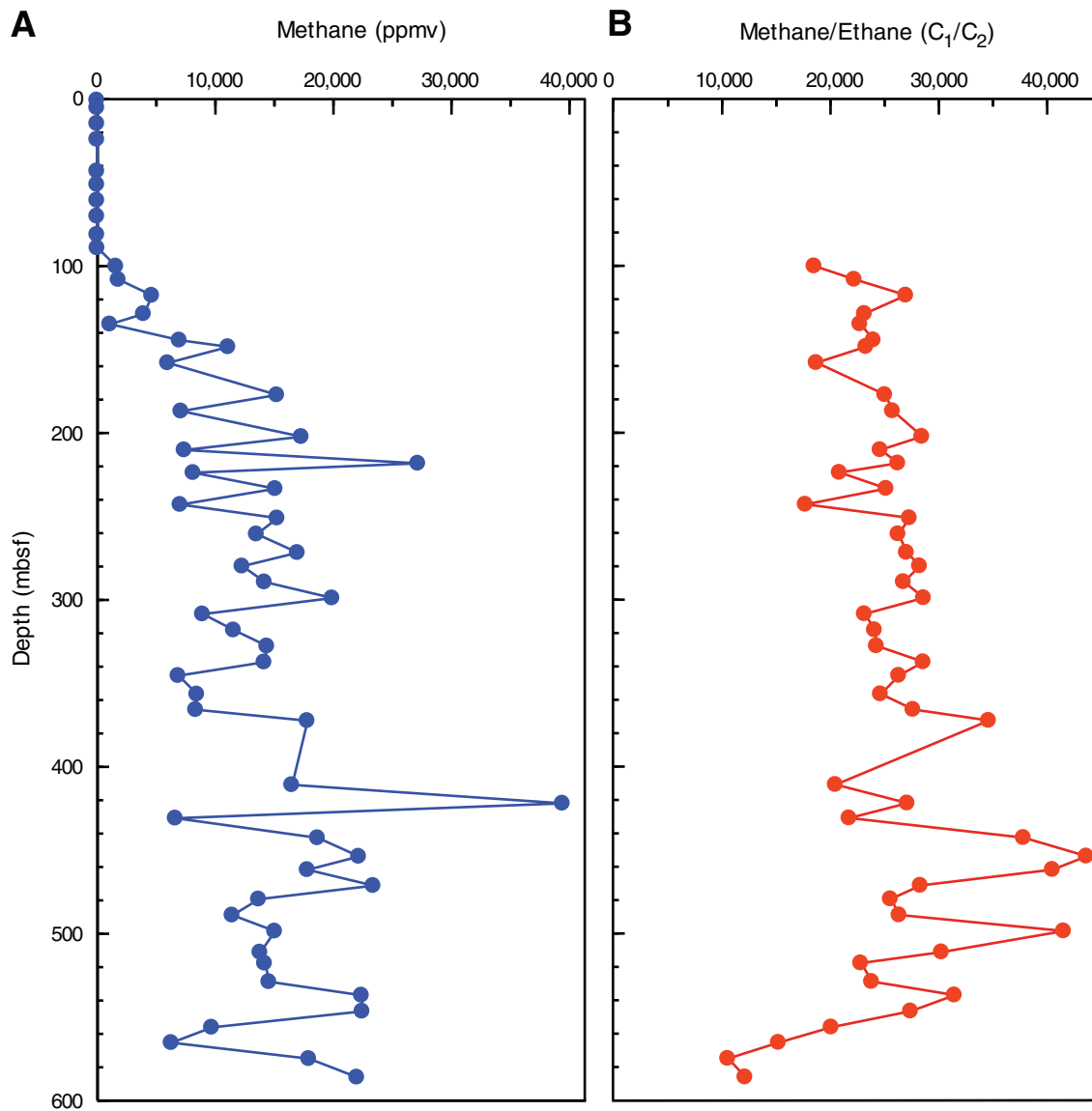


Figure F35. Plot of calcium carbonate data, Site U1359.

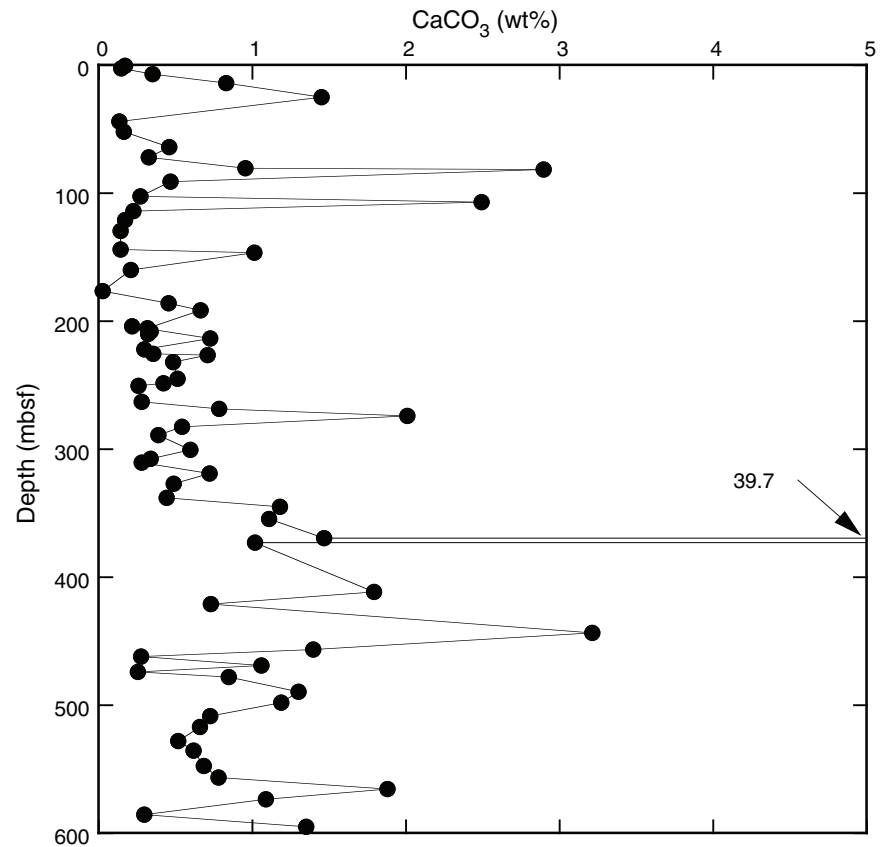


Figure F36. Plots of total carbon, sulfur, nitrogen, total organic carbon (TOC), and carbon/nitrogen ratios, Site U1359.

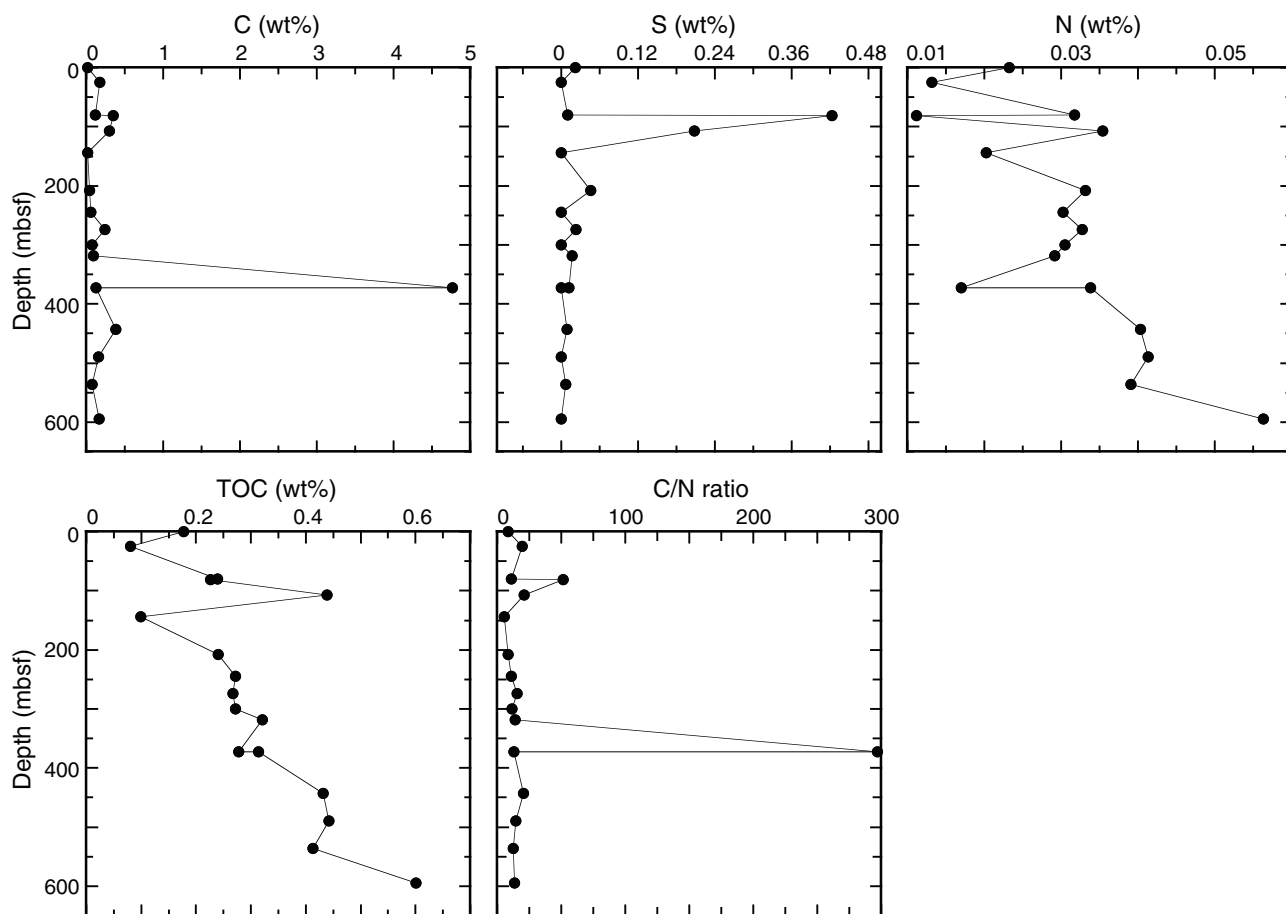




Figure F37. Plots of bulk geochemical data and calculated molar ratios for the chemical index of alteration (CIA), Site U1359. For details on CIA calculation see text. Shaded areas = intervals distinguished based on geochemical data.

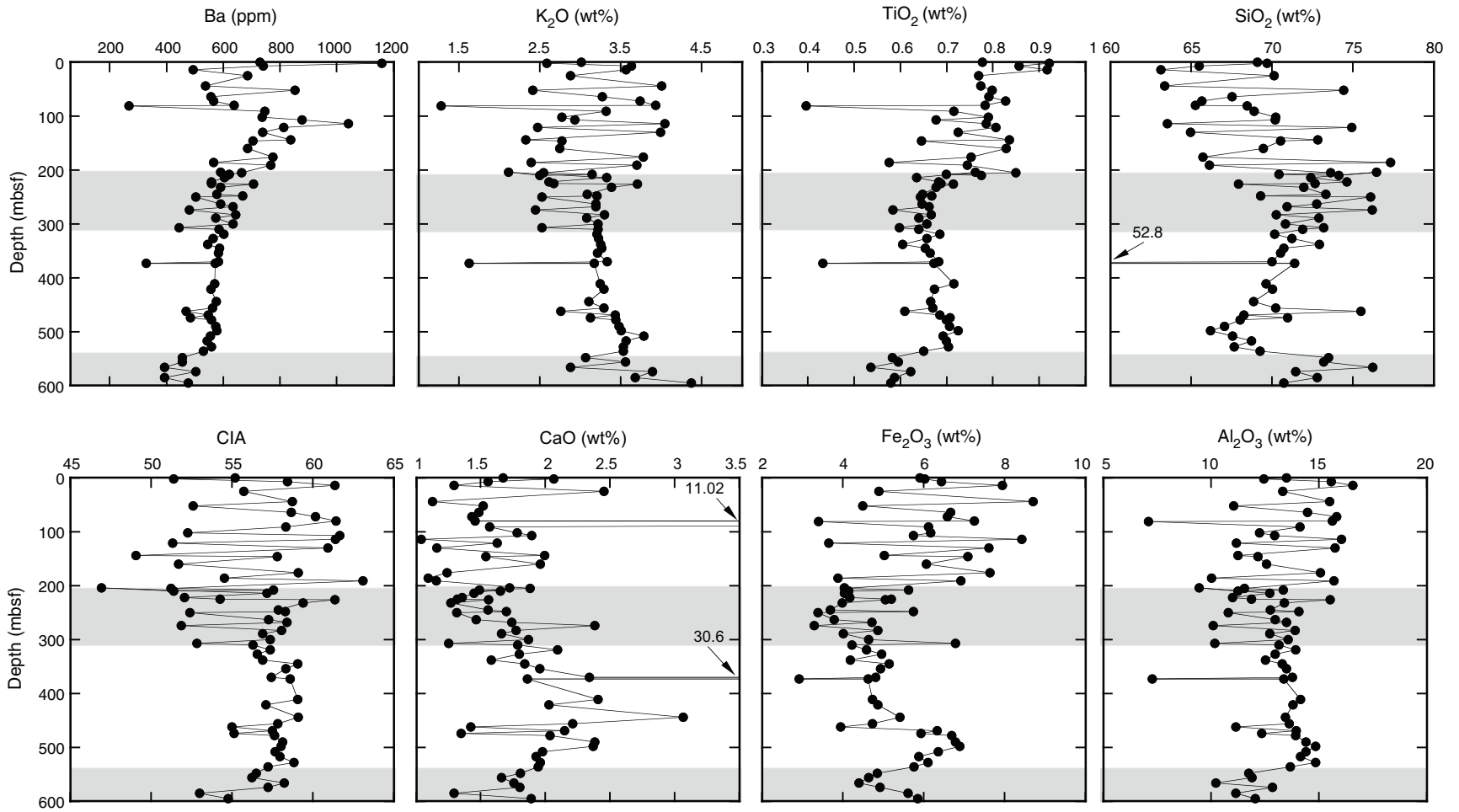


Figure F38. Interstitial water profiles for dissolved inorganic carbon (DIC), alkalinity, sulfate, and magnesium, Hole U1359B.

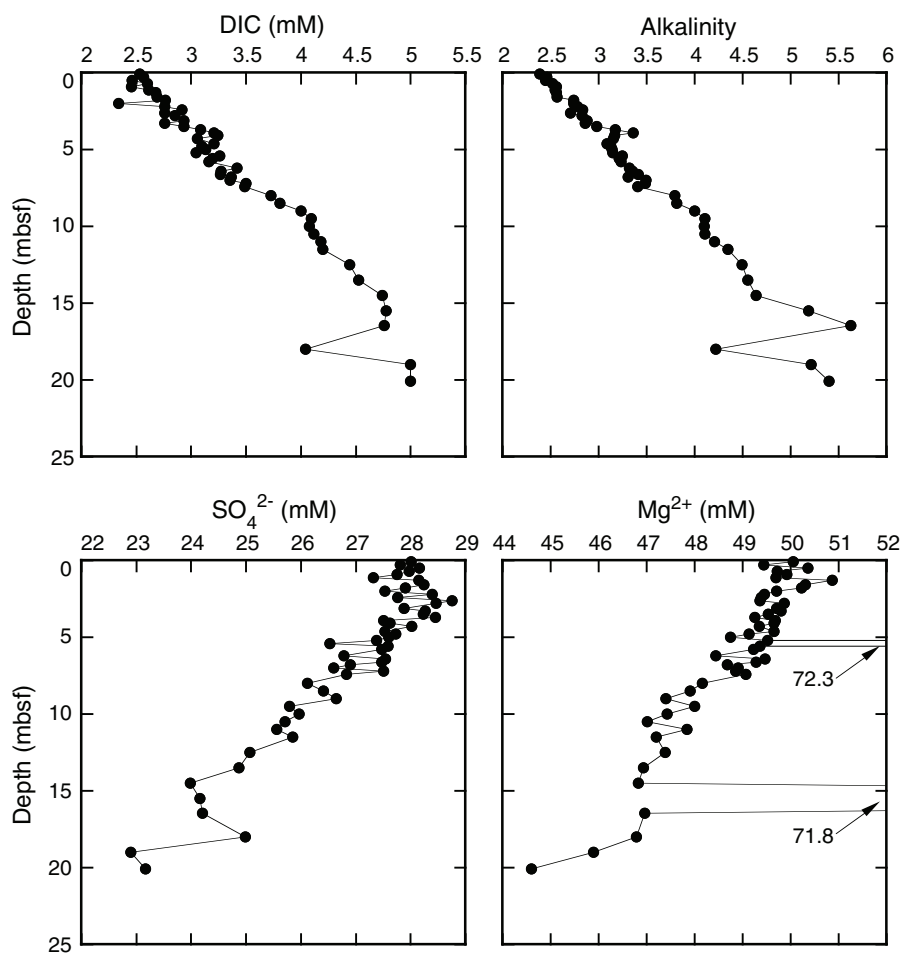


Figure F39. Interstitial water profiles for manganese, ammonium, silica, and phosphate, Hole U1359B. Open circles = samples that were squeezed first (i.e., with only minor time delay).

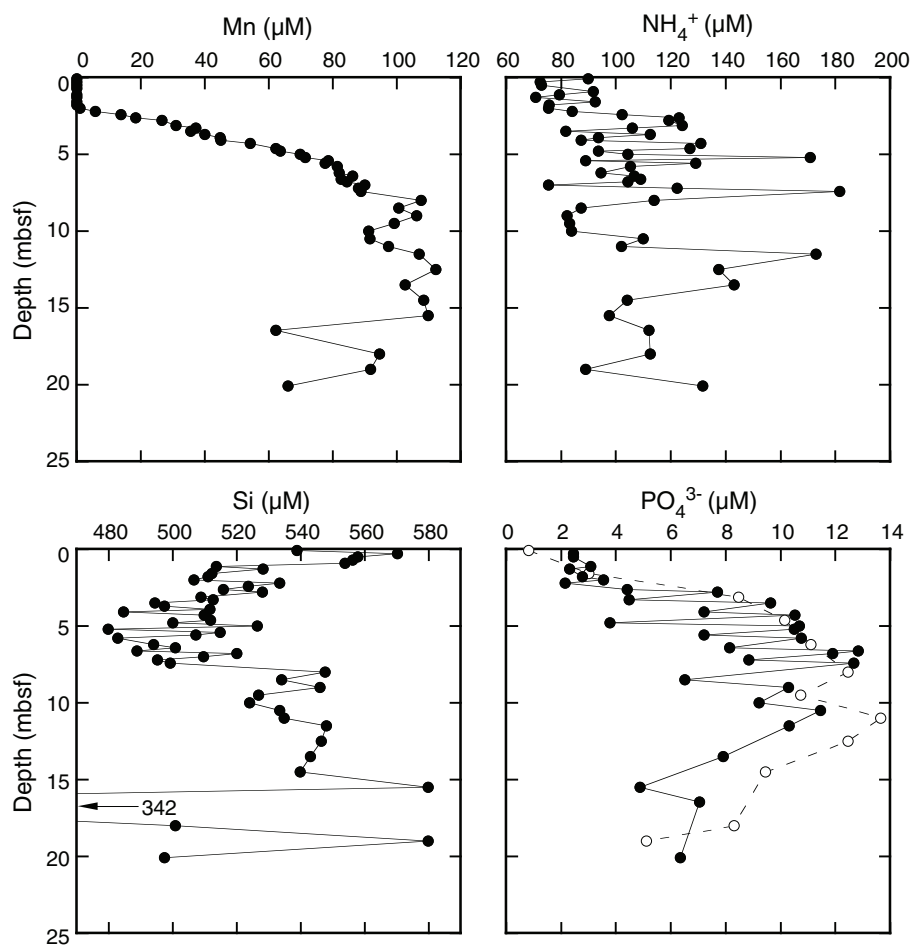


Figure F40. Interstitial water profiles for the sum of nitrite and nitrate (NO_x), strontium, chloride, and boron, Hole U1359B.

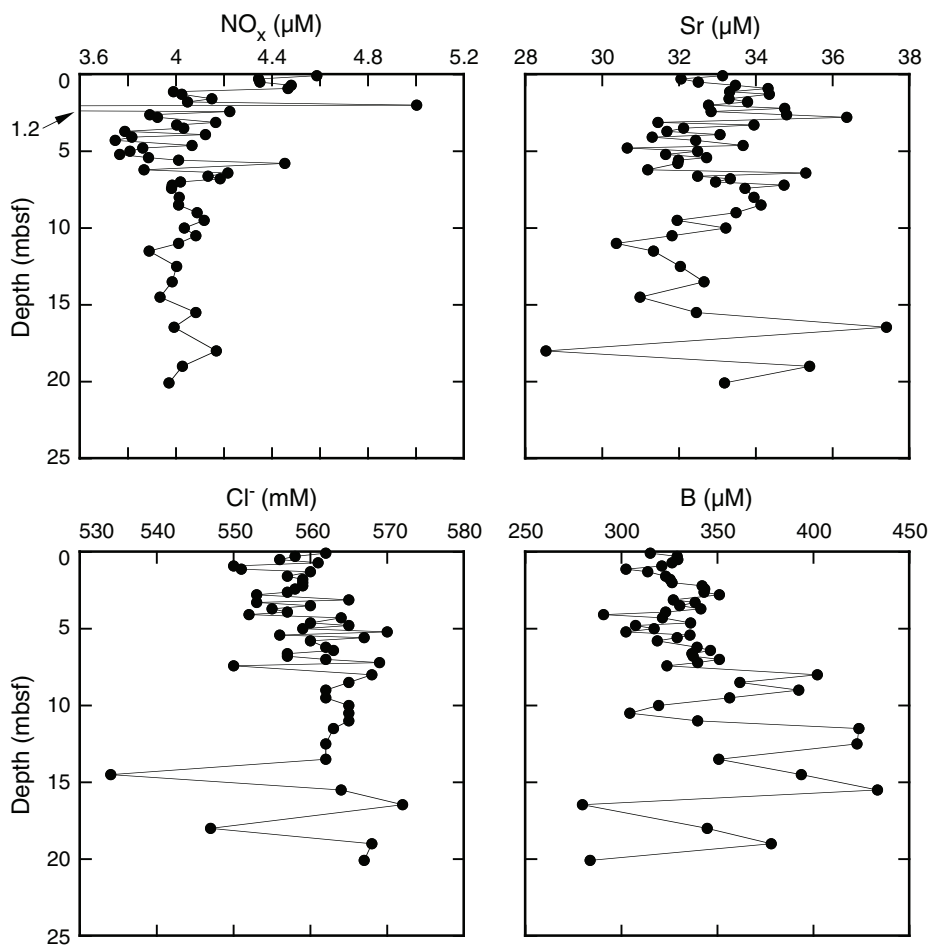




Figure F41. Plots of magnetic susceptibility data, Site U1359.

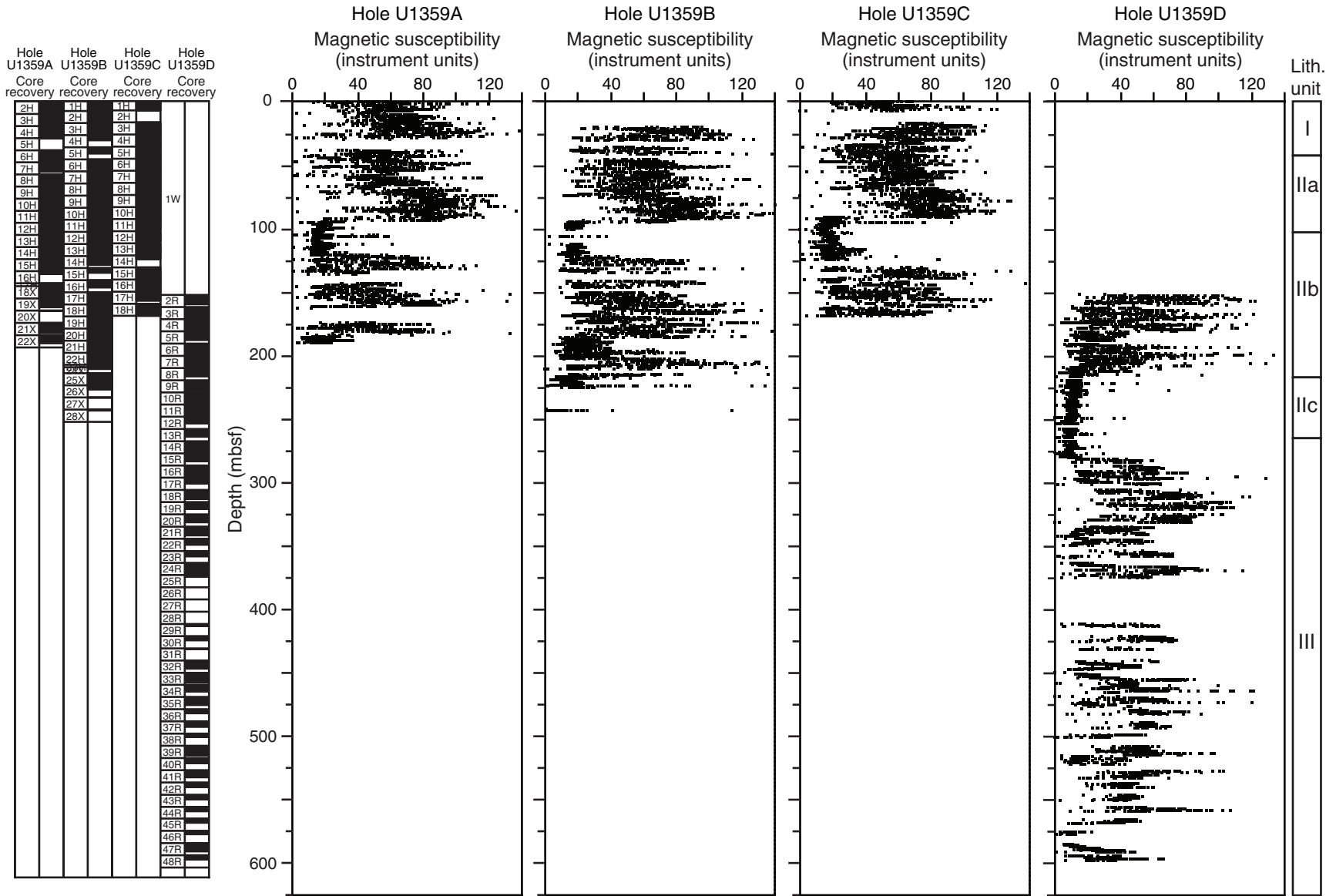




Figure F42. Plots of magnetic susceptibility data from 0 to 250 mbsf, Site U1359.

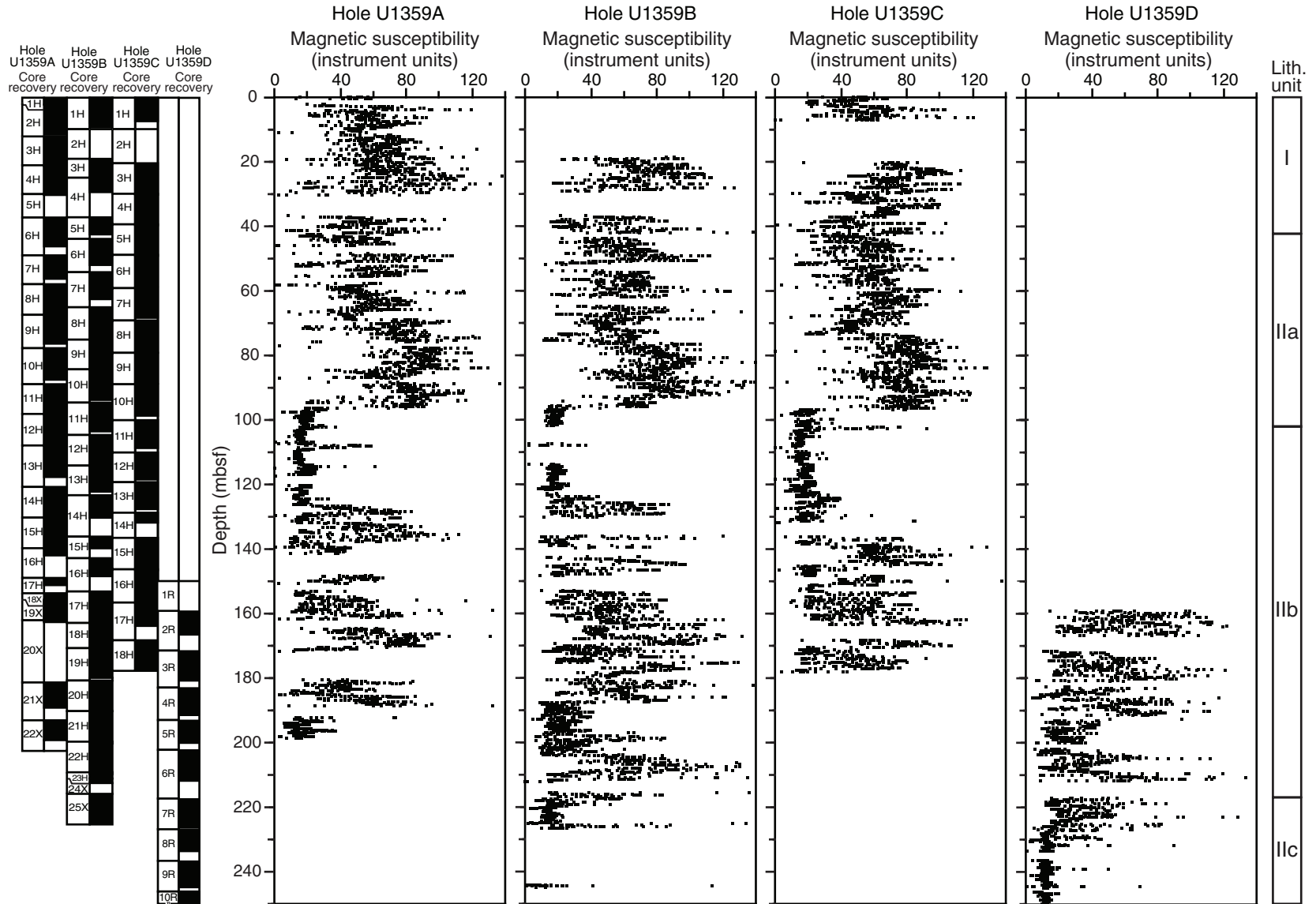




Figure F43. Plots of natural gamma radiation (NGR) data, Site U1359.

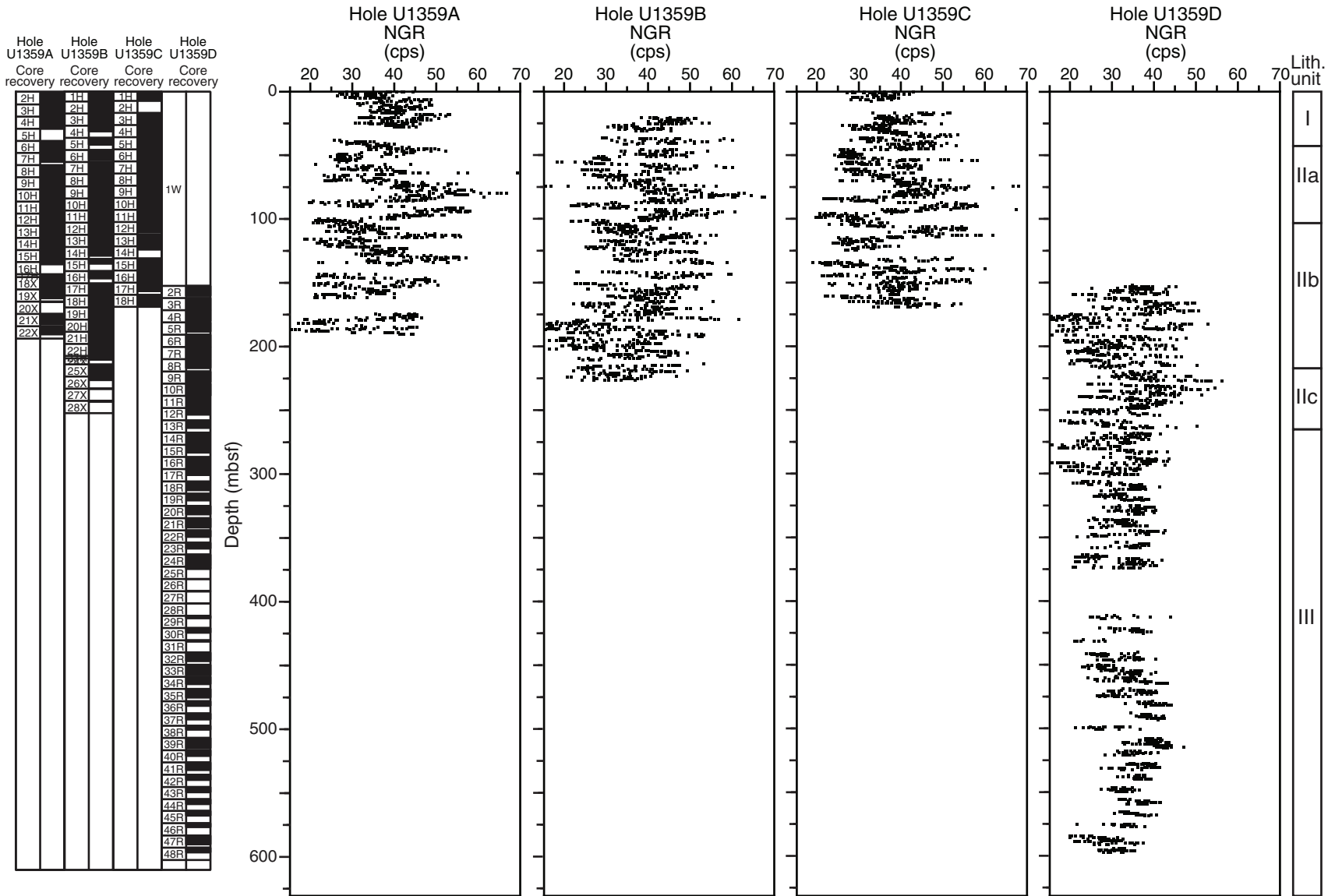




Figure F44. Plots of natural gamma radiation (NGR) data from 0 to 250 mbsf, Site U1359.

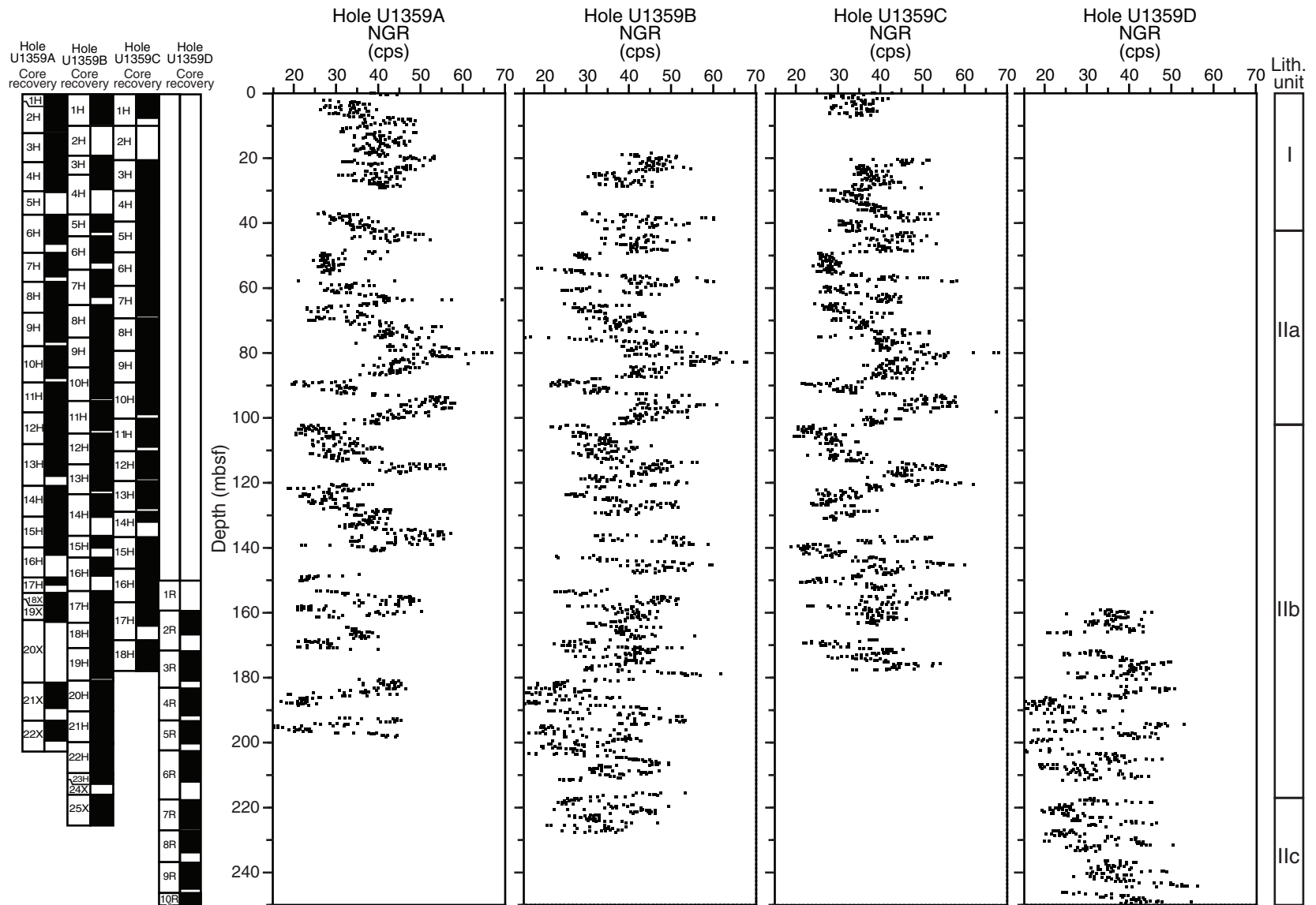


Figure F45. Plots of magnetic susceptibility and natural gamma radiation (NGR) data, Hole U1359D.

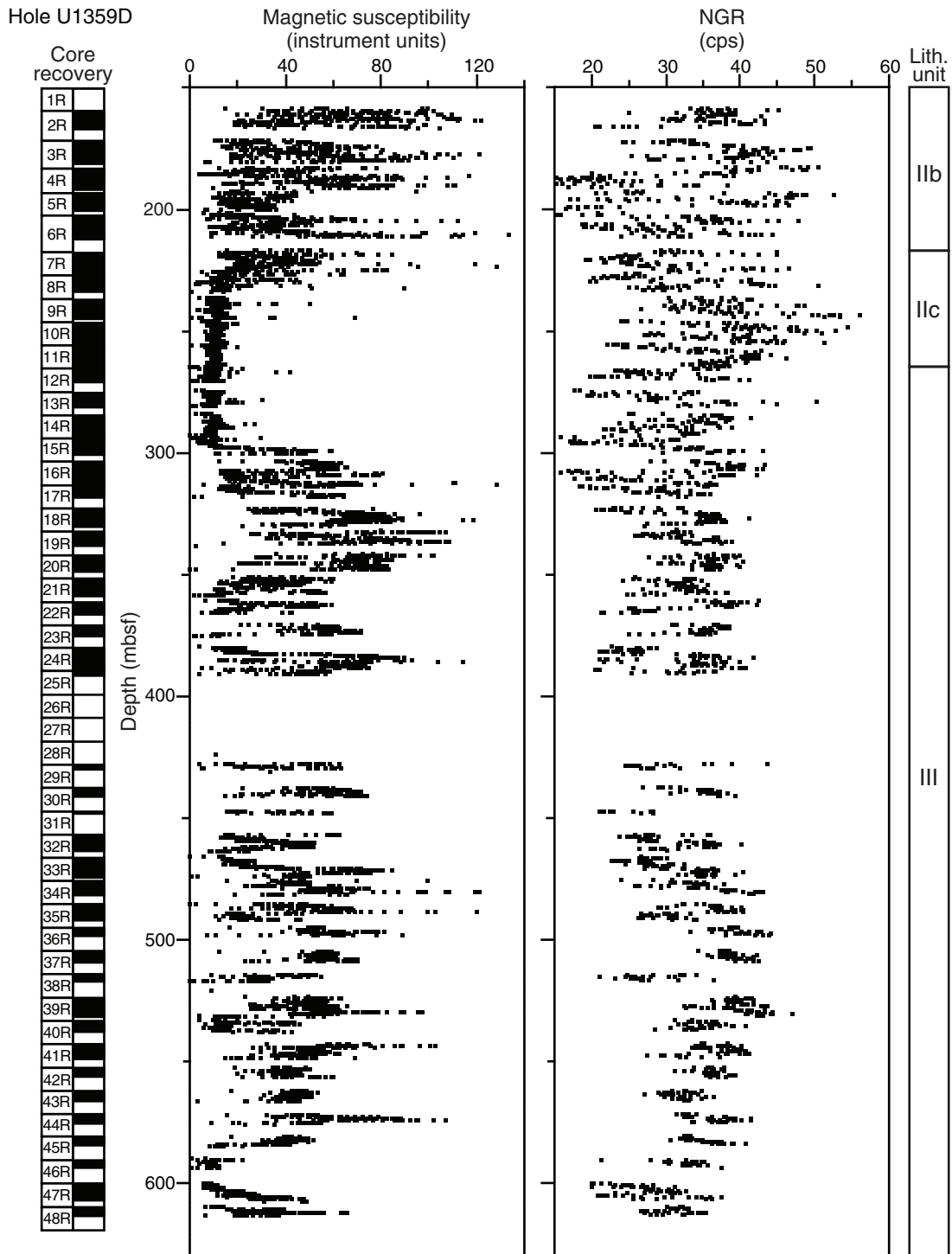




Figure F46. Plots of gamma ray attenuation (GRA) density (gray squares) and wet bulk density from discrete samples (red circles), Site U1359.

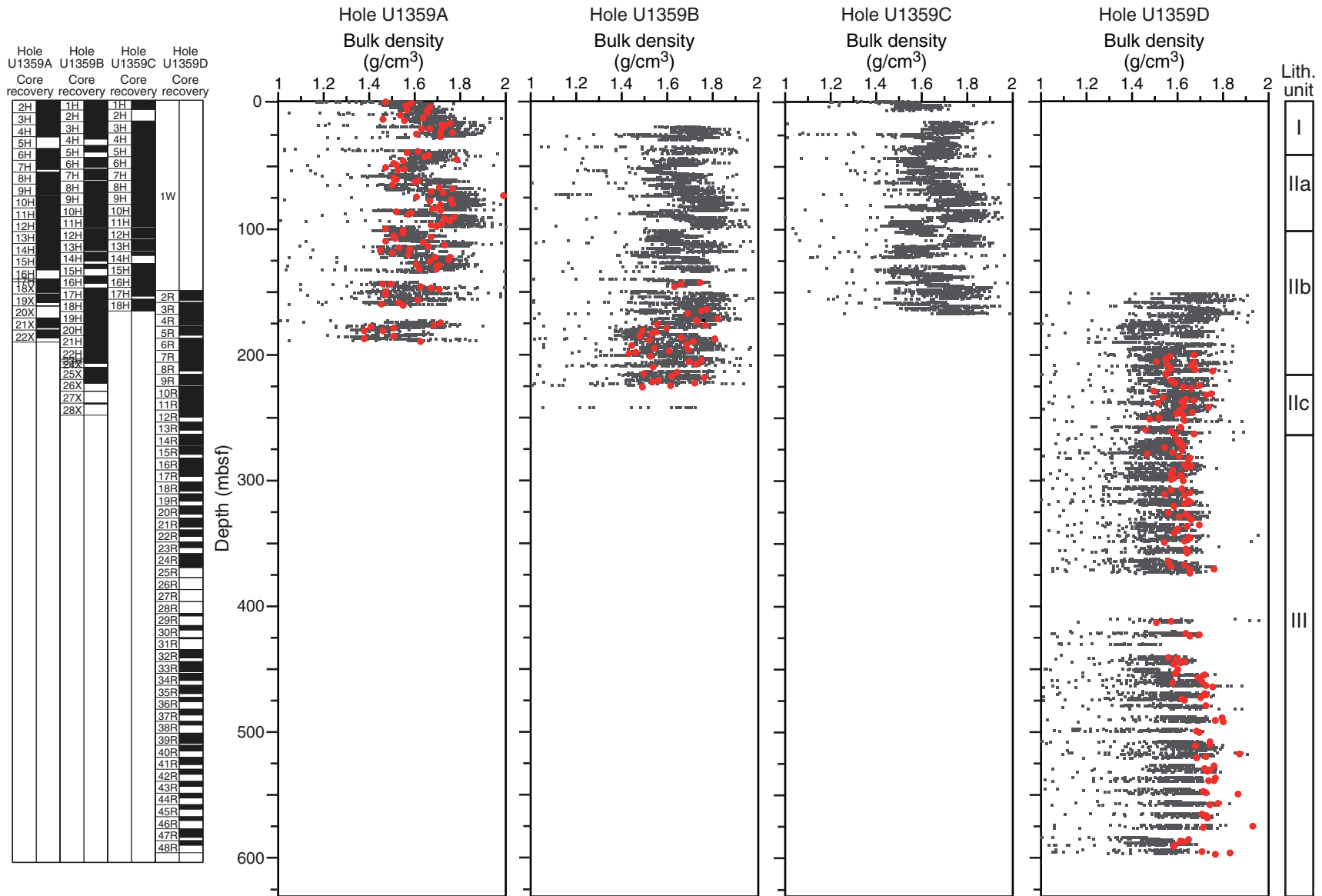




Figure F47. Plots of gamma ray attenuation (GRA) density (gray squares) and wet bulk density from discrete samples (red circles) from 0 to 250 mbsf, Site U1359.

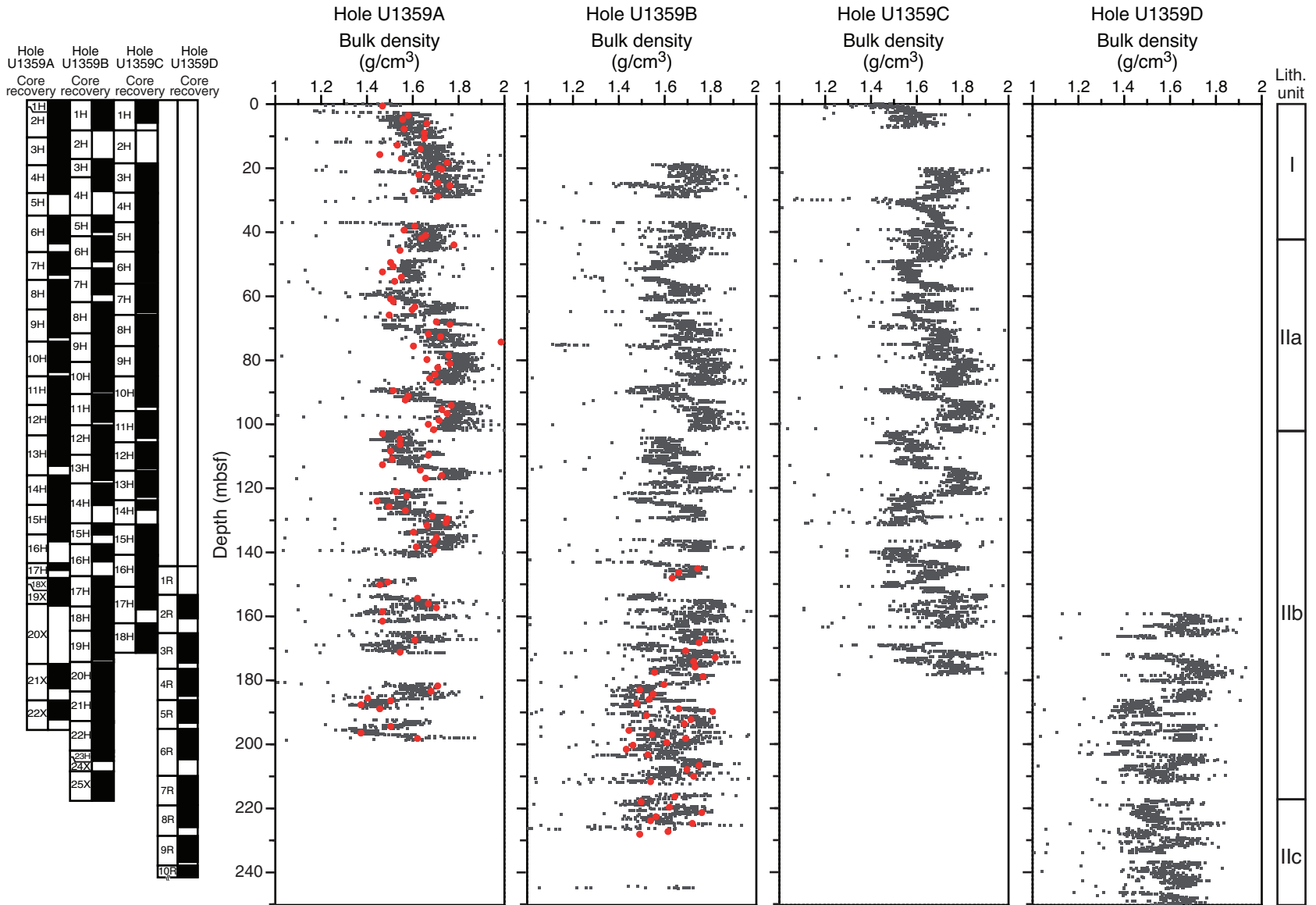


Figure F48. Plot of gamma ray attenuation (GRA) density measurements (gray squares) and wet bulk density from discrete samples (red circles), Hole U1359D.

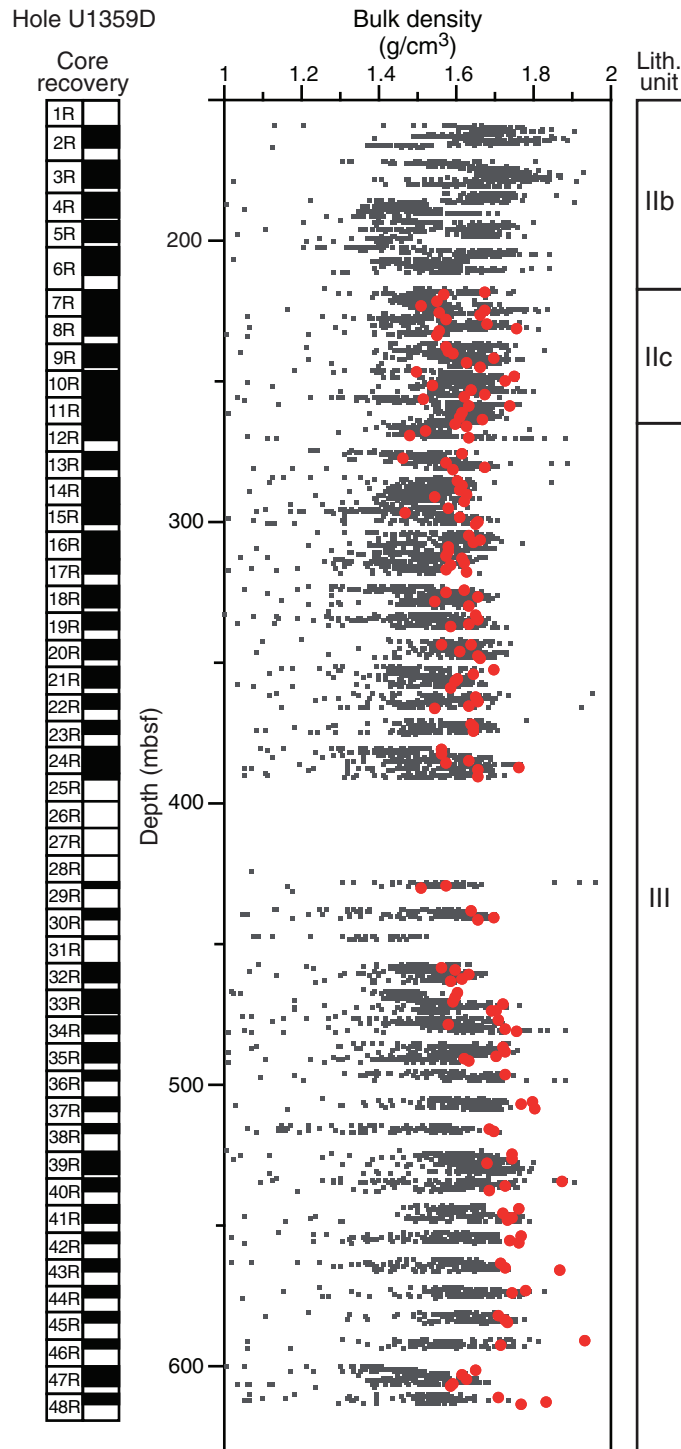


Figure F49. Plot of *P*-wave logger (PWL) and discrete *P*-wave velocity measurements, Site U1359.

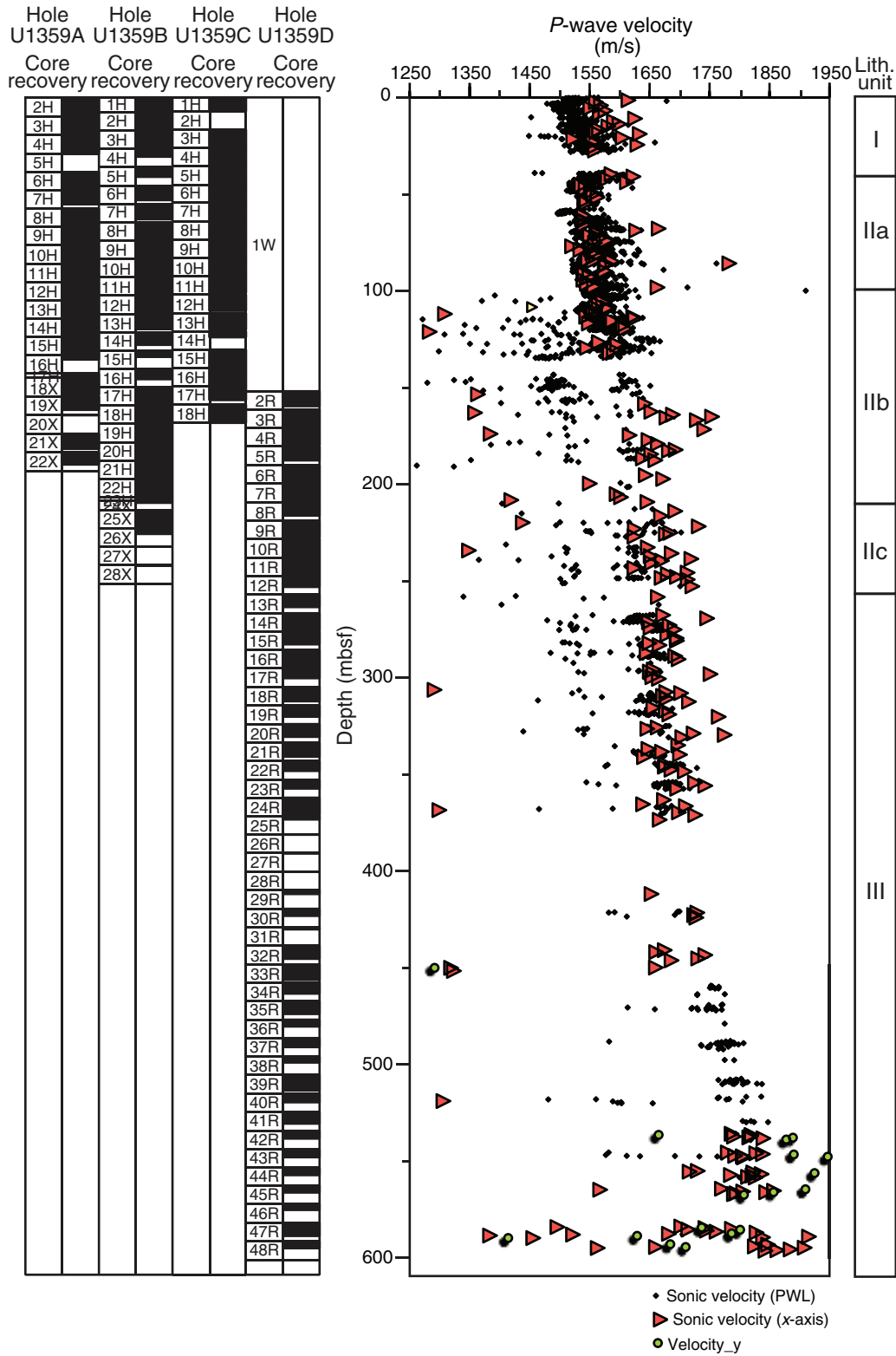


Figure F50. Plot of *P*-wave logger (PWL) and split-core discrete *P*-wave velocity measurements, Hole U1359D.

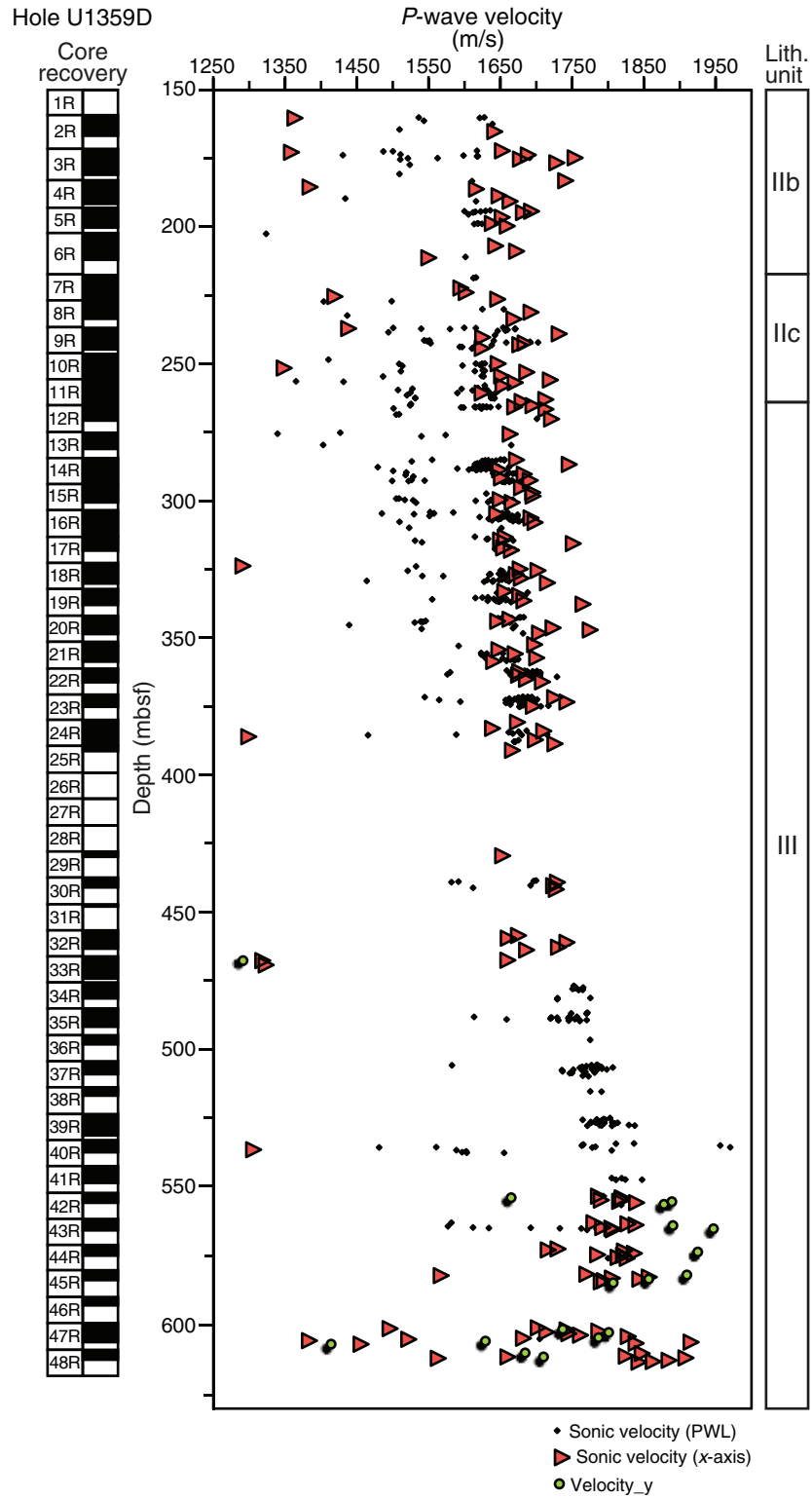


Figure F51. Plots of grain density and porosity, Site U1359.

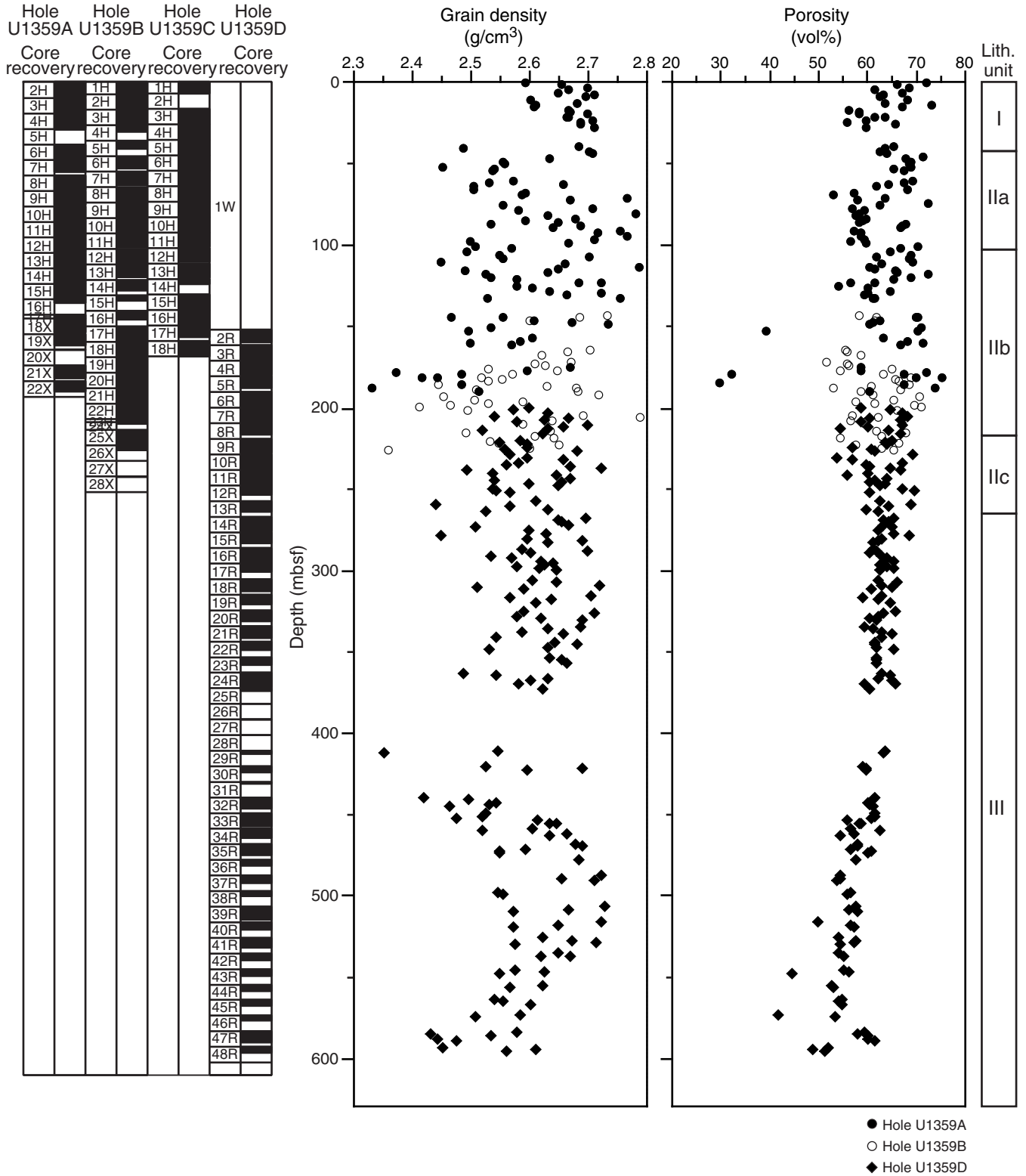


Figure F52. Plots of grain density and porosity from 0 to 220 mbsf, Site U1359.

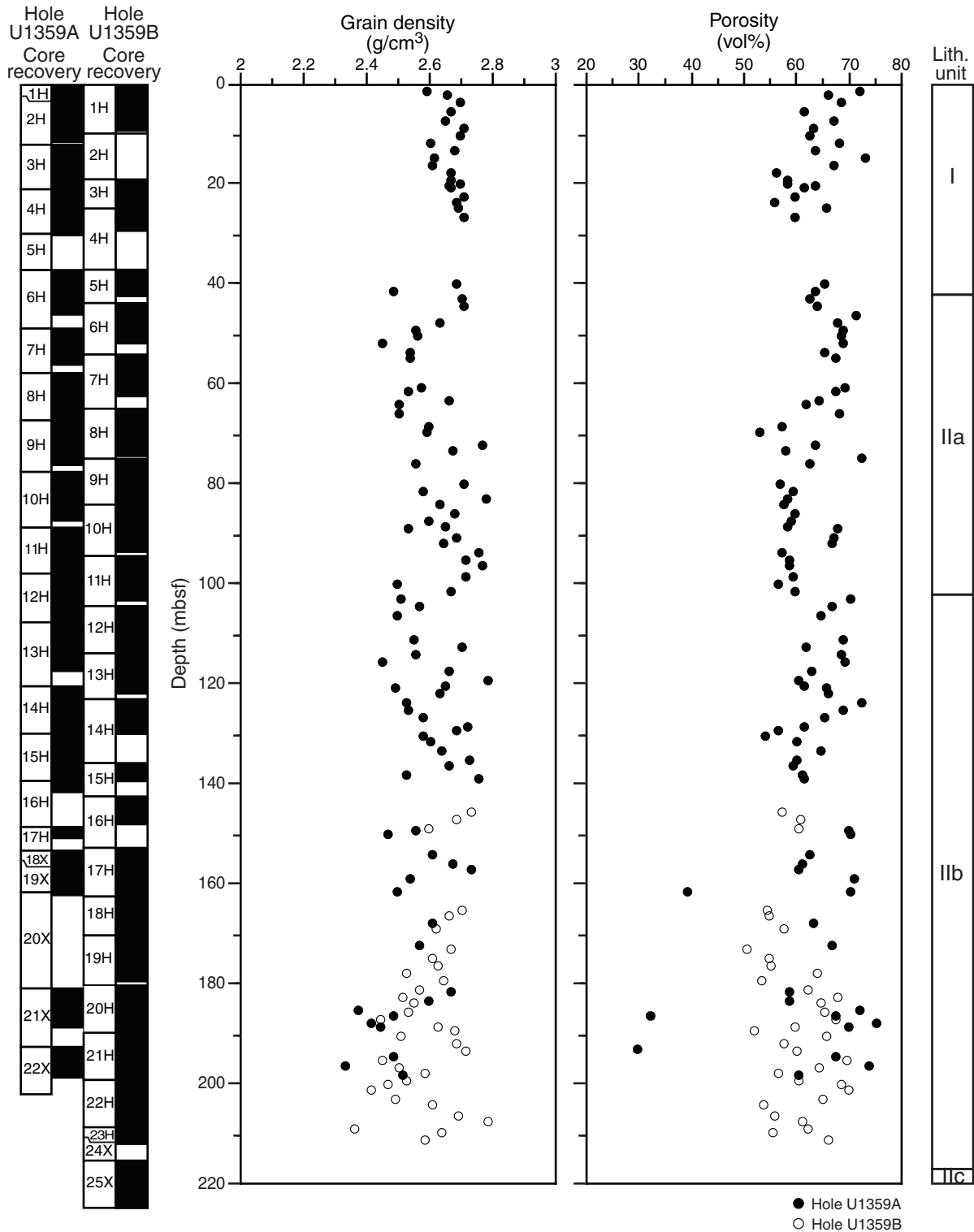


Figure F53. Plots of grain density and porosity from 220 to 620 mbsf, Hole U1359D.

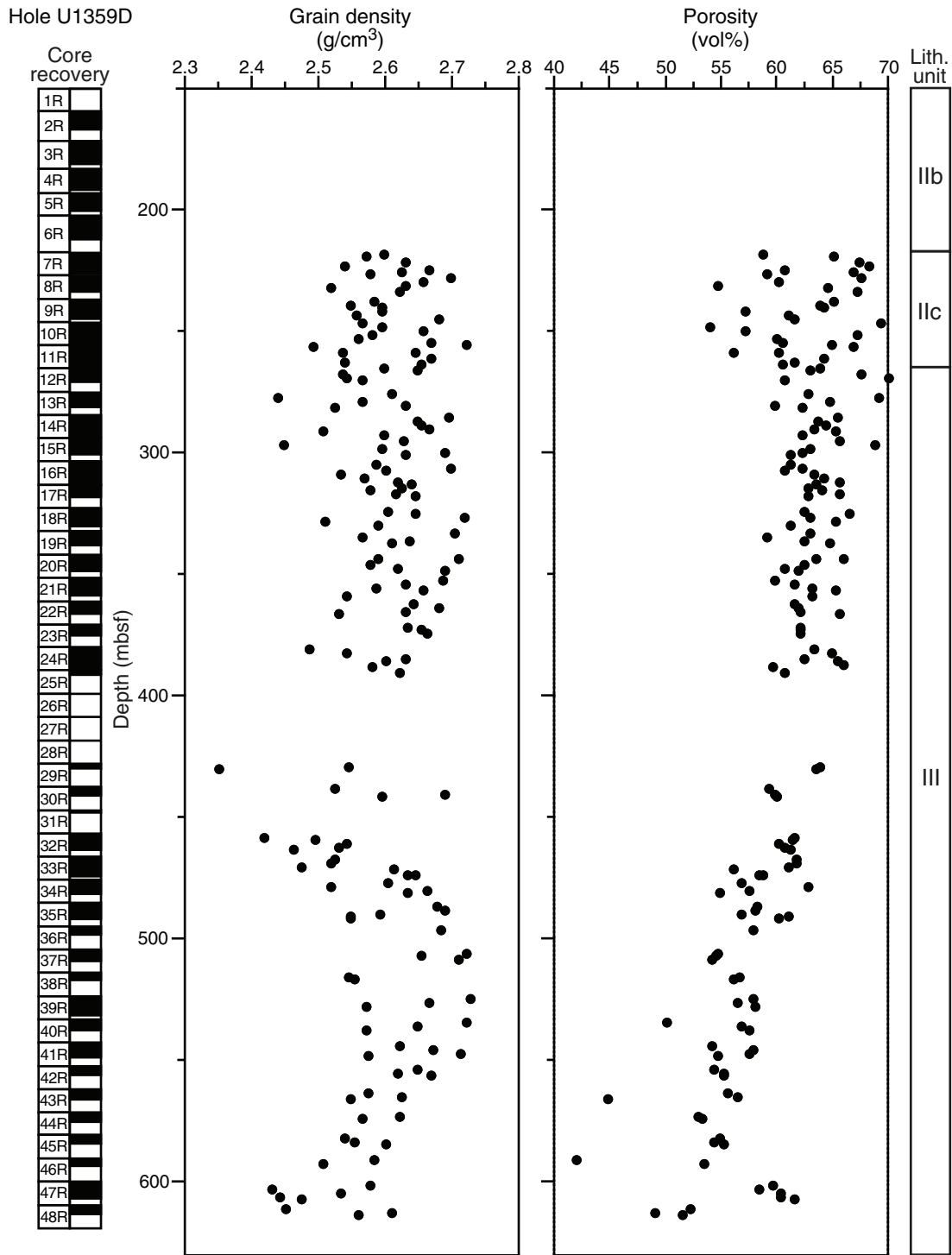


Figure F54. Plots of wet bulk and dry density, Site U1359A.

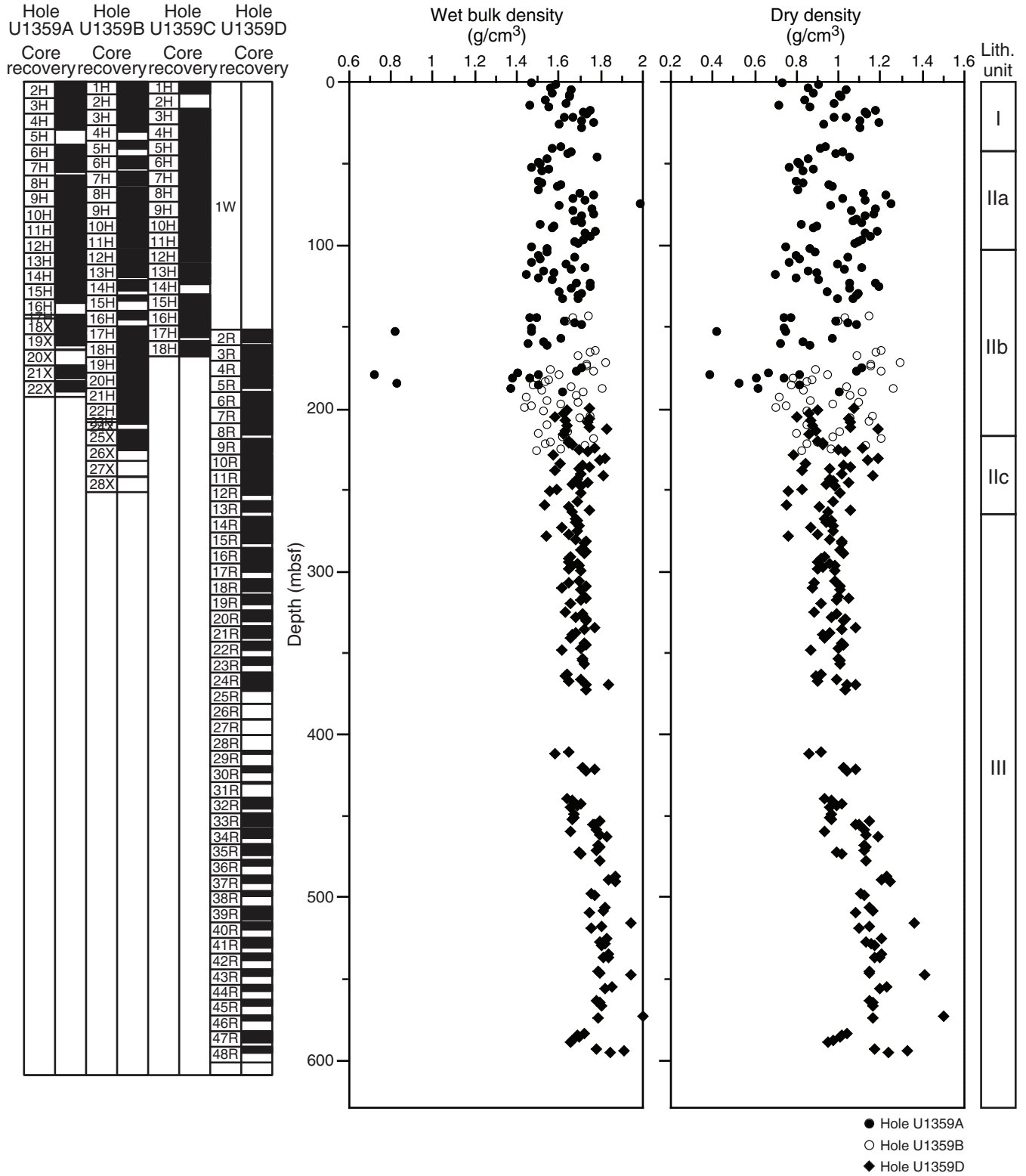


Figure F55. Plots of wet bulk and dry density from 0 to 220 mbsf, Site U1359.

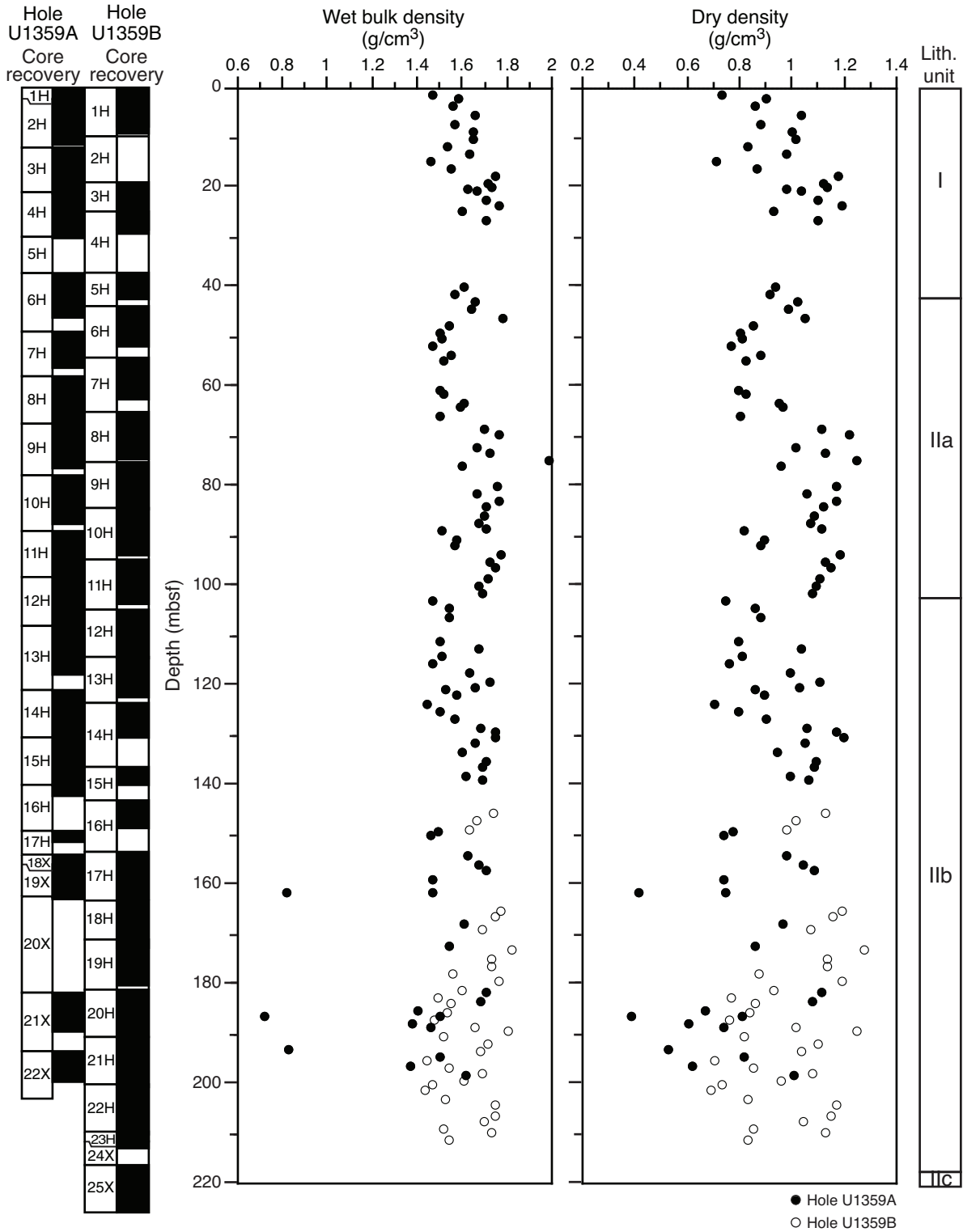


Figure F56. Plots of wet bulk and dry density from 220 to 620 mbsf, Hole U1359D.

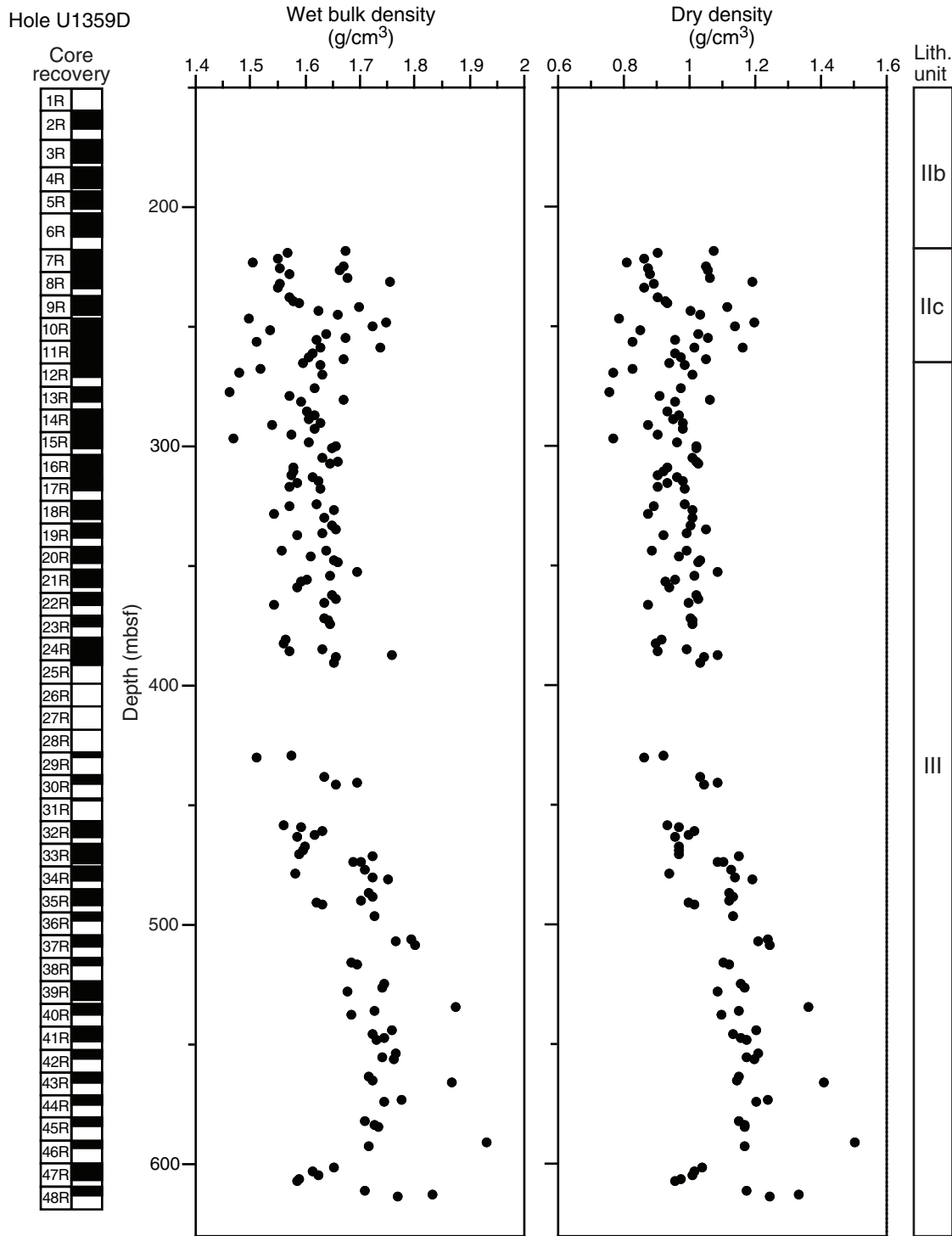


Figure F57. Plots of relative moisture content and void ratio, Site U1359.

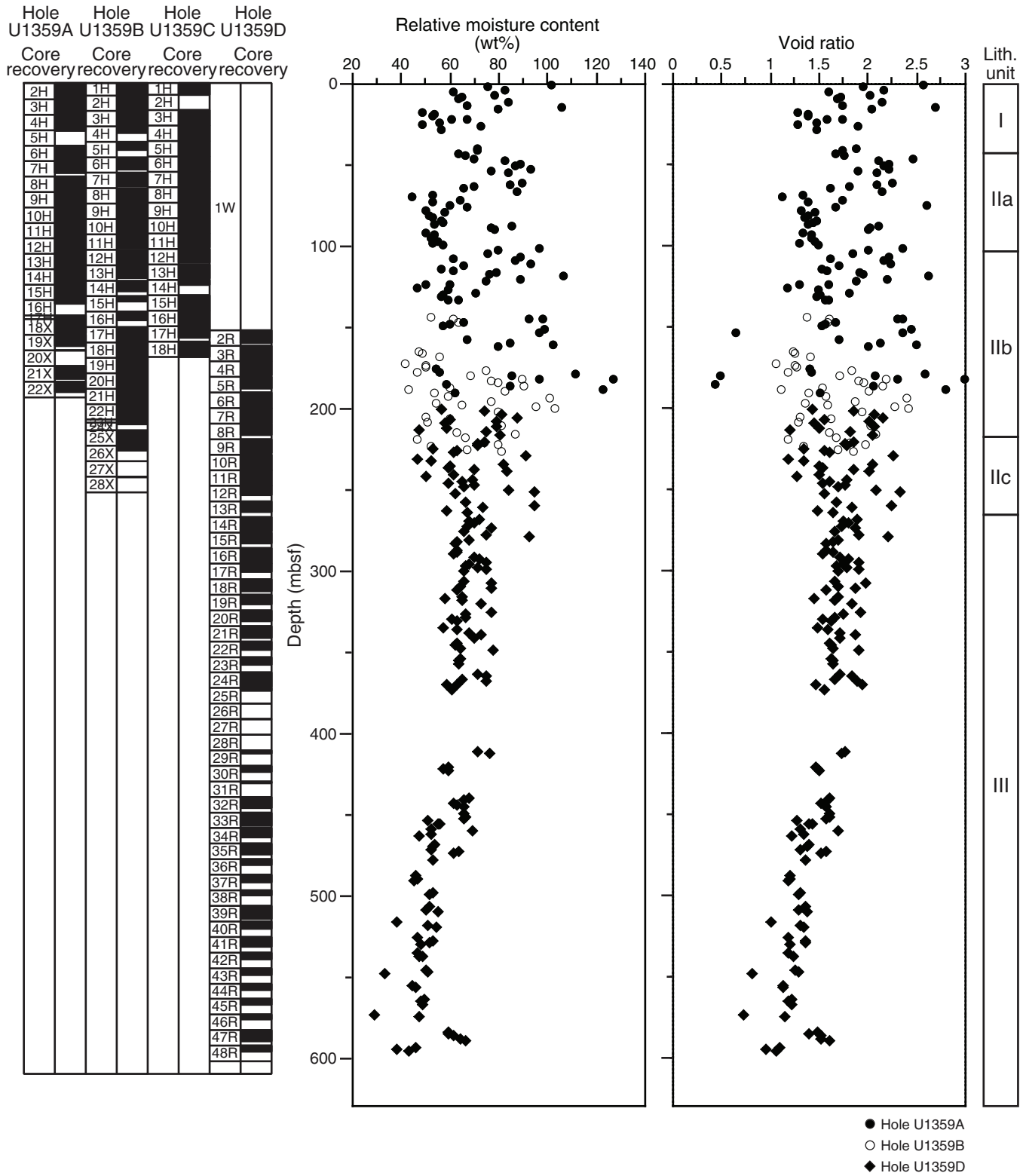


Figure F58. Plots of relative moisture content and void ratio from 0 to 220 mbsf, Site U1359.

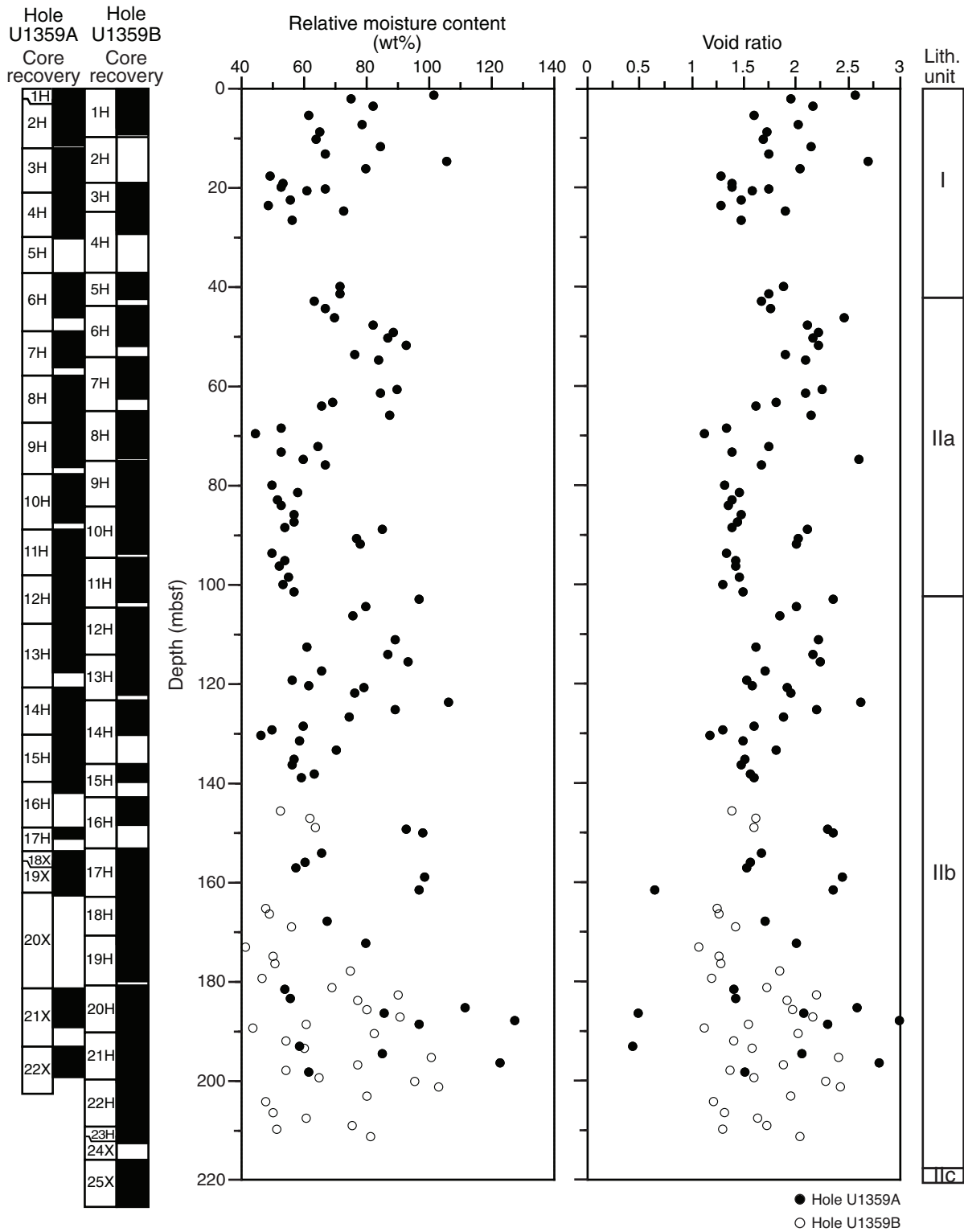


Figure F59. Plots of relative moisture content and void ratio from 220 to 620 mbsf, Hole U1359D.

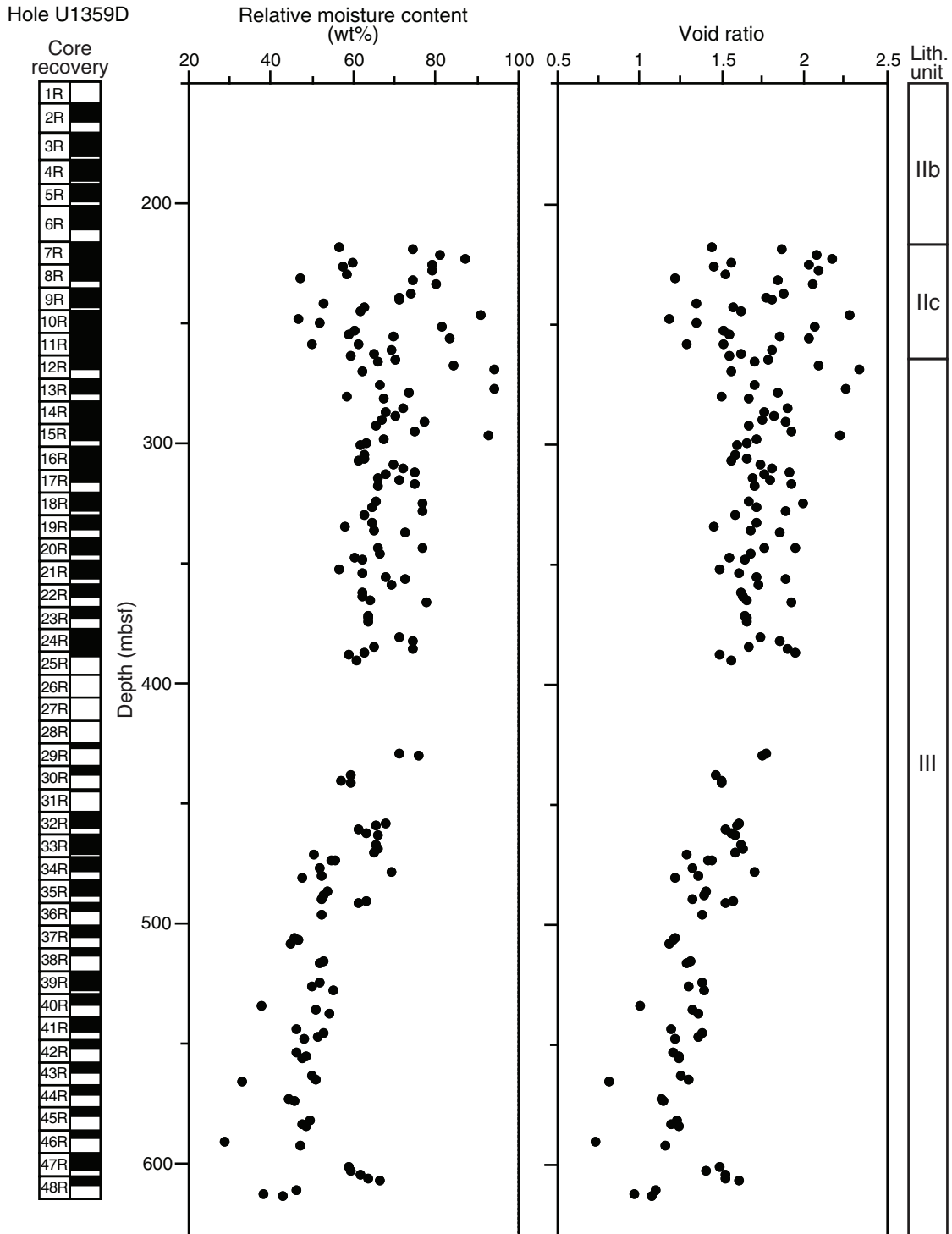


Figure F60. Plot of thermal conductivity measurements, Site U1359.

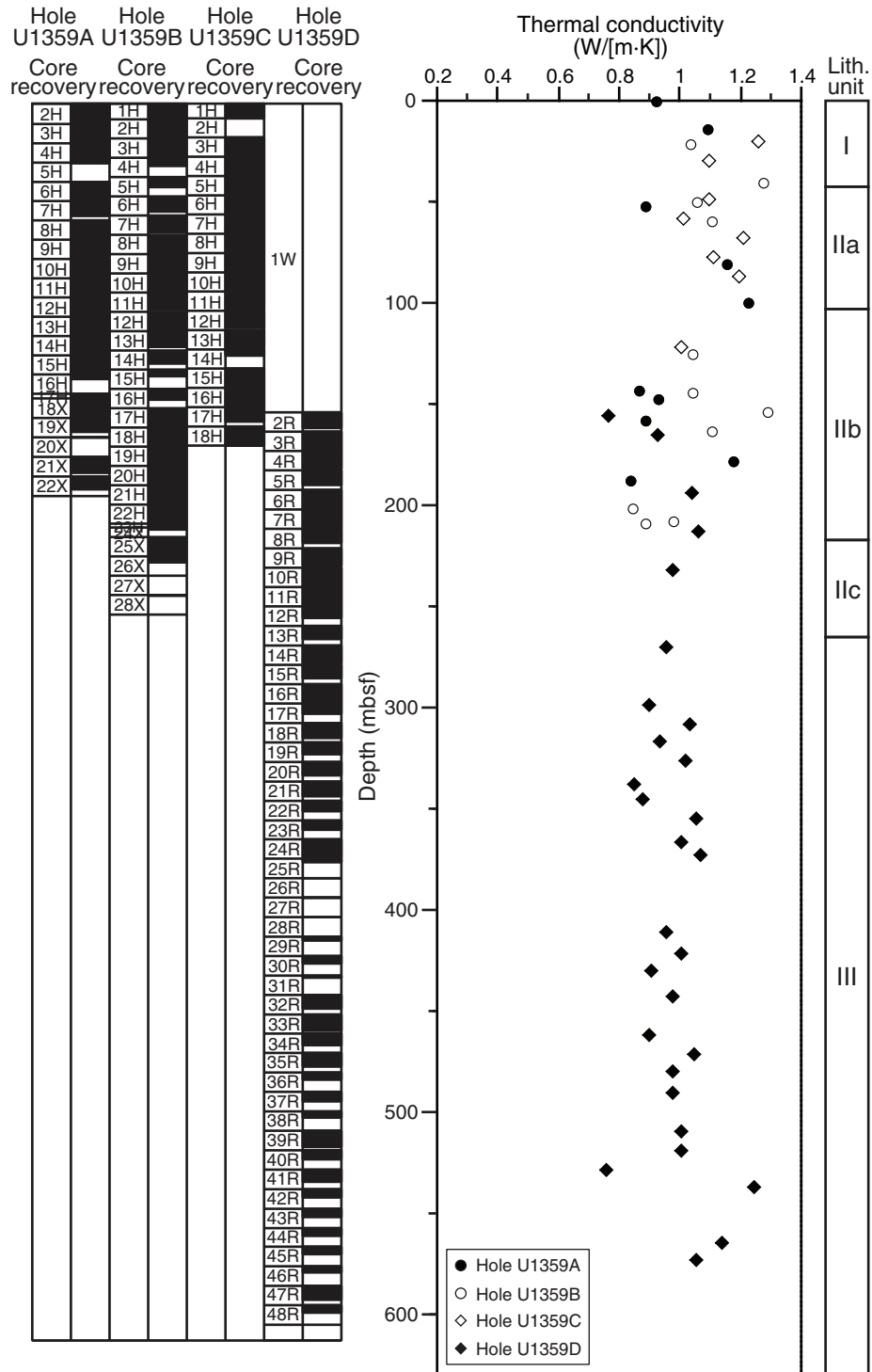




Figure F61. Natural gamma radiation (NGR) data and spliced record, Site U1359. Data offset: Hole U1359A = 50 cps, Hole U1359B = 100 cps, Hole U1359C = 100, Hole U1359D = 200 cps.

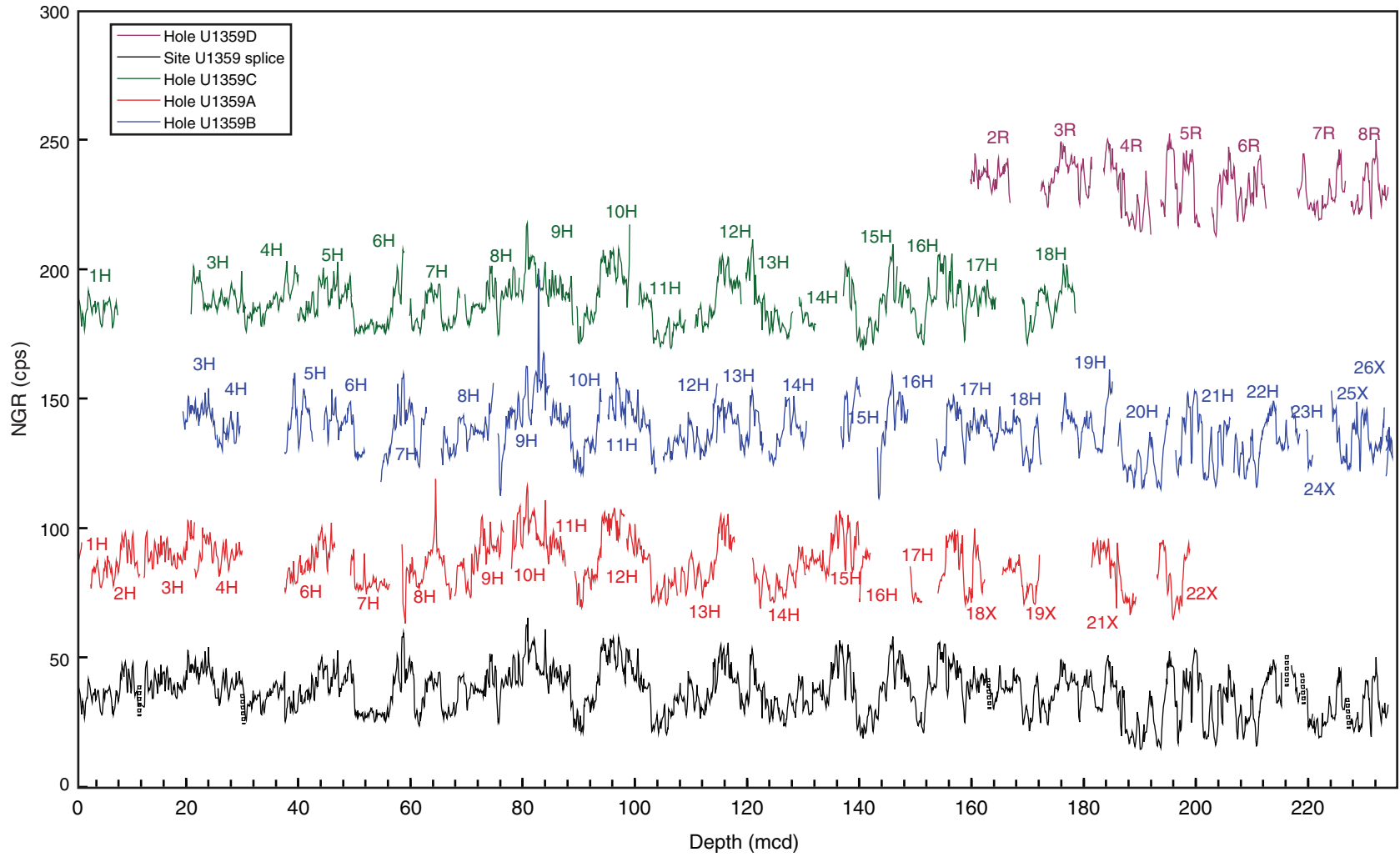




Figure F62. Gamma ray attenuation (GRA) bulk density data and spliced record, Site U1359. Data offset: Hole U1359A = 0.4 g/cm³, Hole U1359B = 0.8 g/cm³, Hole U1359C = 1.3 g/cm³, Hole U1359D = 1.6 g/cm³.

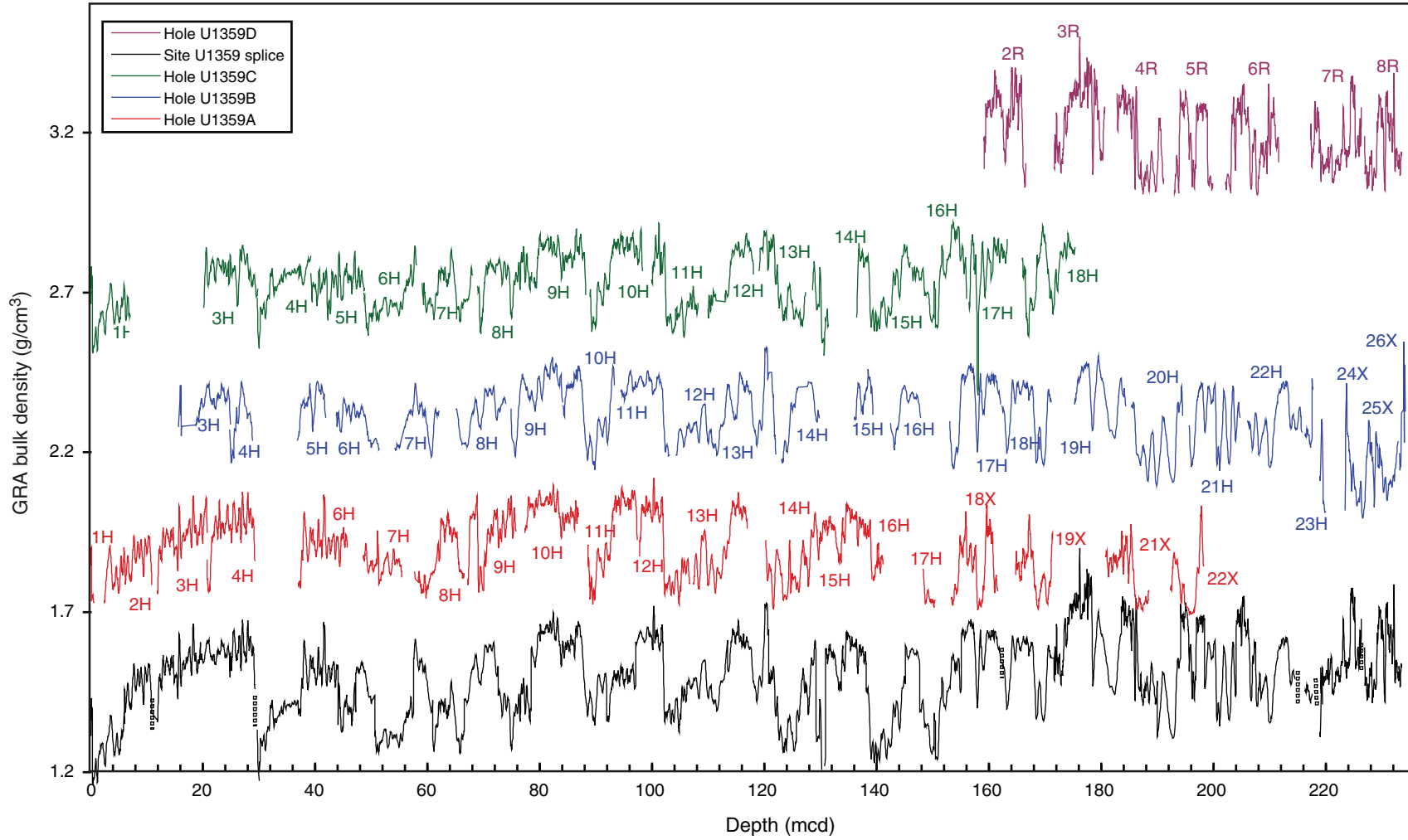




Figure F63. Magnetic susceptibility data and spliced record, Site U1359. Data offset: Hole U1359A = 100 instrument units, Hole U1359B = 200 instrument units, Hole U1359C = 300 instrument units, Hole U1359D = 400 instrument units.

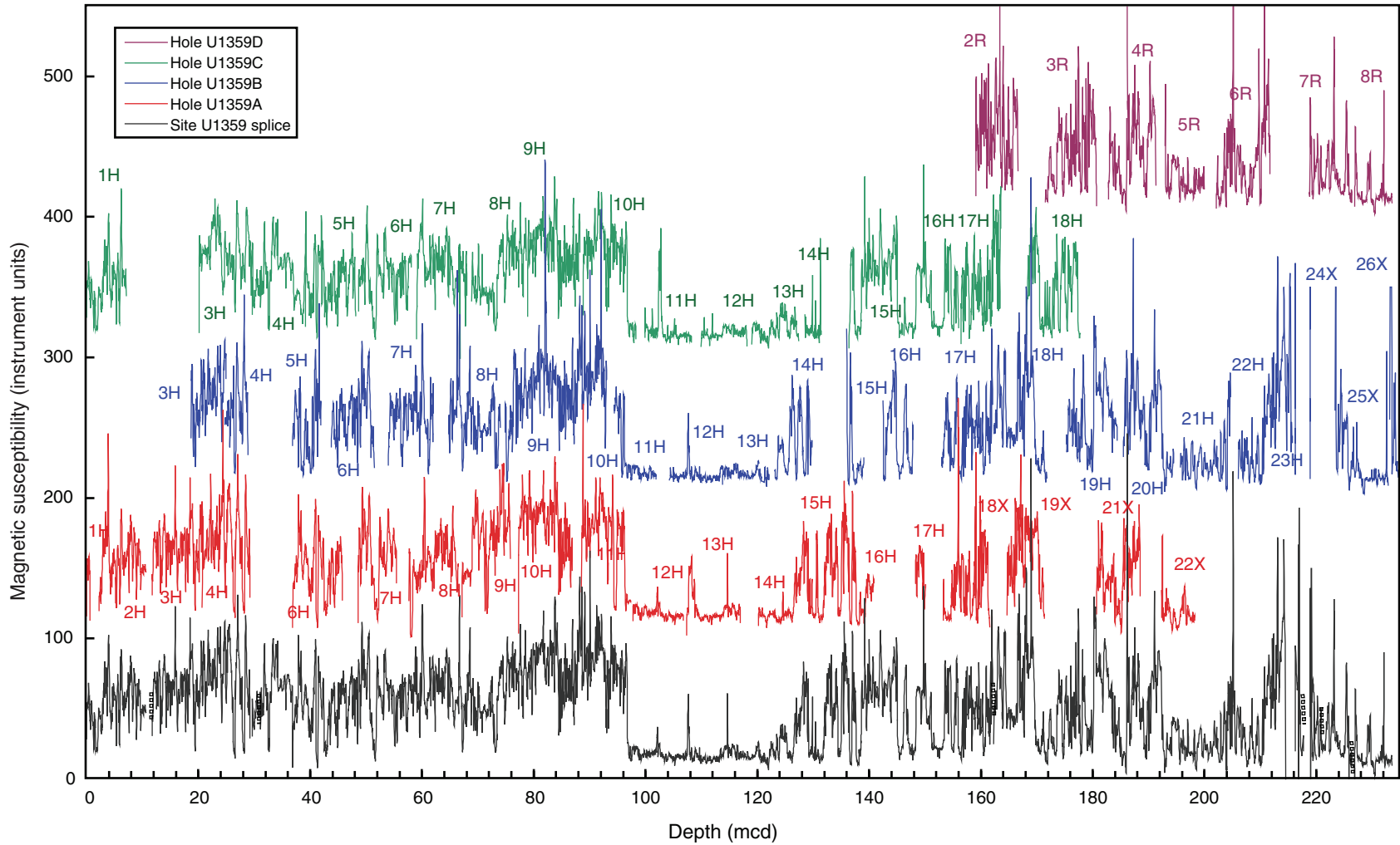


Figure F64. Plots of meters below seafloor vs. meters composite depth growth rates, Site U1359. A. Hole U1359A. (Continued on next two pages.)

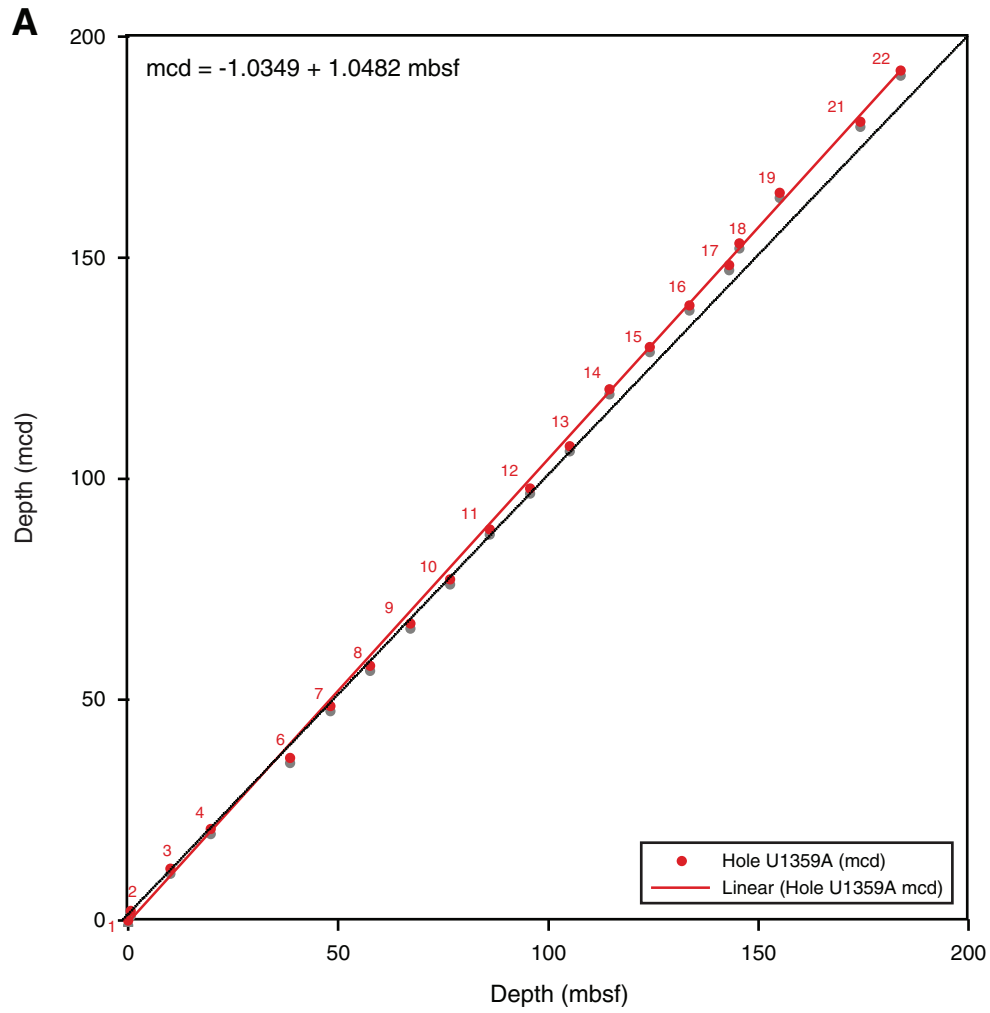


Figure F64 (continued). B. Hole U1359B. (Continued on next page.)

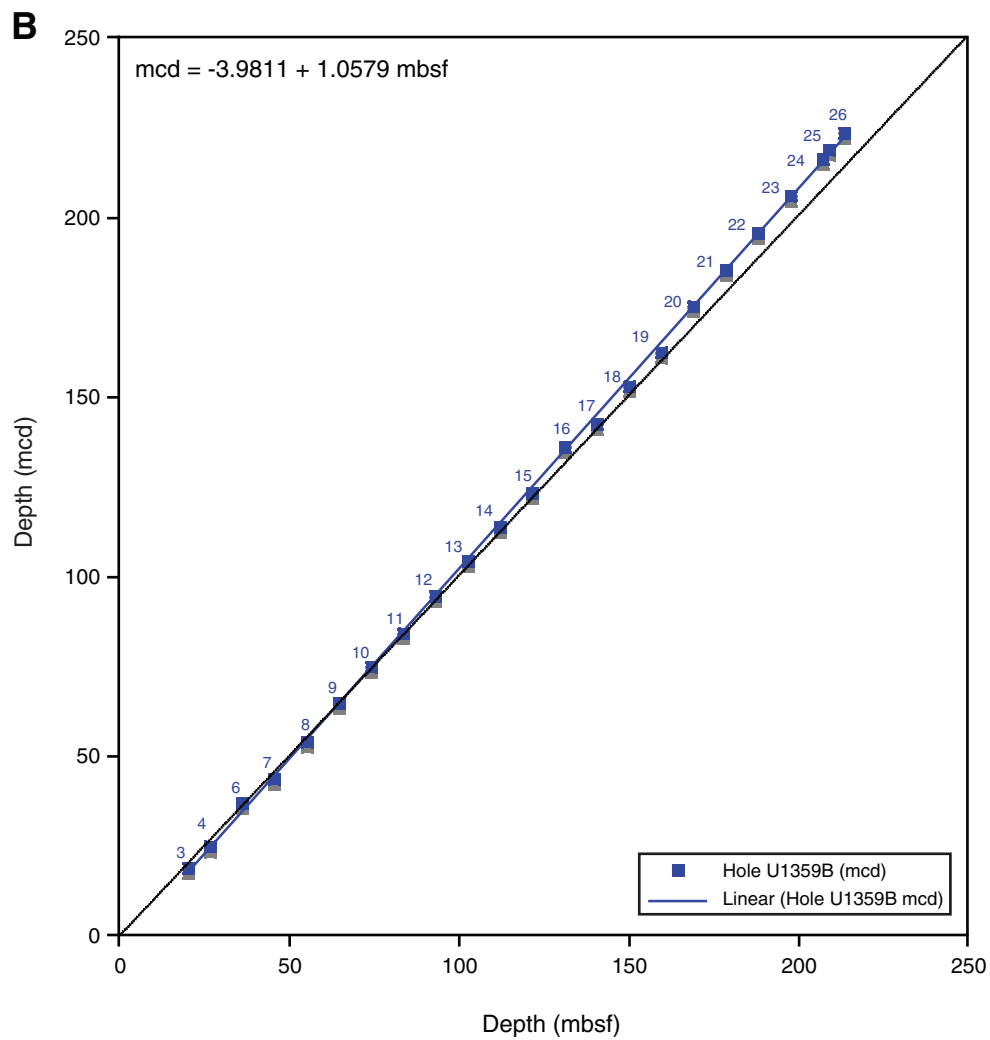


Figure F64 (continued). C. Hole U1359C.

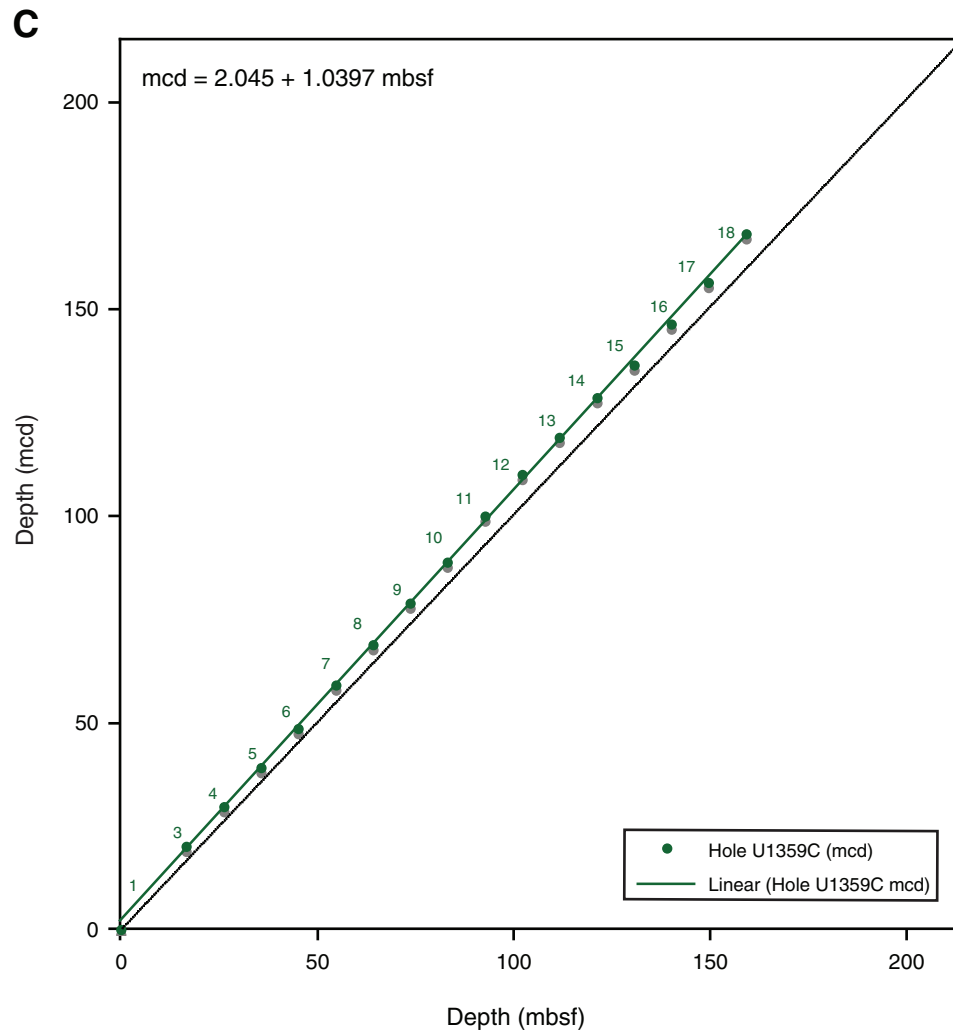


Figure F65. Logging operations summary diagram, with the wireline depths of different logging passes in the borehole. Drillers and core depths for this hole are ~5 m shallower (see text). Triple combo = triple combination, FMS = Formation MicroScanner.

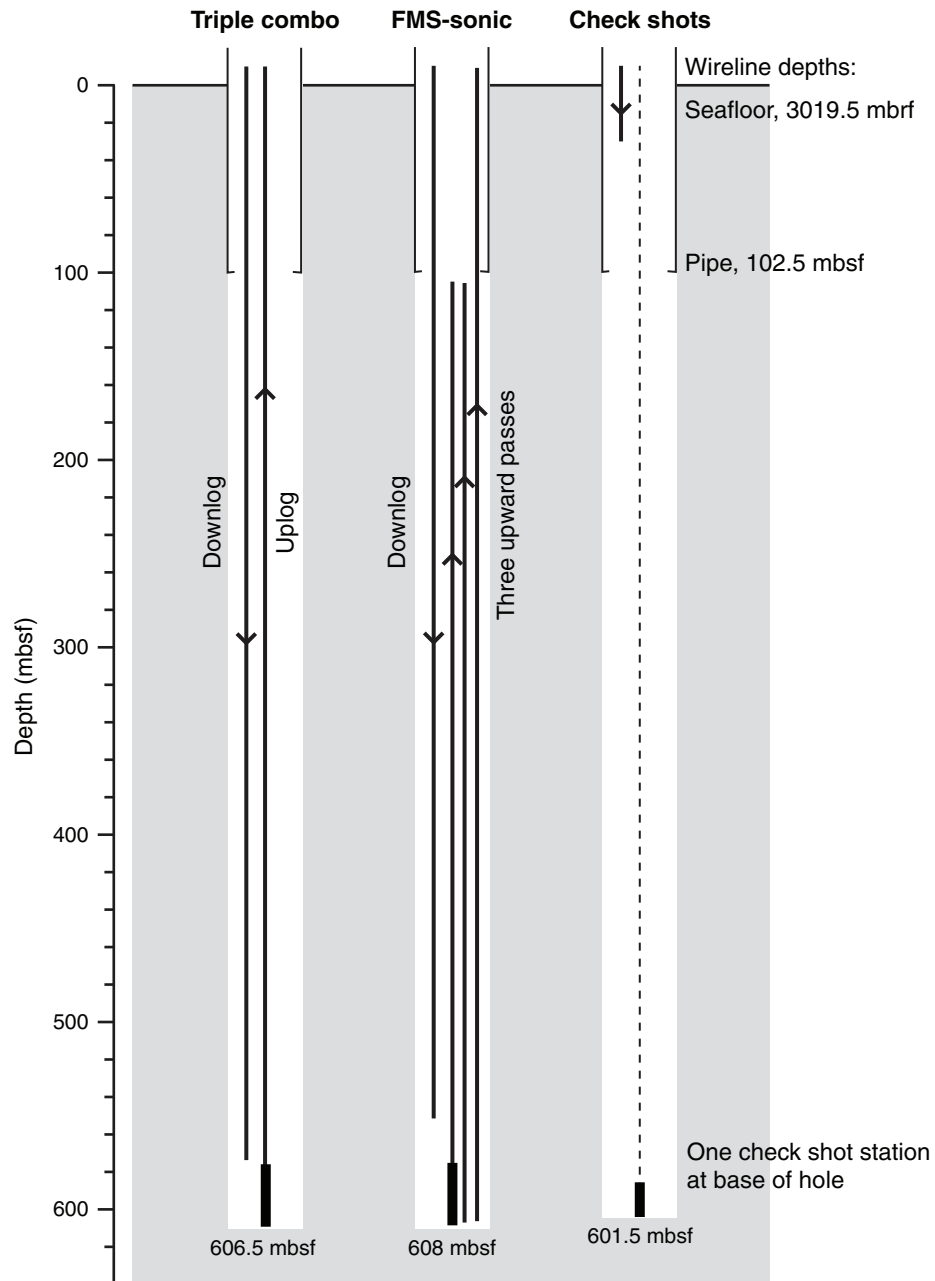


Figure F66. Natural gamma radiation (NGR) logs, Hole U1359D. Core data have been shifted down by ~5 m to give a better depth match to the log data. HSGR = total spectral gamma ray.

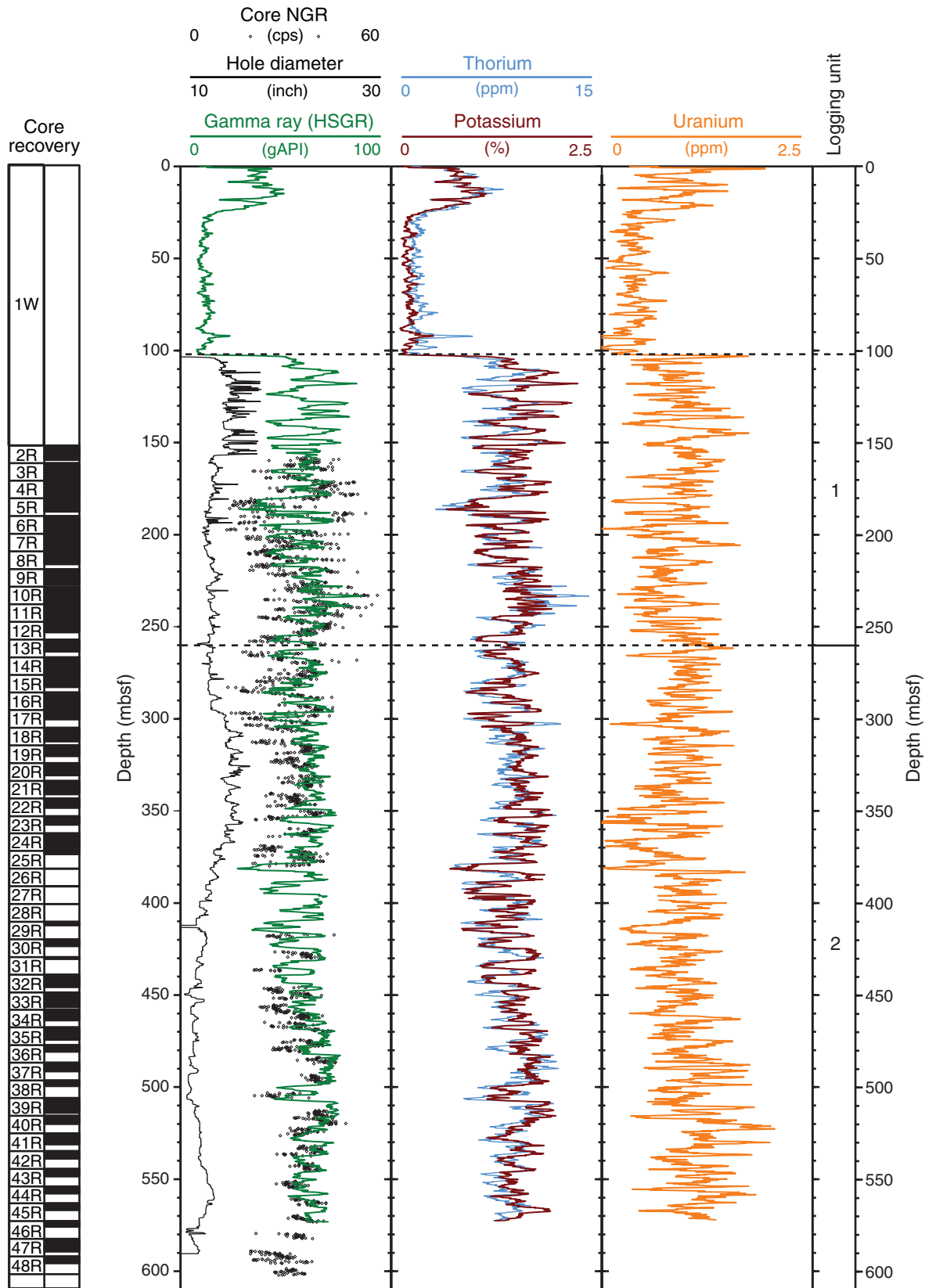


Figure F67. Comparison of downhole natural gamma radiation (NGR) and bulk density logs from 360 to 400 mbsf, with lithology, gamma ray attenuation (GRA) density, and NGR from Cores 318-U1359D-24R and 25R. Diatom-rich layers can be identified in the log data. Note that Core 25R would be moved downward by 3 m to match the log data. The nannofossil-rich sediments at the base of Core 318-U1359D-24R and the top of Core 25R appear to be part of a thicker nannofossil-rich interval. HSGR = total spectral gamma ray, RHOM = bulk density, HROM = high-resolution bulk density.

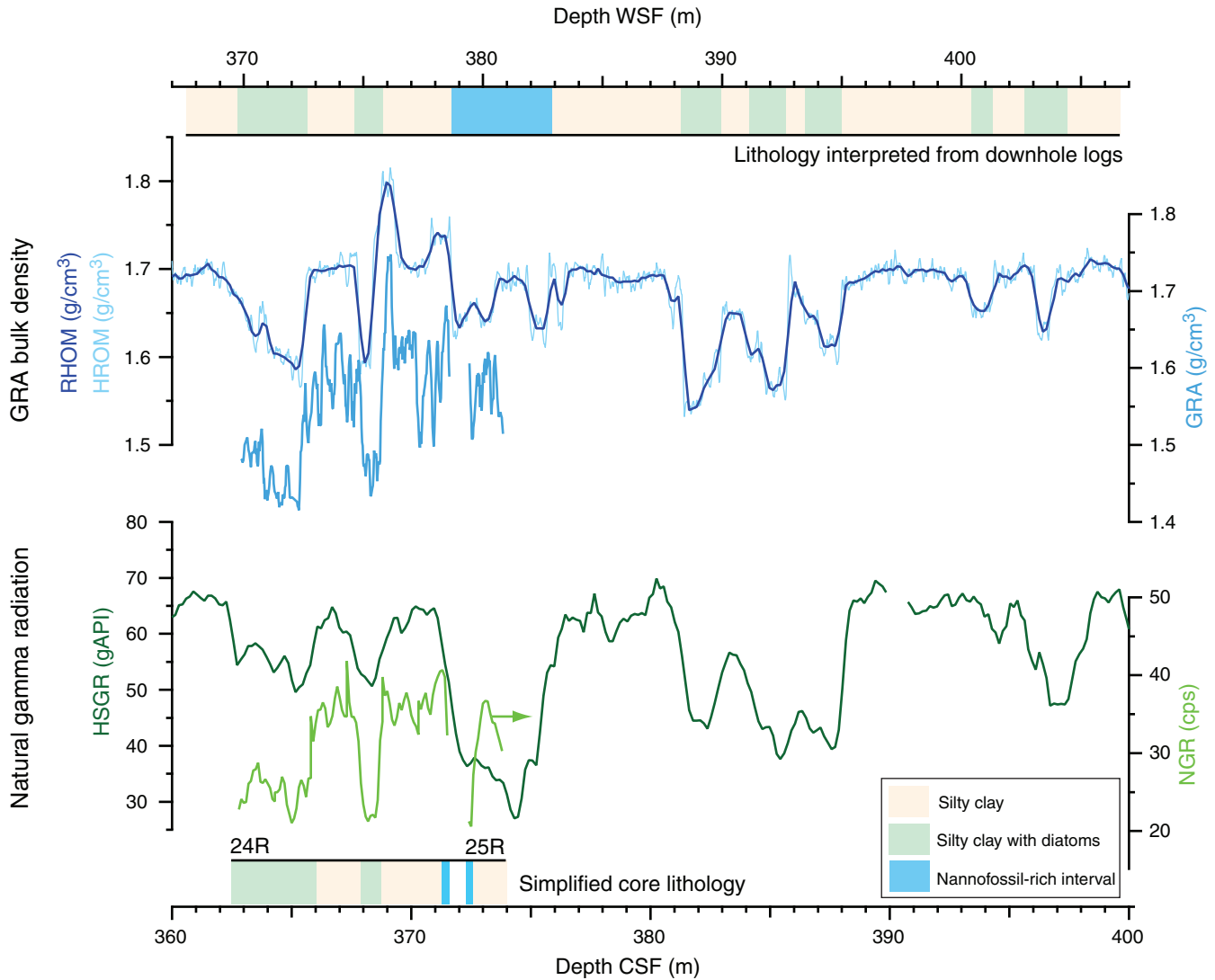


Figure F68. Examples of Formation MicroScanner (FMS) images, Hole U1359D. **A.** Centimeter-scale dropstones. **B.** A dropstone 20 cm in diameter. **C.** Resistive beds, dipping to the east and west, near the base of the hole.

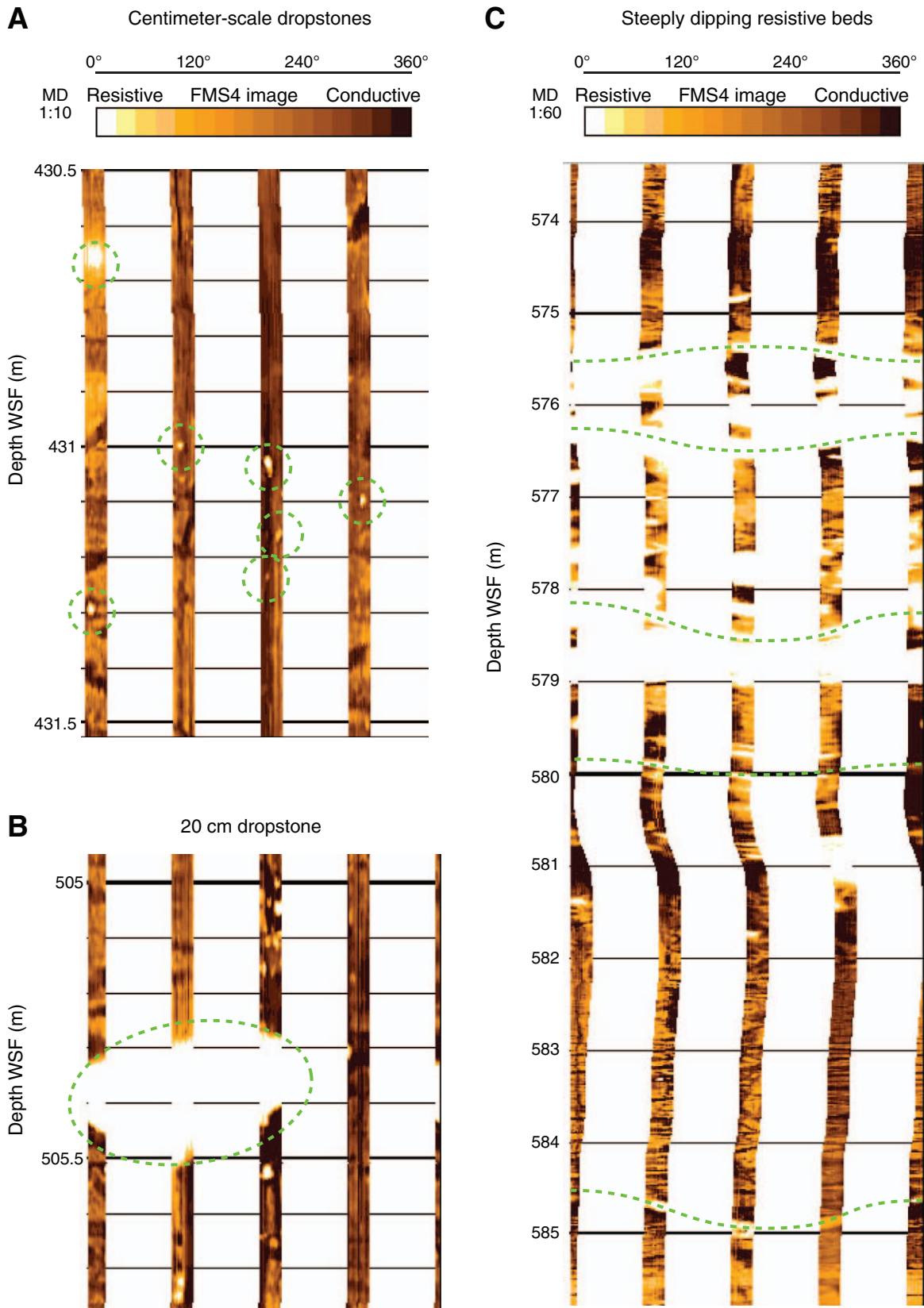


Figure F69. Plot of compressional wave velocity measurements, Site U1359.

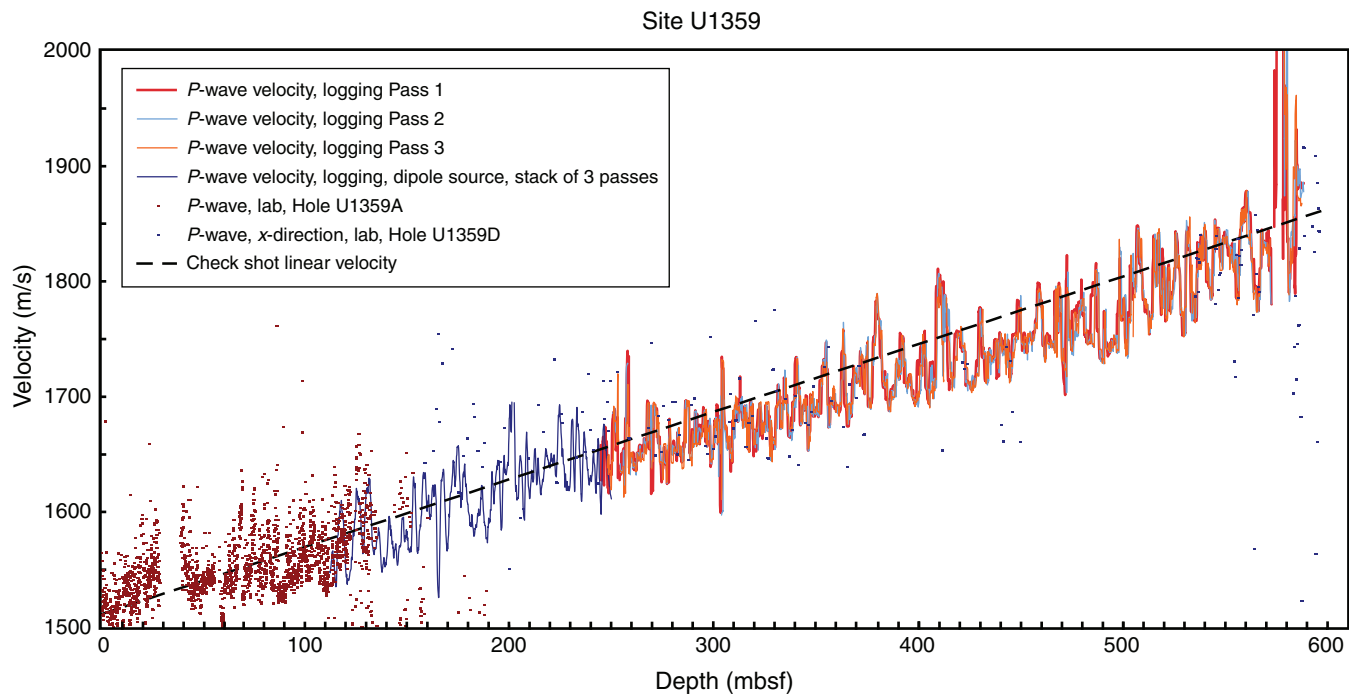


Figure F70. Plots of heat flow calculations, Hole U1359A. **A.** Advanced piston corer temperature tool (APCT-3) sediment temperatures in Hole U1359A. **B.** Temperature gradient. **C.** Bullard plot in which heat flow is calculated from a linear fit of the temperature data.

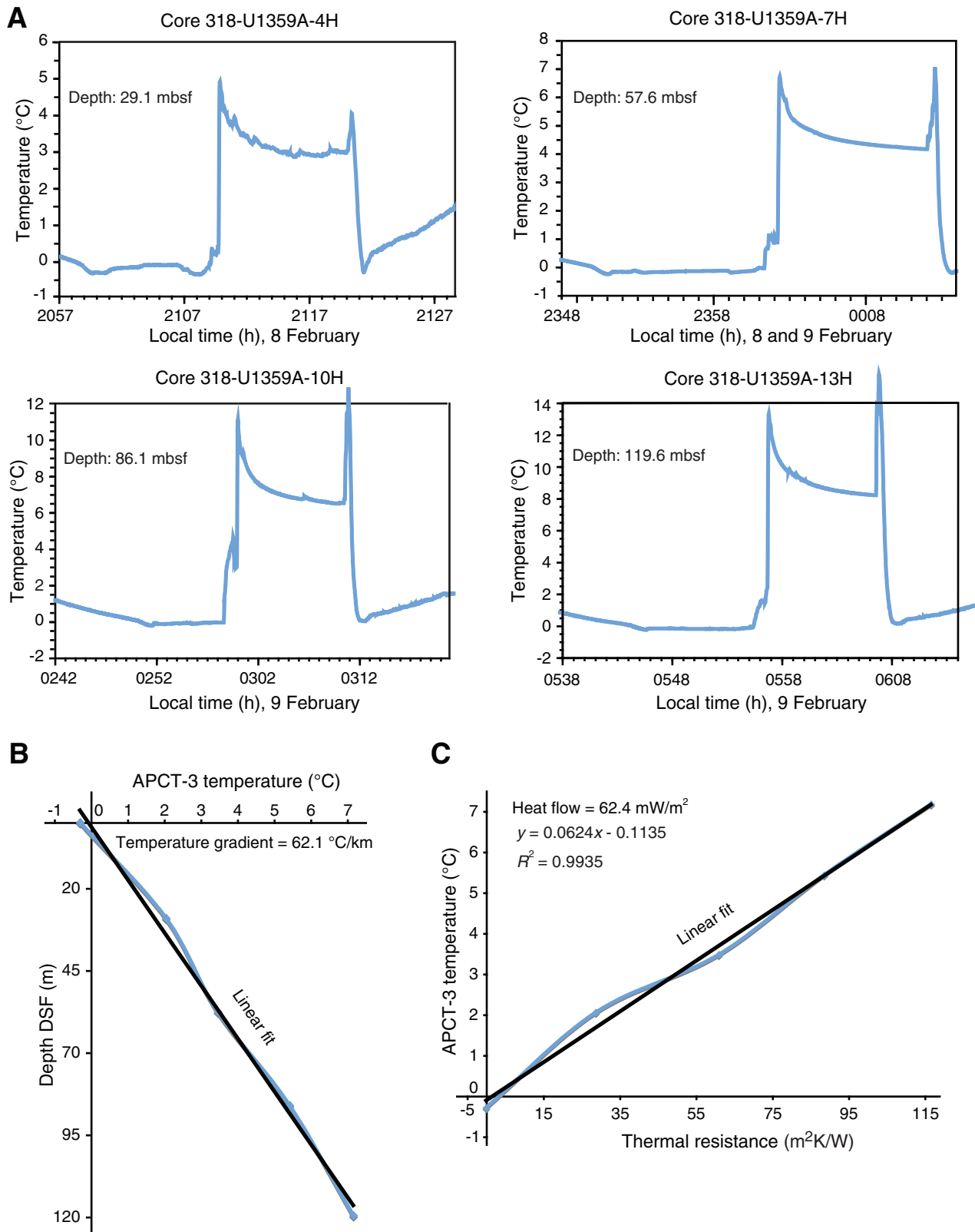


Table T1. Coring summary, Site U1359. (See table notes.) (Continued on next two pages.)

Site U1359

Time on site (h): 209.75

Holes U1359A, U1359B, and U1359C

89.25 (0700 h, 8 February–0015 h, 12 February 2010)

Hole U1359D

120.50 (2215 h, 19 February–2245 h, 24 February 2010)

Hole U1359A

Latitude: 64°54.2377'S

Longitude: 143°57.6825'E

Time on hole (h): 34.00 (0700 h, 8 February–1700 h, 9 February 2010)

Seafloor (drill pipe measurement from rig floor, m DRF): 3020.9

Distance between rig floor and sea level (m): 11.1

Water depth (drill pipe measurement from sea level, m): 3009.9

Total penetration (m DSF): 193.5

Total depth (drill pipe measurement from rig floor, m DRF): 3214.4

Total length of cored section (m): 193.5

Total core recovered (m): 154.1

Core recovery (%): 80

Total number of cores: 22

Hole U1359B

Latitude: 64°54.2431'S

Longitude: 143°57.6553'E

Time on hole (h): 29.67 (1700 h, 9 February–2240 h, 10 February 2010)

Seafloor (drill pipe measurement from rig floor, m DRF): 3018.8

Distance between rig floor and sea level (m): 11.1

Water depth (drill pipe measurement from sea level, m): 3007.7

Total penetration (m DSF): 252.0

Total depth (drill pipe measurement from rig floor, m DRF): 3270.8

Total length of cored section (m): 252.0

Total core recovered (m): 198.92

Core recovery (%): 79

Total number of cores: 28

Hole U1359C

Latitude: 64°54.2477'S

Longitude: 143°57.6248'E

Time on hole (h): 25.58 (2240 h, 10 February–0015 h, 12 February 2010)

Seafloor (drill pipe measurement from rig floor, m DRF): 3022.3

Distance between rig floor and sea level (m): 11.1

Water depth (drill pipe measurement from sea level, m): 3011.1

Total penetration (m DSF): 168.7

Total depth (drill pipe measurement from rig floor, m DRF): 3191.0

Total length of cored section (m): 168.7

Total core recovered (m): 150.73

Core recovery (%): 89

Total number of cores: 18

Hole U1359D

Latitude: 64°54.2596'S

Longitude: 143°57.5624'E

Time on hole (h): 120.5 (2215 h, 19 February–2245 h, 24 February 2010)

Seafloor (drill pipe measurement from rig floor, m DRF): 3023.0

Distance between rig floor and sea level (m): 11.1

Water depth (drill pipe measurement from sea level, m): 3011.9

Total penetration (m DSF): 602.2

Total depth (drill pipe measurement from rig floor, m DRF): 3625.2

Total length of cored section (m): 450.0

Total core recovered (m): 269.72

Core recovery (%): 60

Total number of cores: 47

Core	Date (2010)	Local time (h)	Depth DSF-B (m)			Depth CSF-A (m)		Length of core recovered (m)	Recovery (%)
			Top of cored interval	Bottom of cored interval	Interval advanced (m)	Top of cored interval	Bottom of cored interval		
318-U1359A-									
1H	8 Feb	1820	0.0	0.6	0.6	0.00	0.67	0.67	112
2H	8 Feb	1920	0.6	10.1	9.5	0.60	9.54	8.94	94
3H	8 Feb	2000	10.1	19.6	9.5	10.10	19.32	9.22	97
4H	8 Feb	2100	19.6	29.1	9.5	19.60	28.56	8.96	94

Table T1 (continued). (Continued on next page.)

Core	Date (2010)	Local time (h)	Depth DSF-B (m)			Depth CSF-A (m)		Length of core recovered (m)	Recovery (%)
			Top of cored interval	Bottom of cored interval	Interval advanced (m)	Top of cored interval	Bottom of cored interval		
5H	8 Feb	2140	29.1	38.6	9.5	29.10	29.34	0.24	3
6H	8 Feb	2230	38.6	48.1	9.5	38.60	47.73	9.13	96
7H	8 Feb	2330	48.1	57.6	9.5	48.10	55.37	7.27	77
8H	9 Feb	0025	57.6	67.1	9.5	57.60	66.60	9.00	95
9H	9 Feb	0120	67.1	76.6	9.5	67.10	75.80	8.70	92
10H	9 Feb	0220	76.6	86.1	9.5	76.60	86.56	9.96	105
11H	9 Feb	0305	86.1	95.6	9.5	86.10	95.22	9.12	96
12H	9 Feb	0355	95.6	105.1	9.5	95.60	104.89	9.29	98
13H	9 Feb	0455	105.1	114.6	9.5	105.10	115.05	9.95	105
14H	9 Feb	0545	114.6	124.1	9.5	114.60	124.26	9.66	102
15H	9 Feb	0630	124.1	133.6	9.5	124.10	133.70	9.60	101
16H	9 Feb	0715	133.6	143.1	9.5	133.60	135.80	2.20	23
17H	9 Feb	0815	143.1	145.4	2.3	143.10	145.46	2.36	103
18X	9 Feb	1045	145.4	155.0	9.6	145.40	153.96	8.56	89
19X	9 Feb	1205	155.0	164.6	9.6	155.00	161.88	6.88	72
20X	9 Feb	1255	164.6	174.2	9.6	164.60	164.65	0.05	1
21X	9 Feb	1355	174.2	183.9	9.7	174.20	182.16	7.96	82
22X	9 Feb	1450	183.9	193.5	9.6	183.90	190.26	6.36	66
Cored totals:					193.5			154.08	80
Total interval cored:					193.5				
318-U1359B-									
1H	9 Feb	1835	0.0	7.7	7.7	0.00	7.74	7.74	101
2H	9 Feb	1930	7.7	17.2	9.5	7.70	16.85	9.15	96
3H	9 Feb	2010	17.2	26.7	9.5	17.20	26.73	9.53	100
4H	9 Feb	2050	26.7	36.2	9.5	26.70	31.13	4.43	47
5H	9 Feb	2135	36.2	45.7	9.5	36.20	41.60	5.40	57
6H	9 Feb	2215	45.7	55.2	9.5	45.70	53.67	7.97	84
7H	9 Feb	2335	55.2	64.7	9.5	55.20	63.52	8.32	88
8H	10 Feb	0040	64.7	74.2	9.5	64.70	74.22	9.52	100
9H	10 Feb	0125	74.2	83.7	9.5	74.20	83.78	9.58	101
10H	10 Feb	0205	83.7	93.2	9.5	83.70	93.14	9.44	99
11H	10 Feb	0250	93.2	102.7	9.5	93.20	101.97	8.77	92
12H	10 Feb	0345	102.7	112.2	9.5	102.70	112.55	9.85	104
13H	10 Feb	0430	112.2	121.7	9.5	112.20	120.32	8.12	85
14H	10 Feb	0525	121.7	131.2	9.5	121.70	128.67	6.97	73
15H	10 Feb	0610	131.2	140.7	9.5	131.20	134.84	3.64	38
16H	10 Feb	0655	140.7	150.2	9.5	140.70	146.35	5.65	59
17H	10 Feb	0750	150.2	159.7	9.5	150.20	159.54	9.34	98
18H	10 Feb	0835	159.7	169.2	9.5	159.70	169.24	9.54	100
19H	10 Feb	0925	169.2	178.7	9.5	169.20	178.59	9.39	99
20H	10 Feb	1015	178.7	188.2	9.5	178.70	188.12	9.42	99
21H	10 Feb	1105	188.2	197.7	9.5	188.20	198.15	9.95	105
22H	10 Feb	1155	197.7	207.2	9.5	197.70	207.73	10.03	106
23H	10 Feb	1245	207.2	209.0	1.8	207.20	209.04	1.84	102
24X	10 Feb	1510	209.0	213.7	4.7	209.00	210.46	1.46	31
25X	10 Feb	1605	213.7	223.3	9.6	213.70	223.36	9.66	101
26X	10 Feb	1700	223.3	232.8	9.5	223.30	226.64	3.34	35
27X	10 Feb	1820	232.8	242.4	9.6	232.80	232.96	0.16	2
28X	10 Feb	1930	242.4	252.0	9.6	242.40	243.11	0.71	7
Cored totals:					252.0			198.92	79
Total interval cored:					252.0				
318-U1359C-									
1H	11 Feb	0005	0.0	7.2	7.2	0.00	7.25	7.25	101
2H	11 Feb	0105	7.2	16.7	9.5	7.20	7.20	0.00	0
3H	11 Feb	0230	16.7	26.2	9.5	16.70	26.60	9.90	104
4H	11 Feb	0320	26.2	35.7	9.5	26.20	36.03	9.83	103
5H	11 Feb	0405	35.7	45.2	9.5	35.70	45.62	9.92	104
6H	11 Feb	0500	45.2	54.7	9.5	45.20	54.88	9.68	102
7H	11 Feb	0540	54.7	64.2	9.5	54.70	63.94	9.24	97
8H	11 Feb	0625	64.2	73.7	9.5	64.20	74.20	10.00	105
9H	11 Feb	0710	73.7	83.2	9.5	73.70	83.25	9.55	101
10H	11 Feb	0800	83.2	92.7	9.5	83.20	92.90	9.70	102
11H	11 Feb	0850	92.7	102.2	9.5	92.70	101.32	8.62	91
12H	11 Feb	0935	102.2	111.7	9.5	102.20	110.61	8.41	89
13H	11 Feb	1025	111.7	121.2	9.5	111.70	120.29	8.59	90
14H	11 Feb	1115	121.2	130.7	9.5	121.20	124.28	3.08	32

Table T1 (continued).

Core	Date (2010)	Local time (h)	Depth DSF-B (m)			Depth CSF-A (m)		Length of core recovered (m)	Recovery (%)
			Top of cored interval	Bottom of cored interval	Interval advanced (m)	Top of cored interval	Bottom of cored interval		
15H	11 Feb	1205	130.7	140.2	9.5	130.70	140.61	9.91	104
16H	11 Feb	1250	140.2	149.7	9.5	140.20	150.24	10.04	106
17H	11 Feb	1340	149.7	159.2	9.5	149.70	156.87	7.17	75
18H	11 Feb	1425	159.2	168.7	9.5	159.20	169.04	9.84	104
					Cored totals:	168.7		150.73	89
					Total interval cored:	168.7			
			Depth DSF-A (m)						
			Top of cored interval	Bottom of cored interval					
318-U1359D-									
1W	20 Feb	1150	0.0	152.2	152.2	0.00	0.15	0.15	0
2R	20 Feb	1250	152.2	161.8	9.6	152.20	159.95	7.75	81
3R	20 Feb	1335	161.8	171.3	9.5	161.80	171.12	9.32	98
4R	20 Feb	1420	171.3	180.9	9.6	171.30	180.00	8.70	91
5R	20 Feb	1510	180.9	190.5	9.6	180.90	188.07	7.17	75
6R	20 Feb	1555	190.5	200.1	9.6	190.50	200.32	9.82	102
7R	20 Feb	1640	200.1	209.7	9.6	200.10	209.40	9.30	97
8R	20 Feb	1730	209.7	219.3	9.6	209.70	216.64	6.94	72
9R	20 Feb	1815	219.3	228.9	9.6	219.30	227.73	8.43	88
10R	20 Feb	1900	228.9	238.4	9.5	228.90	238.77	9.87	104
11R	20 Feb	1945	238.4	248.0	9.6	238.40	248.22	9.82	102
12R	20 Feb	2035	248.0	257.6	9.6	248.00	253.66	5.66	59
13R	20 Feb	2125	257.6	267.2	9.6	257.60	264.06	6.46	67
14R	20 Feb	2215	267.2	276.8	9.6	267.20	276.07	8.87	92
15R	20 Feb	2300	276.8	286.3	9.5	276.80	283.43	6.63	70
16R	20 Feb	2355	286.3	295.9	9.6	286.30	295.95	9.65	101
17R	21 Feb	0105	295.9	305.5	9.6	295.90	300.99	5.09	53
18R	21 Feb	0210	305.5	315.1	9.6	305.50	312.90	7.40	77
19R	21 Feb	0325	315.1	324.7	9.6	315.10	320.83	5.73	60
20R	21 Feb	0420	324.7	334.3	9.6	324.70	331.36	6.66	69
21R	21 Feb	0555	334.3	343.9	9.6	334.30	341.57	7.27	76
22R	21 Feb	0655	343.9	353.5	9.6	343.90	348.94	5.04	52
23R	21 Feb	0810	353.5	362.8	9.3	353.50	358.14	4.64	50
24R	21 Feb	0910	362.8	372.4	9.6	362.80	371.86	9.06	94
25R	21 Feb	1010	372.4	382.0	9.6	372.40	374.11	1.71	18
26R	21 Feb	1115	382.0	391.6	9.6	382.00	382.00	0.00	0
27R	21 Feb	1220	391.6	401.2	9.6	391.60	391.62	0.02	0
28R	21 Feb	1320	401.2	410.8	9.6	401.20	401.20	0.00	0
29R	21 Feb	1430	410.8	420.4	9.6	410.80	412.83	2.03	21
30R	21 Feb	1520	420.4	430.0	9.6	420.40	424.08	3.68	38
31R	21 Feb	1615	430.0	439.6	9.6	430.00	431.04	1.04	11
32R	21 Feb	1710	439.6	449.2	9.6	439.60	446.36	6.76	70
33R	21 Feb	1805	449.2	458.7	9.5	449.20	457.23	8.03	85
34R	21 Feb	1900	458.7	468.2	9.5	458.70	464.36	5.66	60
35R	21 Feb	2000	468.2	477.8	9.6	468.20	474.91	6.71	70
36R	21 Feb	2100	477.8	487.4	9.6	477.80	481.38	3.58	37
37R	21 Feb	2150	487.4	497.0	9.6	487.40	492.02	4.62	48
38R	21 Feb	2250	497.0	506.6	9.6	497.00	500.08	3.08	32
39R	21 Feb	2350	506.6	516.2	9.6	506.60	514.51	7.91	82
40R	22 Feb	0055	516.2	525.8	9.6	516.20	520.60	4.40	46
41R	22 Feb	0205	525.8	535.4	9.6	525.80	531.72	5.92	62
42R	22 Feb	0310	535.4	545.0	9.6	535.40	539.42	4.02	42
43R	22 Feb	0430	545.0	554.6	9.6	545.00	549.09	4.09	43
44R	22 Feb	0530	554.6	563.8	9.2	554.60	558.42	3.82	42
45R	22 Feb	0640	563.8	573.4	9.6	563.80	567.44	3.64	38
46R	22 Feb	0750	573.4	583.0	9.6	573.40	576.45	3.05	32
47R	22 Feb	0940	583.0	592.6	9.6	583.00	589.96	6.96	72
48R	22 Feb	1145	592.6	602.2	9.6	592.60	596.31	3.71	39
					Cored totals:	602.2		269.72	60
					Total interval cored:	450.0			

Notes: DRF = drilling depth below rig floor. DSF-A = drilling depth below seafloor determined by tagging seafloor, DSF-B = drilling depth below seafloor determined by mudline core recovery, CSF-A = core depth below seafloor, overlap if long. Local time = UTC + 11 h.

Table T2. Unit boundary depths as identified in each of the Site U1359 holes and correlation of these depths to meters composite depth. (See table notes.)

	Depth (mbsf)				Depth (mcd)
	Hole U1359A	Hole U1359B	Hole U1359C	Hole U1359D	
Unit I (T)	0.00	<7.58*	0.00	Not cored	0.00
Subunit IIa (T)	43.54	>41.60*	38.64	Not cored	42.07
Subunit IIb (T)	99.87	100.85	95.17	Not cored	102.10
Subunit IIc (T)	Not cored	208.18	Not cored	200.10	217.24
Unit III (T)	Not cored	Not cored	Not cored	247.10	264.24
Unit III (B)	Not cored	Not cored	Not cored	596.32	613.46

Notes: * = unit boundary was not recovered. T = top, B = bottom.

Table T3. Siliceous microfossil abundance and preservation, Hole U1359A. This table is available in an [oversized format](#).

Table T4. Siliceous microfossil abundance and preservation, Hole U1359B. This table is available in an [oversized format](#).

Table T6. Siliceous microfossil abundance and preservation, Hole U1359D. This table is available in an [over-sized format](#).**Table T7.** Radiolarian age constraints, Site U1359. (See table note.) (Continued on next page.)

Core, section	Depth (mbsf)	Minimum age constraint	Age (Ma)	Maximum age constraint	Age (Ma)
318-U1359A-					
1H-CC	0.67			LO <i>Antarctissa cylindrica</i>	0.6
2H-CC	9.54			LO <i>Antarctissa cylindrica</i>	0.6
3H-CC	19.32	LO <i>Antarctissa cylindrica</i>	0.6	LO <i>Pterocanium charybdenum trilobum</i>	0.8
4H-CC	28.56	LO <i>Pterocanium charybdenum trilobum</i>	0.8	LO <i>Eucyrtidium calvertense</i>	1.9
5H-CC	29.34	LO <i>Pterocanium charybdenum trilobum</i>	0.8	LO <i>Eucyrtidium calvertense</i>	1.9
6H-CC	47.73	FO <i>Cycladophora davisiana</i>	2.6	FO <i>Helotholus vema</i>	4.2
7H-CC	55.37	FO <i>Cycladophora davisiana</i>	2.6	FO <i>Helotholus vema</i>	4.2
8H-CC	66.60	FO <i>Cycladophora davisiana</i>	2.6	FO <i>Helotholus vema</i>	4.2
9H-CC	75.80	LO <i>Desmospyris spongiosa</i>	2.3	LCO <i>Lychnocanium grande</i>	5
10H-CC	86.56				
11H-CC	95.22	LO <i>Desmospyris spongiosa</i>	2.3	LCO <i>Lychnocanium grande</i>	5
12H-CC	104.89	LO <i>Eucyrtidium pseudoinflatum</i>	4.2	LCO <i>Lychnocanium grande</i>	5
13H-CC	115.05	LO <i>Desmospyris spongiosa</i>	2.3	LO <i>Cycladophora spongothrax</i>	9.1
14H-CC	124.26	LCO <i>Lychnocanium grande</i>	5	LO <i>Cycladophora spongothrax</i>	9.1
15H-CC	133.70	LCO <i>Lychnocanium grande</i>	5	LO <i>Cycladophora spongothrax</i>	9.1
16H-CC	135.80	LCO <i>Lychnocanium grande</i>	5	LO <i>Cycladophora spongothrax</i>	9.1
17H-CC	145.43	LCO <i>Lychnocanium grande</i>	5	LO <i>Cycladophora spongothrax</i>	9.1
18X-CC	153.96	LCO <i>Lychnocanium grande</i>	5	LO <i>Cycladophora spongothrax</i>	9.1
19X-CC	161.88	LCO <i>Lychnocanium grande</i>	5	LO <i>Cycladophora spongothrax</i>	9.1
21X-CC	182.07	LCO <i>Lychnocanium grande</i>	5	LO <i>Cycladophora spongothrax</i>	9.1
22X-CC	190.26	LCO <i>Lychnocanium grande</i>	5	LO <i>Cycladophora spongothrax</i>	9.1
318-U1359B-					
4H-CC	31.13			LO <i>Antarctissa cylindrica</i>	0.6
5H-CC	41.55	LO <i>Antarctissa cylindrica</i>	0.6	LO <i>Desmospyris spongiosa</i>	2.3
7H-CC	63.39	LO <i>Desmospyris spongiosa</i>	2.3	LCO <i>Lychnocanium grande</i>	5
8H-CC	74.22	LO <i>Desmospyris spongiosa</i>	2.3	LCO <i>Lychnocanium grande</i>	5
10H-CC	93.14	LO <i>Desmospyris spongiosa</i>	2.3	LCO <i>Lychnocanium grande</i>	5
11H-CC	101.97	LO <i>Eucyrtidium pseudoinflatum</i>	4.2	LCO <i>Lychnocanium grande</i>	5
12H-CC	112.60				
13H-CC	120.30	LO <i>Eucyrtidium pseudoinflatum</i>	4.2	LCO <i>Lychnocanium grande</i>	5
14H-CC	128.67	LO <i>Eucyrtidium pseudoinflatum</i>	4.2	LCO <i>Lychnocanium grande</i>	5
15H-CC	134.84	LO <i>Eucyrtidium pseudoinflatum</i>	4.2	LCO <i>Lychnocanium grande</i>	5
16H-CC	146.35				
17H-CC	159.54	LO <i>Eucyrtidium pseudoinflatum</i>	4.2	LCO <i>Lychnocanium grande</i>	5
18H-CC	169.24	LO <i>Eucyrtidium pseudoinflatum</i>	4.2	LCO <i>Lychnocanium grande</i>	5
19H-CC	178.59	LO <i>Eucyrtidium pseudoinflatum</i>	4.2	LCO <i>Lychnocanium grande</i>	5
20H-CC	188.09	LO <i>Amphymenium challengerae</i>	6.2	FO <i>Amphymenium challengerae</i>	6.8
21H-CC	198.15	LO <i>Amphymenium challengerae</i>	6.2	FO <i>Amphymenium challengerae</i>	6.8
22H-CC	207.68	FO <i>Amphymenium challengerae</i>	6.8	FO <i>Acrosphaera? labrata</i>	7.8
23H-CC	208.90	FO <i>Acrosphaera? labrata</i>	7.8	LO <i>Cycladophora spongothrax</i>	9.1
24X-CC	210.46	FO <i>Acrosphaera? labrata</i>	7.8	LO <i>Cycladophora spongothrax</i>	9.1
25X-CC	223.36	LO <i>Cycladophora spongothrax</i>	9.1	FO <i>Acrosphaera australis</i>	10.4
26X-CC	226.64	LO <i>Cycladophora spongothrax</i>	9.1	FO <i>Acrosphaera australis</i>	10.4
28X-CC	243.11	LO <i>Cycladophora spongothrax</i>	9.1	FO <i>Acrosphaera australis</i>	10.4
318-U1359D-					
2R-CC	159.95	LO <i>Eucyrtidium pseudoinflatum</i>	4.2	LCO <i>Lychnocanium grande</i>	5
3R-CC	171.12	LO <i>Eucyrtidium pseudoinflatum</i>	4.2	LCO <i>Lychnocanium grande</i>	5
4R-CC	180.00	LCO <i>Lychnocanium grande</i>	5	FO <i>Cycladophora spongothrax</i>	9.1
5R-CC	188.07	LCO <i>Lychnocanium grande</i>	5	FO <i>Cycladophora spongothrax</i>	9.1
6R-CC	200.32	LCO <i>Lychnocanium grande</i>	5	FO <i>Cycladophora spongothrax</i>	9.1
7R-CC	209.40	LCO <i>Lychnocanium grande</i>	5	FO <i>Cycladophora spongothrax</i>	9.1
8R-CC	216.64	LO <i>Cycladophora spongothrax</i>	9.1	FO <i>Acrosphaera australis</i>	10.4
9R-CC	227.73	LO <i>Cycladophora spongothrax</i>	9.1	FO <i>Acrosphaera australis</i>	10.4
10R-CC	238.77	LO <i>Cycladophora spongothrax</i>	9.1	FO <i>Acrosphaera australis</i>	10.4
11R-CC	248.22	LO <i>Cycladophora spongothrax</i>	9.1	FO <i>Acrosphaera australis</i>	10.4
12R-CC	253.66	LO <i>Cycladophora spongothrax</i>	9.1	FO <i>Acrosphaera australis</i>	10.4
13R-CC	264.06	LO <i>Cycladophora spongothrax</i>	9.1	FO <i>Acrosphaera australis</i>	10.4
14R-CC	276.07	LO <i>Cycladophora spongothrax</i>	9.1	FO <i>Acrosphaera australis</i>	10.4
15R-CC	283.43	LO <i>Cycladophora spongothrax</i>	9.1	FO <i>Acrosphaera australis</i>	10.4
16R-CC	295.95	LO <i>Cycladophora spongothrax</i>	9.1	FO <i>Acrosphaera australis</i>	10.4
17R-CC	300.99	LO <i>Cycladophora spongothrax</i>	9.1	FO <i>Acrosphaera australis</i>	10.4

Table T7 (continued).

Core, section	Depth (mbsf)	Minimum age constraint	Age (Ma)	Maximum age constraint	Age (Ma)
18R-CC	312.90	FO <i>Acrosphaera australis</i>	10.4	FO <i>Eucyritidium pseudoinflatum</i>	10.5
19R-CC	320.83				
20R-CC	331.36	FO <i>Acrosphaera australis</i>	10.4	FO <i>Eucyritidium pseudoinflatum</i>	10.5
21R-CC	341.57	FO <i>Acrosphaera australis</i>	10.4	FO <i>Eucyritidium pseudoinflatum</i>	10.5
22R-CC	348.94	FO <i>Acrosphaera australis</i>	10.4	FO <i>Eucyritidium pseudoinflatum</i>	10.5
23R-CC	358.14	FO <i>Eucyritidium pseudoinflatum</i>	10.5	LO <i>Actinomma golowini</i>	10.8
24R-CC	371.86	FO <i>Eucyritidium pseudoinflatum</i>	10.5	LO <i>Actinomma golowini</i>	10.8
25R-CC	374.11	LO <i>Actinomma golowini</i>	10.8	LO <i>Actinomma golowini</i>	10.8
27R-CC	391.62				
29R-CC	412.83				
30R-CC	424.08	LO <i>Actinomma golowini</i>	10.8	FO <i>Actinomma golowini</i>	13.5
31R-CC	431.04	LO <i>Actinomma golowini</i>	10.8	FO <i>Actinomma golowini</i>	13.5
32R-CC	446.36	LO <i>Actinomma golowini</i>	10.8	FO <i>Actinomma golowini</i>	13.5
33R-CC	457.23	LO <i>Actinomma golowini</i>	10.8	FO <i>Actinomma golowini</i>	13.5
34R-CC	464.36	LO <i>Actinomma golowini</i>	10.8	FO <i>Actinomma golowini</i>	13.5
35R-CC	474.91	LO <i>Actinomma golowini</i>	10.8	FO <i>Actinomma golowini</i>	13.5
36R-CC	481.38				
37R-CC	492.02				
38R-CC	500.08	LO <i>Cycladophora humerus</i>	10.6	FO <i>Desmospyris megarocephalis</i>	12.8
39R-CC	514.51				
40R-CC	520.60	LO <i>Cycladophora humerus</i>	10.6	FO <i>Desmospyris megarocephalis</i>	12.8
41R-CC	531.72				
42R-CC	539.12				
43R-CC	549.09				
44R-CC	558.42				
46R-CC	576.45				
47R-CC	589.96				
48R-CC	596.31				

Note: FO = first occurrence, LCO = last common occurrence, LO = last occurrence.

Table T8. Calcareous nannofossil abundance and preservation, Hole U1359D. (See table notes.)

Core, section, interval (cm)	Depth (m)		Abundance	Preservation	<i>Reticulolenestra minuta</i> / <i>Dictyococites productus</i>	<i>Reticulolenestra minutula</i> / <i>Dictyococites antarcticus</i>	<i>Reticulolenestra pseudoumblicus</i> / <i>Reticulolenestra gelida</i>
	Top	Bottom					
318-U1359D- 25R-1, 9–10	372.49	372.5	A	G	A	A	A
33R-2, 90–92	451.6	451.62	B				
33R-4, 33–35	454.03	454.05	B				
34R-2, 70–71	460.9	460.91	B				
34R-4, 19–20	463.39	463.4	R	M	R	R	R
35R-1, 82–83	469.02	469.03	R	M	R	R	R
35R-4, 72–73	473.42	473.43	B				
36R-1, 59–60	478.39	478.4	B				
37R-1, 72–74	488.12	488.14	C	M	C	C	F
38R-2, 62–63	499.12	499.13	B				
39R-1, 80–82	507.4	507.42	B				
40R-3, 63–64	519.83	519.84	B				
41R-2, 85–86	528.15	528.16	B				
48R-1, 74–74	593.34	593.34	B				

Notes: Abundance: A = abundant, C = common, F = few, R = rare, B = barren. Preservation: G = good, M = moderate. See “[Biostratigraphy](#)” in the “[Methods](#)” chapter for abundance and preservation definitions.

Table T9. Palynology, Holes U1359A and U1359D. (See table notes.)

Core, section, interval (cm)	Depth (mbsf)		Preservation	Dinocysts	Sporomorphs	Acritarchs	Foraminifer test linings	Black phytoclasts	Brown phytoclasts	Amorphous organic matter	Saccate pollen	Nothofagus pollen	Other pollen	Spores	Fungal spores	Sporomorphs reworked	Total dinocysts counted	Brigantidinium spp. psilate	Brigantidinium spp. rugulate	Cryodinium spp.	Echinidinium sp.	Enneadocysta dictyostila	Habibacysta tectata	Impagidinium brown	Impagidinium spp. indet.	Lejeunecysta spp.	"Round browns" indet., psilate	"Round browns" indet., rugulate	Selenopemphix nephroides psilate small	Selenopemphix thin walled	Spiniferites spp. indet.	Vozzhernikovia apertura	Vozzhernikovia spp. indet.	Algae sp. A			
	Top	Bottom																																			
318-U1359A-																																					
1H-CC, 0	0.62	0.62	M	B	A	B	B	F	F	F	F	B	B	A	B	12	0																				
2H-CC, 13	9.49	9.49	M	B	A	B	B	F	F	F	F	B	B	A	B	10	0																				
3H-CC, 11	19.27	19.27	M	B	A	B	B	F	F	F	F	B	B	A	B	15	0																				
4H-CC, 32	28.51	28.51	P	B	T	B	B	T	T	T	B	B	B	T	B	2	0																				
5H-CC, 18	29.28	29.28	P	B	T	B	B	T	T	T	B	B	B	T	B	4	0																				
6H-CC, 16	47.68	47.68	M	T	T	B	F	T	T	A	B	T	B	F	B	3	7		2				2		2	1											
7H-CC, 31	55.32	55.32	P	B	F	B	B	T	T	B	T	B	T	F	B	16	0																				
8H-CC, 10	66.55	66.55	M	T	F	B	B	B	T	B	T	B	T	F	B	17	1						1														
9H-CC, 3	75.75	75.75	M	F	C	B	T	T	T	T	T	B	T	C	B	24	15	3								10		2									
12H-CC, 24	104.84	104.84	P	B	F	B	B	B	T	B	T	B	T	F	B	9	0																				
15H-CC, 6	133.64	133.64	M	T	F	B	T	T	T	B	T	B	T	F	B	19	9	1							1	6		1									
18X-CC, 18	153.74	153.96	G	F	C	T	T	F	C	B	F	B	T	C	T	71	21	4		3			2	1	1	4	3							3			
21X-CC, 0	182.02	182.16	P	B	T	B	B	B	B	B	B	B	B	T	B	3	0																				
318-U1359D-																																					
6R-CC, 15-20	200.26	200.32	P	B	B	B	B	T	B	T	B	B	B	B	B		0																				
9R-CC, 17-22	227.68	227.73	P	T	T	B	B	A	B	T	T	B	B	T	B	3	1	1																			2
12R-CC, 17-22	253.61	253.66	G	C	T	T	F	F	F	F	T	B	B	T	B	2	31	3					11														
15R-CC, 14-19	283.38	283.43	M	C	T	T	T	T	T	T	T	B	B	T	B	1	16	3			1			1	1	2	2	2				3			1		
16R-CC, 16-21	295.9	295.95	G	C	T	B	B	T	T	T	T	B	T	T	B	1	19	9			1	3	3					4	1			1					
18R-CC, 0-5	312.85	312.9	P	T	T	B	T	T	T	T	T	B	B	T	B	1	3																				
21R-CC, 9-13	341.53	341.57	G	C	T	B	B	T	T	T	T	B	T	T	B	1	21	8			3						9	1									
25R-CC, 16-21	374.06	374.11	G	C	F	B	B	T	T	T	T	B	B	F	B	3	21	10	1								6	3					1				
29R-CC, 17-22	412.78	412.83	M	F	T	B	T	F	F	F	T	B	B	B	B	17	5						4				8										
32R-CC, 18-23	446.31	446.36	M	F	B	B	T	T	T	T	B	B	B	B	B	19	2			6			2		4	3	2										
35R-CC, 23-28	474.86	474.91	G	T	A	B	T	F	A	T	F	B	T	A	T	58	6	2					1		1	1	2										
38R-CC, 19-24	500.03	500.08	G	F	C	T	T	F	C	T	T	B	T	C	B	28	11	4		1				1		5											
40R-CC, 17-22	520.55	520.60	P	T	F	B	B	T	T	B	T	B	T	F	B	14	6	1					1	4													
44R-CC, 11-16	558.37	558.42	M	F	T	B	T	T	T	T	B	T	T	T	B	3	47	3	2					22	2	6	2	8		1	1						
45R-CC, 18-20	567.42	567.44	M	T	T	B	B	F	T	T	B	B	T	T	B	2	7	5	1					1													
47R-CC, 20-26	589.9	589.96	G	C	F	B	T	F	F	T	T	T	T	C	B	13	74	15		4																	
48R-CC, 20-25	596.26	596.31	G	C	F	B	T	T	T	T	T	T	B	F	B	4	41	12	4		3			19		2		1									

Notes: Preservation: G = good, M = medium, P = poor. Abundance: A = abundant, C = common, F = few, R = rare, T = trace, B = barren. See "Biostratigraphy" in the "Methods" chapter for abundance and preservation definitions.



Table T11. Biostratigraphic events and chronostratigraphy, Site U1359. This table is available in an [oversized format](#).**Table T12.** Magnetostratigraphic tie points, Site U1359. (See [table notes](#).)

Chron boundary	Age (Ma)	Core, section, interval (cm)		Depth (mbsf)		Depth (mcd)	
		Top	Bottom	Top	Bottom	Top	Bottom
318-U1359A-		318-U1359A-	318-U1359A-				
C1n (o)	0.781	3H-5, 10	3H-5, 15	16.20	16.25	17.82	17.87
C1r.1n (y)	0.988	4H-3, 40	4H-3, 45	23.00	23.05	24.08	24.13
C1r.1n (o)	1.072	4H-3, 120	4H-4, 90	23.80	25.00	24.88	26.08
C1r.2n (y)	1.173	4H-6, 20	4H-6, 25	27.30	27.35	28.38	28.43
C1r.2n (o)	1.185	4H-6, 65	4H-6, 70	27.75	27.80	28.83	28.88
C2An.1n (y)	2.581	6H-4, 95	6H-5, 100	44.05	44.70	42.29	42.94
C2An.3n (o)	3.596	9H-2, 115	9H-2, 120	69.75	69.80	69.81	69.86
318-U1359B-		318-U1359B-	318-U1359B-				
C2An.1n (y)	2.581	6H-1, 35	6H-1, 35	46.05	46.05	44.06	44.06
C2An.1r (y)	3.032	7H-3, 75	7H-3, 80	58.95	59.00	57.69	57.74
C3n.1n (y)	4.187	11H-2, 60	11H-2, 95	95.30	95.65	96.50	96.85
C3n.1n (o)	4.300	11H-3, 135	11H-3, 140	97.55	97.60	98.75	98.80
C3n.2n (y)	4.493	12H-7, 35	12H-7, 55	112.01	112.16	113.51	113.71
C3n.2n (o)	4.631	13H-3, 115	13H-3, 120	116.35	116.40	117.90	117.95
C3n.3n (y)	4.799	13H-6, 80	14H-2, 85	120.50	124.05	122.05	125.42
C3n.3n (o)	4.896	14H-4, 40	15H-1, 35	127.60	131.55	127.97	136.32
C3n.4n (y)	4.997	16H-1, 130	16H-1, 130	142.05	142.05	143.74	143.74
C3n.4n (o)	5.235	16H-4, 85	17H-1, 35	146.05	150.55	147.79	153.31
C3An.1n (y)	6.033	20H-4, 25	20H-4, 25	183.45	183.45	190.12	190.12
C3An.1n (o)	6.252	20H-6, 45	21H-1, 35	186.65	188.55	193.32	196.00
C3An.2n (y)	6.436	21H-4, 135	21H-4, 140	194.05	194.10	201.50	201.55
C3An.2n (o)	6.733	22H-5, 30	22H-5, 35	204.03	204.08	212.33	212.38
318-U1359C-		318-U1359C-	318-U1359C-				
C2An.1n (y)	2.581	5H-2, 75	5H-2, 80	37.95	38.00	41.38	41.43
C2An.1r (y)	3.032	7H-1, 20	7H-1, 30	54.90	55.00	59.24	59.34
C2An.1r (o)	3.116	7H-2, 95	7H-2, 100	57.15	57.20	61.49	61.54
C3n.3n (y)	4.799	13H-5, 35	13H-5, 40	118.05	118.10	125.37	125.42
C3n.4n (y)	4.997	15H-2, 110	15H-2, 115	133.30	133.35	139.00	139.05
C3n.4n (o)	5.235	16H-4, 140	16H-6, 10	146.11	147.83	152.17	153.89
318-U1359D-		318-U1359D-	318-U1359D-				
C3An.1n (y)	6.033	4R-5, 105	4R-5, 110	178.35	178.40	189.85	189.90
C3An.1n (o)	6.252	5R-1, 95	5R-1, 115	181.85	182.05	193.92	194.12
C3An.2n (y)	6.436	6R-1, 35	6R-1, 35	190.85	190.85	202.42	202.42
C3An.2n (o)	6.733	6R-5, 85	6R-6, 120	197.35	199.20	208.92	210.77
C4n.1n (y)	7.528	6R-7, 50	7R-1, 85	200.00	200.95	211.57	218.09
C4n.2n (o)	8.108	7R-3, 90	7R-3, 95	204.00	204.05	221.14	221.19
C4An (y)	8.769	7R-4, 140	7R-5, 10	206.00	206.20	223.14	223.34
C4An (o)	9.098	7R-7, 35	8R-1, 10	209.07	209.80	226.21	226.94
C5n.2n (y)	9.987	8R-2, 140	8R-3, 10	212.60	212.80	229.74	229.94
C5n.2n (o)	11.040	24R-4, 135	24R-4, 140	368.65	368.70	385.79	385.84
C5An.1n (y)	12.014	40R-2, 85	40R-2, 90	518.55	518.60	535.69	535.74
C5An.2n (o)	12.415	45R-2, 120	47R-1, 15	566.50	583.15	583.64	600.29

Notes: y = young, o = old. Correlations shown in Figure [F8](#). Ages from Gradstein et al. (2004) timescale.

Table T13. Major and trace element concentrations, Site U1359. This table is available in an [oversized format](#).



Table T14. Chemical composition of interstitial waters, Hole U1359B. (See table notes.)

Core, section, interval (cm)	Depth (mbsf)	pH	Salinity	Cl ⁻ (mM)	Na ⁺ (mM)	SO ₄ ²⁻ (mM)	NH ₄ ⁺ (μM)	NO _x (μM)	Alkalinity	DIC (mM)	PO ₄ ³⁻ (μM)	Mg ²⁺ (mM)	Ca ²⁺ (mM)	K ⁺ (mM)	Si (μM)	Sr (μM)	B (μM)	Mn (μM)
318-U1359B-																		
1H-1, 10–20	0.1	7.00	33.5	562	463.8	28.0	89.9	4.6	2.4	2.5	0.8	50.1	10.0	11.2	538.8	33.1	314.9	0.00
1H-1, 30–40	0.3	7.04	NA	558	465.4	27.8	72.3	4.3	2.5	2.6	2.5	49.4	9.9	11.5	570.1	32.0	328.9	0.00
1H-1, 50–60	0.5	7.03	NA	556	472.0	28.2	72.9	4.3	2.4	2.5	2.5	50.4	10.0	11.9	557.8	32.5	329.4	0.00
1H-1, 70–80	0.7	7.02	NA	561	465.5	28.0	NA	4.5	2.5	2.6	3.3	49.7	9.9	11.7	556.2	33.5	326.2	0.00
1H-1, 90–100	0.9	7.05	NA	550	466.1	27.8	91.8	4.5	2.6	2.5	3.1	49.9	10.0	11.7	553.8	34.3	320.9	0.00
1H-1, 110–120	1.1	7.03	NA	551	460.8	27.3	79.4	4.0	2.5	2.6	2.3	49.7	9.9	11.3	513.6	33.3	302.4	0.00
1H-1, 130–140	1.3	7.08	NA	560	471.6	28.1	70.8	4.0	2.6	2.7	3.0	50.9	10.2	11.7	528.1	34.4	313.6	0.00
1H-2, 10–20	1.6	6.94	33.5	557	473.6	28.2	92.4	4.2	2.6	2.7	2.8	50.3	10.1	11.5	512.1	33.3	322.9	0.00
1H-2, 30–40	1.8	6.76	33.5	559	471.2	27.9	75.7	4.0	2.7	2.8	3.5	50.2	10.0	11.8	511.0	33.8	325.3	0.00
1H-2, 50–60	2.0	7.03	NA	559	465.3	27.5	75.4	5.0	2.7	2.3	2.1	49.7	9.9	11.6	506.5	32.8	326.2	0.92
1H-2, 70–80	2.2	7.04	NA	559	459.7	28.4	84.0	1.2	2.8	2.8	2.3	49.4	10.0	11.6	533.3	34.7	341.9	5.70
1H-2, 90–100	2.4	7.04	NA	558	466.7	27.8	102.2	4.2	2.8	2.9	4.4	49.4	9.9	12.0	523.6	32.8	343.3	13.75
1H-2, 110–120	2.6	7.05	NA	557	460.0	28.8	122.9	3.9	2.7	2.8	7.7	49.4	10.1	11.6	515.8	34.8	342.9	18.47
1H-2, 130–140	2.8	7.03	NA	553	459.8	28.5	119.2	3.9	2.8	2.8	8.5	49.9	10.1	11.7	528.0	36.4	351.0	26.60
1H-3, 10–20	3.1	7.01	33.5	565	468.4	27.9	124.1	4.2	2.9	2.9	4.5	49.7	9.9	11.3	508.7	31.4	327.1	30.94
1H-3, 30–40	3.3	7.08	NA	553	461.4	28.3	105.9	4.0	2.9	2.8	9.6	49.8	10.1	11.7	512.6	33.9	338.1	37.09
1H-3, 50–60	3.5	7.09	NA	560	457.3	28.2	81.6	4.0	3.0	2.9	8.5	49.5	10.1	11.7	494.4	32.1	330.4	35.64
1H-3, 70–80	3.7	7.18	NA	555	458.8	28.5	112.4	3.8	3.2	3.1	9.5	49.3	10.1	12.2	497.4	31.7	341.3	40.00
1H-3, 90–100	3.9	7.28	NA	557	470.5	27.5	93.6	4.1	3.4	3.2	7.2	49.7	10.1	12.1	511.6	33.1	323.0	44.75
1H-3, 110–120	4.1	7.27	NA	552	458.3	27.6	87.4	3.8	3.2	3.2	10.5	49.7	10.2	10.8	484.6	31.3	290.6	44.97
1H-3, 130–140	4.3	7.12	NA	564	461.5	28.0	130.9	3.7	3.2	3.1	10.2	49.3	10.1	11.8	509.8	32.4	321.2	54.27
1H-4, 10–20	4.6	7.08	33.5	560	471.2	27.5	126.9	4.1	3.1	3.2	3.8	49.7	10.1	11.6	511.7	33.7	336.1	62.21
1H-4, 30–40	4.8	7.12	NA	565	458.8	27.7	93.6	3.9	3.1	3.1	10.7	49.1	10.1	11.8	500.1	30.7	307.4	63.50
1H-4, 50–60	5.0	7.12	NA	559	459.0	27.6	104.4	3.8	3.1	3.1	10.5	48.7	10.1	10.8	526.4	32.5	316.9	69.75
1H-4, 70–80	5.2	7.12	NA	570	457.6	27.4	170.7	3.8	3.1	3.0	10.6	49.5	10.2	10.3	479.8	31.6	302.3	71.45
1H-4, 90–100	5.4	7.09	33.5	556	562.2	26.5	89.0	3.9	3.2	3.3	7.2	72.3	14.5	12.4	514.9	32.7	335.7	78.67
1H-4, 110–120	5.6	7.14	NA	567	463.9	27.6	129.1	4.0	3.2	3.2	10.8	49.4	10.2	11.7	507.1	32.0	329.0	77.57
1H-4, 130–140	5.8	7.12	NA	560	462.9	27.5	105.3	4.5	3.2	3.2	11.1	49.2	10.2	11.9	482.8	32.0	318.5	81.46
1H-5, 10–20	6.2	7.13	33.5	562	468.0	26.8	94.5	3.9	3.3	3.4	8.1	48.4	9.9	11.3	494.1	31.2	339.4	82.07
1H-5, 30–40	6.4	7.13	NA	563	467.5	27.5	106.6	4.2	3.4	3.3	12.8	49.5	10.3	11.8	500.8	35.3	346.2	86.23
1H-5, 50–60	6.6	7.13	NA	557	463.5	27.5	109.0	4.1	3.4	3.3	11.9	49.3	10.2	11.6	488.8	32.5	336.5	82.50
1H-5, 70–80	6.8	7.07	NA	557	460.1	26.9	104.4	4.2	3.3	3.4	11.8	48.7	10.0	11.6	519.9	33.3	337.3	84.41
1H-5, 90–100	7.0	7.09	NA	562	468.5	26.6	75.4	4.0	3.5	3.4	8.8	48.9	10.0	10.5	509.6	32.9	351.0	89.93
1H-5, 110–120	7.2	7.08	NA	569	463.8	27.5	122.3	4.0	3.5	3.5	12.7	48.9	10.3	11.7	495.3	34.7	339.6	88.00
1H-5, 130–140	7.4	7.09	NA	550	459.1	26.8	181.5	4.0	3.4	3.5	12.5	49.1	10.1	11.3	499.1	33.7	323.5	88.71
2H-1, 30–40	8.0	7.18	33.5	568	471.7	26.1	114.0	4.0	3.8	3.7	6.5	48.2	10.1	11.6	547.7	33.9	402.0	107.65
2H-1, 80–90	8.5	7.09	NA	565	464.3	26.4	87.4	4.0	3.8	3.8	10.3	47.9	10.1	11.9	534.1	34.1	361.7	100.53
2H-1, 130–140	9.0	7.13	NA	562	465.7	26.6	82.2	4.1	4.0	4.0	10.7	47.4	10.0	11.8	546.0	33.5	392.3	106.26
2H-2, 30–40	9.5	7.30	33.5	562	471.7	25.8	83.1	4.1	4.1	4.1	9.2	48.0	10.1	11.9	526.7	31.9	356.4	99.14
2H-2, 80–90	10.0	7.29	NA	565	467.7	26.0	83.7	4.0	4.1	4.1	11.5	47.4	10.1	12.1	524.0	33.2	319.4	91.24
2H-2, 130–140	10.5	7.20	NA	565	467.0	25.7	110.0	4.1	4.1	4.1	13.6	47.0	10.0	11.6	533.4	31.8	304.1	91.65
2H-3, 30–40	11.0	7.29	33.5	565	476.0	25.6	101.9	4.0	4.2	4.2	10.3	47.8	10.0	11.4	534.8	30.4	339.6	97.39
2H-3, 80–90	11.5	7.24	NA	563	467.8	25.9	172.9	3.9	4.3	4.2	12.5	47.2	10.1	11.8	548.0	31.3	423.7	107.04
2H-4, 30–40	12.5	7.33	33.5	562	479.9	25.1	137.4	4.0	4.5	4.4	7.9	47.4	10.1	11.9	546.3	32.0	422.7	112.14
2H-4, 130–140	13.5	7.30	NA	562	466.1	24.9	143.0	4.0	4.6	4.5	9.5	46.9	10.1	11.0	542.9	32.7	350.7	102.66
2H-5, 80–90	14.5	7.27	33.5	534	473.7	24.0	104.1	3.9	4.6	4.7	4.9	46.8	10.1	11.6	539.8	31.0	393.8	108.34
2H-6, 30–40	15.5	7.35	33.5	564	597.0	24.2	97.6	4.1	5.2	4.8	7.0	71.8	15.1	12.6	579.9	32.4	433.2	109.79
2H-6, 124–134	16.4	7.98	NA	572	469.0	24.2	112.1	4.0	5.6	4.8	8.3	47.0	10.3	12.5	341.6	37.4	279.6	62.20
3H-1, 80–90	18.0	7.32	33.5	547	470.1	25.0	112.4	4.2	4.2	4.0	5.1	46.8	9.9	11.7	500.7	28.5	344.7	94.52
3H-2, 30–40	19.0	7.31	NA	568	473.2	22.9	89.0	4.0	5.2	5.0	6.3	45.9	10.0	11.4	579.8	35.4	378.1	91.80
3H-2, 140–150	20.1	7.67	NA	567	468.5	23.2	131.6	4.0	5.4	5.0	8.8	44.6	9.9	12.5	497.4	33.2	283.6	66.04

Notes: NO_x = sum of nitrite and nitrate concentrations. NA = not analyzed.

Table T15. Composite depth scale, Site U1359.

Core	Offset (m)	Top depth		Core	Offset (m)	Top depth	
		(mbsf)	(mcd)			(mbsf)	(mcd)
318-U1359A-				9H	5.20	73.70	78.90
1H	0.00	0.00	0.00	10H	5.65	83.20	88.85
2H	1.62	0.60	2.22	11H	7.17	92.70	99.87
3H	1.62	10.10	11.72	12H	7.74	102.20	109.94
4H	1.08	19.60	20.68	13H	7.32	111.70	119.02
6H	-1.76	38.60	36.84	14H	7.32	121.20	128.52
7H	0.45	48.10	48.55	15H	5.70	130.70	136.40
8H	0.08	57.60	57.68	16H	6.06	140.20	146.26
9H	0.06	67.10	67.16	17H	6.73	149.70	156.43
10H	0.65	76.60	77.25	18H	8.99	159.20	168.19
11H	2.44	86.10	88.54	318-U1359D-			
12H	2.14	95.60	97.74	2R	6.85	152.20	159.05
13H	2.22	105.10	107.32	3R	9.76	161.80	171.56
14H	5.59	114.60	120.19	4R	11.50	171.30	182.80
15H	5.59	124.10	129.69	5R	12.07	180.90	192.97
16H	5.59	133.60	139.19	6R	11.57	190.50	202.07
17H	5.21	143.10	148.31	7R	17.14	200.10	217.24
18X	7.83	145.40	153.23	8R	17.14	209.70	226.84
19X	9.70	155.00	164.70	9R	17.14	219.30	236.44
21X	6.47	174.20	180.67	10R	17.14	228.90	246.04
22X	8.40	183.90	192.30	11R	17.14	238.40	255.54
318-U1359B-				12R	17.14	248.00	265.14
1H	0.00	0.00	0.00	13R	17.14	257.60	274.74
2H	0.00	7.70	7.70	14R	17.14	267.20	284.34
3H	-1.60	17.20	15.60	15R	17.14	276.80	293.94
4H	-1.95	26.70	24.75	16R	17.14	286.30	303.44
5H	0.62	36.20	36.82	17R	17.14	295.90	313.04
6H	-1.99	45.70	43.71	18R	17.14	305.50	322.64
7H	-1.26	55.20	53.94	19R	17.14	315.10	332.24
8H	0.06	64.70	64.76	20R	17.14	324.70	341.84
9H	0.62	74.20	74.82	21R	17.14	334.30	351.44
10H	0.45	83.70	84.15	22R	17.14	343.90	361.04
11H	1.20	93.20	94.40	23R	17.14	353.50	370.64
12H	1.55	102.70	104.25	24R	17.14	362.80	379.94
13H	1.55	112.20	113.75	25R	17.14	372.40	389.54
14H	1.37	121.70	123.07	26R	17.14	382.00	399.14
15H	4.77	131.20	135.97	27R	17.14	391.60	408.74
16H	1.74	140.70	142.44	28R	17.14	401.20	418.34
17H	2.76	150.20	152.96	29R	17.14	410.80	427.94
18H	2.59	159.70	162.29	30R	17.14	420.40	437.54
19H	6.04	169.20	175.24	31R	17.14	430.00	447.14
20H	6.67	178.70	185.37	32R	17.14	439.60	456.74
21H	7.45	188.20	195.65	33R	17.14	449.20	466.34
22H	8.30	197.70	206.00	34R	17.14	458.70	475.84
23H	9.02	207.20	216.22	35R	17.14	468.20	485.34
24X	9.88	209.00	218.88	36R	17.14	477.80	494.94
25X	9.69	213.70	223.39	37R	17.14	487.40	504.54
26X	9.81	223.30	233.11	38R	17.14	497.00	514.14
27X	9.81	232.80	242.61	39R	17.14	506.60	523.74
28X	9.81	242.40	252.21	40R	17.14	516.20	533.34
318-U1359C-				41R	17.14	525.80	542.94
1H	0.00	0.00	0.00	42R	17.14	535.40	552.54
3H	3.43	16.70	20.13	43R	17.14	545.00	562.14
4H	3.43	26.20	29.63	44R	17.14	554.60	571.74
5H	3.43	35.70	39.13	45R	17.14	563.80	580.94
6H	3.43	45.20	48.63	46R	17.14	573.40	590.54
7H	4.34	54.70	59.04	47R	17.14	583.00	600.14
8H	4.70	64.20	68.90	48R	17.14	592.60	609.74

Table T16. Splice tie points, Site U1359.

Hole, core, section, interval (cm)	Depth			Hole, core, section, interval (cm)	Depth	
	(mbsf)	(mcd)			(mbsf)	(mcd)
318-				318-		
U1359C-1H-5, 8	6.08	6.08	Tie to	U1359A-2H-3, 86	4.46	6.08
U1359A-2H-6, 90	9.00	10.62	Append	U1359A-3H-1, 0	10.10	11.72
U1359A-3H-6, 35	17.96	19.58	Tie to	U1359B-3H-3, 88	21.18	19.58
U1359B-3H-7, 18	26.48	24.88	Tie to	U1359A-4H-3, 120	23.80	24.88
U1359A-4H-6, 108	28.18	29.26	Append	U1359C-4H-1, 0	26.20	29.63
U1359C-4H-5, 120	33.40	36.83	Append	U1359A-6H-1, 0	38.60	36.84
U1359A-6H-5, 123	45.83	44.06	Tie to	U1359C-5H-4, 43	40.63	44.06
U1359C-5H-6, 60	43.80	47.23	Tie to	U1359B-6H-3, 52	49.22	47.23
U1359B-6H-5, 83	52.63	50.64	Tie to	U1359C-6H-2, 51	47.21	50.64
U1359C-6H-7, 23	54.14	57.57	Tie to	U1359B-7H-3, 63	58.83	57.57
U1359B-7H-5, 102	62.21	60.95	Tie to	U1359C-7H-2, 42	56.62	60.95
U1359C-7H-6, 4	62.25	66.58	Tie to	U1359B-8H-2, 33	66.53	66.58
U1359B-8H-6, 31	72.51	72.57	Tie to	U1359C-8H-3, 66	67.86	72.57
U1359C-8H-7, 54	73.74	78.44	Tie to	U1359B-9H-3, 63	77.83	78.44
U1359B-9H-4, 78	79.48	80.10	Tie to	U1359A-10H-2, 135	79.45	80.10
U1359A-10H-7, 25	85.85	86.50	Tie to	U1359B-10H-2, 85	86.05	86.50
U1359B-10H-6, 24	91.43	91.88	Tie to	U1359C-10H-3, 3	86.23	91.88
U1359C-10H-6, 78	91.47	97.13	Tie to	U1359B-11H-2, 122	95.93	97.13
U1359B-11H-4, 129	98.99	100.19	Tie to	U1359A-12H-2, 95	98.05	100.19
U1359A-12H-6, 95	104.06	106.20	Tie to	U1359B-12H-2, 45	104.65	106.20
U1359B-12H-7, 32	111.93	113.48	Tie to	U1359A-13H-5, 16	111.26	113.48
U1359A-13H-7, 15	114.15	116.37	Tie to	U1359B-13H-2, 111	114.82	116.37
U1359B-13H-5, 105	119.25	120.80	Tie to	U1359C-13H-2, 28	113.48	120.80
U1359C-13H-5, 70	118.41	125.73	Tie to	U1359A-14H-4, 103	120.13	125.73
U1359A-14H-7, 52	123.62	129.22	Tie to	U1359C-14H-1, 69	121.90	129.22
U1359C-14H-3, 64	123.55	130.87	Tie to	U1359A-15H-1, 118	125.28	130.87
U1359A-15H-6, 96	132.56	138.15	Tie to	U1359C-15H-2, 25	132.45	138.15
U1359C-15H-6, 126	139.46	145.16	Tie to	U1359B-16H-2, 121	143.41	145.16
U1359B-16H-4, 75	145.95	147.69	Tie to	U1359C-16H-1, 143	141.63	147.69
U1359C-16H-6, 132	149.05	155.11	Tie to	U1359B-17H-2, 65	152.35	155.11
U1359B-17H-7, 50	159.32	162.08	Append	U1359B-18H-1, 0	159.70	162.29
U1359B-18H-7, 51	169.00	171.59	Tie to	U1359D-3R-1, 3	161.83	171.59
U1359D-3R-5, 95	168.75	178.50	Tie to	U1359B-19H-3, 26	172.46	178.50
U1359B-19H-6, 83	177.53	183.57	Tie to	U1359D-4R-1, 77	172.06	183.57
U1359D-4R-5, 121	178.51	190.01	Tie to	U1359B-20H-4, 14	183.34	190.01
U1359B-20H-7, 14	187.45	194.11	Tie to	U1359D-5R-1, 115	182.04	194.11
U1359D-5R-4, 90	186.30	198.37	Tie to	U1359B-21H-2, 122	190.92	198.37
U1359B-21H-6, 81	196.55	203.99	Tie to	U1359D-6R-2, 42	192.42	203.99
U1359D-6R-5, 18	196.68	208.25	Tie to	U1359B-22H-2, 95	200.15	208.25
U1359B-22H-6, 96	206.20	214.49	Append	U1359B-23H-1, 0	207.20	216.22
U1359B-23H-1, 150	208.70	217.72	Append	U1359B-24X-1, 0	209.00	218.88
U1359B-24X-1, 110	210.10	219.98	Append	U1359D-7R-2, 35	201.95	219.09
U1359D-7R-7, 48	209.20	226.34	Append	U1359D-8R-1, 0	209.70	226.84

Table T17. Temperature profiles, Hole U1359A. (See table notes.)

Core	Depth (mbsf)	Temperature (°C)	Thermal resistance (m ² K/W)
318-U1359A-			
4H	29.1	2.05	28.76
7H	57.6	3.47	61.01
10H	86.1	5.43	88.59
13H	119.6	7.17	116.64

Notes: Thermal resistance was calculated from thermal conductivity data (see “Physical properties”) corrected for in situ conditions (see “Downhole logging” in the “Methods” chapter).